Water Mass Changes in the North and South Pacific oceans between the 1960s and 1985-94

Annie Pik Shan WONG

BSc (Hons.)
University of New South Wales

MPOSc
University of Tasmania

A thesis submitted in fulfilment of the requirements for the degree of Doctor of Philosophy, Institute of Antarctic and Southern Ocean Studies, University of Tasmania, Australia.

Hobart
1999

Statement

This thesis contains no material which has been accepted for the award of any other degree or diploma in any tertiary institution, and that, to the best of my knowledge and belief, this thesis contains no material previously published or written by another person, except where due reference is made in the text of the thesis.

This thesis may be made available for loan and limited copying in accordance with the *Copyright Act 1968.*

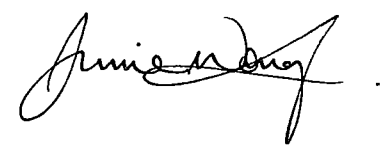

Abstract

Comparisons have been made along five modern hydrographic sections against historical hydrographic data to investigate water mass changes in the North and South Pacific oceans. The five modern hydrographic sections were sampled in the decade 1985-94, while the historical data were mostly from the late 1960s. Below the seasonal mixed layer, statistically significant temporal differences in temperature and salinity have been detected in the water masses that occur in the top 2000 dbar of the water column. These differences in water mass properties are assumed to result from sea surface changes at the formation regions.

Of all the water mass changes, the most spatially coherent ones come from the shallow salinity maxima of North Pacific Subtropical Water (NPSTW) and South Pacific Subtropical Water (SPSTW), and the intermediate salinity minima of North Pacific Intermediate Water (NPIW) and Antarctic Intermediate Water (AAIW). The two shallow salinity maxima, NPSTW and SPSTW, have shown signs of salinity increase, while the two intermediate salinity minima, NPIW and AAIW, have become fresher and, except along 17°S, have become warmer. Since NPSTW and SPSTW originate under the high evaporative cells of the subtropical North and South Pacific, and NPIW and AAIW acquire their properties near the polar gyres, these changes in the ocean interior imply an increase in net evaporation over the mid-latitudes, and an increase in net precipitation over the high-latitudes in both hemispheres. Together these results imply a strengthening of the hydrological cycle over the North and South Pacific oceans.

Outputs from a coupled climate model show that under increasing atmospheric CO_2, the model ocean responds with a warming of the water column in the top 300 dbar. Superimposed on this background warming trend is a decrease in salinity in the two intermediate salinity minima of the Pacific (NPIW and AAIW), and corresponds to near-surface freshening where their respective isopycnals outcrop. Hence the freshening signature that has been detected in NPIW and AAIW from observational data is qualitatively consistent with this climate model's response to increasing CO_2. However, natural variability cannot be discarded as a possible cause for the observed changes.

The steric sea level change for the area in the Pacific between 60°N and 31.5°S over the roughly 20-year study period is estimated to be a rise of 0.85 mm/yr. This is larger than that estimated by numerical models, and so demonstrates the usefulness of observational studies such as this in testing the effectiveness of numerical models in simulating the natural variability of the climate system.

Acknowledgements

This project was carried out under a National Greenhouse Advisory Committee PhD scholarship, with extra resources provided by the Antarctic Cooperative Research Centre. I wish to thank these organisations for their support.

The data presented in this thesis have been collected by many scientists, technicians, officers and crew on many research ships over many decades, collated and disseminated by various oceanographic institutions. I am grateful to these people, for our knowledge of the ocean is built on their patient effort in collecting these scientific data.

I wish to thank my two supervisors, Nathan Bindoff and John Church, without whose insightful comments and technical expertise, this project would have a very hard time coming into focus, let alone to fruition. Their revitalizing interest in the topic of ocean climate change has added much spark to this research.

The following people are gratefully acknowledged for providing patient discussions on various technical topics: Dave Jackett on neutral surfacing; Trevor McDougall on things that no one dares ask; Sue Wijffels on various facets of the Pacific; Tony Hirst, Bill Budd and Xingren Wu on the coupled climate model; and James Patterson on almost every computer and printer problem I have had. I would also like to acknowledge Dr.Harry Bryden for providing the WOCE P21 data, and Dr.Tony Hirst for providing the averaged CSIRO model output.

On a personal level, thanks to all the friendly faces around IASOS, and to those who I have hiked and climbed and got drunk with in Tassie over the past eight years. Inspirations have come from strange places.

Lastly, to Brendan Buckley, who has stood by me despite the distance.

Contents

Chapter 1

Introduction

1.1 Detection of decadal changes

In recent years, there is a growing focus on documenting long-term, large-scale variability and changes in the earth's climate system, in an attempt to detect climate change "signals" caused by the enhanced greenhouse effect. Most of these studies have focused on surface air temperature as a single study parameter. These studies range from using large-scale averaging methods for investigating long-term mean trends (e.g. Jones (1988)), to using pattern-based methods for comparing spatial patterns of change in observations with those from model forecasts (e.g. Barnett and Schlesinger (1987), Parker et al. (1994)).

Pattern-based methods are part of the so-called "fingerprint" method. The fingerprint method involves the identification of a multivariate signal that is unique to the enhanced greenhouse effect (e.g. Santer et al. (1995)). The multivariate signal can involve several parameters at one location, or a single parameter at several locations, or several parameters at several locations. For example, Karoly et al. (1994) used the zonal mean atmospheric temperature change (one parameter) as a function of height and latitude (several locations) to define their multivariate signal.

Similar pattern-based detection of multivariate signals in the ocean interior has not been carried out on a global basis, primarily because of the limited availability of long-term, large-scale oceanographic observations. However, it is important to study decadal-scale changes in the ocean because not only is the ocean an integral part of the climate system, but it also plays an important role in modifying the global distribution of heat and freshwater. In model experiments with increasing greenhouse gas forcings, certain qualitatively consistent changes are apparent in the ocean circulation, e.g. reductions in deep

water formation in the North Atlantic (e.g. Mikolajewicz et al. (1990)). However, it is not clear how the properties of the water masses that are responsible for inter-basin exchange of heat and salt will alter under the enhanced greenhouse effect.

All waters in the world's oceans have characteristics that ultimately are the results of atmospheric conditions at the sea surface from some point in time, that have subsequently been modified along the subduction paths. The surface conditions that have effects on the water masses of the world's oceans therefore include surface temperature, surface salinity, and surface wind stress curl. Surface temperature and salinity control the strength of the buoyancy-driven convection, as well as give the water masses their potential temperature (θ) - salinity (S) properties. Surface wind stress curl determines the subduction rates due to Ekman pumping and the wind-driven circulation, both of which are responsible for distributing the water masses (Woods 1985). The circulation of the water masses around the global ocean, and their subsequent mixing, serve to distribute these surface information into the interior of the ocean. Any significant long-term changes to these surface conditions will therefore manifest themselves at some later time in the ocean interior beneath the seasonally-affected surface mixed layer.

Historically, most large-scale oceanographic studies have attempted to explore the ocean interior with little focus on variability. As data sets have grown in recent years, more emphasis has been placed on studying oceanic variability and long-term changes, with the North Atlantic being the most studied ocean, because of the relatively dense data sets available. Since the mid 1980s, many one-time surveys and repeat surveys have been conducted around the world's oceans under the World Ocean Circulation Experiment (WOCE). As a result of WOCE, there are now opportunities to explore long-term interior changes in other ocean basins. This thesis presents the first systematic study of decadal-scale changes in the North and South Pacific oceans, using five one-time hydrographic surveys from WOCE that are situated in areas with dense historical hydrographic data.

1.2 Observations of changes in the ocean interior

The North Atlantic

Most studies that utilize oceanographic observations to document large-scale changes in the ocean's interior have been carried out in the North Atlantic, where several deep-ocean transects have been repeated over the past 20 to 30 years. Based on repeats of two hydrographic lines along 24°30' N and 36°16' N, Roemmich and Wunsch (1984) reported ocean-wide warming in the subtropical North Atlantic, from 700 m to 3000 m, between 1957/1959 and 1981. Another repeat survey along 24°30' N during 1992 showed that this mid-depth warming had continued, and that the subtropical North Atlantic was responding to wind and buoyancy forcing conditions of the past 35 years (Parrilla et al. 1994). Bryden et al. (1996) quantified the observed changes along 24°N, and showed that the warming from 1957 to 1981 observed by Roemmich and Wunsch (1984) was principally due to downward displacements of isopycnals, while the continued warming from 1981 to 1992 observed by Parrilla et al. (1994) was more likely the result of changes in the water mass characteristics. A 73-year time-series established using data from a hydrographic station at Bermuda (western subtropical Atlantic) also shows a long-term temperature increase trend in the 1500-2500 dbar layer (Joyce and Robbins 1996). More recently, Joyce et al. (1999) showed that in the western part of the subtropical gyre between 20°N and 35°N, Labrador Sea Water has become colder and fresher since 1992, and the warming trend observed by Bryden et al. (1996) has continued to 1997.

Further north, Brewer et al. (1983) observed widespread decrease in salinity along approximately 59°N, between 1962 and 1981, that corresponded to a decrease of surface salinity of the North Atlantic over the past three decades. Read and Gould (1992) also reported cooling and freshening of subpolar North Atlantic water between Greenland and the United Kingdom, between 1962/1981 and 1991, and proposed that the changes were caused by variations in the renewal of Labrador Sea Water (LSW). In 1993, the 36°16' N line was repeated again. A zonal band occupied by LSW, that was seen to have warmed between 1959 and 1981 (Roemmich and Wunsch 1984), was seen to have cooled between 1981 and 1993 (Tereschenkov et al. 1995), in accordance with the result of Read and Gould (1992). Dickson et al. (1996) reviewed the

recent changes in the North Atlantic and proposed that winter convection at the three convective renewal sites of the North Atlantic: the Greenland/Iceland Sea, the Labrador Sea, and the Sargasso Sea, evolved in phase but at difference signs during this century, and that this decadal evolution was driven by the North Atlantic Oscillation.

Where repeats of ocean-wide transects are not available, some investigators use historical data where and when the coverage allows for studying large-scale ocean variability over time. Levitus (1989) composited and compared two pentads of historical hydrographic observations: 1955-1959 and 1970-1974, and found the intermediate depths of the North Atlantic subtropical gyre to be colder and fresher during 1970-1974, compared to 1955-1959. This is different from the result of Roemmich and Wunsch (1984), which spanned another decade after the 1970s. In the subarctic region, Levitus (1989) found that the western half of the North Atlantic have warmed and become more saline, while the eastern half south of Iceland was found to have cooled and freshened. Changes in the subtropical gyre were seen to be consistent with an upward displacement of density surfaces, in contrast to the eastern subarctic gyre, where T-S changes were nearly density-compensating. Thus different phenomena seemed to be responsible for T-S changes in different regions of the North Atlantic.

Antonov (1993) used historical hydrographic station data to construct a set of annual-mean ocean temperature time series for the period 1957-1981, for both the North Atlantic and the North Pacific. While there were large areas in both oceans where cooling trends or warming trends dominated, as a whole, the ocean temperature averaged over the North Atlantic Ocean, from the equator to 70°N, showed warming from 600-700 m to 2500-3000 m, comparable to the result of Roemmich and Wunsch (1984).

The Pacific

The Pacific Ocean is different from the North Atlantic in that, excluding the Southern Ocean portion, no deep or bottom water is formed locally. Its abyssal waters are renewed by input from the Southern Ocean, and have renewal rates of the order of centuries. This slow advection allows ample time for mixing, and so the deep waters of the Pacific have more uniform water properties than the other major ocean basins. Water masses formed within the Pacific occupy the permanent thermocline and the intermediate depths of the Pacific Ocean, and have renewal rates of the order of decades. The Pacific

Ocean is therefore an ideal ocean to test the hypothesis that if any significant changes have occurred in the atmosphere over the Pacific region during the past few decades, then these changes should manifest themselves in the permanent thermocline and the intermediate depths of the Pacific Ocean, while the water mass properties of the deep Pacific should remain largely unchanged. Any deep Pacific changes would therefore imply Southern Ocean changes. Antonov (1993) has observed no significant ocean temperature changes in the North Pacific, averaged from the equator to 60°N, below 500-700 m over the 25 years between 1957-1981. During the same period the North Atlantic has been observed to have warmed from 600-700 m to 2500-3000 m. It was concluded that this asymmetry was due to the different deep water ventilation mechanisms at the two oceans.

The Pacific does not enjoy as many repeat surveys as the North Atlantic. To date, the few repeat hydrographic transects that could be used to study water mass decadal changes are mostly restricted to the western basins. In the North Pacific, the Japanese Meteorological Agency has been repeating an oceanographic survey along the 137°E meridian since 1967 (designated WOCE PR2). Suga et al. (1989) and Suga and Hanawa (1995a) have successfully used this time-series data set to demonstrate that the interannual variability of the volume of North Pacific Subtropical Mode Water is strongly related to the Kuroshio meanders. Using the same data set, Qiu and Joyce (1992) have shown that the subduction of North Pacific Intermediate Water (NPIW) is also dependent on the Kuroshio meanders. Shuto (1996) found correlations between the interannual variations of the areas of the tropical saline water and NPIW, and the wind-stress curl minimum in the area southeast of Japan.

In the South Pacific, the western portions of the 1967 SCORPIO transects along 28°S and 43°S, between Australia and New Zealand, were reoccupied in 1989 and 1990. Using these repeats, Bindoff and Church (1992) observed cooling on isopycnals, but warming at constant depths, in waters in the main thermocline along both latitudes, as well as in intermediate levels along 43°S. Johnson et al. (1994) studied three hydrographic sections across the Samoa Passage, spanning 25 years, and detected decadal-scale variability in modified North Atlantic Deep Water (NADW) in the Samoa Passage: NADW salinity signature in the Samoa Passage was absent in 1968, strong in 1987, and weak again in 1992. Bindoff and Wunsch (1992) compared a climatologically mapped section with a modern hydrographic section at 15°S in the South Pacific Ocean, and observed significant east-west difference in the spatial pattern of

temperature and salinity changes in the top 300 dbar that could be related to the 1987 El Niño.

Analysis on isopycnals

Ocean processes observed on isobaric surfaces contain effects of heave and Rossby waves. Hence for the purpose of studying water mass property changes, isopycnal surfaces are a more appropriate coordinate system for analysis. In a study concerning the ocean's response to a warmed atmosphere, Church et al. (1991) pointed out the counter-intuitive feature that, in a "warming without salinity change" scenario, the effect of warmed water subducted into the thermocline would be to cause an observed cooling (and corresponding freshening) on isopycnals. Bindoff and McDougall (1994) expanded this concept and formalised three "pure" processes that could result in subsurface changes in θ and S. These three idealised subduction processes are called "pure warming (or cooling)", "pure freshening (or salinification)", and "pure heaving". An inverse approach was employed to distribute any observed subsurface temporal changes into three components, due to these three processes.

By this method, the observations of Bindoff and Church (1992) from the Tasman Sea were interpreted as the result of surface warming in the formation region of Subantarctic Mode Water (SAMW), and surface freshening in the formation region of Antarctic Intermediate Water (AAIW). Johnson and Orsi (1997) presented more observations on isopycnals from repeats of a meridional line along 170°W (between 1968/9 and 1990), and a zonal line along roughly 35°S (between 1969 and 1991). They supported previous findings by Bindoff and Church (1992) and Johnson et al. (1994): that the observed changes in SAMW and AAIW in the southwest Pacific were consonant with surface warming and freshening in the southern high latitudes, and that there had been a reduction in strength of the modified NADW between 1987 and 1992.

Similar investigation has being carried out for the subtropical Indian Ocean, and the same water mass changes have been observed: that SAMW appeared to have been affected by surface warming, and AAIW by surface freshening (Bindoff and McDougall in press).

1.3 Natural variability in the Pacific climate system

The Pacific coupled ocean-atmosphere system has been known to exhibit decadal variability. Perhaps the most well-known climate phenomenon in the Pacific region is the El Niño - Southern Oscillation in the equatorial Pacific, which has decadal effects over the rest of the Pacific region and the Southern Ocean. For example, Jacobs et al. (1994) derived from satellite data that mid-latitude Rossby waves, generated by reflection of an equatorial Kelvin wave from the American coasts in response to the 1982-83 El Niño, propagated to the northwest corner of the Pacific Ocean a decade later. These Rossby waves appeared to have caused a northward re-routing of the Kuroshio Current, which led to significant increases in SST in the northwestern Pacific during 1991. More recently, White and Peterson (1996) suggested that, through atmospheric teleconnection, El Niño activities in the equatorial Pacific might have initiated what is now known as the Antarctic Circumpolar Wave observed in the Southern Ocean.

One of the better-known examples of coupled ocean-atmosphere variability in the Pacific is the simultaneous changes in SSTs, surface winds and organised convection observed over the tropical Pacific during the 1970s and the 1980s. These anomalies represent a shift in the background state of the coupled ocean-atmosphere system over the tropical Pacific, and seem to have forced changes in the mid-latitude atmospheric circulation (Graham 1994). Trenberth and Hurrell (1994) provided further evidence that between 1976 and 1988, the North Pacific went through an anomalous period that was characterised by a deep Aleutian low.

To determine the physical mechanisms behind this kind of decadal-scale climate variability, many investigators have analysed data from coupled ocean-atmosphere models. These studies have provided much insight into the ocean's response to external forcings in the Pacific region. Latif and Barnett (1994) and Latif and Barnett (1996) have shown that the ocean and atmosphere can form a positive feedback system that is capable of amplifying disturbances. For example, when the North Pacific subtropical gyre is anomalously strong, more warm waters are transported north by the Kuroshio, leading to a reduced meridional SST gradient. The westerlies are subsequently reduced, which, in turn, reduces the mixing in the ocean and thus strengthens the initial positive SST anomaly. Changes in the wind stress curl eventually force the subtropical

gyre to weaken, but because the ocean's response lags behind the wind stress curl change, an oscillatory mode is set up that has a period of decades. By using all historical temperature profiles available at the National Oceanographic Data Center, Zhang and Levitus (1997) observed a clockwise rotation of temperature anomalies, at 250 m depth, propagating around the entire North Pacific between 1961 and 1990, that resembles the decadal-scale oscillation suggested by Latif and Barnett (1994) and Latif and Barnett (1996).

Evidence from sea surface temperature records shows that the changes that took place in the 1970s and the 1980s in the Pacific are part of a pattern of interdecadal climate variability known as the Pacific Decadal Oscillation (PDO) (Mantua et al. 1997). The PDO is centred over the mid-latitude North Pacific, and has, during this century alone, changed polarity around 1925, 1947 and 1977.

Relatively few studies on similar coupled ocean-atmosphere variability in the South Pacific have been done, partly owing to a lack of data in the region. However, by using NCEP-NCAR reanalysis data, Garreaud and Battisti (1999) have demonstrated that the South Pacific also displays interdecadal (ENSO-like) variability in sea surface temperature, and whose spatial patterns are symmetrical about the equator with their counterpart in the North Pacific.

1.4 Objectives and layout of the thesis

The aim of this thesis is to undertake the first systematic study of decadal changes in the interior of the North and South Pacific oceans, using five newly available trans-oceanic hydrographic surveys from the World Ocean Circulation Experiment (WOCE), and subsequently infer variations in the surface conditions from the observed subsurface differences. The observed changes are compared with outputs from a coupled climate model with increasing CO_2 to identify qualitative consistencies between model outputs and observations. Whether climate change can be detected in ocean observations or not, comparison studies that employ modern large-scale ocean observations, such as the one presented in this thesis, introduce new knowledge about ocean variability and change. This knowledge is important for validating numerical models that are used to predict climate variability and change.

The specific objectives of this thesis therefore are:

- to determine if any significant changes have occurred in the interior of the North and South Pacific oceans over the past decades;
- to determine the relative roles of the surface conditions that can cause water mass property changes: change in surface temperature, and change in surface net precipitation rate; and
- to determine whether the patterns of these observed changes are consistent with outputs from numerical models with greenhouse gas increases over the same period.

To detect decadal changes in the ocean interior, relatively randomly distributed historical hydrographic data are compared with five modern one-time CTD transects that have been surveyed during WOCE. The historical data are objectively mapped to the coordinates of the modern one-time transects, so that these spatially disparate data sets can be compared as pseudo-repeats. The observed changes presented in this thesis are therefore temporal differences between two time snap-shots, and so are not the same type of time-series studies such as the investigation done along the North Pacific 137°E meridian (e.g. Suga and Hanawa (1995a)), or work done at ocean stations such as that at Bermuda (Joyce and Robbins 1996). The nature of this study is more akin to the North Atlantic work by Bryden et al. (1996) along

24°N, and Read and Gould (1992) along 59°N. The uniqueness of this study lies in its large spatial scale: by systematically studying two adjoining ocean basins, the North and South Pacific, this work is able to identify consistent changes in water masses that are of planetary scales, and to estimate steric height change in the Pacific over the past 20 years.

The diagnostic method of Bindoff and McDougall (1994) is used to analyse and interpret subsurface temporal changes in temperature and salinity along these transects. Chapter 2 describes this method. Chapter 3 introduces the data sets used in this thesis, and details the interpolation procedure that has been applied to the data. The manner in which the Bindoff and McDougall (1994) method have been applied to the data sets are also explained. Chapters 4 and 5 describe the decadal changes observed along five one-time WOCE transects in the North and South Pacific oceans. It will be seen that significant water mass property changes have occurred in the top 2000 dbar of the water column. In Chapter 6, differences found in the observations are compared with differences for the same period from a climate model experiment that has been forced by an increasing level of equivalent atmospheric carbon dioxide. It is found that the observed upper ocean warming and the large-scale freshening of North Pacific Intermediate Water and Antarctic Intermediate Water are qualitatively consistent with the transient response of the model experiment under an enhanced greenhouse effect, but spatially different because of poor propagation of water masses in the model. Discussion and conclusions of the results of this thesis are presented in Chapters 7 and 8.

Chapter 2

A method for analysing temporal changes in hydrographic data

The main analysis tool in this thesis is a diagnostic method developed by Bindoff and McDougall (1994) for identifying the surface process (or processes) responsible for the subsurface temporal changes in potential temperature and salinity, observed along repeats of hydrographic sections. The method utilizes the relations between isobaric and isopycnal differences in potential temperature θ, salinity S, and pressure P (for isopycnal surfaces) under three idealised processes: *pure warming* (*cooling*), *pure freshening* (*salinification*), and *pure heaving*, to determine the factors responsible for changes in the ocean interior. A linear system is established using these three processes as basis functions, and then inverse methods are employed to estimate the strength of these three processes in causing the observed changes. The assumptions and theories behind this method are presented in this chapter.

2.1 Water mass properties and subduction

Temperature (θ) and salinity (S) properties of water masses are derived, directly or indirectly, at the sea surface, and are then injected into the ocean interior by subduction. The term *subduction* is usually referred to as the process by which waters of the surface mixed layer are pumped into the permanent thermocline, following the isopycnal surfaces of their own densities. However, *subduction* in this thesis is used to include several mechanisms.

In the low and middle latitudes, the permanent thermocline is ventilated when waters of the surface mixed layer are subducted by a combination of downward Ekman pumping and geostrophic flows through the sloping surface

marking the top of the permanent thermocline (Woods 1985). Both these mechanisms are wind-driven. Intermediate water masses, which are spread along intermediate depths below the thermocline in the subtropical gyres, are not ventilated by wind-driven subduction, but are ventilated by subduction due to convection (buoyancy-driven) (p. 54-59, Tomczak and Godfrey (1994)). Convective mixing occurs at the poleward side of the subtropical gyres, where deep mixed layers are formed by winter cooling. In other words, intermediate waters are not directly derived from the surface mixed layer, but are partly the product of subsurface mixing. In high latitudes, intense surface cooling and deep wintertime convection lead to the formation of deep and bottom waters, which join the global thermohaline circulation as abyssal layers.

Whatever the driving agent, water masses after subduction follow surfaces of constant potential vorticity within each isopycnal layer (Luyten et al. 1983). With time, the properties of a water mass as derived from its source region may be abated by mixing along its spreading path. That is, away from its source region, the θ and S properties of a water mass are at least partly determined by the effects of mixing. However, in the ocean interior, the transfer of properties is dominated more by isopycnal processes than by mixing processes. Hence in this thesis, it is assumed that interior water mass changes are caused, as the first approximation, by changes in sea surface conditions at the source regions.

Traditionally, comparisons of hydrographic data have been done at constant depths. But viewing differences on isobars alone is inadequate for diagnosing the cause of the change, because differences on isobars contain the effects of both true water mass property changes and isopycnal movements. On the other hand, θ and S differences observed on isopycnals can be due to lateral "wobble" of a water mass, or can be due to real water mass property changes as a result of altered surface conditions. In the case of a real θ-S characteristic change, information provided by observations on isopycnals alone are also inadequate for interpreting the cause of the change. For example, when the θ-S changes are not density-compensating (i.e. when viewed along isobars, a change in temperature is not accompanied by a compensating change in salinity, hence causing a change in the density of a water mass), a water mass would move to a different isopycnal, and so examining differences along a constant density surface alone would not be adequate. The most thorough analysis of water mass changes therefore requires the complementary views from the two reference frames: on isobars and on isopycnals. The relations between these two reference frames are developed in the following section.

2.2 The relations between θ-S changes on isobars and on isopycnals

Following the notation of Bindoff and McDougall (1994), let $\theta'|_z$ and $S'|_z$ be the subsurface temporal changes in θ and S respectively at a constant pressure z (dbar), and let $\theta'|_n$ and $S'|_n$ be those changes at a constant density (kg m^{-3}). We have chosen to use *neutral density* γ^n (McDougall 1987), which, by definition, has the property that $\alpha\nabla_n\theta = \beta\nabla_n S$, where the gradient operator ∇_n is defined on a neutral surface in space. The definition is also true for a neutral surface in time, so that

$$\alpha\theta'|_n = \beta S'|_n \tag{2.1}$$

The two variables, $\theta'|_z$ and $\theta'|_n$ (similarly for $S'|_z$ and $S'|_n$), are related by the temporal change in pressure, N', of the density surface γ^n. Consider a θ-S curve that has undergone changes from time t_1 to time t_2, as depicted in Figure 2.1. For a water parcel at point 1, $\theta'|_n = \theta_2 - \theta_1$ and $\theta'|_z = \theta_3 - \theta_1$. So that $\theta'|_n - \theta'|_z = \theta_2 - \theta_3$. Similarly, $S'|_n - S'|_z = S_2 - S_3$.

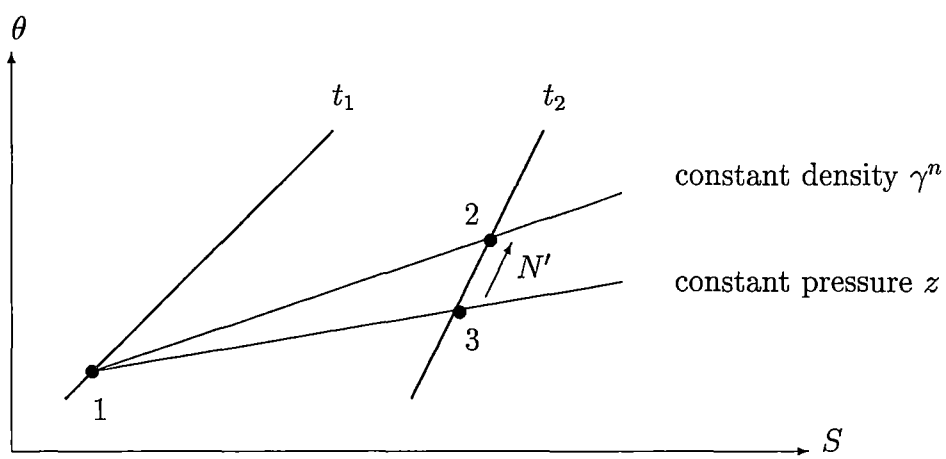

Figure 2.1: A schematic diagram of a θ-S curve that has undergone changes from time t_1 to time t_2.

By assuming that the vertical motions are small, $\theta_2 - \theta_3$ and $S_2 - S_3$ can be approximated by the first term of the Taylor's series expansion. Hence, $\theta_2 - \theta_3 = N'\theta_z$ and $S_2 - S_3 = N'S_z$. Here, the z-axis is positive upward, so $N' = P_2 - P_3$ is positive if the constant density surface becomes shallower in time. θ_z and S_z are the vertical potential temperature and salinity gradients

respectively in pressure coordinates, and are evaluated at the time-averaged pressure of $P_m = (P_2 + P_3)/2$. As the gradients are evaluated at the time-averaged pressures, the quadratic terms in the Taylor's series expansions are eliminated, so that the first-order expansions have errors which are cubic rather than quadratic. It is also consistent with the numerical method used for labelling the neutral surfaces (Jackett and McDougall 1997). The relations between θ and S changes on isobars and on isopycnals can then be written as:

$$\theta'|_n - \theta'|_z = N'\theta_z \tag{2.2}$$

$$S'|_n - S'|_z = N'S_z \tag{2.3}$$

These relations can be further expressed in terms of the slope of the θ-S curve, which is given by the *stability ratio* (Turner 1981),

$$R_\rho = \alpha\theta_z/\beta S_z \tag{2.4}$$

where

$$\alpha = -\frac{1}{\rho}\frac{\partial\rho}{\partial\theta}\,|_{S,p}$$

is the thermal expansion coefficient with unit $^\circ C^{-1}$, and

$$\beta = \frac{1}{\rho}\frac{\partial\rho}{\partial S}\,|_{\theta,p}$$

is the haline contraction coefficient (pss^{-1}). Multiplying Equations 2.2 and 2.3 respectively by α and β, and using Definition 2.4, gives

$$\alpha\theta'|_n - \alpha\theta'|_z = \alpha(\theta_2 - \theta_3) = \alpha N'\theta_z = R_\rho\beta(S_2 - S_3) \tag{2.5}$$

$$\beta S'|_n - \beta S'|_z = \beta(S_2 - S_3) = \beta N'S_z = \frac{1}{R_\rho}\alpha(\theta_2 - \theta_3) \tag{2.6}$$

The six variables $\alpha\theta'|_z$, $\beta S'|_z$, $\alpha\theta'|_n$, $\beta S'|_n$, $\alpha N'\theta_z$, and $\beta N'S_z$, are dimensionless variables. While Equations 2.5 and 2.6 are valid for all subsurface temporal θ-S changes, they can be reduced to three simple relations that describe the resultant θ-S changes specific to three "pure" processes: *pure warming* (*cooling*), *pure freshening* (*salinification*), and *pure heaving.* These three processes are described in the following section.

2.3 Three "pure" processes responsible for the changes

In the Bindoff and McDougall (1994) diagnostic method, observed temporal changes in θ and S are assumed to be the result of a combination of three ventilation processes: *pure warming (cooling)*, *pure freshening (salinification)*, and *pure heaving*. The *pure warming (cooling)* process assumes that sea surface temperature has changed, but surface salinity has remained constant. The *pure freshening (salinification)* process assumes that sea surface temperature has remained constant, but surface salinity has changed (due to changes in evaporation and/or precipitation patterns). Both of these processes will cause θ-S property changes, which are advected into the ocean interior. The third process, *pure heaving*, assumes that neither sea surface temperature nor surface salinity has changed (hence no changes in water mass θ-S property), but that vertical movements of the isopycnals cause temporal changes in θ and S when observed at constant depths. Such vertical motions of isopycnals can be caused by altered surface wind-stress curl patterns, which can in turn alter oceanic circulation and thus the depths of isopycnals. The theoretical relationships between $\alpha\theta'|_z$, $\beta S'|_z$, $\alpha\theta'|_n$, and $\beta S'|_n$ under these three processes are developed below.

2.3.1 Pure warming (cooling)

The first ventilation process assumes that surface temperature has increased or decreased, but surface salinity has remained constant. The subduction process is also assumed to have remained unchanged. This scenario is termed *pure warming* or *pure cooling*. The resulting θ-S change is non density-compensating. In the case of *pure warming*, fluid that normally subducts along density γ_1^n will subduct along a lighter density γ_2^n. As fluids are being redirected from γ_1^n to γ_2^n, the isopycnals inbetween γ_1^n and γ_2^n are pushed downward, but the depths of the isopycnals below γ_1^n and above γ_2^n remain constant. The overall volume between γ_1^n and γ_2^n remains constant. Consequently the volume-averaged temperature between γ_1^n and γ_2^n increases, while the volume-averaged salinity remains unchanged. In other words, at a constant depth, the potential temperature will increase, but the salinity is unchanged; the salt content of the surface waters is preserved as they subduct into the ocean interior under this idealised ventilation scheme.

Therefore, if z is the average pressure between γ_1^n and γ_2^n at a geographic location, then $\theta'|_z > 0$ and $S'|_z = 0$ for *pure warming*. Similarly, $\theta'|_z < 0$ and $S'|_z = 0$ for *pure cooling*. Since $S'|_z = 0$ in both cases, from Equation 2.6, $\beta S'|_n = \beta(S_2 - S_3) = \beta N' S_z$. It follows from Equations 2.1 and 2.5 that

$$\alpha\theta'|_n - \alpha\theta'|_z = R_\rho\beta(S_2 - S_3) = R_\rho\beta S'|_n = R_\rho\alpha\theta'|_n$$

So for the *pure warming (cooling)* scenario,

$$\boxed{\alpha\theta'|_n = \frac{\alpha\theta'|_z}{1 - R_\rho} = \beta N' S_z} \tag{2.7}$$

Thus at areas where $R_\rho > 1$ (e.g. at the permanent thermocline), *pure warming* manifests itself as a temperature and salinity decrease on neutral surfaces, and is accompanied by a downward displacement of isopycnals.

2.3.2 Pure freshening (salinification)

The second ventilation process assumes that surface salinity has decreased or increased, but surface temperature has remained constant. Again, the subduction process is assumed to have remained unchanged. This scenario is termed *pure freshening* or *pure salinification*. The resultant θ-S change is also non density-compensating. Following similar logic as for the *pure warming (cooling)* scenario, a water mass that has undergone *pure freshening* (or *salinification*) will, after subducting along a lighter (or denser) isopycnal, cause the volume-averaged salinity between the initial and final isopycnals to decrease (or increase), while the average temperature remains unchanged at a constant depth. Therefore, $S'|_z < 0$, $\theta'|_z = 0$ for *pure freshening*, and $S'|_z > 0$, $\theta'|_z = 0$ for *pure salinification*. In both cases, $\theta'|_z = 0$; in other words, the heat content of the surface waters between isopycnals is preserved as they subduct into the ocean interior. From Equation 2.5, $\alpha\theta'|_n = \alpha(\theta_2 - \theta_3) = \alpha N' \theta_z$. Using Equations 2.1 and 2.6,

$$\beta S'|_n = \beta S'|_z + \frac{1}{R_\rho}\alpha(\theta_2 - \theta_3) = \beta S'|_z + \frac{1}{R_\rho}\alpha\theta'|_n = \beta S'|_z + \frac{1}{R_\rho}\beta S'|_n$$

So for the *pure freshening (salinification)* scenario,

$$\boxed{\beta S'|_n = \frac{\beta S'|_z}{1 - 1/R_\rho} = \alpha N' \theta_z} \tag{2.8}$$

Thus at the permanent thermocline (where $R_\rho > 1$), *pure freshening* manifests itself as a temperature and salinity decrease on neutral surfaces, and similar to *pure warming*, is accompanied by a downward displacement of isopycnals.

2.3.3 Pure heaving

In the last of the three "pure" processes, both surface temperature and salinity remain constant (so the water mass properties remain unaffected), but the isopycnals undergo vertical displacements. This scenario is called *pure heaving*. Vertical movements of isopycnals can be the result of variations in the wind-driven circulation and the subduction rates, which can be due to long-term changes in the surface wind stress curl. Short-term fluctuations such as mesoscale eddies and Rossby waves can also cause movements of isopycnals. Even a short term increase or decrease in the volume of a particular water mass would lead to a change in thickness between the respective density layers, resulting in vertical displacements of isopycnals. As there is no θ-S property change, $\alpha\theta'|_n = \beta S'|_n = 0$. So from Equations 2.2 and 2.3,

$$\begin{aligned} \alpha\theta'|_z &= -\alpha(\theta_2 - \theta_3) \\ \beta S'|_z &= -\beta(S_2 - S_3) \end{aligned}$$

In other words, the changes observed along the isobars are those of a constant water mass structure being moved upward or downward in pressure coordinates, and are related by the slope of the θ-S curve. Therefore, for *pure heaving*,

$$\boxed{\alpha\theta'|_z = -\alpha N'\theta_z \text{ and } \beta S'|_z = -\beta N' S_z} \tag{2.9}$$

2.4 The role of the stability ratio, R_ρ

It is evident from Equations 2.7 and 2.8, that in *pure warming (cooling)* and *pure freshening (salinification)*, θ and S changes observed on isobars can be of the same or of the opposite signs as when the same changes are observed on isopycnals. By definition, along a neutral surface, a change in θ is always compensated by an "equal" change in S (see Definition 2.1), so $\alpha\theta'|_n$ and $\beta S'|_n$ always have the same sign. On the other hand, $\alpha\theta'|_n$ and $\alpha\theta'|_z$ (similarly for $\beta S'|_n$ and $\beta S'|_z$) are proportional to each other, with the constant of

proportionality varying according to the stability ratio R_ρ. For example, when $R_\rho > 1$, $\alpha\theta'|_n$ and $\alpha\theta'|_z$ have opposite signs under Equation 2.7. This means that under *pure warming*, when a water mass is observed to have warmed at a constant depth ($\alpha\theta'|_z > 0$), the corresponding observation along a constant density surface will reveal a decrease in temperature ($\alpha\theta'|_n < 0$). Church et al. (1991) were the first to point out this counter-intuitive feature, that in a "warming without salinity change" scenario, the effect of warmed water subducted into the thermocline (where $R_\rho > 1$) was to cause an observed cooling (and corresponding freshening) on isopycnals.

In the ocean, the water column can have R_ρ values ranging from $+\infty$ to $-\infty$. The denominators in Equations 2.7 and 2.8 impose the constraints that at the parts of the water column where $R_\rho = 1$, *pure warming (cooling)* and *pure freshening (salinification)* are not well-defined. Consequently, in this diagnostic method, the water column is divided into three "well-defined" ranges : $1 < R_\rho < +\infty$, $-\infty < R_\rho < 0$ and $0 < R_\rho < 1$. Figure 2.2 illustrates R_ρ varying through the water column.

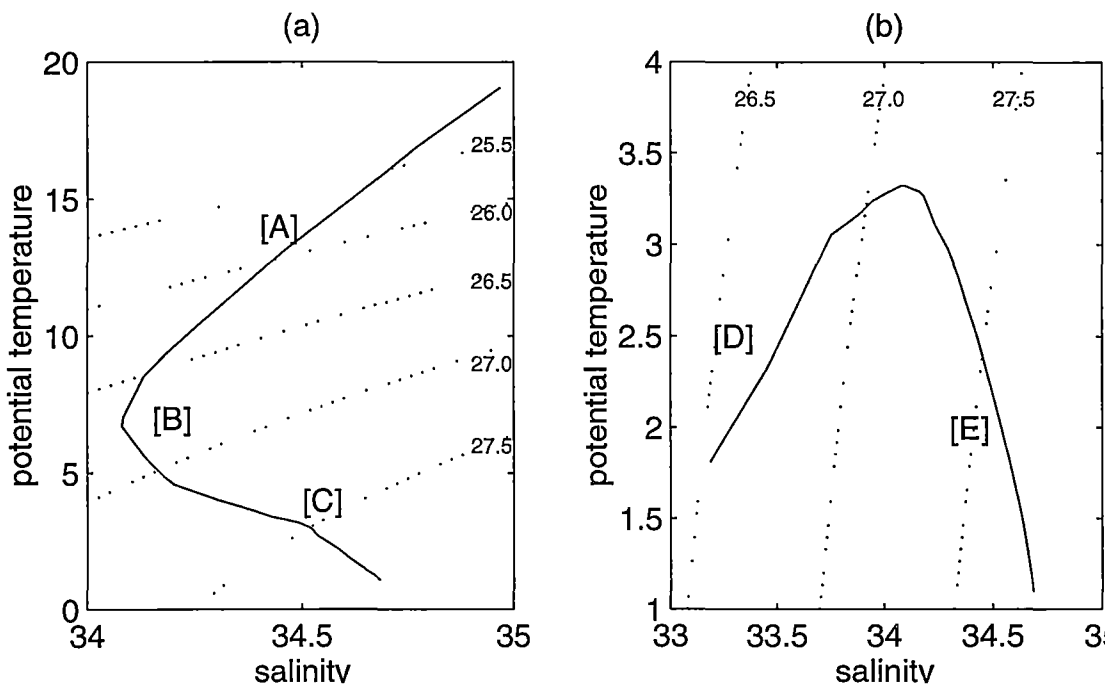

Figure 2.2: Two θ-S curves showing examples of R_ρ in the water column, (a) from the central subtropical Pacific, and (b) from the western subarctic Pacific. [A] $1 < R_\rho < +\infty$, [B] $R_\rho = \infty$, [C] $-\infty < R_\rho < 0$, [D] $0 < R_\rho < 1$, and [E] $-\infty < R_\rho < 0$. The approximate positions of the neutral surfaces (dotted lines) are superimposed.

In the central subtropical North Pacific below 100 dbar (Figure 2.2 a), temperature decreases monotonically with depth, giving $\alpha\theta_z > 0$ throughout the water column. In region [A], which is in the main thermocline, salinity values decrease monotonically with depth (until a minimum is reached), giving $\beta S_z > 0$. However, $\alpha\theta_z \gg \beta S_z$, consequently $R_\rho > 1$ in region [A]. On a conventional θ-S plot, where salinity is plotted against potential temperature, $R_\rho > 1$ is therefore the part of the θ-S curve with a positive slope. Region [B] is at the salinity minimum, which in this case represents North Pacific Intermediate Water (NPIW). There, $\beta S_z = 0$ and $R_\rho = \infty$. In region [C], the θ-S curve has a negative slope. Salinity increases monotonically with depth to the bottom, giving $\beta S_z < 0$ and $R_\rho < 0$.

In another example, in the western subarctic Pacific (Figure 2.2 b), salinity increases monotonically with depth from the surface, giving $\beta S_z < 0$ throughout the water column. The main thermocline is absent. Instead, temperature increases slightly to a maximum at about 500 dbar, then decreases monotonically with depth to the bottom. Therefore in region [D], $\alpha\theta_z < 0$, but because $\alpha\theta_z \ll \beta S_z$, $0 < R_\rho < 1$. Region [E] has the same θ-S structure as region [C], having $R_\rho < 0$.

Within these three "well-defined" ranges, different signs of $\alpha\theta'|_n$ and $\alpha\theta'|_z$ (similarly for $\beta S'|_n$ and $\beta S'|_z$), at various parts of the water column can be the manifestation of the same surface process. For example, waters in the main thermocline ($R_\rho > 1$) that have undergone *pure freshening* will show a decrease in salinity both on isobars and on isopycnals, whereas waters in region [D] in Figure 2.2 ($0 < R_\rho < 1$) will show freshening on isobars but salinity increase on isopycnals, under the same *pure freshening* process.

Table 2.1 summarizes the resulting θ and S changes on isobars and isopycnals, due to *pure warming (cooling)* and *pure freshening (salinification)*, for the three "well-defined" ranges of R_ρ. The special cases where $R_\rho = \pm\infty$ and $R_\rho = 0$ will be discussed in the next section.

	Pure Warming $\alpha\theta'\|_z > 0$ $\beta S'\|_z = 0$	Pure Cooling $\alpha\theta'\|_z < 0$ $\beta S'\|_z = 0$	Pure Freshening $\alpha\theta'\|_z = 0$ $\beta S'\|_z < 0$	Pure Salinification $\alpha\theta'\|_z = 0$ $\beta S'\|_z > 0$
$1 < R_\rho < +\infty$	$\beta S'\|_n = \alpha\theta'\|_n < 0$	$\beta S'\|_n = \alpha\theta'\|_n > 0$	$\beta S'\|_n = \alpha\theta'\|_n < 0$	$\beta S'\|_n = \alpha\theta'\|_n > 0$
$-\infty < R_\rho < 0$	$\beta S'\|_n = \alpha\theta'\|_n > 0$	$\beta S'\|_n = \alpha\theta'\|_n < 0$	$\beta S'\|_n = \alpha\theta'\|_n < 0$	$\beta S'\|_n = \alpha\theta'\|_n > 0$
$0 < R_\rho < 1$	$\beta S'\|_n = \alpha\theta'\|_n > 0$	$\beta S'\|_n = \alpha\theta'\|_n < 0$	$\beta S'\|_n = \alpha\theta'\|_n > 0$	$\beta S'\|_n = \alpha\theta'\|_n < 0$

Table 2.1: The different signs of $\alpha\theta'|_n$, $\beta S'|_n$, $\alpha\theta'|_z$ and $\beta S'|_z$ for the two "pure" processes that involve water mass changes: (i) *pure warming (cooling)*, and (ii) *pure freshening (salinification)*, for various values of R_ρ.

2.5 Decomposing water mass changes into three components

Any observed changes in water mass characteristics can be decomposed into these three processes. This is done by setting up a linear system, using the three "pure" processes as a basis. Inverse methods are then applied to estimate the strength of each component.

Equations 2.7, 2.8 and 2.9 define the relations between the stability ratio R_ρ and the six "observable" variables: $\alpha\theta'|_n$, $\alpha\theta'|_z$, $\alpha N'\theta_z$, $\beta S'|_n$, $\beta S'|_z$, and $\beta N'S_z$, for each of the three "pure" processes. These are related to change in *in-situ* density by the Equation of State: $\rho^{-1}\rho'|_z = \beta S'|_z - \alpha\theta'|_z$. Let the three model parameters: $\rho^{-1}\rho'|_z A^w$, $\rho^{-1}\rho'|_z A^f$, and $\rho^{-1}\rho'|_z A^h$, be the relative strength of each process in causing the observed changes, then a linear non-homogeneous system of the form $\mathrm{G}\,\mathbf{m} = \mathbf{d}$ can be found, where the model parameters $\mathbf{m} = \rho^{-1}\rho'|_z \cdot [A^w, A^f, A^h]$ can be estimated, using inverse methods, from the data: $\mathbf{d} = [\,\alpha\theta'|_z, \alpha\theta'|_n, \alpha N'\theta_z, \beta S'|_z, \beta S'|_n, \beta N'S_z\,]$. In this system, positive values of $\rho^{-1}\rho'|_z A^w$ would indicate density changes caused by *pure cooling*, while negative values would indicate *pure warming*. Similarly, positive values of $\rho^{-1}\rho'|_z A^f$ indicate density changes caused by *pure salinification*, and

negative values indicate *pure freshening*. Lastly, negative values of $\rho^{-1}\rho'|_z A^h$ mean downward movement of isopycnals, i.e. density surfaces deepen in time.

Appendix A details the setting up of the linear system $\mathrm{G}\,\mathbf{m} = \mathbf{d}$, for all values of R_ρ, except for when $R_\rho = 1$, where the system is undefined. In deriving this linear system, the first term of the Taylor's series expansion has been used to obtain $\alpha\theta'|_n - \alpha\theta'|_z = \alpha N'\theta_z$ and $\beta S'|_n - \beta S'|_z = \beta N' S_z$ (see Equations 2.2 and 2.3). Hence our linear system is accurate to the first order.

The model matrix G takes the form:

$$\mathrm{G} = \frac{1}{R_\rho - 1} \cdot \begin{bmatrix} -(R_\rho - 1) & 0 & -R_\rho \\ 1 & R_\rho & 0 \\ R_\rho & R_\rho & R_\rho \\ 0 & (R_\rho - 1) & -1 \\ 1 & R_\rho & 0 \\ 1 & 1 & 1 \end{bmatrix}$$

for the three "well-defined" ranges : $1 < R_\rho < +\infty$, $-\infty < R_\rho < 0$ and $0 < R_\rho < 1$. The three columns represent the effects of *pure warming/cooling*, *pure freshening/salinification* and *pure heaving* respectively, on the six observable variables. The set of three vectors, comprised of the three columns, is not linearly independent. The set of six observable variables also is not linearly independent. In fact, the rank (the number of linearly independent rows or columns in a matrix) of the matrix G is 2.

To solve the system $\mathrm{G}\,\mathbf{m} = \mathbf{d}$, each column of G is first normalised by its L_2 norm to improve its condition number. This is done by forming a diagonal matrix of weights W, then forming a new weighted matrix $\mathrm{G}' = \mathrm{G}\,\mathrm{W}$. The weighted matrix G' is consequently decomposed by singular value decomposition: $\mathrm{G}' = U\Lambda V^{\mathrm{T}}\,\mathrm{W}^{-1}$. The eigenvalues, which are the diagonal elements in Λ, are either positive distinct or zero. A particular solution of the form:

$$\mathbf{m}_{est} = \mathrm{W}\,V_k\,\Lambda_k^{-1}\,U_k^{\mathrm{T}}\,\mathbf{d} \tag{2.10}$$

is considered, where Λ_k is the $k \times k$ diagonal matrix containing the k positive distinct eigenvalues in Λ. The operator $V_k\,\Lambda_k^{-1}\,U_k^{\mathrm{T}}$ is called the "natural generalised inverse", and the solution is called the "natural solution" to the inverse problem (Menke (1984), p.121).

(i) solution to the under-determined problem

G, as mentioned previously, has rank equals 2, so the system $\mathrm{G}\,\mathbf{m} = \mathbf{d}$ with $\mathbf{m}$ having 3 model parameters: $\rho^{-1}\rho'|_z\, A^w$, $\rho^{-1}\rho'|_z\, A^f$ and $\rho^{-1}\rho'|_z\, A^h$, is under-determined. If an under-determined system has at least one solution, then the solution set is infinite. Here, only the natural solution (Equation 2.10) is considered, with $k = 2$, i.e. two eigenvalues are retained. In the under-determined case, the natural solution is equivalent to the minimum length solution (Menke (1984), p.119), i.e. $\mathbf{m}_{est}^{\mathrm{T}} \cdot \mathbf{m}_{est}$ is minimized (the L_2 norm of the solution length is minimized). Solving $\mathrm{G}\,\mathbf{m} = \mathbf{d}$ as an under-determined system has the effect of distributing the variance needed to explain the data between all three processes, thus revealing the relative strength of each process in causing the observed θ and S changes. However, where the strengths of the signals are weak and noise dominates the observations (e.g. in deeper waters), this solution tends to distribute the variance equally between all three processes. Hence at those places, this solution should be used critically. 90% error bars are provided with this solution and should give an indication of the reliability of the solution.

(ii) solution to the over-determined problem

If it is assumed that only one process is present and that the other two processes are absent, then there is only one model parameter, and $\mathrm{G}\,\mathbf{m} = \mathbf{d}$ becomes an over-determined system. In this case, Equation 2.10 is used with $k = 1$, i.e. one eigenvalue is retained. In the over-determined case, the natural solution is equivalent to the least squares solution, where $[\mathbf{d} - \mathrm{G}\,\mathbf{m}_{est}]^{\mathrm{T}} \cdot [\mathbf{d} - \mathrm{G}\,\mathbf{m}_{est}]$ is minimized (the L_2 norm of the prediction error is minimized). When solving for the single-process system, the percentage variance explained by each single process is defined by $\dfrac{\mathbf{d}_{est}^{\mathrm{T}} \cdot \mathbf{d}_{est}}{\mathbf{d}^{\mathrm{T}} \cdot \mathbf{d}}$. Solving $\mathrm{G}\,\mathbf{m} = \mathbf{d}$ as an over-determined system for each individual parameter has the advantage of showing which single process best explains the observations.

(iii) solution to the evenly-determined problem: the special cases of θ-S extrema

At salinity minima and maxima, vertical salinity gradients S_z equal zero, so $R_\rho = \pm\infty$. *Pure warming/cooling* (Equation 2.7) simplifies to

$$\alpha\theta'|_n = \frac{\alpha\theta'|_z}{1 - R_\rho} = \frac{\alpha\theta'|_z / R_\rho}{1/R_\rho - 1} \longrightarrow 0 \quad \text{as} \quad R_\rho \longrightarrow \infty$$

However, $\alpha\theta'|_n = \beta S'|_n = 0$ is exactly the conditions for *pure heaving*. The subsurface changes as a result of *pure warming/cooling* and *pure heaving* therefore exhibit the same relations at salinity minima and maxima. In other words, at precisely $R_\rho = \pm\infty$, *pure warming/cooling* and *pure heaving* collapse into a single process: $A^w \parallel A^h$. The linear system degenerates into:

$$\rho^{-1}\rho'|_z \cdot \begin{bmatrix} -1 & 0 \\ 0 & 1 \\ 1 & 1 \\ 0 & 1 \\ 0 & 1 \\ 0 & 0 \end{bmatrix} \cdot \begin{bmatrix} A^w \parallel A^h \\ A^f \end{bmatrix} = \begin{bmatrix} \alpha\theta'|_z \\ \alpha\theta'|_n \\ \alpha N'\theta_z \\ \beta S'|_z \\ \beta S'|_n \\ \beta N' S_z \end{bmatrix}.$$

The model matrix $\mathrm{G} = \begin{bmatrix} -1 & 0 \\ 0 & 1 \\ 1 & 1 \\ 0 & 1 \\ 0 & 1 \\ 0 & 0 \end{bmatrix}$ still has rank equal 2 in this degenerate case. This means that the two columns in G are linearly independent, and that the linear system $\mathrm{G}\,\mathbf{m} = \mathbf{d}$ is now evenly-determined, with only two model parameters: $\rho^{-1}\rho'|_z\,(A^w \parallel A^h)$ and $\rho^{-1}\rho'|_z\,A^f$.

At temperature minima and maxima, vertical temperature gradients θ_z equal zero, so $R_\rho = 0$. *Pure freshening/salinification* (Equation 2.8) simplifies to

$$\beta S'|_n = \frac{\beta S'|_z}{1 - 1/R_\rho} = \frac{\beta S'|_z\, R_\rho}{R_\rho - 1} \longrightarrow 0 \quad \text{as} \quad R_\rho \longrightarrow 0$$

Therefore, *pure freshening/salinification* and *pure heaving* also collapse into a single process: $A^f \parallel A^h$, and in this case the linear system becomes:

$$\rho^{-1}\rho'|_z \cdot \begin{bmatrix} 1 & 0 \\ 1 & 0 \\ 0 & 0 \\ 0 & -1 \\ 1 & 0 \\ 1 & 1 \end{bmatrix} \cdot \begin{bmatrix} A^w \\ A^f \parallel A^h \end{bmatrix} = \begin{bmatrix} \alpha\theta'|_z \\ \alpha\theta'|_n \\ \alpha N'\theta_z \\ \beta S'|_z \\ \beta S'|_n \\ \beta N' S_z \end{bmatrix}.$$

$\mathrm{G} = \begin{bmatrix} 1 & 0 \\ 1 & 0 \\ 0 & 0 \\ 0 & -1 \\ 1 & 0 \\ 1 & 1 \end{bmatrix}$ also has rank equal 2. Again there are only two model parameters: $\rho^{-1}\rho'|_z A^w$ and $\rho^{-1}\rho'|_z (A^f \parallel A^h)$, so $\mathrm{G}\,\mathbf{m} = \mathbf{d}$ is also evenly-determined when $R_\rho = 0$.

The natural solution in Equation 2.10, with $k = 2$, is therefore the unique solution for these two evenly-determined problems. In other words, when $R_\rho = \pm\infty$, although the inverse method cannot distinguish between $\rho^{-1}\rho'|_z A^w$ and $\rho^{-1}\rho'|_z A^h$, $\rho^{-1}\rho'|_z A^f$ is well-resolved. Similarly, when $R_\rho = 0$, although the inverse method cannot distinguish between $\rho^{-1}\rho'|_z A^f$ and $\rho^{-1}\rho'|_z A^h$, $\rho^{-1}\rho'|_z A^w$ is well-resolved.

Chapter 3

Observational data sets and treatment of data

In this chapter, the observational data sets, and the interpolation procedure that has been applied to the data, are presented. The observational data sets used can be classed into two groups. The first group is the collection of historical hydrographic data sampled before the 1980s. The second group is the set of modern hydrographic one-time transects that were sampled during the 1980s and 1990s under the World Ocean Circulation Experiment (WOCE). Decadal changes in the interior of the North and South Pacific oceans are examined by comparing these two groups of observational data. The ways in which the Bindoff and McDougall (1994) method (developed in Chapter 2) have been applied to the data are also explained.

3.1 Observational data sets

3.1.1 Historical hydrographic data sets

The main historical data set used in this thesis is the world data set compiled by J.L. Reid and A.W. Mantyla. The data set has been compiled over many years and from many sources, and has been used in various world ocean studies by the same authors. It is edited constantly as new data become available and some data are eliminated. Only stations that reach close to the bottom are included (pers. comm. with J. Reid). The version of the North and South Pacific historical data set used in this study was obtained in 1994 from an anonymous ftp site at Scripps Institute of Oceanography. This version contains 1332 hydrographic casts that span the years from 1929 to 1980 for the

North Pacific, and 1778 hydrographic casts that span the years from 1925 to 1980 for the South Pacific. The data set consists mainly of Nansen casts. Figure 3.1 shows the locations of these data points.

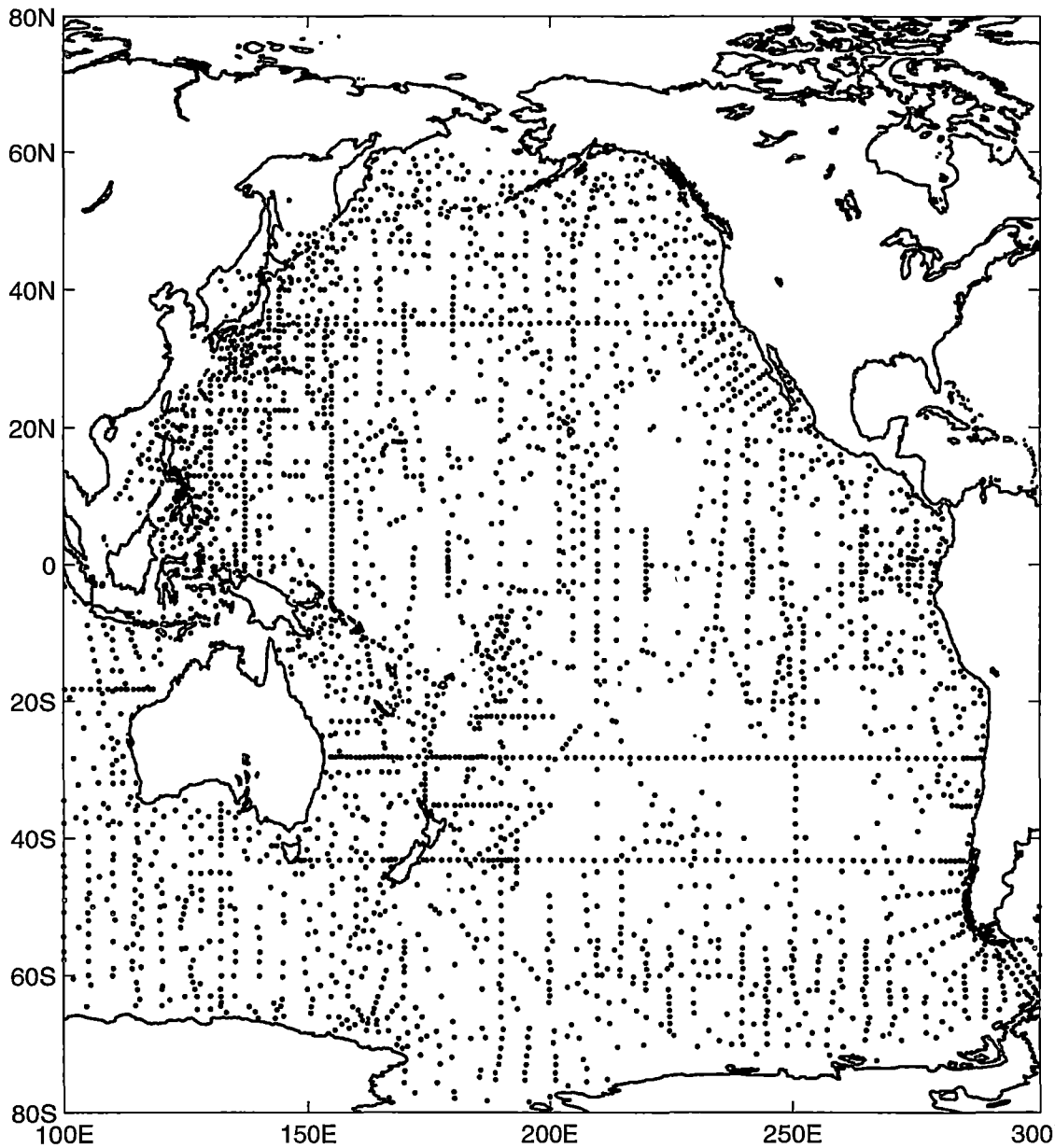

Figure 3.1: The locations of the data points in the Reid and Mantyla Pacific data set.

South of 30°S, more historical hydrographic data are available in the form of two atlases: the "Southern Ocean Atlas" by Gordon et al. (1982), and the

"Hydrographic Atlas of the Southern Ocean" by Olbers et al. (1992). Both of these atlases contain more Southern Ocean data points than the Reid and Mantyla world data set. The Olbers et al. (1992) atlas includes German and Russian data and so has a greater data density than the Gordon et al. (1982) atlas. It is for this reason that the Olbers et al. (1992) atlas data set is chosen as our historical hydrographic data set for the part of the South Pacific south of 30°S.

The Olbers atlas data set contains both Nansen and CTD casts. Each cast has been interpolated onto 42 standard depth levels. Harris (1996) performed further data quality tests on this data set and reduced the number of "clean casts" from 38818 to 23806. This thesis utilises the set of 23806 Olbers "clean casts" as described in Harris (1996). Figure 3.2 shows the locations of the "clean casts" between longitudes 100°E and 300°E.

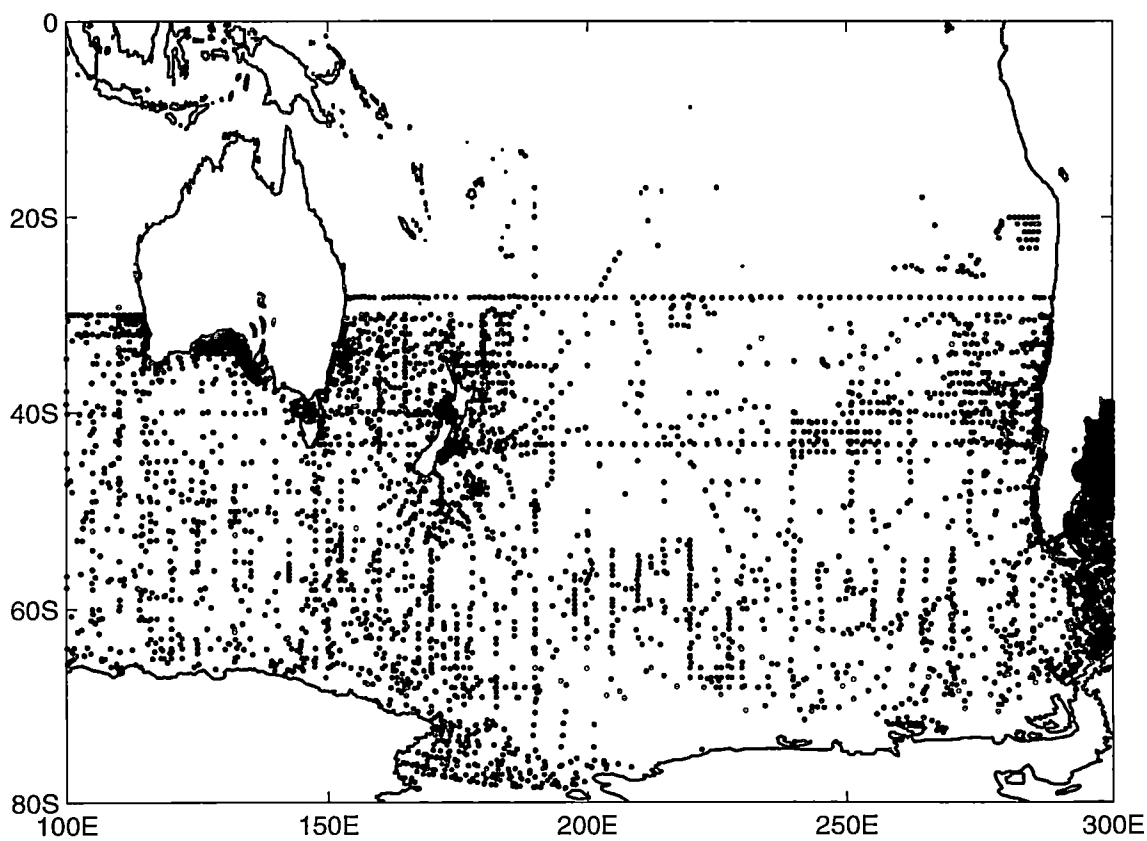

Figure 3.2: The locations of the Olbers "clean casts" between longitudes 100°E and 300°E.

3.1.2 Modern WOCE transects

WOCE, the World Ocean Circulation Experiment, is a project of the World Climate Research Programme. Its goal is to collect high quality data sets of the global ocean, so that a comprehensive description of the global ocean and its circulation can be established. The data are also intended for use with numerical models, so that the ability of numerical models for climate prediction can be improved. During the 1980s and the 1990s, many intensive one-time hydrographic surveys were carried out in the Pacific Ocean. By 1997, at the time of writing of this thesis, six trans-Pacific one-time hydrographic surveys were available from the WOCE Hydrographic Program publicly available data archive, accessible via an anonymous ftp site at nemo.ucsd.edu (the North American mirror site). These six[1] publicly available WOCE Pacific transects are P1, P3, P4, P6, P16 and P17.

Of these six surveys, four are used in this thesis because they lie in areas with sufficient historical data for the purpose of comparison. These four WOCE sections are P1, P3, P4 and P16. P6, the zonal transect that occupies the nominal latitude of 32.5°S, lies in a historically data sparse area, and is therefore deemed not suitable for the purpose of this study. P16 and P17 are two meridional transects that lie close to each other, occupying the nominal longitudes of 150.5°W and 135°W respectively. P16 was chosen over P17 because of the slightly more abundant historical data distribution around it.

In addition to the above four publicly available transects, another more recently completed WOCE Pacific hydrographic surveys has been provided by the principal investigator for use in this study. This is P21 (preliminary data), provided by Dr. Harry Bryden of Southampton Oceanography Centre. Together, these five transects form a set of modern Pacific data for comparison against the historical data.

Figure 3.3 shows the cruise tracks of these five transects. Table 3.1 lists the sampling dates, the nominal positions, and the chief scientists for these cruises.

[1] Along P19, only the short Antarctic section, P19A, which runs from 70°S to 67.5°S along 85°W, was publicly available by 1998.

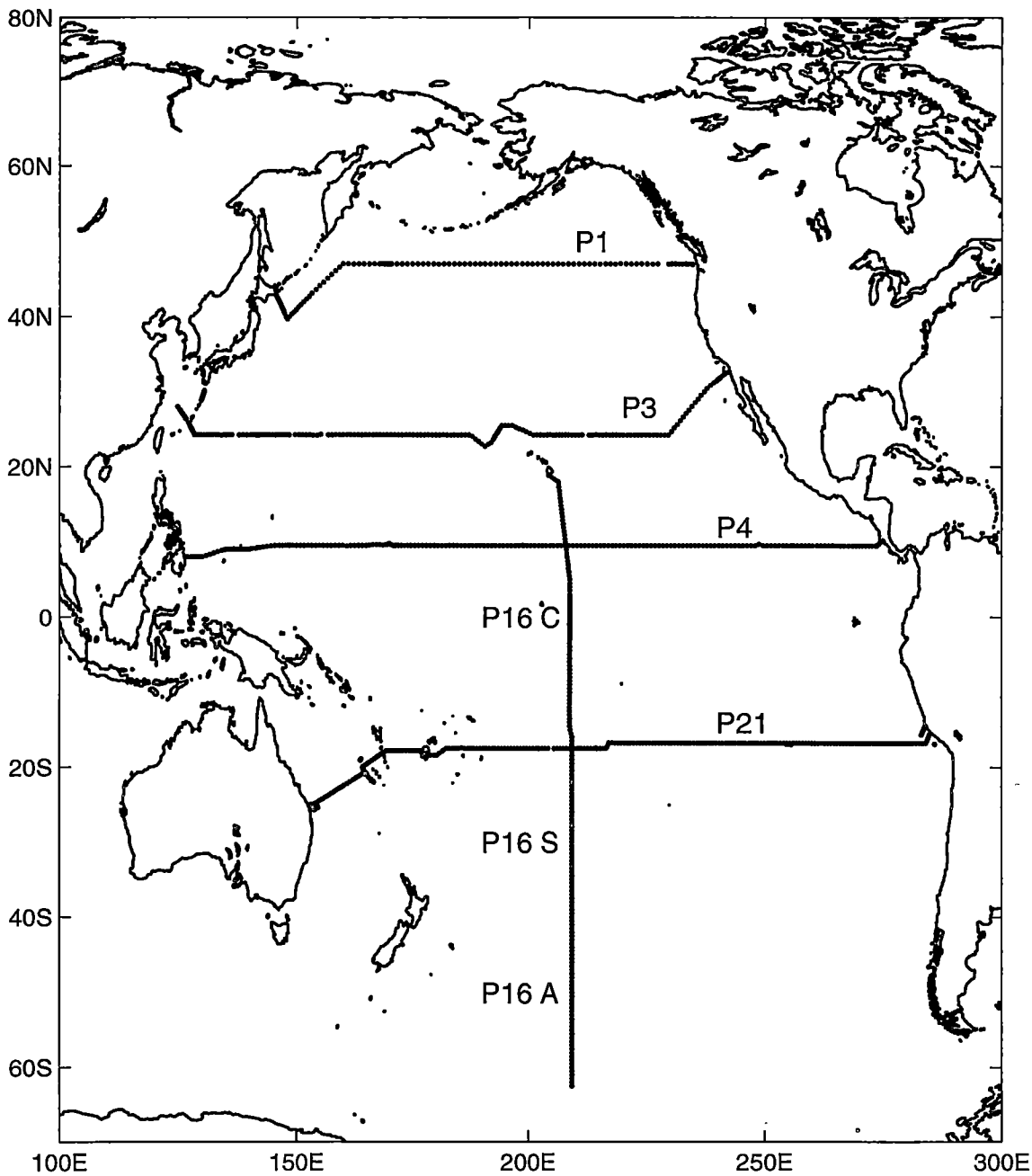

Figure 3.3: The cruise tracks of the five modern WOCE Pacific transects that are used in this thesis.

Transect	Sampling dates	Nominal position	Chief scientist
P1	5 Aug to 7 Sep 1985	47°N	L.Talley
P3	30 Mar to 3 Jun 1985	24°N	J.Swift/D.Roemmich
P4	9 Feb to 10 May 1989	9.5°N	J.Toole/E.Brady/H.Bryden
P16 S P16 C P16 A	11 Aug to 25 Aug 1991 1 Sep to 30 Sep 1991 12 Oct to 28 Oct 1992	150.5°W 155°W 150.5°W	J.Swift L.Talley J.Reid
P21	27 Mar to 25 Jun 1994	17.5°S	M.McCartney/H.Bryden

Table 3.1: The sampling dates, nominal positions, and chief scientists for the seven WOCE Pacific transects used in this thesis.

3.2 Treatment of data

To compare the two sets of data: the modern WOCE set and the historical set, some interpolations need to be done so that the data points occupy common coordinates, vertically and laterally. This section details the interpolation procedures in the order that have been applied to the data. Then the calculations for obtaining the variables needed in the diagnostic method are described.

3.2.1 Vertically interpolating to neutral surfaces

Vertically, most historical measurements were taken from Nansen bottles at discrete depths. On the other hand, the modern WOCE data were obtained by continuous electronic CTD profilers. The first interpolation step therefore involves vertically subsampling all WOCE CTD casts to imitate the vertical spacings between bottles samples. For this purpose, a set of 38 pressure levels, that represent the bottle sample depths in an average Nansen cast, have been chosen. These 38 standard pressure levels are listed in Table 3.2. All WOCE CTD in-situ temperature (IPTS-68) and salinity (PSS-78) have been

subsampled at these 38 standard pressures, by averaging 10 dbar above and below each level. All historical in-situ temperature and salinity data have also been linearly interpolated to this set of 38 standard pressures, except for data from the Olbers atlas, which have already been interpolated onto a similar set of 42 standard depths (m) during the production of the atlas.

Level	Pressure	Level	Pressure	Level	Pressure	Level	Pressure
1	0	11	400	21	1400	31	3750
2	10	12	500	22	1500	32	4000
3	20	13	600	23	1750	33	4250
4	50	14	700	24	2000	34	4500
5	75	15	800	25	2250	35	4750
6	100	16	900	26	2500	36	5000
7	150	17	1000	27	2750	37	5500
8	200	18	1100	28	3000	38	6000
9	250	19	1200	29	3250		
10	300	20	1300	30	3500		

Table 3.2: The 38 standard pressures (dbar) that are chosen to imitate an average Nansen cast. All WOCE CTD casts have been subsampled at these pressures, and all Reid and Mantyla historical data points have been linearly interpolated to these levels.

In-situ temperature and salinity on these 38 standard pressures (or the 42 standard depths for the Olbers atlas data), from the historical data and the WOCE data, are then labelled with neutral densities (Jackett and McDougall 1995; Jackett and McDougall 1997). Neutral density γ^n (in kg m^{-3}) is preferred to potential density because the ambiguity associated with choosing reference pressures for potential density is eliminated. A set of γ^n surfaces is subsequently selected. Quadratic interpolation then provides in-situ temperature, salinity and pressure (and therefore potential temperature) on these specific γ^n surfaces, for every data point. In this manner, all historical casts and all modern WOCE CTD casts are vertically interpolated to a set of common neutral density coordinates.

The choice of γ^n surfaces is different for various parts of the Pacific. For example, for data along the WOCE P4 section, and for the historical data around it, the vertical spacing between surfaces in the main thermocline is closer than that for data along the WOCE P3 section, because there are more thermocline water masses to be resolved along P4. However, these differences in vertical spacings are only slight. In general, the vertical spacings between γ^n

surfaces are typically 0.25 (kg m^{-3}) between 23.0 and 25.0 γ^n, 0.1 between 25.0 and 26.0 γ^n, 0.05 between 26.0 and 27.3 γ^n, and 0.02 between 27.3 and 28.1 γ^n, with more surfaces being placed at the θ-S extremas.

3.2.2 Laterally interpolating to the WOCE coordinates

Because the historical data are distributed quasi-randomly around the WOCE cruise tracks, it makes more sense statistically to interpolate the historical data to the WOCE coordinates than to some arbitrary grids that involves extrapolating the WOCE data. Interpolation of the historical data to the coordinates of the WOCE transects has been carried out by an objective mapping technique. Objective mapping is the desirable method of interpolation because not only does it give an estimate that is unbiased and best linear in the least square sense, it also gives an error variance for each estimated point (e.g. Bretherton et al. (1976); Roemmich (1983); McIntosh (1990)).

The objective estimate, Ψ_{grid}, of a property field at the desired grid, is given by the general formula $\Psi_{grid} = \overline{\Psi} + \underline{w} \cdot (\Psi - \overline{\Psi})$, where Ψ denotes the group of original data used in the estimate, and $\overline{\Psi}$ denotes the mean value of the group. The coefficient, $\underline{w} = C_{dg}\, C_{dd}^{-1}$, is the data-grid covariance normalised by the data-data covariance. The coefficient matrix also takes into account the signal variance and the noise variance of the property field Ψ. The covariance function is here assumed to be Gaussian, with both a longitudinal scale and a latitudinal scale.

Objective mapping of the historical data to the WOCE coordinates is done on neutral surfaces, because in the ocean, lateral averaging and integration are better carried out on isopycnals than on isobars. Lozier et al. (1994) have demonstrated that isobaric-averaging can produce "anomalous anomalies" in θ-S characteristics, in areas with sloping isopycnals and strong curvature in the θ-S curve. On the other hand, since oceanic properties mix primarily along isopycnals, lateral interpolation on density surfaces is more like true oceanic processes.

On each neutral surface then, the mapped historical properties are potential temperature θ, salinity S and pressure P. A two-step mapping technique has been employed: the first step uses a set of long length scales, the second uses a set of short length scales. The mapping procedure and the length scales used are listed in Appendix B. Although the historical observations were made over a long time span, they were collected mostly in the late 1960s, with a

standard deviation of about 7 years. Hence interpolating an ensemble of historical data (along isopycnals) is acceptable for the purpose of this study, because variations of θ-S properties along isopycnals within the historical data are not as important as those over the roughly 20-year period between the mean historical observations and the WOCE sampling.

After objective mapping, local potential densities ρ (referred to mid-pressures) have been computed from the estimated fields of θ, S and P at the WOCE coordinates to ensure that the estimated fields still accurately form the required neutral surfaces. This procedure ensures that the mapping stage of the θ, S and P fields does not modify the densities.

A neutral surface can be regarded as a potential density surface with a locally-referenced pressure (McDougall 1987). Therefore if A and B are two points on a pair of adjacent hydrographic casts (see Figure 3.4), and A and B lie on a neutral surface, then $\rho_A = \rho(S_A, \theta_A(\overline{P}), \overline{P})$ should equal to $\rho_B = \rho(S_B, \theta_B(\overline{P}), \overline{P})$, where $\overline{P} = (P_A + P_B)/2$.

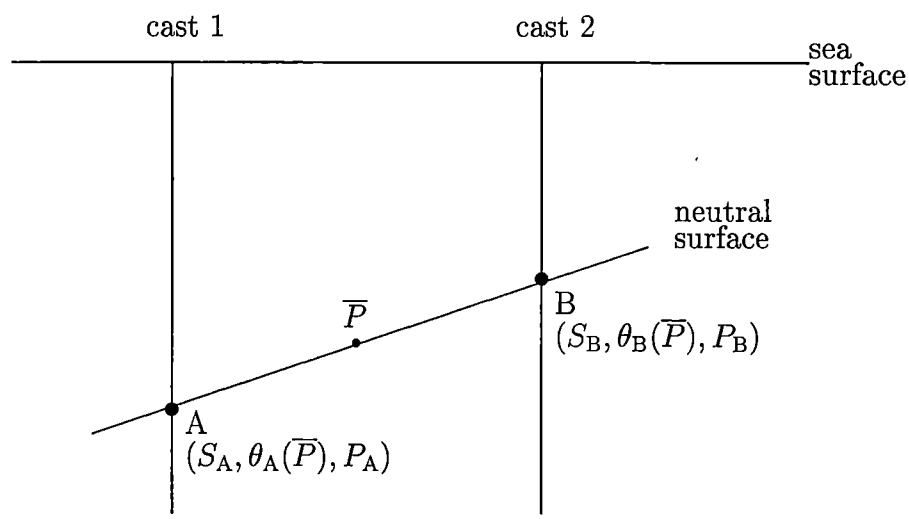

Figure 3.4: A pair of adjacent hydrographic casts, with points A and B lying on a neutral surface. By definition, a neutral surface is equivalent to a locally-referenced potential density surface.

Since the present instrumental error in density is 0.005 kg m^{-3}, for every adjacent station pair along a transect, the objectively mapped θ, S and P are accepted as to constitute the required neutral surface if,

$$|\rho_A - \rho_B| < 0.005 \tag{3.1}$$

Amongst all the mapped fields used in this study, the surfaces which fail this criterion mostly reside either in the top 200 dbar of the water column, or in the deep ocean where depths are greater than 4000 dbar. Because the historical data have been collected over many seasons and many years, the noise levels associated with the property fields are large in the top 200 dbar, which contains the seasonal mixed layer, leading to large variations in densities. Vertical inversions in the mapped pressure field usually accompany these shallow surfaces. On the other hand, very few historical data exist in the deep ocean below 4000 dbar; there, the objective estimates are unreliable, thus causing unrealistic variations in densities.

In the ensuing chapters, where temporal changes in the North and South Pacific are described, the parts of the water column where isopycnal inaccuracies are large by Equation 3.1, and where pressure inversions occur, are discarded from the discussion.

3.2.3 Calculating R_ρ and the six variables

After objective mapping, there are then two sets of hydrographic data that occupy the same WOCE coordinates and the same neutral surfaces, but are separated in time. The diagnostic method of Bindoff and McDougall (1994), described in Chapter 2, is then used to analyse subsurface temporal θ, S and P changes along the WOCE transects. Recall from Chapter 2, that the diagnostic method relies on the relations between the stability ratio R_ρ and the six "observable" variables: $\alpha\theta'|_n$, $\alpha\theta'|_z$, $\alpha N'\theta_z$, $\beta S'|_n$, $\beta S'|_z$, and $\beta N'S_z$. The procedure used in this thesis for calculating the six "observable" variables and R_ρ is slightly different from that used in Bindoff and McDougall (1994). In the original 1994 paper, the six variables and R_ρ are calculated as terms which have been averaged over a number of casts on neutral surfaces. In this thesis, the six variables and R_ρ are calculated, and the three model parameters $\rho^{-1}\rho'|_z A^w$, $\rho^{-1}\rho'|_z A^f$, $\rho^{-1}\rho'|_z A^h$ are solved, for every data point on neutral surfaces. Spatial averages are then taken to facilitate discussion.

To elucidate the calculations of R_ρ and the six variables, a schematic diagram is shown in Figure 3.5 which depicts two hydrographic casts that occupy the same coordinates, but are separated in time. For every data point and on every neutral surface γ^n, θ_a and θ_b are known, so the first variable $\theta'|_n$ is easily obtained by $\theta'|_n = \theta_b - \theta_a$.

Now consider the top and bottom triangles defined by (a,b,d) and (a,b,c)

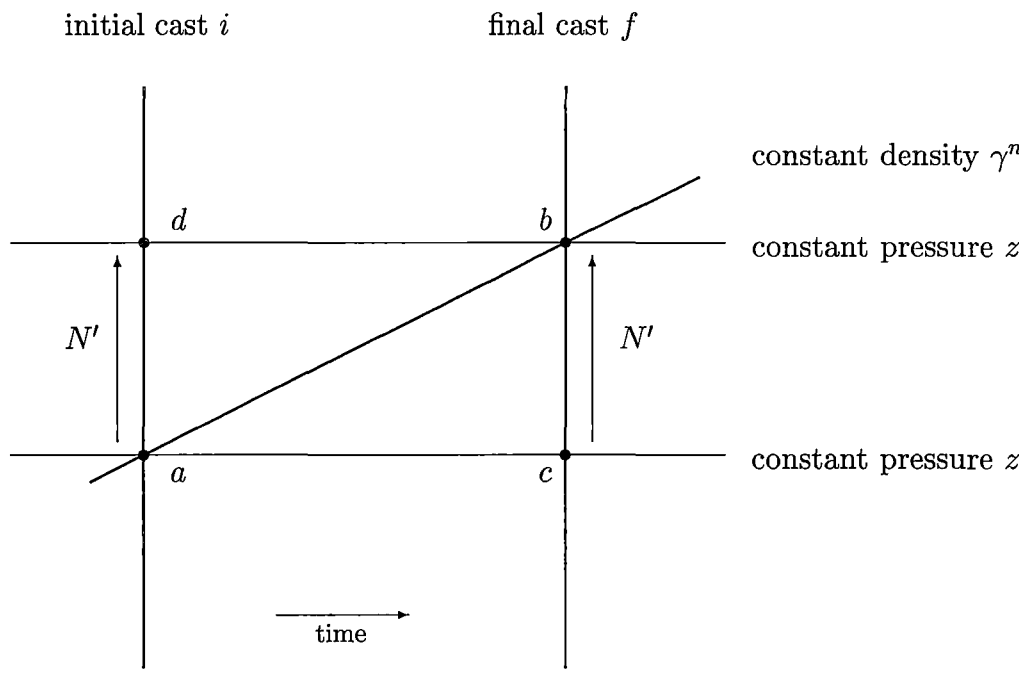

Figure 3.5: A schematic diagram of two hydrographic casts that are fixed in space but separated in time.

respectively in Figure 3.5. Recall from Chapter 2 (see Equation 2.5), that by the first term of the Taylor's series expansion, $\theta'|_n - \theta'|z_i = N'\,\theta_z^f\,(P_m)$ in the bottom triangle, and $\theta'|_n - \theta'|z_f = N'\,\theta_z^i\,(P_m)$ in the top triangle, with $P_m = (z_i + z_f)/2$ being the time-averaged depth of the neutral surface γ^n. Averaging the top and bottom triangles therefore gives

$$\theta'|_n - \theta'|_{z=p_m} = N' \cdot \frac{\theta_z^i\,(P_m) + \theta_z^f\,(P_m)}{2} \qquad (3.2)$$

where $\theta'|_{z=p_m} = \theta^f(P_m) - \theta^i(P_m)$. So associated with each neutral surface γ^n, the second variable $\theta'|_z$ is evaluated at the time-averaged depth P_m of γ^n. $\theta^f(P_m)$ and $\theta^i(P_m)$ have been obtained by linear interpolation from the potential temperature fields on neutral surfaces. Furthermore, the coefficients α and β have been evaluated at the time-averaged depth P_m of each neutral surface as well, to be consistent with the Taylor's series expansion.

The third variable $\alpha N'\theta_z$ is calculated as $\alpha N'\theta_z \equiv \alpha\theta'|_n - \alpha\theta'|_{z=p_m}$, according to Equation 2.5 from Chapter 2.

The remaining three variables: $\beta S'|_n$, $\beta S'|_z$, and $\beta N' S_z$, have been calculated in similar fashions.

The stability ratio R_ρ was suggested by Bindoff and McDougall (1994) to be evaluated as

$$R_\rho = \frac{\alpha\theta'|_n - \alpha\theta'|_z}{\beta S'|_n - \beta S'|_z}$$

However, this method tends to produce unnecessary infinity values of R_ρ in the data sets. A more consistent way of calculating the stability ratio is directly from its definition of $R_\rho = \alpha\theta_z/\beta S_z$. The vertical gradients θ_z and S_z are evaluated according to Equation 3.2, that is, associated with each γ^n,

$$\theta_z = \frac{\theta_z^i\,(P_m) + \theta_z^f\,(P_m)}{2}$$

where $\theta_z^i(P_m)$ and $\theta_z^f(P_m)$ are evaluated from the θ fields on neutral surfaces from the mapped historical data (the initial casts) and the WOCE data (the final casts) respectively, then linearly interpolated to the time-averaged depth P_m associated with each γ^n. The same procedure is used to calculate S_z.

These six variables and R_ρ are used to form the linear system $\mathrm{G}\,\mathbf{m} = \mathbf{d}$ for every data point on neutral surfaces. The strengths of the three "pure" processes in causing the observed temporal changes at each data point, as represented by the three model parameters: $\rho^{-1}\rho'|_z\,A^w$, $\rho^{-1}\rho'|_z\,A^f$, and $\rho^{-1}\rho'|_z\,A^h$, are then estimated by solving the linear system as an under-determined problem, as described in Chapter 2 (Section 2.4 (i)). Sectionally-averaged density anomalies: $\overline{\rho^{-1}\rho'|_z\,A^w}$, $\overline{\rho^{-1}\rho'|_z\,A^f}$, and $\overline{\rho^{-1}\rho'|_z\,A^h}$, are evaluated as simple averages of the pointwise anomalies.

To estimate the percentage of data variance explained by a single process, the linear system $\mathrm{G}\,\mathbf{m} = \mathbf{d}$ is solved as an over-determined problem, as described in Chapter 2 (Section 2.4 (ii)). However, when considering averages over a section, the six variables and R_ρ are first obtained pointwise, then the system $\mathrm{G}\,\overline{\mathbf{m}} = \overline{\mathbf{d}}$ is solved.

In the following chapters, the results from the North and South Pacific oceans will be discussed in terms of these six variables and the corresponding R_ρ, and the solutions to the inverse problem $\mathrm{G}\,\mathbf{m} = \mathbf{d}$.

Chapter 4

Observed changes in the North Pacific Ocean

Subsurface temporal changes of θ, S and P observed along three zonal WOCE transects in the North Pacific Ocean are presented in this chapter. These three transects are P1 (47°N), P3 (24.25°N) and P4 (9.5°N). Along each of these three zonal transects, temporal changes are described as spatial differences and as sectionally averaged differences, on neutral surfaces first, then on isobars. When discussing spatial differences, pointwise mapping errors (Appendix B, Equation B.4) are referred to. When discussing sectionally averaged differences, confidence intervals based on the T-distribution are used as a measure of the statistical significance. Appendix C describes the calculations of confidence intervals for various parameters. The results from the inverse method, which separates these temporal changes of θ, S and P into three components due to *pure warming/cooling*, *pure freshening/salinification* and *pure heaving*, are presented, and their implications discussed.

It should be stressed here that neutral density is used in this study. Neutral density is preferred to the more commonly used potential density, because the ambiguity of choosing reference pressures is eliminated. However, the numerical values of neutral density, γ^n (kg m^{-3}), are very similar to those of potential density referenced to 0 dbar, σ_θ (kg m^{-3}). To facilitate discussion relating to other oceanographic studies which used σ_θ , a plot for cross-referencing between the two kinds of densities is shown in Figure 4.1. Hence, for example, $25.0\,\gamma^n = 25.0\,\sigma_\theta$, $26.0\,\gamma^n = 25.9\,\sigma_\theta$, and $27.0\,\gamma^n = 26.8\,\sigma_\theta$. From hereon, neutral density will simply be denoted by γ^n, with the unit kg m^{-3} omitted.

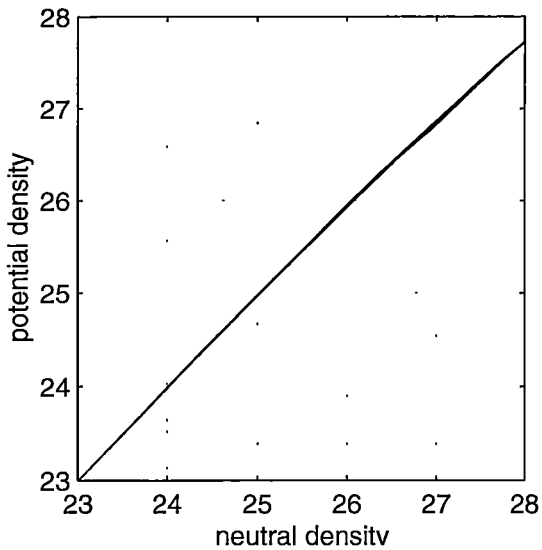

Comparison of γ^n values with σ_θ values, based on data along the WOCE P1, P3 and P4 sections.

Figure 4.1:

4.1 Differences along the WOCE P1 section

The WOCE P1 section is a nominally zonal transect within the subarctic gyre of the North Pacific. Figure 4.2 shows a schematic diagram that is adapted from the map of Favorite et al. (1976), of the circulation of the subarctic North Pacific at 300 m. To the north, the subarctic gyre is bounded by a westward flow: the Alaskan Stream, from the Gulf of Alaska to the Bering Sea. Part of this flow branches off near 200°E, flowing southeastward and forming the cyclonic Alaskan gyre in the northeastern Pacific. Further to the west, the southwest-flowing East Kamchatka Current marks the western boundary of the subarctic gyre, and subsequently separates, near the Kuril Islands, into the southward-flowing Oyashio Current and the eastward-flowing Subarctic Current. Roemmich and McCallister (1989)'s inverse calculations show that across 185°E (175°W) and 208°E (152°W), the eastward flow along 47°N extends to at least 1000 m. As the Subarctic Current flows east, a divergence occurs in the upper 250 m at about 210°E (150°W): one branch turning north into the Gulf of Alaska, thus closing the subarctic gyre, and one branch turning south into the California Current (Favorite et al. 1976). Below 300 m, this divergence occurs closer to the coast of the North American continent and farther southward. The narrow northward-flowing California Undercurrent, which is generally observed at depths below 200 m, is not shown in Figure 4.2.

The WOCE cruise track of P1 (TPS47) runs along the nominal latitude of

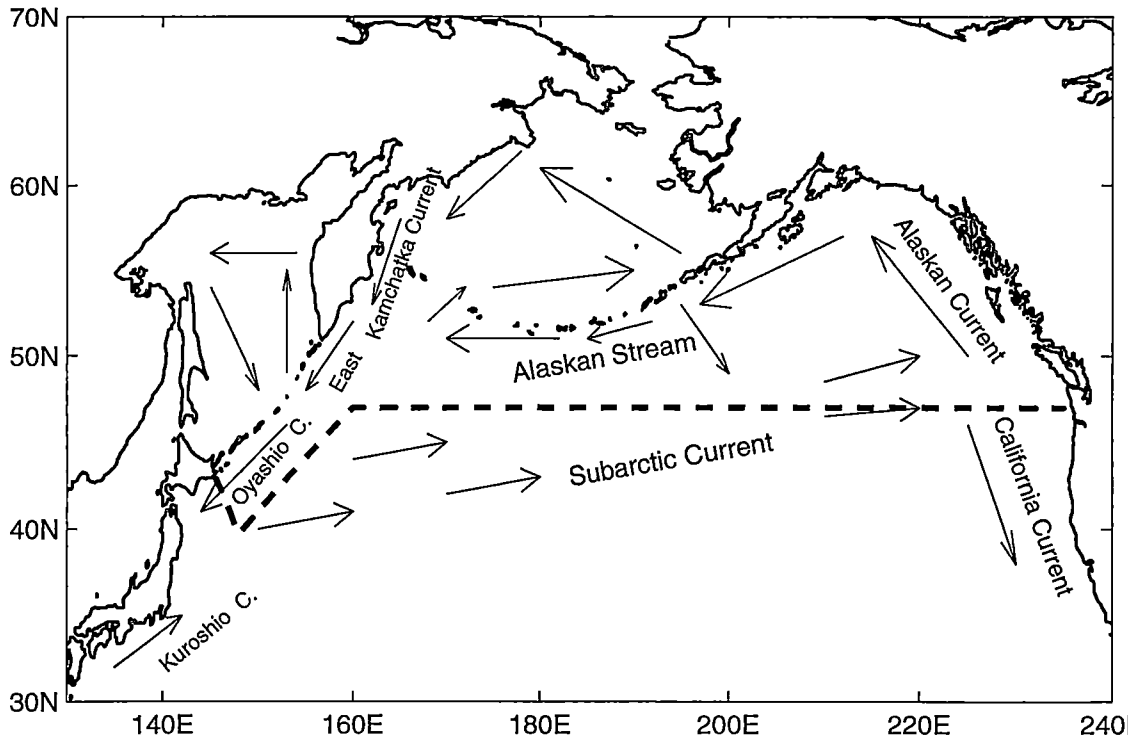

Figure 4.2: Schematic diagram showing the cyclonic gyre and the current systems in the subarctic North Pacific. The dashed line marks the cruise track of the WOCE P1 section.

47°N, except for a small section near Japan, where the cruise track follows a southeasterly, then northeasterly line after leaving Hokkaido (Figure 4.2). Hence, P1 lies within the eastward-flowing Subarctic Current, which forms the southern limb of the cyclonic subarctic gyre (Talley et al. 1991; Taft 1995). The entire section consists of 113 CTD casts. For mapping to the coordinates of P1, 299 historical data points north of 36°N in the North Pacific have been selected from the Reid and Mantyla Pacific data set (Figure 4.3).

These 299 historical data points span the years from 1955 to 1980 (Figure 4.4 a). The majority of casts was sampled between the mid-1960s and the early 1970s. Indeed the mean year of sampling for these 299 historical data points is 1966, with the standard deviation being 5 years. The median year of sampling is also 1966. As WOCE P1 was sampled during August 1985, any observed temporal differences along P1 can thus be treated as roughly 19 ± 5 years differences. The most frequent month of sampling for these 299 historical data points is August (Figure 4.4 b), the same month as when observations along P1 were carried out during WOCE. Hence the likelihood of seasonal aliasing in the observed temporal changes is minimal.

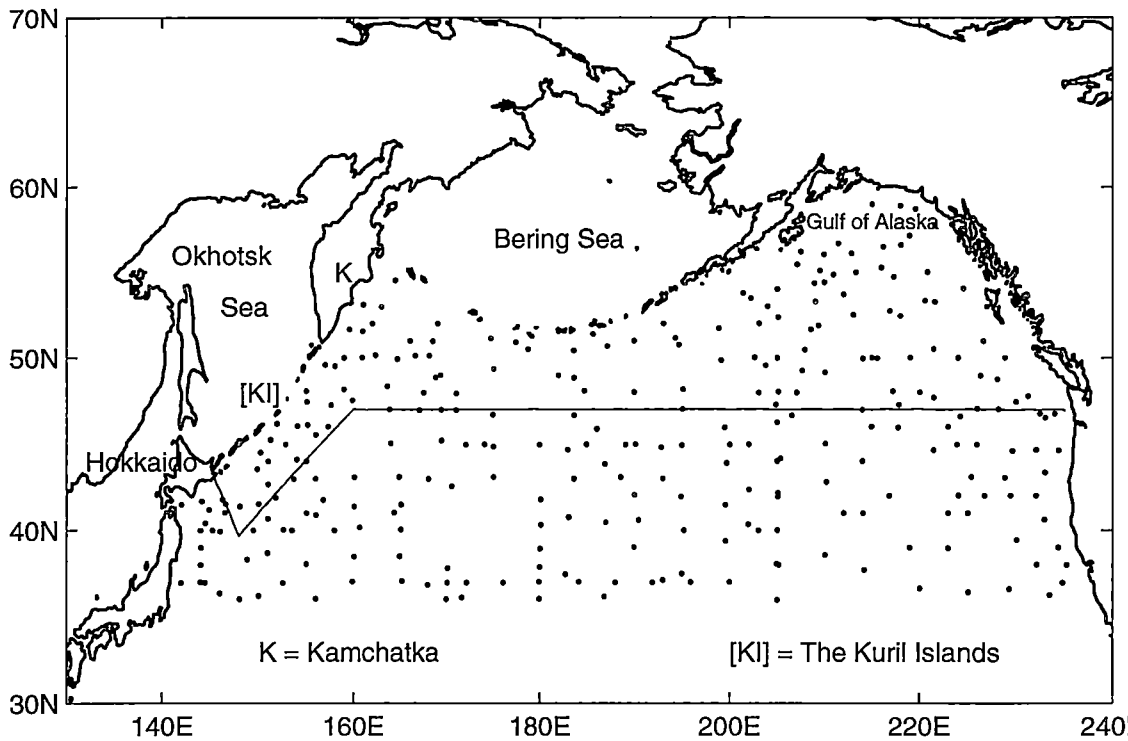

Figure 4.3: The cruise track of the WOCE P1 section, and the distribution of the 299 historical data points that have been used in the mapping to the coordinates of WOCE P1.

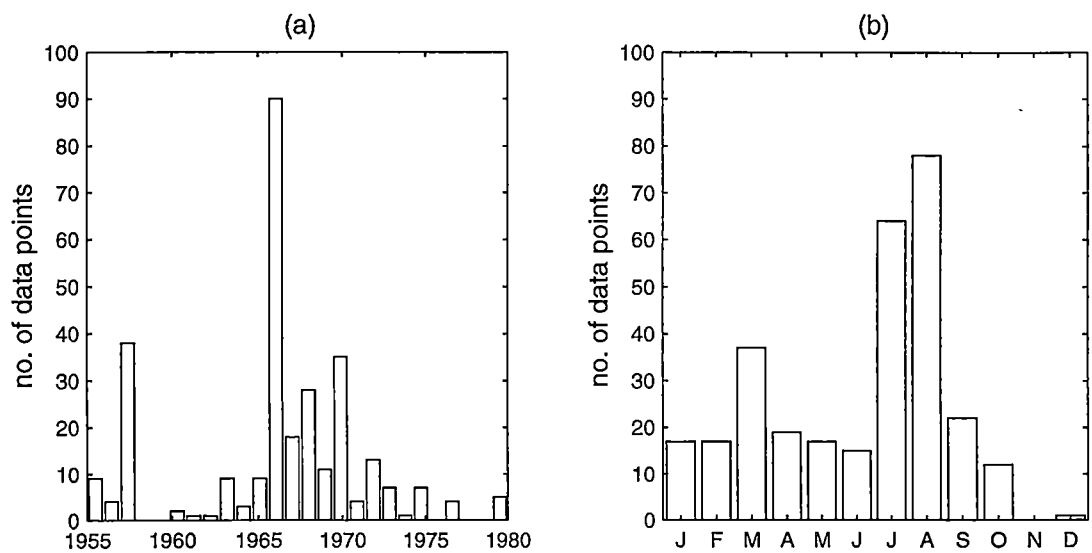

Figure 4.4: (a) The year distribution and (b) the month distribution, of the 299 historical data points used in the mapping to the coordinates of the WOCE P1 section.

The vertical section of potential temperature in the top 1000 dbar along P1, based on the WOCE data, is shown in Figure 4.5. Below 1000 dbar, the vertical temperature structure is one of monotonic decrease with depth, and so is not shown. Figure 4.5 shows an intense but shallow seasonal thermocline that is characteristic of the subarctic in late summer, when the top 50 to 100 dbar of the water column is warmed by the increased solar radiation. Beneath the seasonal thermocline, a temperature minimum ($\theta < 3°$) is present west of 180°E; its core at around 150 dbar has a density of roughly 26.7 γ^n. This temperature minimum marks the remnant of the winter mixed layer in the western subarctic Pacific (Talley et al. 1991), with the coldest water ($\theta < 2°$) found to the west of 165°E believed to be water from the Bering Sea and the Okhotsk Sea, that has been transported southward by the East Kamchatka Current (Taft 1995). Beneath the temperature minimum is a temperature maximum, with values greater than 3.5°C observed around 175°E at 350 dbar (roughly 27.3 γ^n) during WOCE 1985. Beneath this maximum, temperature decreases monotonically with depth.

The vertical salinity section along P1 (not shown) is a simple picture of monotonic increase in salinity with depth. The only exception to this monotonically increasing salinity structure is at the western boundary, where a slight salinity minimum was observed during WOCE 1985 at depths of about 300 dbar, around 147°E. At that longitude, the cruise track of P1 extends south to 40°N, and Talley et al. (1991) has attributed this isolated salinity minimum as due to North Pacific Intermediate Water (NPIW). No other well-defined NPIW was observed along P1 during WOCE 1985, although some "eroded" NPIW, identified by a "plateau" in the σ_θ-S curve, was found to the east, between 222°E and 231°E (138°W and 129°W). Talley (1993)'s map of potential density of NPIW confirms that NPIW is found primarily south of 45°N.

Due to the monotonic increase in salinity and the monotonic decrease in temperature with depth, the stability ratio $R_\rho = \alpha\theta_z/\beta S_z$ is negative everywhere along P1, except beneath the temperature minimum layer in the west, where temperature increases slightly to a maximum, before decreasing monotonically with depth to the bottom. This brief vertical temperature increase results in $0 < R_\rho < 1$ for densities 26.7 to 27.4 γ^n, between 150°E and 180°E.

Vertical section of neutral density is shown in Figure 4.6 and reveals the major currents across P1. Isopycnals along P1 slope downward from west to east in general, indicating broad northward flow relative to a deep reference level (> 1000 dbar) across most of the section (Talley et al. 1991). At the

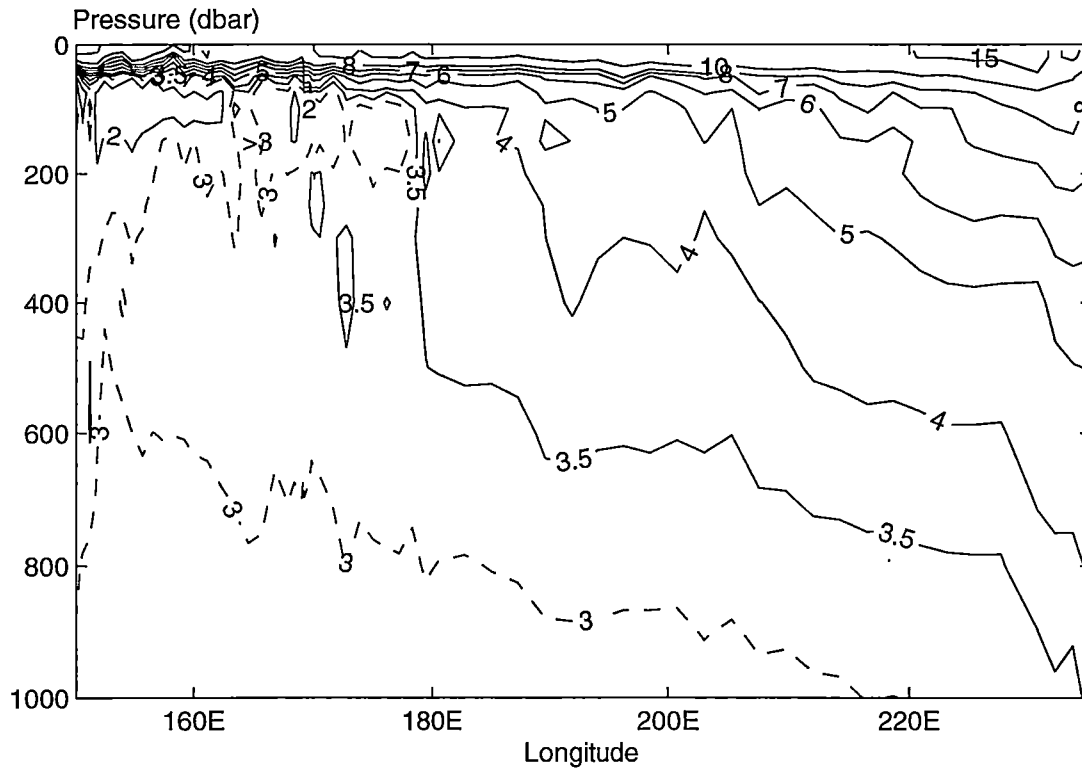

Figure 4.5: Profile of potential temperature (°C) for the upper 1000 dbar along 47°N, based on CTD data from the WOCE P1 section. The narrow region west of 150°E is not shown.

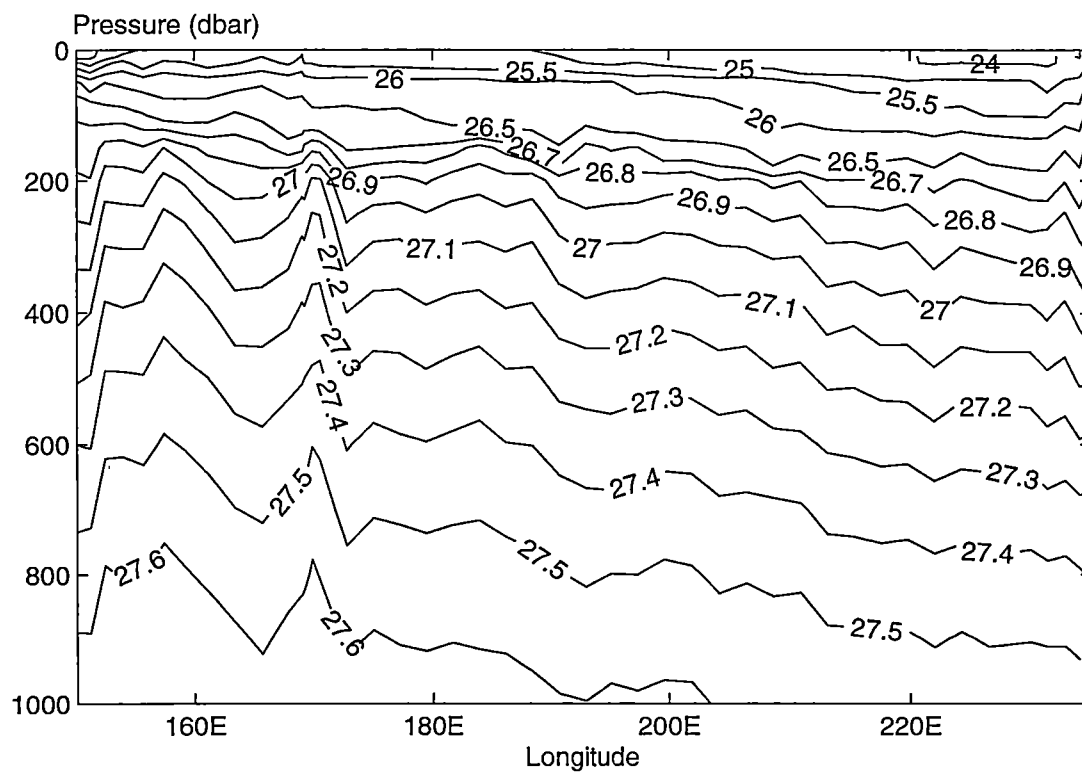

Figure 4.6: Profile of neutral density (kg m^{-3}) along 47°N, as in Figure 4.5.

eastern boundary, the upward-sloping isopycnals in the top 200 dbar mark the southward-flowing California Current, while beneath 200 dbar, the reversal of isopycnal slopes marks the northward-flowing California Undercurrent. To the west, the cruise track follows a northeasterly line between 150°E and 160°E. Hence the upward-sloping isopycnals from 150°E to 160°E actually mark the eastward-flowing Subarctic Current. The narrow region west of 150°E is the highly variable Kuroshio-Oyashio confluence zone (Talley et al. 1991) and is not shown in Figures 4.5 and 4.6.

The θ-S diagram of the historical data after objectively mapped to P1 is compared with that of the WOCE 1985 data in Figure 4.7. Water with temperature greater than 8°C is in the seasonal thermocline. Most of the WOCE data in the seasonal thermocline have salinity values between 32.5 and 33.5, while the objectively mapped historical data display a wider salinity range in the seasonal thermocline. This is to be expected as the historical data have been collected over many years. Consequently, the mapped property fields in the top 100 dbar, which represents the seasonal thermocline, fail to accurately form the required neutral surfaces between adjacent station pairs, by Equation 3.1, defined in Chapter 3 (Section 3.2.2). These inaccurate neutral surfaces in the top 100 dbar of the P1 section range from $< 25.5\,\gamma^n$ at the eastern end of the transect, to $< 26.5\,\gamma^n$ at the western end of the transect. These shallow densities are excluded from our discussion.

A feature in the seasonal thermocline that the mapping technique failed to produce can be seen in Figure 4.7 (a) as the part of the θ-S curve with temperature greater than 8°C and salinity between 34.0 and 34.5. These are the surface waters in the Kuroshio-Oyashio confluence zone. Examination of the data set shows that such high salinity values do exist amongst the surface waters in the Kuroshio-Oyashio region in the historical data, but have not been produced by the mapping technique at the corresponding P1 coordinates, principally because our method of mapping tends not to produce reliable estimates at the boundaries of the mapping region.

Below the seasonal thermocline, a prominent salinity minimum, which is not present in the WOCE data, can be seen in the objectively mapped historical data (Figure 4.7 b) at $\theta < 3$°C, with salinity around 33.0. This salinity minimum, with density between 26.4 and 26.5 γ^n, is found at approximately 43°N, 146°E, again in the Kuroshio-Oyashio confluence zone. Examination of the data set reveals that such low salinity values do exist within that density range in the historical data in that region, and that this salinity minimum is not

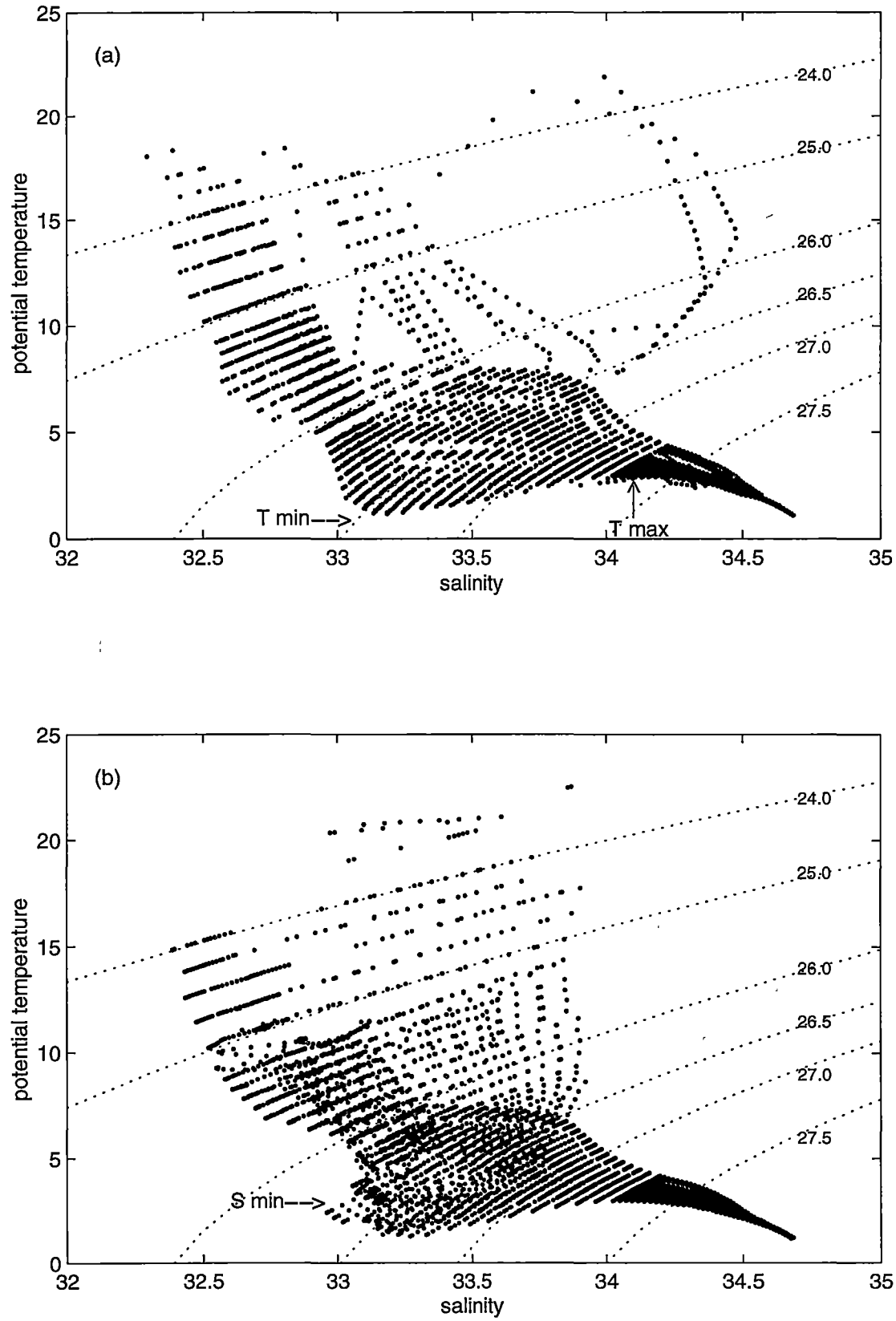

Figure 4.7: θ-S diagram on neutral surfaces along P1, (a) from the WOCE 1985 section, and (b) from the historical data objectively mapped to the coordinates of P1. Lines of constant neutral density are superimposed.

an artefact of the mapping technique. Its absence in the WOCE data therefore is a manifestation of the high upper-layer variability in the Kuroshio-Oyashio region. This variability is also highlighted by the fact that west of 148°E, the mapped θ and S fields in the top 200 dbar (23.5 to 26.9 γ^n) display such large variations on isopycnals that all neutral surfaces shallower than 26.9 γ^n fail the criterion as described by Equation 3.1 in Chapter 3. Vertical inversions in the mapped pressure field are also common amongst the top 200 dbar in the Kuroshio-Oyashio region.

The seasonal thermocline and the Kuroshio-Oyashio region along P1 are therefore excluded from our discussion. For the rest of the P1 section away from the Kuroshio-Oyashio region, the objective estimates are realistic below 100 dbar and preserve the neutral surface definition to within instrumental error (see Equation 3.1). The ratios of the standard deviation of the mapping residuals to that of the *a priori* noise, for all three mapped fields θ, S and P on neutral surfaces below 100 dbar, are between 0.8 and 1.0, indicating good length scales fit in the mapping procedure (see Equation B.3 in Appendix B). Any temporal changes observed below the seasonal thermocline along P1 are therefore statistically reliable.

Observed temporal changes on neutral surfaces

Figures 4.8, 4.9 and 4.10 show the temporal changes in potential temperature, salinity and pressure on neutral surfaces (i.e. $\theta'|_n$, $S'|_n$, N') along P1, obtained by subtracting objectively mapped historical observations from the WOCE observations. Negative changes in temperature therefore mean that the water has become cooler on neutral surfaces, and negative changes in salinity mean that the water has become fresher on neutral surfaces. Negative changes in pressure on neutral surfaces mean that the surfaces have deepened. Because temperature and salinity changes on neutral surfaces are proportional, their spatial distributions are identical. The dashed line marks the level below which the objective estimates of θ, S and P on neutral surfaces are realistic by Equation 3.1. It corresponds roughly to the 100 dbar level, that is, the base of the seasonal thermocline. Note that surfaces shallower than 25.5 γ^n are not shown, because they do not extend over the entire transect (see Figure 4.6). Also, the contour intervals are not regular, but are selected to best display the spatial distribution of the differences.

Below the seasonal thermocline, temporal changes along P1 display a

rough east-west trend. The point of demarcation for this east-west trend is at approximately 205°E. East of this longitude, water displays temperature and salinity increase on neutral surfaces, and to the west, cooling and freshening on neutral surfaces. An exception to the broad temperature and salinity decrease on neutral surfaces to the west is the narrow region between 163°E and 166°E, in the density range 26.5 to 27.0 γ^n, that is, within the temperature minimum layer. There, three WOCE casts (Stations 41 to 43) display a lens-like feature of relatively warm temperature minimum ($\theta > 3$°C, see Figure 4.5). Talley et al. (1991) has attributed this as due to some subtropical influence. The objective mapping technique cannot resolve such mesoscale features, and so has estimated θ at that coordinate to be close to 2°C. Hence the WOCE observations at that coordinate appear to be warmer (and saltier) on neutral surfaces by more than 1°C.

In general, temperature and salinity differences along P1 exceed 0.1°C and 0.02 pss respectively above the 27.4 γ^n surface, and are greater than the pointwise mapping errors at those levels. The biggest temperature difference (decrease of more than 1°C on neutral surfaces) occur west of 160°E and at about 180°E, between densities 26.5 γ^n and 27.0 γ^n, that is, in the temperature minimum layer (Figure 4.8). The corresponding salinity decrease on neutral surfaces is greater than 0.1 pss (Figure 4.9).

Temporal differences in pressure on neutral surfaces (N') display an even more distinct east-west pattern (Figure 4.10). Neutral surfaces have deepened mostly uniformly east of 205°E, and have become mostly uniformly shallower to the west. Differences are negligible above 26.5 γ^n; below 26.5 γ^n, differences are generally greater than 20 dbar, and greater than the pointwise mapping errors. West of 160°W, some isopycnals have become shallower by as much as 100 dbar.

Amongst the broad area west of 205°E that exhibits shallowing of isopycnals, two narrow regions show disparate differences. The first region centres at 165°E and extends from 26.6 γ^n to the bottom, the second at 190°E and extends from 26.9 to 27.4 γ^n. These two regions are where reversals of isopycnal slopes are evident in the WOCE data (see Figure 4.6). Hence they represent mesoscale features in the WOCE data that the objective mapping technique cannot resolve, and not some long-term changes to isopycnal depths of the area.

Below 26.5 γ^n, sectional averages taken to the east and west of 205°E show that θ and S changes on neutral surfaces are pronounced to 27.4 γ^n (Figure 4.11 a to d). Between 26.5 γ^n and 27.4 γ^n, the density-averaged cooling

and freshening are 0.4°C and 0.06 pss respectively west of 205°E. These are significant above the 90% confidence levels. Within the same density range, the density-averaged warming and salinity increase are 0.1°C and 0.01 pss respectively east of 205°E. However, these increases are not significant above the 90% confidence levels. Changes in pressure on neutral surfaces are less than 40 dbar on average for surfaces shallower than 27.4 γ^n (Figure 4.11 e, f). Below 27.4 γ^n, average pressure differences are greater west of 205°E (> 40 dbar) than those to the east. Overall, these pressure differences are significant above the 90% confidence levels for most surfaces west of 205°E, but not to the east.

Note that these temporal changes in θ and S between 26.5 and 27.4 γ^n could be the result of lateral movements of the large-scale distribution of the θ-S properties on neutral surfaces. At 47°N, temperature and salinity on neutral surfaces increase eastward and southward. For example, on the 27.0 γ^n surface, the zonal gradient of temperature along 47°N have been estimated from the historical data to be roughly 0.1°C per 2°longitude, while the meridional gradient is about 0.3°C per 2°latitude west of 210°E, and 0.1°C per 2°latitude east of 210°E. Thus, the temperature decrease observed on the 27.0 γ^n surface to the west of 205°E could be due to a 400 km eastward shift, or a 200 km southward shift, in water masses, and would result in a shoaling of isopycnals. Similarly, the temperature increase observed to the east of 205°E could be due to a 400 km westward shift, or a 200 km northward shift of water masses, and would result in a deepening of isopycnals. The corresponding change in salinity could also be accounted for in the same way. The observed pattern of pressure changes of the neutral surfaces is also consistent with this lateral shifting scheme. Hence in the absence of other tracer data, such as oxygen or nutrients, it is difficult to determine whether the observed changes are due to lateral movements of the subarctic waters, or whether they represent real water mass properties changes over time.

Below 27.4 γ^n, θ and S changes on neutral surfaces are more uniform on a basin-wide scale. Basin-wide averages from 150°E to 230°E (not shown) show temperature and salinity decreases on neutral surfaces, throughout the water column below 27.4 γ^n. However, these sectionally-averaged changes are less than 0.03°C for temperature and less than 0.004 pss for salinity, and are not significant for most surfaces at the 90% confidence levels. Talley et al. (1991) have noted that an addition of 0.003 to the bottom salinity values of P1 would match those presented in Mantyla and Reid (1983), who used standard seawater samples from the pre-PSS78 salinity scale. Taking the average value for α to be

1.30×10^{-4}, and the average value for β to be 7.56×10^{-4}, for water below 1000 dbar along 47°N, an addition of 0.003 pss to the average salinity on neutral surfaces deeper than 27.4 γ^n would lead to a corresponding increase in average temperature of 0.02°C (Equation 2.1). This is sufficient to reduce the observed temperature decrease on neutral surfaces below 27.4 γ^n to close to instrumental error. Hence the observed θ and S differences on neutral surfaces below 27.4 γ^n could be due to systematic error between the WOCE measurements and the historical measurements. The absence of significant water mass changes below 27.4 γ^n at 47°N therefore reflects the sluggish ventilation of waters in the deep North Pacific relative to those in the deep North Atlantic.

As an aside, the pressure difference of the neutral surfaces as a result of systematic error in salinity is negligible. On the other hand, neutral surfaces below 27.4 γ^n ($\approx$ 600 dbar along 47°N) have, on average, become shallower by about 26 dbar, which is significant at the 90% level. Such an upward heave would result in a cooling of less than 0.03°C at depths below 600 dbar, when viewed along isobars, over the roughly 20-year period. As will be seen in the following section, this heave-related cooling on isobars has been observed, and agrees with Antonov (1993)'s isobaric zonal averages that in the subpolar gyre below 800 m, ocean temeprature differences are less than 0.1°C per 25 years, and which Antonov (1993) considered negligibly small.

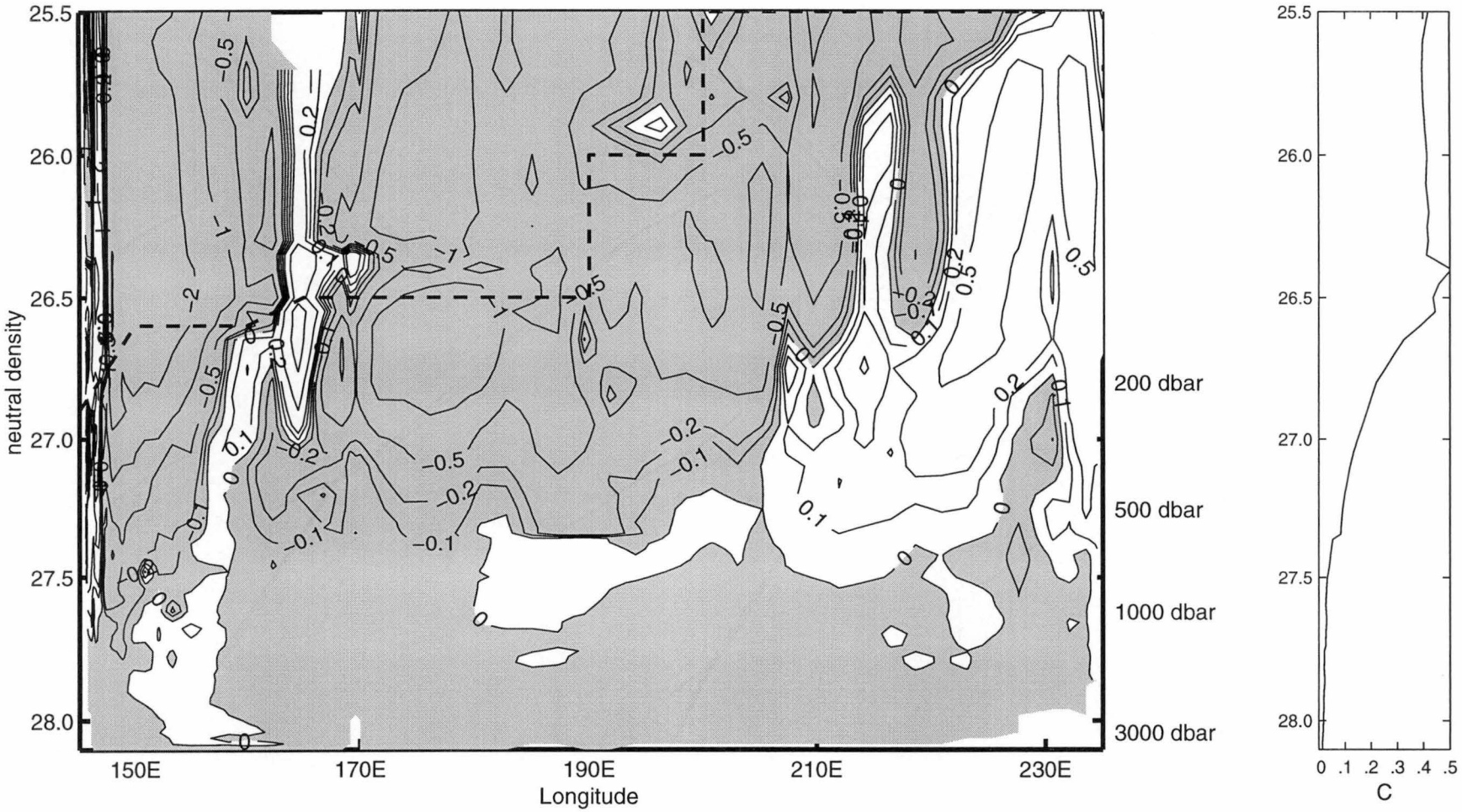

Figure 4.8: (Left) $\theta'|_n$ (°C) along P1. The shaded parts indicate areas with a temperature decrease on neutral surfaces. The average pressures of the neutral surfaces are shown on the right-hand y-axis. The dashed line marks the level below which the objective estimates are realistic. (Right) The right-hand panel shows the average pointwise mapping errors for θ, as a function of neutral density γ^n.

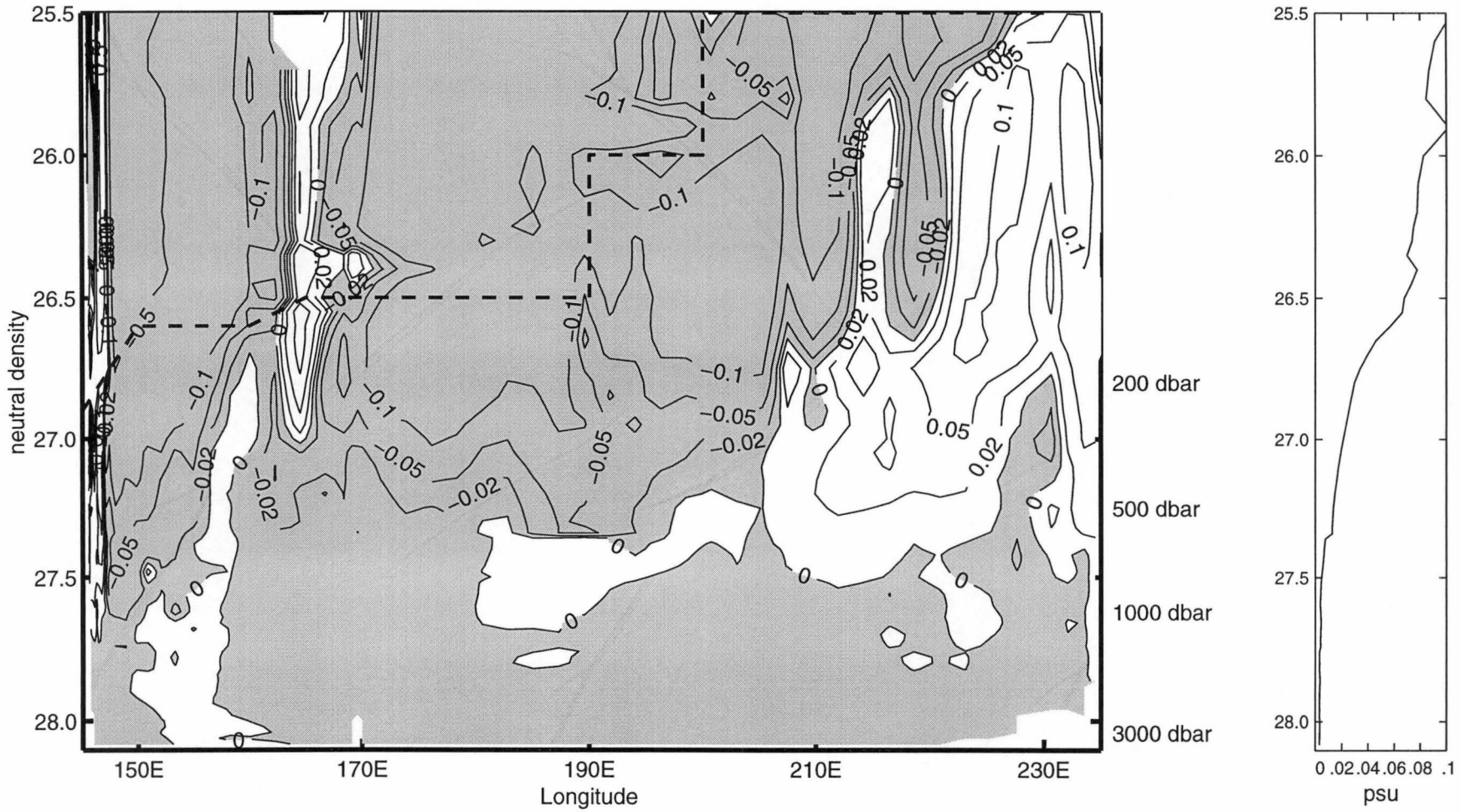

Figure 4.9: (Left) $S'|_n$ (pss) along P1. The shaded parts indicate areas with a salinity decrease on neutral surfaces. The average pressures of the neutral surfaces are shown on the right-hand y-axis. The dashed line marks the level below which the objective estimates are realistic. (Right) The right-hand panel shows the average pointwise mapping errors for S, as a function of neutral density γ^n.

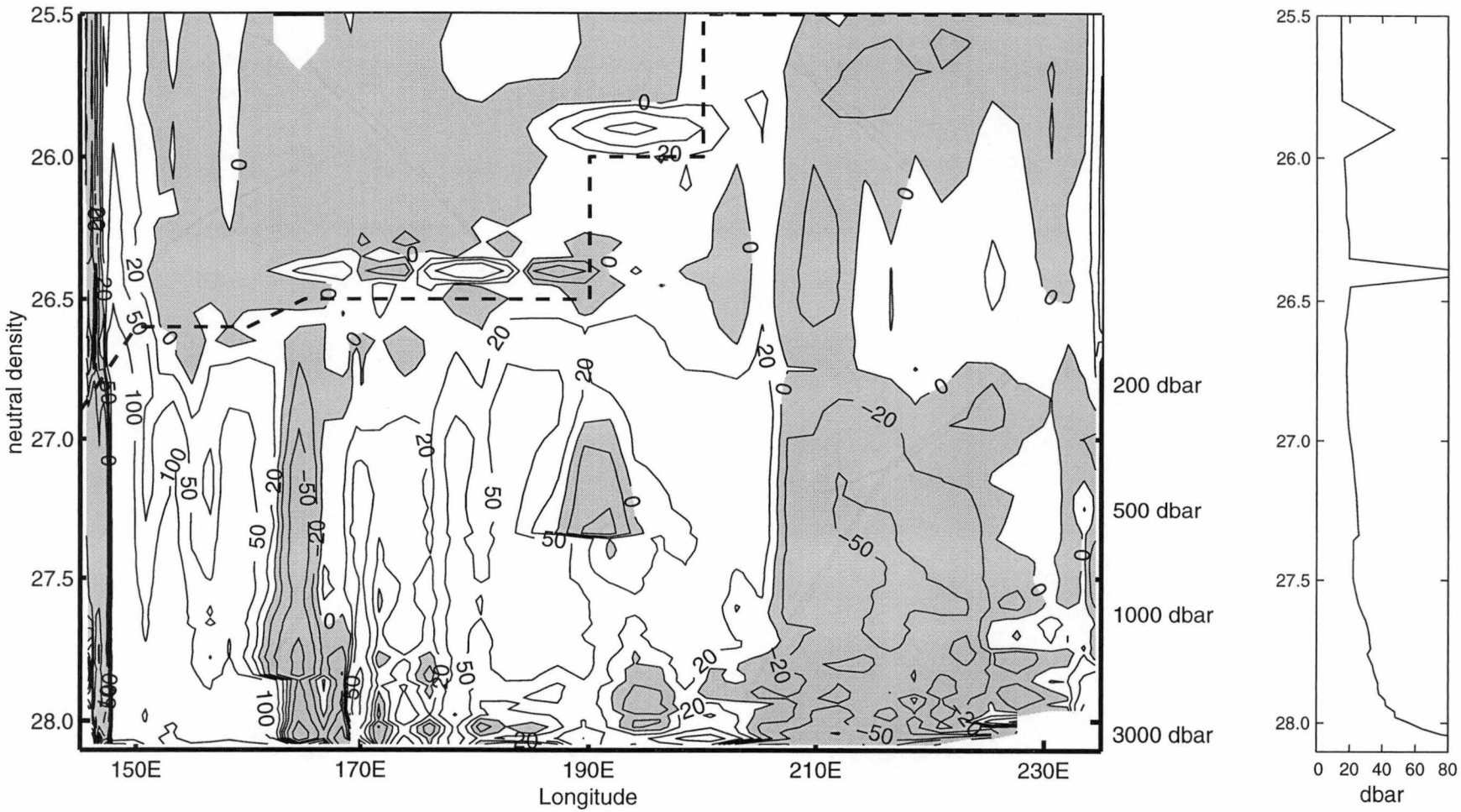

Figure 4.10: (Left) N' (dbar) along P1. The shaded parts indicate a deepening of neutral surfaces. The average pressures of the neutral surfaces are shown on the right-hand y-axis. The dashed line marks the level below which the objective estimates are realistic. (Right) The right-hand panel shows the average pointwise mapping errors for P, as a function of neutral density γ^n.

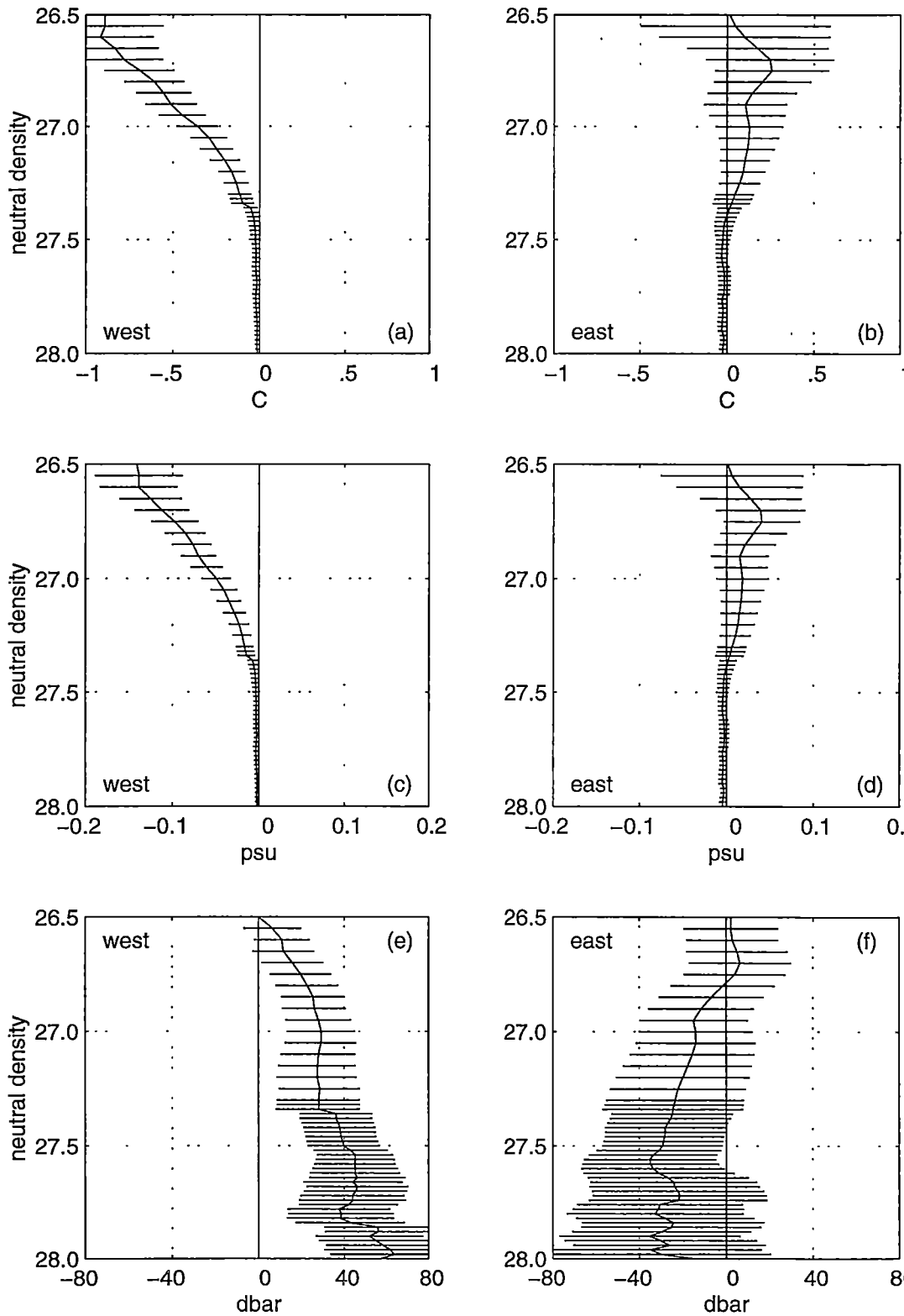

Figure 4.11: Sectional averages between 150°E and 205°E ('west'), and between 205°E and 230°E ('east'), on neutral surfaces below 26.5 γ^n. The error bars indicate 90% confidence intervals estimated by the T-distribution. (a) $\overline{\theta'|_n}$ 'west'. (b) $\overline{\theta'|_n}$ 'east'. (c) $\overline{S'|_n}$ 'west'. (d) $\overline{S'|_n}$ 'east'. (e) $\overline{N'}$ 'west'. (f) $\overline{N'}$ 'east'.

Observed temporal changes on isobars

Temperature and salinity differences on isobars (i.e. $\theta'|_z$ and $S'|_z$) in the top 2000 dbar along P1 are shown in Figure 4.12. Above 200 dbar, cooling and freshening dominate, except for the small region east of 220°E, where significant warming on isobars can be seen (Figure 4.12 a). These changes are unlikely the result of seasonal differences between the historical data and the WOCE data, because the majority of historical data were collected in August, the same month as when WOCE P1 was sampled.

Below 200 dbar, $\theta'|_z$ and $S'|_z$ along P1 display the same east-west division as $\theta'|_n$, $S'|_n$ and N'. To the west of 205°E, significant cooling on isobars (> 0.05 °C) can be seen between 200 dbar and 1600 dbar, accompanied by salinity increase on isobars. To the east of 205°E below 200 dbar, significant warming is accompanied by general freshening on isobars, except for the region between 215°E and 230°E, where significant salinity increase on isobars can be seen between 200 dbar to 400 dbar (Figure 4.12 b).

Combining the observations on isobars with those on neutral surfaces, some qualitative conclusions can be drawn when the stability ratio R_ρ along P1 is taken into account. R_ρ is everywhere negative along P1, except for around the temperature maximum west of 180°E, where $0 < R_\rho < 1$ between 26.7 and 27.4 γ^n. Hence, to the east of 205°E for example, the observed temperature and salinity increase on neutral surfaces above 27.4 γ^n ($\approx$ 700 dbar to the east), combined with warming and freshening on isobars below 200 dbar ($\approx$ 26.7 γ^n to the east), are therefore consistent with the *pure warming* scenario, but are inconsistent with *pure freshening* (see Table 2.1 in Chapter 2, Section 2.3). The pressure-averaged warming and freshening on isobars between 200 dbar and 700 dbar are 0.17°C and 0.016 pss respectively, east of 205°E.

To the west of 205°E, the observed temperature and salinity decrease on neutral surfaces above 27.4 γ^n ($\approx$ 600 dbar to the west), combined with cooling but salinity increase on isobars below 200 dbar ($\approx$ 26.9 γ^n to the west), are therefore consistent with *pure cooling*. In addition, the *pure salinification* scenario can explain the observations where $0 < R_\rho < 1$. Between 200 dbar and 600 dbar, the pressure-averaged cooling and salinity increase on isobars are 0.25°C and 0.017 pss respectively west of 205°E.

Below 600 dbar, basin-wide averages show cooling of about 0.03°C. As discussed in the previous section, this cooling at depth is due to upward heaving of isopycnals, and is not the result of water mass changes.

These qualitative conclusions are useful for interpreting the general

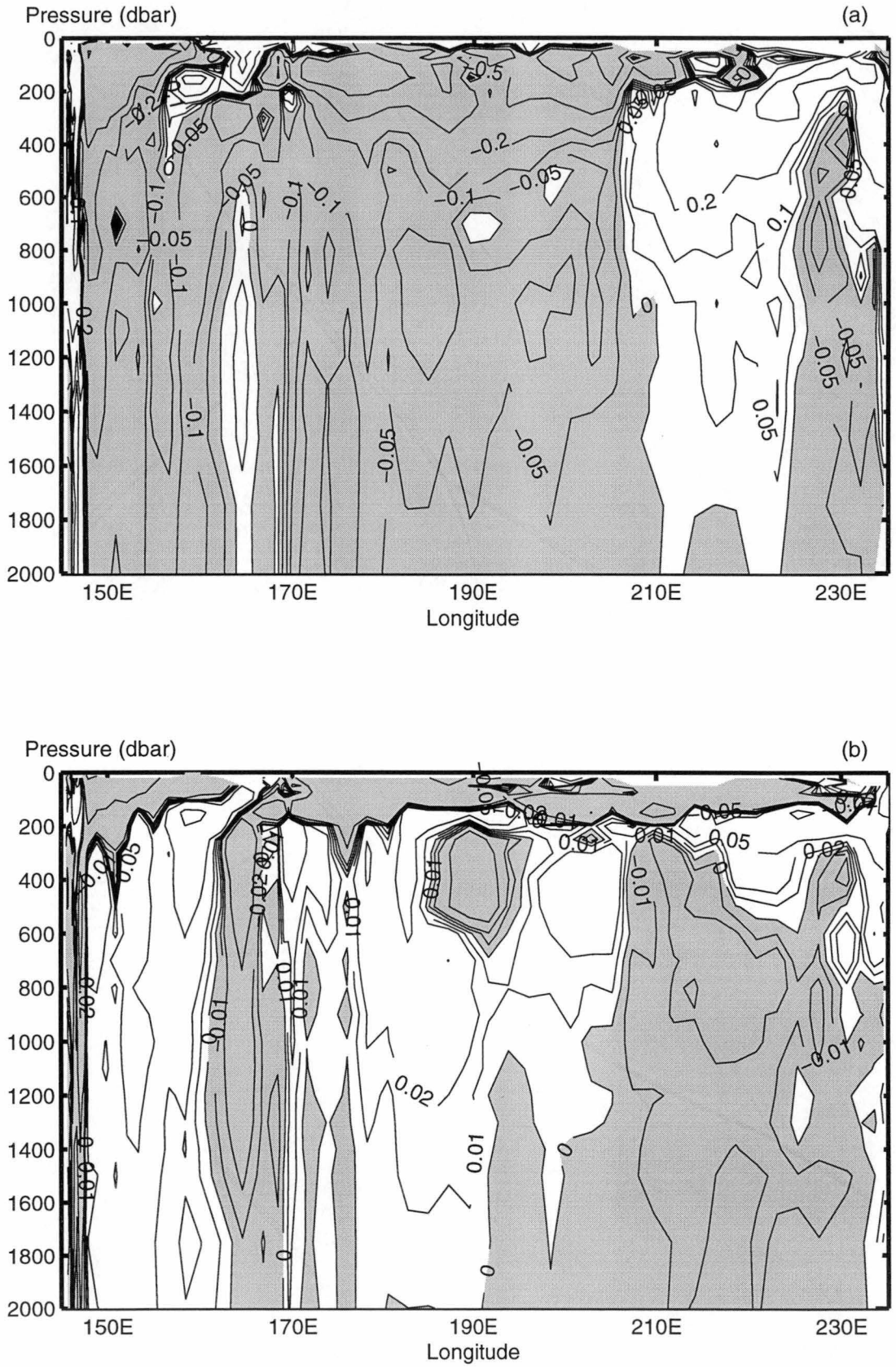

Figure 4.12: (a) $\theta'|_z$ (°C), and (b) $S'|_z$ (pss), for the upper 2000 dbar along P1. Shaded parts indicate, respectively, areas with temperature decrease and salinity decrease on isobars.

broad-scale temporal changes. To resolve the finer details in the observations, and to interpret the combined changes quantitatively, the linear system as formalised in Chapter 2 is solved, and the solutions are discussed in the following section.

Solutions to the inverse problem

This section presents the solutions to the linear system

$$\frac{\rho^{-1}\rho'|_z}{R_\rho - 1} \cdot \begin{bmatrix} -(R_\rho - 1) & 0 & -R_\rho \\ 1 & R_\rho & 0 \\ R_\rho & R_\rho & R_\rho \\ 0 & (R_\rho - 1) & -1 \\ 1 & R_\rho & 0 \\ 1 & 1 & 1 \end{bmatrix} \cdot \begin{bmatrix} A^w \\ A^f \\ A^h \end{bmatrix} = \begin{bmatrix} \alpha\theta'|_z \\ \alpha\theta'|_n \\ \alpha N'\theta_z \\ \beta S'|_z \\ \beta S'|_n \\ \beta N' S_z \end{bmatrix}$$

By solving for the three parameters $\rho^{-1}\rho'|_z A^w$, $\rho^{-1}\rho'|_z A^f$ and $\rho^{-1}\rho'|_z A^h$, the temporal changes observed on neutral surfaces and on isobars are separated into three components, due to the three ventilation scenarios of Bindoff and McDougall (1994). These three parameters have been normalised by their effects on density. Because the three columns in the model matrix are not linearly independent, the system can be solved as an under-determined problem, or as an over-determined problem (see Chapter 2). When the linear system is solved as an under-determined problem, the solution reveals the relative strength of each scenario in causing the observed changes. When the linear system is solved as an over-determined problem, the solution shows which single scenario best represents the observations.

Figure 4.13 shows the solution to the under-determined problem, for neutral surfaces below 25.5 γ^n along P1. West of 205°E, surfaces above 26.5 γ^n are not considered because they are within the seasonal thermocline. Below 26.5 γ^n, *pure cooling* is clearly the stronger process in causing the observed θ and S changes between 26.5 and 27.34 γ^n, while some *pure freshening* is present between 26.5 and 26.7 γ^n (Figure 4.13 a). Below 27.34 γ^n, the changes are small and *pure cooling*, *pure salinification*, and *pure upward heave* show equal strength in causing the observed changes. This is characteristic of the minimum length solution, which, at places where temporal differences are small, tends to distribute the data variance evenly between the three parameters.

East of 205°E, *pure freshening* is the dominant solution and is statistically

significant between 25.5 and 26.0 γ^n (Figure 4.13 b). *Pure cooling* is the strongest process between 26.1 and 26.4 γ^n, while *pure salinification* dominates the observed changes from 26.5 to 26.8 γ^n. *Pure warming* is the strongest process between 26.9 and 27.3 γ^n. However, most of these results to the east of 205°E are not significant at the 90% level below 26.0 γ^n. Below 27.3 γ^n, the majority of the density anomaly is the result of *pure downward heave* (Figure 4.13 b).

The solutions to the over-determined problems are shown in Figure 4.14. To the west of 205°E (Figure 4.14 a), *pure cooling* can be seen to explain more than 60% of the variance for densities between 26.5 and 27.34 γ^n. Below 27.34 γ^n, where the changes are small, *pure upward heave* explains more than 90% of the data variance.

East of 205°E, *pure freshening* explains more than 90% of the variance between 25.5 and 26.0 γ^n (Figure 4.14 b). *Pure cooling* explains more than 60% of the variance in the 26.1 - 26.4 γ^n range, and *pure salinification* explains more than 50% of the variance between 26.5 and 26.8 γ^n. *Pure warming* explains more than 80% of the variance between 26.9 and 27.3 γ^n. Between 27.3 and 27.7 γ^n, *pure downward heave* explains more than 80% of the variance. The dominance of *pure freshening* below 27.7 γ^n east of 205°E (Figure 4.14 b) vanishes from the solution when $\beta S'|_n$ values are increased by $7.56 \times 10^{-4} \times 0.003$, and the corresponding $\alpha\theta'|_n$ values are increased by $1.30 \times 10^{-4} \times 0.02$, for compensating the pre-PSS78 salinity scale used in the historical data.

Table 4.1 summarises the most consistent and dominant solutions in both the under-determined case and the over-determined case. The possible causes and implications of these solutions are explored in the following section.

γ^n	west of 205°E	east of 205°E
25.5 to 26.0		pure freshening
26.0 to 26.5		pure cooling
26.5 to 26.8	pure cooling/pure freshening	pure salinification
26.8 to 27.3	pure cooling	pure warming
> 27.3	pure upward heave	pure downward heave

Table 4.1: The most consistent and dominant ventilation scenarios for explaining the observed subsurface temporal changes along P1.

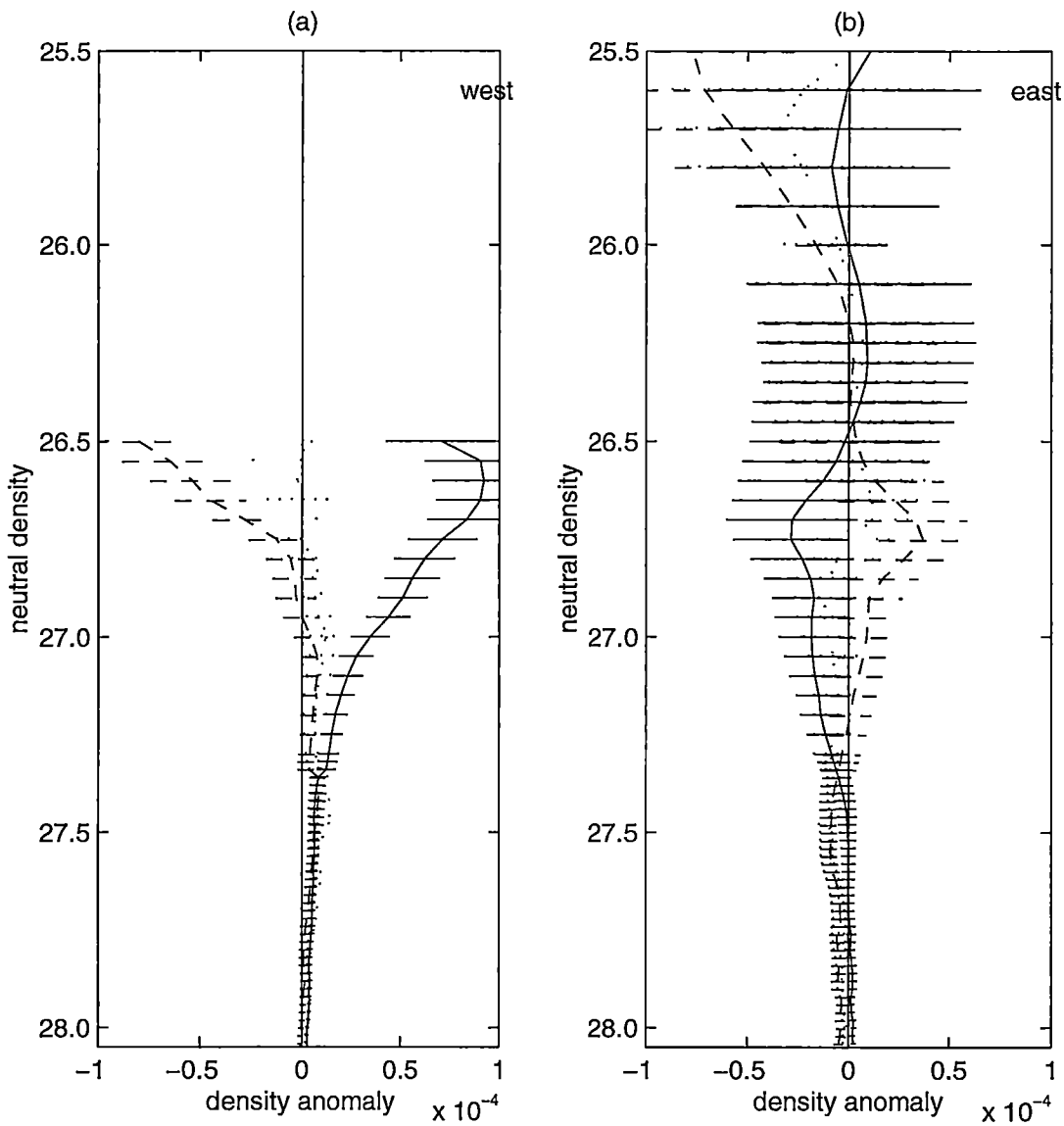

Figure 4.13: Solution to the under-determined problem: density anomaly $\rho^{-1}\rho'|_z$ contributed by each "pure" process, (a) averaged from 150°E to 205°E, and (b) averaged from 205°E to 230°E. — denotes $\overline{\rho^{-1}\rho'|_z A^w}$, - - - denotes $\overline{\rho^{-1}\rho'|_z A^f}$, and .... denotes $\overline{\rho^{-1}\rho'|_z A^h}$. Negative anomalies indicate pure warming, pure freshening and pure downward heave respectively. Horizontal bars mark the 90% confidence intervals.

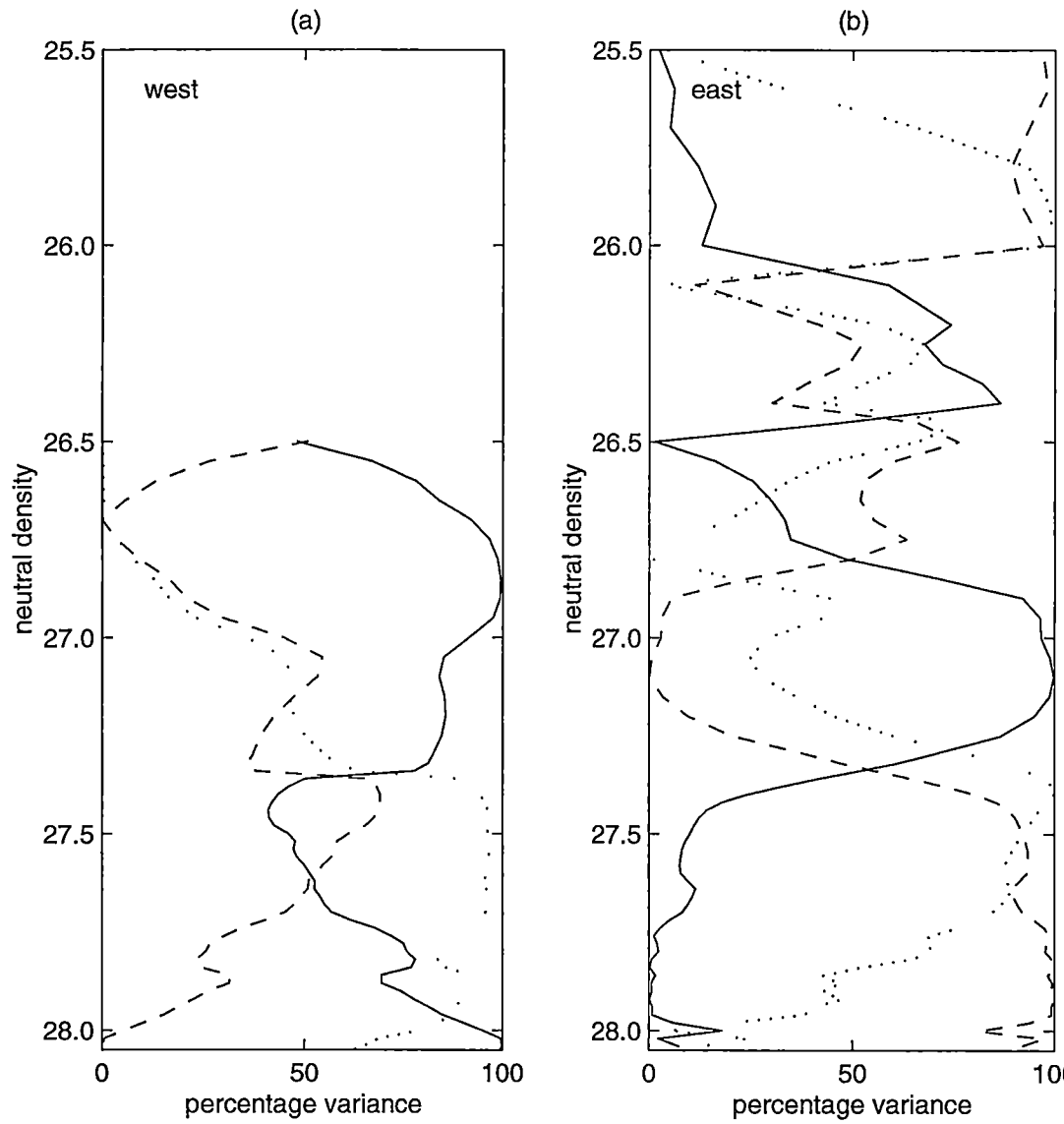

Figure 4.14: Solution to the over-determined problem: percentage of variance of the data explained by a single process, (a) averaged from 150°E to 205°E, and (b) averaged from 205°E to 230°E. — denotes $\overline{\rho^{-1}\rho'|_z A^w}$, - - - denotes $\overline{\rho^{-1}\rho'|_z A^f}$, and .... denotes $\overline{\rho^{-1}\rho'|_z A^h}$.

Discussion

This section discusses the implications of the observed temporal changes. To facilitate discussion, the water column along P1 is divided into three layers: (a) surfaces which outcrop in the North Pacific: 25.5 to 26.8 γ^n, (b) surfaces which show θ-S changes along P1, but do not outcrop in the open North Pacific: 26.9 to 27.3 γ^n, and (c) surfaces below 27.3 γ^n.

(a) 25.5 to 26.8 γ^n

From the winter (Feb-Apr) sea surface density map of Levitus (1982), it can be seen that in the North Pacific, densities between 25.5 and 26.0 γ^n outcrop at a narrow zonal band along roughly 35 - 40°N, and at the northeast Pacific, east of 200°E and north of 40°N. However, only the northeast Pacific (off the west coast of North America and in the Gulf of Alaska) has surface salinity less than 33.0 pss, and is poleward of the WOCE P1 section. Because water in the 25.5 - 26.0 γ^n range along P1 has salinity less than 33.0 pss, it is concluded that this water mass has its origin in the Gulf of Alaska, at the northeast Pacific, north of 45°N and east of 200°E. Hence the *pure freshening* solution for waters east of 205°E along P1, between 25.5 and 26.0 γ^n, implies an increase in surface precipitation minus evaporation rates over the northeastern Pacific. This conclusion is supported by observations of surface salinity trends from four ocean stations off the Pacific coast of Canada (including Ocean Station Papa), which show surface freshening trends over a large area of northeast Pacific (Freeland and Whitney 1997).

On the other hand, densities between 26.1 and 26.4 γ^n outcrop mainly in the northwest Pacific, west of 200°E and north of 40°N. The *pure cooling* solution for waters between 26.1 and 26.4 γ^n along P1 therefore implies a decrease in surface temperatures over the northwestern Pacific prior to 1985.

For densities between 26.5 and 26.8 γ^n, they outcrop only at a limited area near the Kuril Islands and east of Kamchatka (Talley 1991). This density range also includes the temperature minimum layer, which is believed to have an origin in the Bering Sea or the Okhotsk Sea. It is therefore intriguing that waters in this density range along P1 show an east-west division in ventilation scenarios, considering that all waters in this density range share the same source region: the far northwestern Pacific.

Examination of the year distribution of the historical data shows that east of 205°E, the data are dominated by historical casts from 1957, while west of

205°E, the majority of the historical casts were sampled between 1966 and 1970. Hence the signatures to the east of 205°E are for a period that is 10 years longer than those to the west. Hence, within the 26.5 - 26.8 γ^n range along P1, the *pure salinification* solution to the east of 205°E, followed by the *pure cooling* solution to the west (with some effect of *pure freshening*), implies that the Kuril Islands/Kamchatka region during the 1980s has experienced an increase in surface evaporation relative to 1957, then a decrease in surface temperature (with some increase in surface precipitation) relative to 1966-1970. The latter implication concurs with the SST map of Zhang and Levitus (1997), which shows, along 42.5°N, a positive anomaly west of 190°E during 1966-70, and a shift to a negative anomaly by 1980, suggestive of a cycle of temperature anomaly circulating around the North Pacific.

(b) 26.9 to 27.3 γ^n

Densities below the 26.9 γ^n surface do not outcrop anywhere in the open North Pacific (Talley 1991). By studying the $\delta_t = 125$ cl/ton and the 80 cl/ton surfaces (roughly equivalent to 26.9 and 27.4 γ^n), Reid (1965) has shown that the temperature and salinity on these two isopycnals are least along the east coast of Kamchatka and in the Okhotsk Sea, and as the 125 cl/ton and 80 cl/ton waters move eastward from the Okhotsk Sea to the northeastern Pacific, temperature and salinity rise while oxygen values fall. However, while the 125 cl/ton surface occasionally outcrops near Kamchatka and the Kuril Islands, the 80 cl/ton surface does not outcrop anywhere in the North Pacific. Consequently, Reid (1965) concluded that modification of water properties along these two surfaces were achieved by general vertical diffusion around the subarctic gyre, without direct contact with the atmosphere and without convective overturning at specific sites. He then proposed that lateral mixing along the North Pacific circulation would eventually transmit these subarctic characteristics to the subtropical gyre, resulting in the cold, fresh, oxygenated North Pacific Intermediate Water (NPIW).

Reid (1965)'s conclusion was refuted when, during P1, a single CTD station $\theta/S/O_2$ anomaly, observed near the Kuril Islands, led Talley (1991) to deduce that the Okhotsk Sea was the origin of cold, fresh, oxygenated water in the open North Pacific in the density range of 26.8 to 27.6 σ_θ, and that the modification mechanisms were brine rejection during sea ice formation (for densities 26.8 to 27.2 σ_θ) and local vertical mixing (for densities 27.2 to 27.6 σ_θ) in the Okhotsk Sea. Cross isopycnal mixing has been proven to be important

for the deeper isopycnals in the North Pacific by the detection of tritium (Van Scoy et al. 1991) and CFCs (Warner et al. 1996) at the 27.2 σ_θ level: open ocean vertical diffusion alone could not account for the depth to which CFC had penetrated in the North Pacific (700 m in 20 years!). Moreover, the highest concentrations of CFCs on the 26.8 and 27.2 σ_θ surfaces were found near the Okhotsk Sea, further highlighting the processes in the Okhotsk Sea as the primary mechanisms for modifying water properties in the intermediate, non-outcropping density range of the North Pacific. Talley (1993) then proposed that the bulk of the subarctic characteristics were transmitted to the subtropical gyre at the mixed water region of the Kuroshio and the Oyashio, thus limiting the NPIW formation region to the northwestern subtropical gyre.

NPIW does not spread as far north as 47°N. However, water properties along P1 in the density range of 26.9 to 27.3 γ^n (similar density range as NPIW) also have their origin in the Okhotsk Sea, following the conclusion of Talley (1991) and Warner et al. (1996). The different sampling periods of the historical data again result in an east-west division in the temporal changes observed in this density range along P1. So the *pure warming* signature to the east of 205°E in this density range is over a period that is 10 years longer than the *pure cooling* signature to the west. This implies that the Okhotsk Sea outflow during the 1980s is warmer relative to the 1950s, but is colder relative to the 1960s. Again, this concurs with Zhang and Levitus (1997)'s observation, of a cycle of temperature anomaly circulating around the North Pacific.

When the θ and S changes on neutral surfaces are averaged vertically, from 26.5 to 27.3 γ^n, a rough trend can be seen which suggests strongest temperature and salinity decrease west of 160°E, then gradually moderating eastward to 205°E (Figure 4.15). This is consistent with the conclusions that within these densities along 47°N, surface influence comes from the Okhotsk Sea and the Kuril Islands/Kamchatka region, then, after subduction and vertical convection, mixes thus moderates eastward along the eastward-flowing Subarctic Current.

(c) below 27.3 γ^n

Below 27.3 γ^n, θ-S changes are small and are most likely the result of systematic error. However the water column has been affected by *pure downward heave* to the east of 205°E, and *pure upward heave* to the west. As discussed in relation to Figure 4.6, isopycnals along P1 slope downward from west to east in general, indicating broad northward flow relative to a deeper reference level across most of P1. The observed temporal east-west change in

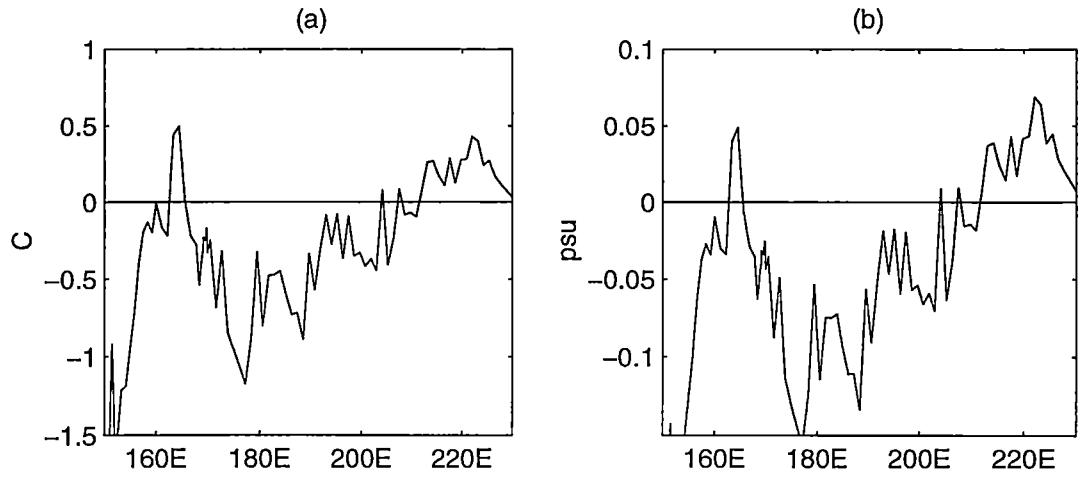

Figure 4.15: Vertical averages of (a) $\theta'|_n$, and (b) $S'|_n$, versus longitude along P1. Vertical averages are taken from 26.5 γ^n to 27.3 γ^n.

neutral surface depths means that the isopycnals are sloping downward more steeply from west to east in the 1980s than in the 1960s. This implies an increase in the northward transport across 47°N.

By the calculations of Roemmich and McCallister (1989), the flow across 47°N, excluding the western and eastern boundaries, is northward between 170°E and 220°E. To determine the change in transport due to *pure heave*, volume transport has been calculated from the WOCE 1985 data, and from the objectively mapped historical data, for all station pairs from 170°E to 220°E, for the water column between 600 dbar ($\approx 27.35\,\gamma^n$) and 2000 dbar ($\approx 27.90\,\gamma^n$), with 2000 dbar being the reference level. The cumulative difference in transport, cumulated westward from 220°E at the eastern boundary, is shown in Figure 4.16. It can be seen that a steady increase in northward transport is apparent across most of P1 between 170°E and 220°E, and the total increase, estimated from the least squares fit line, is a 3 Sv in northward transport.

According to the WOCE P1 data, the total transport across P1 between 170°E and 220°E is approximately 6 Sv northward, between 600 dbar and 2000 dbar. Hence the 3 Sv increase represents a 100% increase in northward transport in this depth range across 47°N, from the 1960s to the 1980s.

An increase in northward transport across 47°N could also imply an increase in velocity of the cyclonic subarctic gyre. Taking the area of the slice of the water column between 170°E and 220°E ($\approx$ 3790 km), and from 600 to 2000 dbar ($\approx$ 1400 m), to be 5.3×10^9 m^2, the 3 Sv increase in northward transport would translate to a 0.057 cm/s increase in eastward velocity along 47°N. Hence over the 20 years from the 1960s to the 1980s, water masses at the

depth range from 600 to 2000 dbar would have been shifted eastward by about 360 km, or approximately 4° to 5° longitude. The resulting salinity decrease on neutral surfaces is less than 0.002 pss.

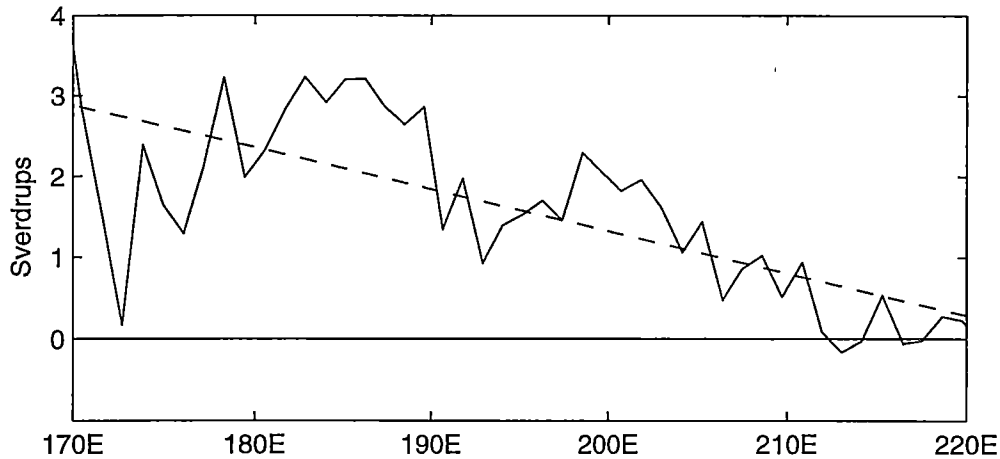

Figure 4.16: Cumulative difference in transport between 600 dbar and 2000 dbar along P1, cumulated westward from 220°E. Positive values indicate northward transport. The dashed line represents the least squares fit for data between 170°E and 220°E.

4.2 Differences along the WOCE P3 section

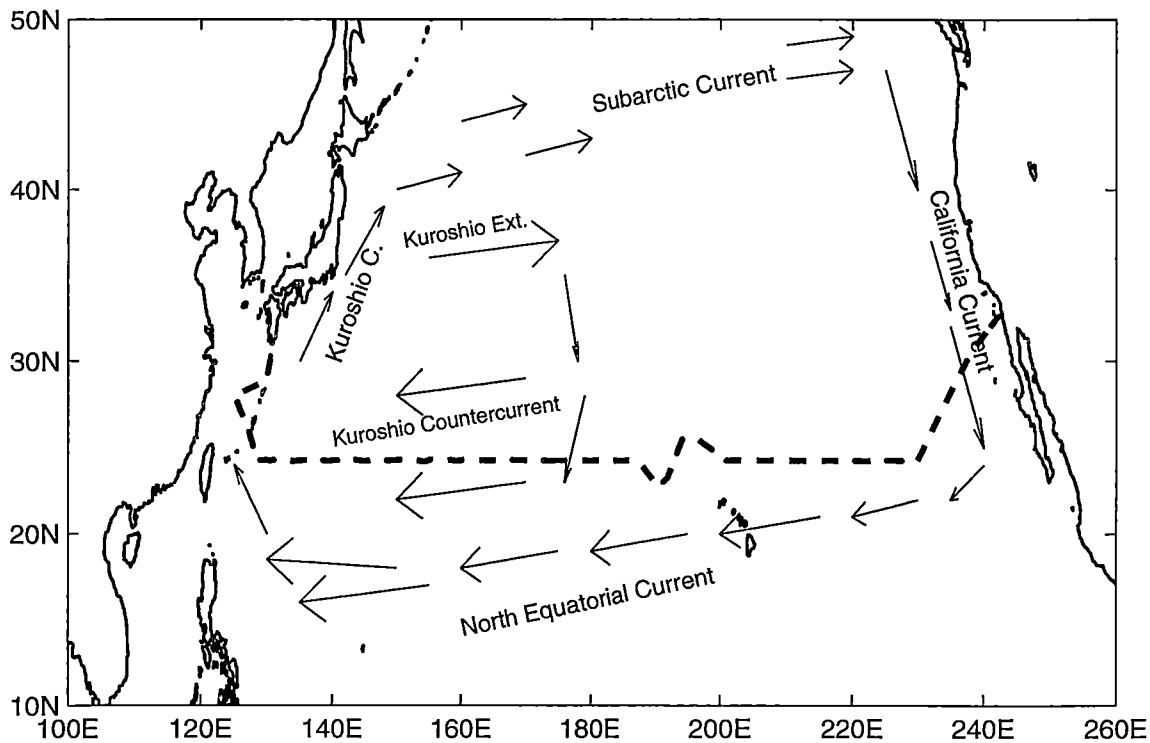

Figure 4.17: Schematic diagram of the North Pacific subtropical gyre. The dashed line marks the cruise track of the WOCE P3 section.

The second North Pacific transect that has been used to study temporal changes is WOCE P3, a zonal section which cuts through the North Pacific subtropical gyre. Figure 4.17 shows the location of the WOCE P3 cruise track in relation to the anticyclonic gyre. The schematic map of the subtropical gyre is adapted from Huang and Qiu (1994)'s acceleration potential map on $\sigma_\theta = 26.2$. The cruise track of P3 begins with a short southwestward leg that runs perpendicular to the coast of California, then turns to follow latitude 24°15' N, and finishes in the East China Sea.

The P3 data set obtained from the WOCE data archive contains 208 CTD casts. 509 historical data points from the Reid and Mantyla Pacific data set that are located between 36°N and 17°N have been used in mapping to the coordinates of P3 (Figure 4.18). These 509 historical data points span the years from 1947 to 1980 (Figure 4.19 a). The majority was sampled between 1966 and 1977. This results in the mean year of sampling being 1970, with the standard deviation being 5.5 years. The median year of sampling is also 1970. As P3 was carried out during April and May 1985, any observed temporal differences along

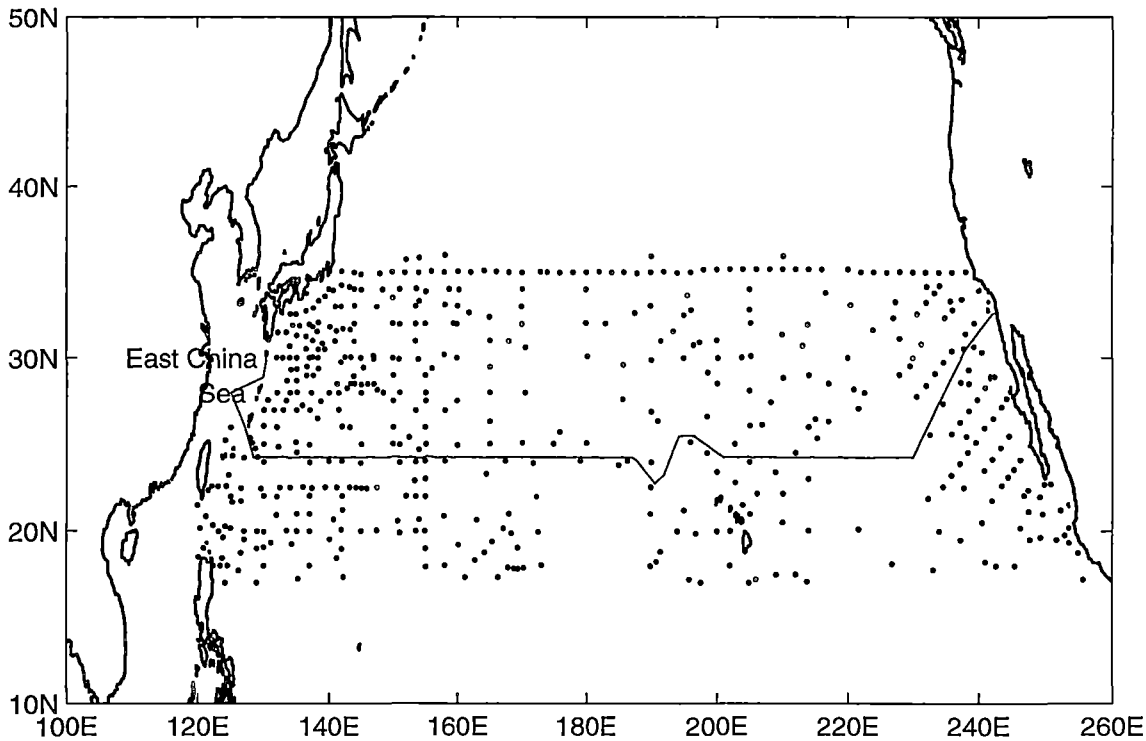

Figure 4.18: The cruise track of the WOCE P3 section, and the distribution of the 509 historical data points that have been used in the mapping to the coordinates of WOCE P3.

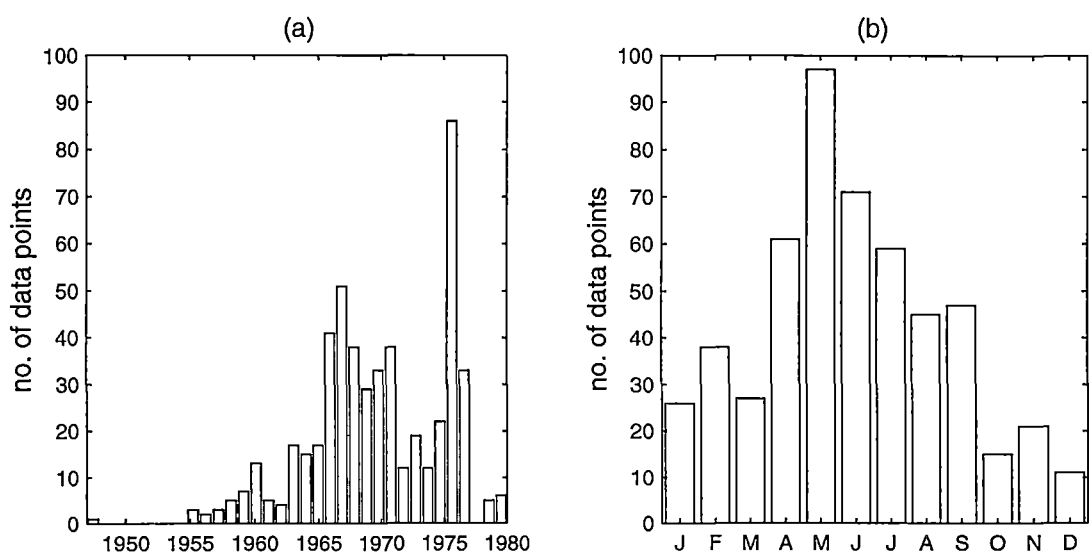

Figure 4.19: (a) The year distribution and (b) the month distribution, of the 509 historical data points in the mapping to the coordinates of the WOCE P3 section.

P3 can therefore be treated as roughly 15 ± 5 years differences. The most frequent month of sampling for these 509 historical data points is May (Figure 4.19 b), the same month as when sampling along P3 was carried out during WOCE. Thus seasonal aliasing in the results should be minimal.

The vertical section of salinity along P3 based on the WOCE CTD data is shown in Figure 4.20. The discontinuity at approximately 194°E is due to a twist in the cruise track when passing through the Hawaiian Islands chain. Salinity reaches a maximum (> 35.2) in the top 200 dbar ($< 25.0\,\gamma^n$) of the water column, due to excess evaporation over precipitation over the interior of the subtropics, away from the coast (Cochrane 1958; Roemmich et al. 1991). This shallow saline water is often called North Pacific Subtropical Water (NPSTW).

Below 200 dbar, two salinity minima can be seen. The shallow salinity minimum (SSM) has $S < 34$, $\theta > 10$°C, and $\gamma^n < 26.4$. It extends from the surface at the eastern end of the transect, westward and downward to about 300 dbar at 224°E (136°W), which is its westernmost extent at this latitude (Roemmich et al. 1991). The bold line in Figure 4.20 marks its extent. The second salinity minimum is present throughout the width of P3, at depths between 300 and 700 dbar. This is North Pacific Intermediate Water (NPIW), and it spans the density range between approximately 26.4 and 27.2 γ^n along P3. Its core salinity is less than 34.1 along 24°N, except at the far western end of the transect, where its salinity is slightly higher. Its core potential temperature is about 7°C. Below the NPIW layer, salinity increases monotonically with depth to the bottom.

Potential temperature along P3 (not shown) decreases monotonically with depth from the surface to the bottom. To the west, a shallow thermostad is present. This is North Pacific Subtropical Mode Water (NPSTMW) and is a feature of the northwestern subtropical gyre. NPSTMW has been identified by many authors as the water mass with vertical temperature gradients less than 1.5°C/100 m (e.g. Hanawa and Suga (1995)). Here, NPSTMW is identified as the thermostad with vertical temperature gradients less than 0.02°C/dbar. During WOCE, NPSTMW along 24°N occupied the water column between 200 and 300 dbar, at approximately 25.5 γ^n, with $\theta \approx 16.5$°C, and $S \approx 34.75$. It extends from about 125°E, east to approximately 160°E (see the shaded region in Figures 4.20 and 4.21).

The stability ratio R_ρ along P3 has a relatively simple structure, with the salinity minimum of NPIW dividing the water column into two areas. From the

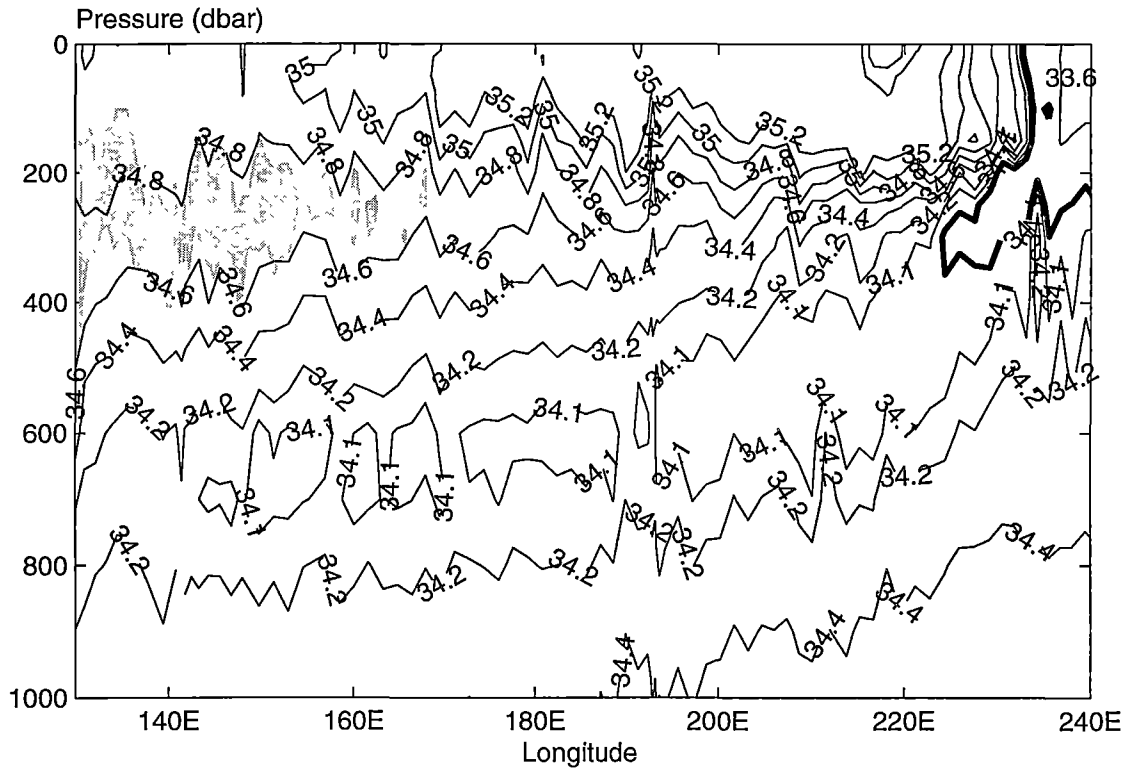

Figure 4.20: Profile of salinity (pss) for the upper 1000 dbar along 24.25°N, based on CTD data from the WOCE P3 section. The shaded area represents the position of NPSTMW. The narrow region west of 130°E is not shown. The bold line marks the 34.0 contour.

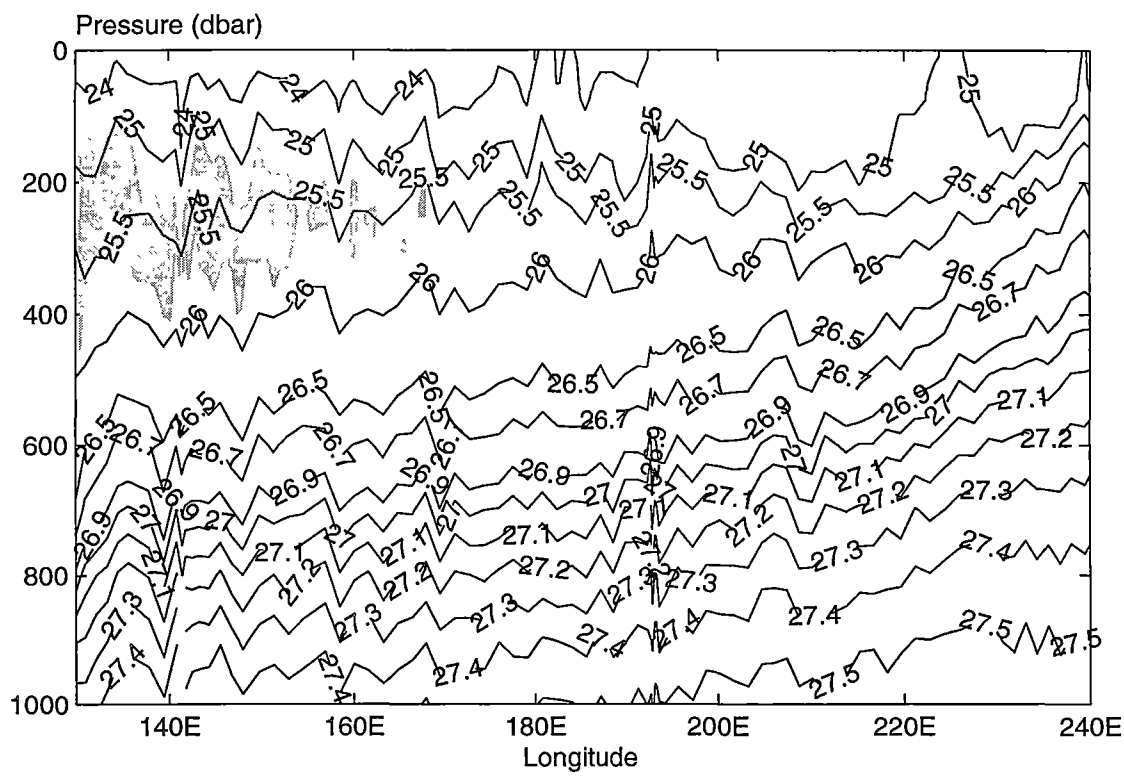

Figure 4.21: Profile of neutral density (kg m^{-3}) along 24.25°N, as in Figure 4.20.

surface down to the salinity minimum of NPIW, except at the eastern end of the transect where the SSM is present, salinity decreases with depth, so $R_\rho > 1$. Below the salinity minimum of NPIW, salinity increases with depth to the bottom, so $R_\rho < 0$. At the salinity minimum, $R_\rho = \infty$.

The vertical section of neutral density is shown in Figure 4.21. The northward-flowing Kuroshio Current, confined to the west of 130°E, is not shown. For the rest of the transect east of 130°E, isopycnals slope upward towards the east, indicating broad southward transport across 24°N. The southward-flowing California Current can be distinguished by the sharp upward-sloping isopycnals in the top 200 dbar of the water column, in the narrow region east of 238°E (Roemmich et al. 1991).

Figure 4.22 shows the θ-S diagram of the water masses along P3, from the WOCE sampling in 1985 (Figure 4.22 a), and from the objectively mapped historical data (Figure 4.22 b). The mapped property fields on neutral surfaces shallower than 25.1 γ^n, which are in the seasonal thermocline, do not accurately form the required neutral surfaces (see Equation 3.1 in Chapter 3). Hence water masses in the top 200 dbar of the water column along P3, such as the surface salinity maximum of NPSTW, are excluded from the discussion. On levels below 25.1 γ^n, the objective estimates of θ, S, and P preserve the neutral surface definition to within instrumental error. The ratios of the standard deviation of the mapping residuals to that of the *a priori* noise, for all three mapped fields θ, S and P on neutral surfaces below 25.1 γ^n, are between 0.8 and 1.0, indicating good length scales fit in the mapping procedure (see Equation B.3 in Appendix B).

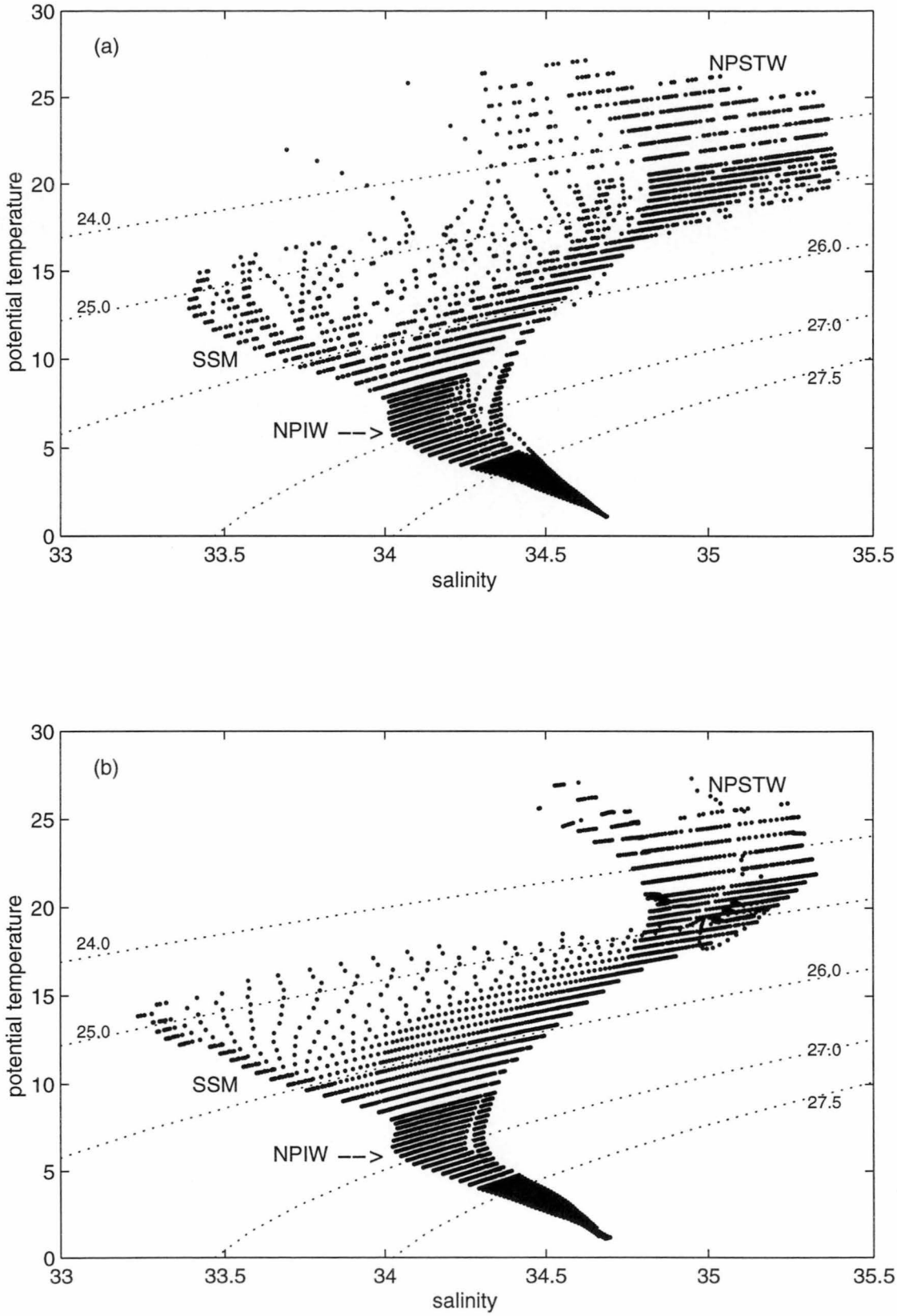

Figure 4.22: θ-S diagram on neutral surfaces along P3, (a) from the WOCE 1985 section, and (b) from the historical data objectively mapped to the coordinates of P3. Lines of constant neutral density are superimposed.

Observed temporal changes on neutral surfaces

Figures 4.23, 4.24 and 4.25 show the temporal differences in potential temperature, salinity and pressure on neutral surfaces (i.e. $\theta'|_n$, $S'|_n$ and N') along P3, from 130°E to 235°E. The Kuroshio Current west of 130°E, and the California Current east of 235°E, are excluded from the discussion, because the objective mapping technique tends not to produce reliable estimates of the hydrographic fields near the boundaries, and because vertical inversions in the mapped pressure field are common in these two areas. The area between 215°E and 230°E, marked by two dashed lines, is an area with very few historical data. This data sparsity results in the pointwise mapping errors for all three mapped fields: θ, S and P, being greater in the longitude range 215°E to 230°E, than the rest of the transect at the same levels. Temporal changes deduced from the mapped fields in this region are therefore treated with caution.

Between 25.0 and 25.5 γ^n, temporal changes are dominated by temperature and salinity decreases on neutral surfaces. $\theta'|_n$ and $S'|_n$ are less than -0.2°C and -0.05 pss respectively at places. The magnitude of these changes are greater than the pointwise mapping errors for those levels. A patch of water centred at 220°E shows an isolated temperature and salinity increase. It is possible that this anomaly is the result of sparse historical data at this longitude, causing the estimated fields to relax toward the *a priori* values.

Between 25.5 and 26.4 γ^n, cooled, freshened patches intersperse with waters that show temperature and salinity increase; it is difficult to discern a coherent pattern within this density range. At places where temperature changes exceed 0.1°C and salinity changes exceed 0.02 pss, these differences are above the pointwise mapping errors at these levels. In particular, the two water masses in this density range, NPSTMW and the SSM, both show significant changes: NPSTMW displays temperature and salinity increases on neutral surfaces, while the SSM displays temperature and salinity decreases on neutral surfaces.

Below the 26.4 γ^n surface, random patches of temperature and salinity increase still exist, but broad areas of cooling and freshening dominate, and are mostly greater than the pointwise mapping errors.

Sectional averages of $\theta'|_n$ and $S'|_n$, taken from 130°E to 235°E (Figure 4.26 a,b), show that the cooling and freshening between 25.0 and 25.5 γ^n are significant above the 90% confidence levels. For densities 25.6 to 26.5 γ^n, θ and S changes on neutral surfaces are not significant above the 90% confidence levels. However, at greater densities, between 26.6 and 27.4 γ^n,

which include the NPIW layer, temperature and salinity decrease are significant at the 90% confidence levels. The maximum sectionally-averaged cooling and freshening of 0.09°C and 0.017 pss, are found on the 27.0 γ^n surface, which is the core density of the NPIW layer.

An unexpected feature of Figure 4.26 (a,b) is that the water column exhibits temperature and salinity decrease on neutral surfaces below 27.5 γ^n ($>$ 1000 dbar) that are significant above the 90% confidence levels. These changes are not uniform with depth, and so it is difficult to attribute them to systematic biases. Examination of the objectively mapped salinity field reveals irregular contours below 2000 dbar ($\approx 27.9\,\gamma^n$), between 170°E and 190°E. It is possible that these deep salinity anomalies are the result of sparse historical data at that longitude range (see Figure 4.18), and suggest that the observed temperature and salinity decreases on neutral surfaces deeper than 27.9 γ^n are likely a consequence of the data inadequacy. However, the maximum sectionally-averaged temperature decrease (0.035°C) and salinity decrease (0.006 pss) occur at 27.88 γ^n ($\approx$ 1800 dbar). This level is below the oxygen minimum layer along 24°N ($\approx$ 1000 dbar, $\approx 27.5\,\gamma^n$), and is above the silicate maximum ($>$ 2000 dbar, $> 27.9\,\gamma^n$). Temporal changes on decadal time-scales are not expected of this water because the residence time of the deep water of the North Pacific is of the order of centuries.

All neutral surfaces from 25.7 γ^n to the deepest surface have become deeper. However, no east-west variation (such as that observed along 47°N) is evident in the spatial pattern of N' along 24°N. The largest sectionally-averaged isopycnal excursion of 25.8 dbar occurs at the 26.9 γ^n surface (Figure 4.26 c). In the NPIW density range, the temporal pressure changes of the neutral surfaces are not uniform with depth. For example, the 26.4 γ^n surface ($\approx$ 430 dbar) has deepened by 14.9 dbar, while the 27.2 γ^n surface ($\approx$ 740 dbar) has deepened by 19.1 dbar. This means that the NPIW layer has increased in thickness by 4.2 dbar, or 1.4%, over the roughly 15-year period between the WOCE sampling and the mean historical period.

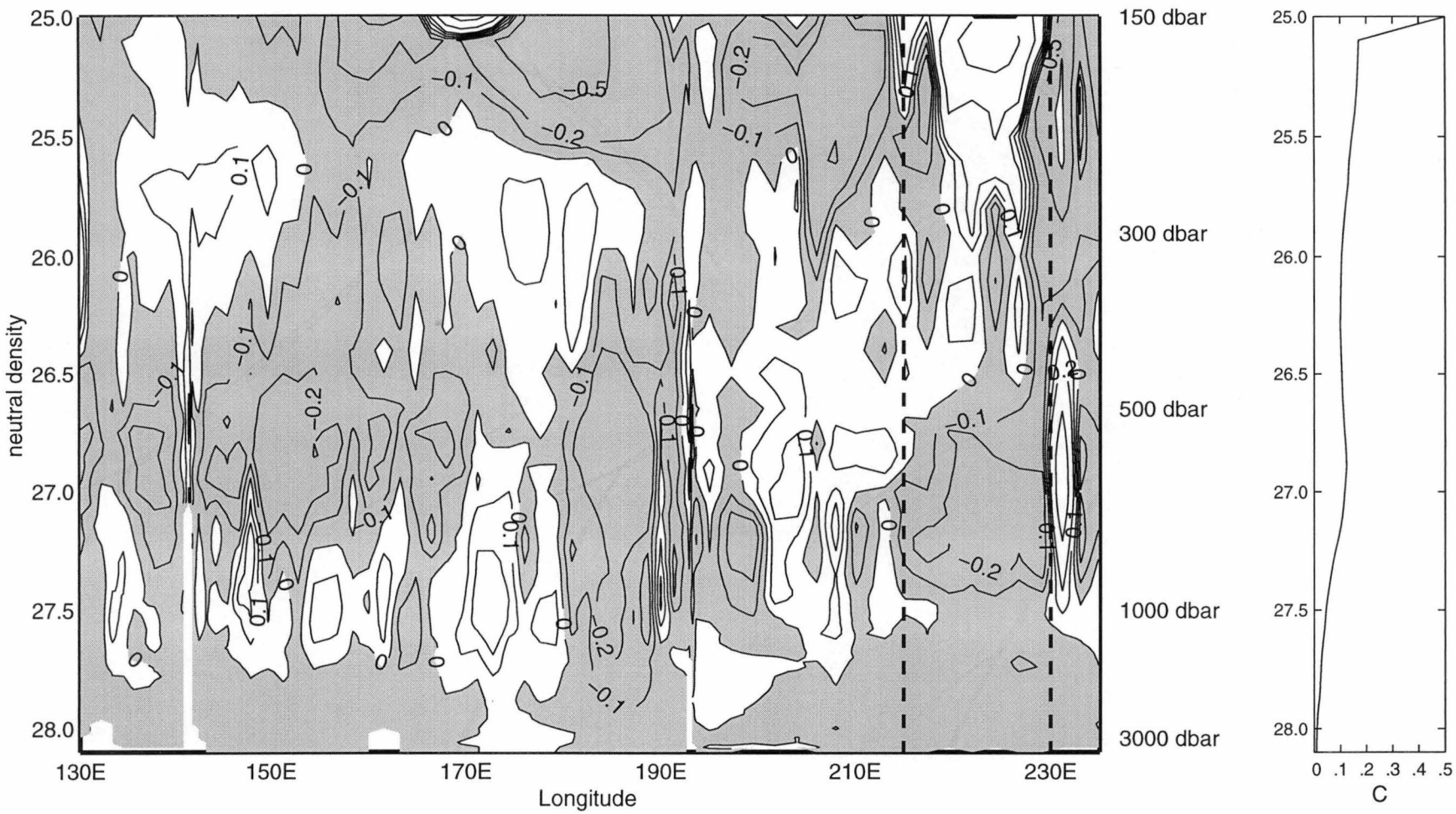

Figure 4.23: (Left) $\theta'|_n$ (°C) along P3. The shaded parts indicate areas with a temperature decrease on neutral surfaces. The average pressures of the neutral surfaces are shown on the right-hand y-axis. (Right) The right-hand panel shows the average pointwise mapping errors for θ, as a function of neutral density γ^n.

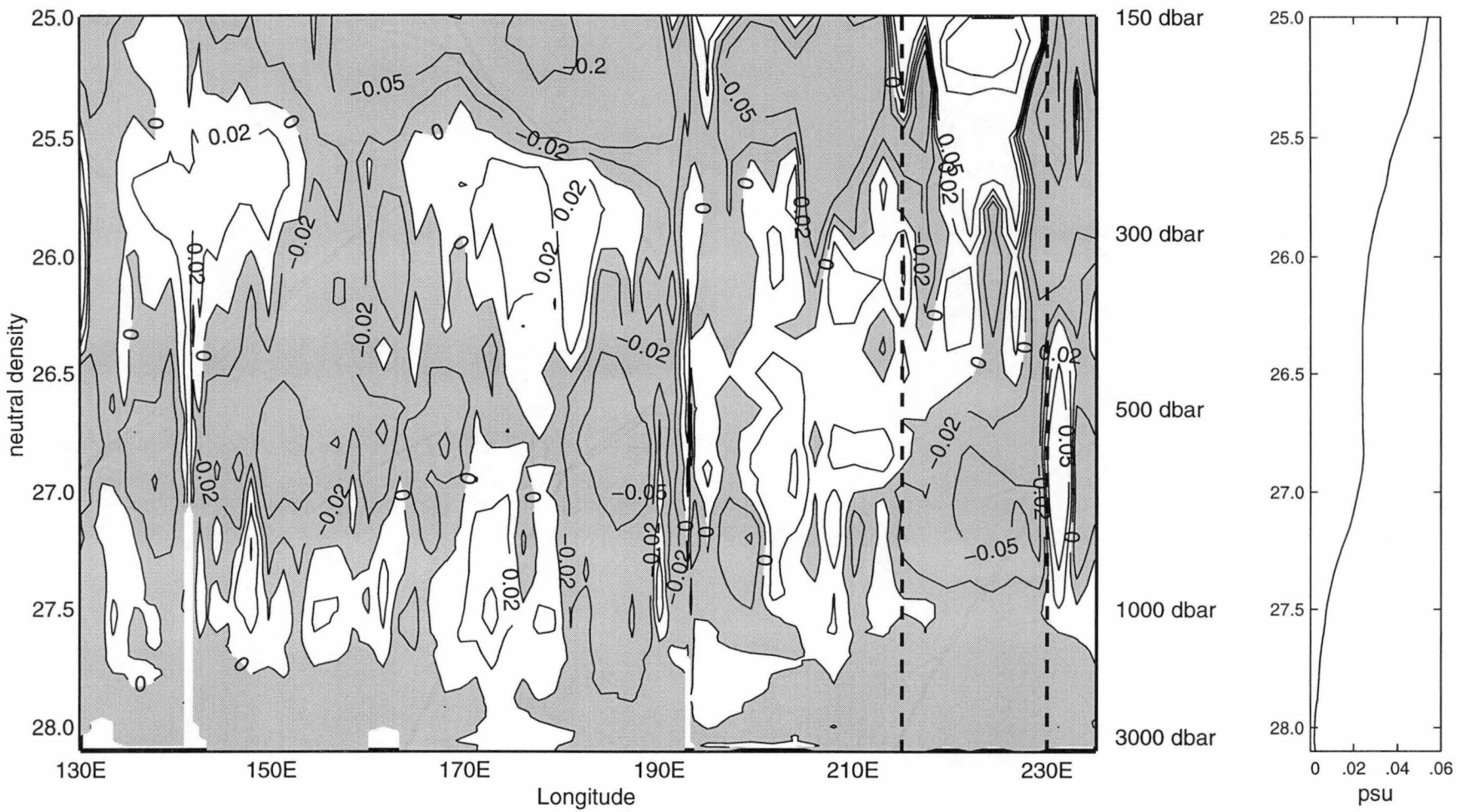

Figure 4.24: (Left) $S'|_n$ (pss) along P3. The shaded parts indicate areas with a salinity decrease on neutral surfaces. The average pressures of the neutral surfaces are shown on the right-hand y-axis. (Right) The right-hand panel shows the average pointwise mapping errors for S, as a function of neutral density γ^n.

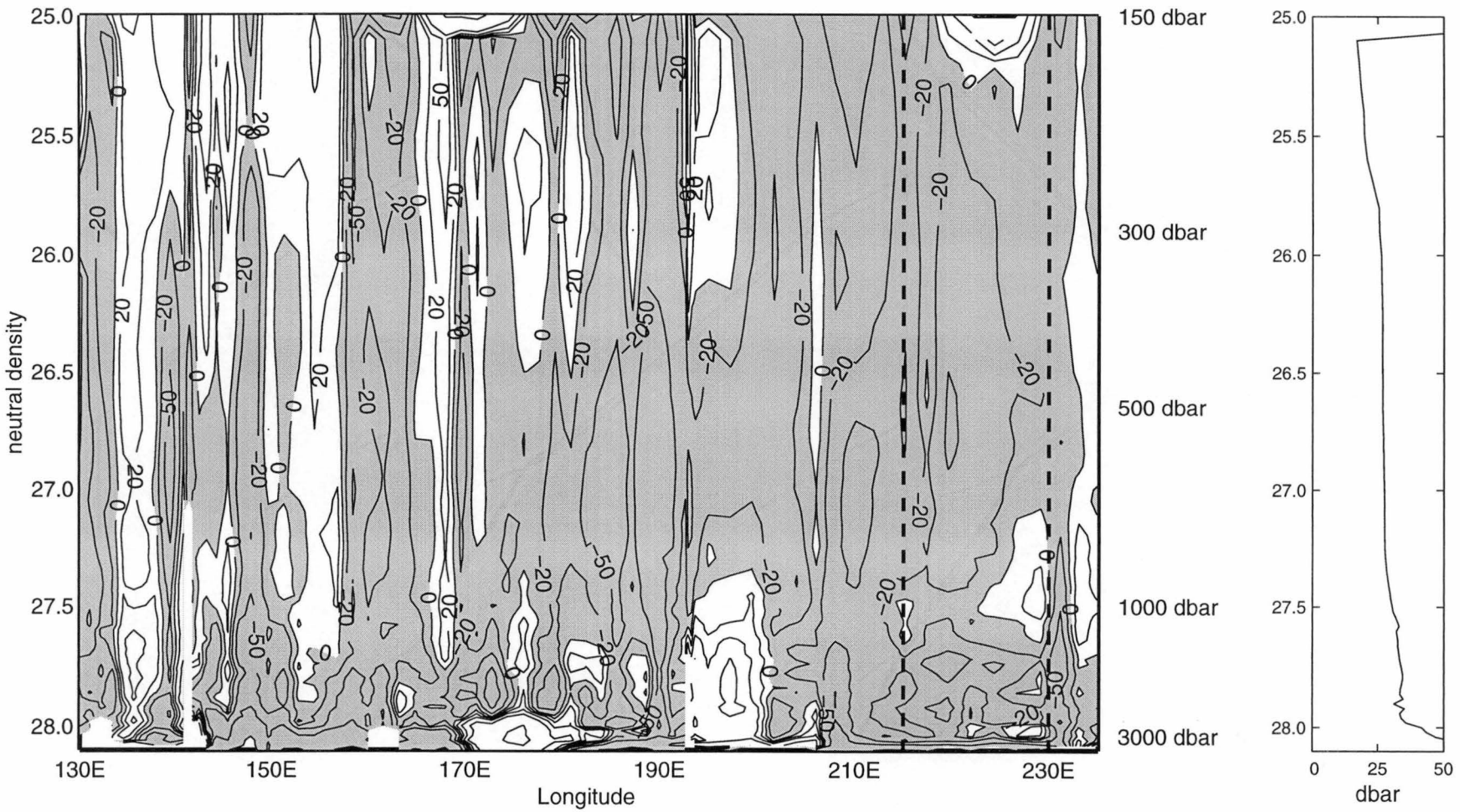

Figure 4.25: (Left) N' (dbar) along P3. The shaded parts indicate a deepening of neutral surfaces. The average pressures of the neutral surfaces are shown on the right-hand y-axis. (Right) The right-hand panel shows the average pointwise mapping errors for P, as a function of neutral density γ^n.

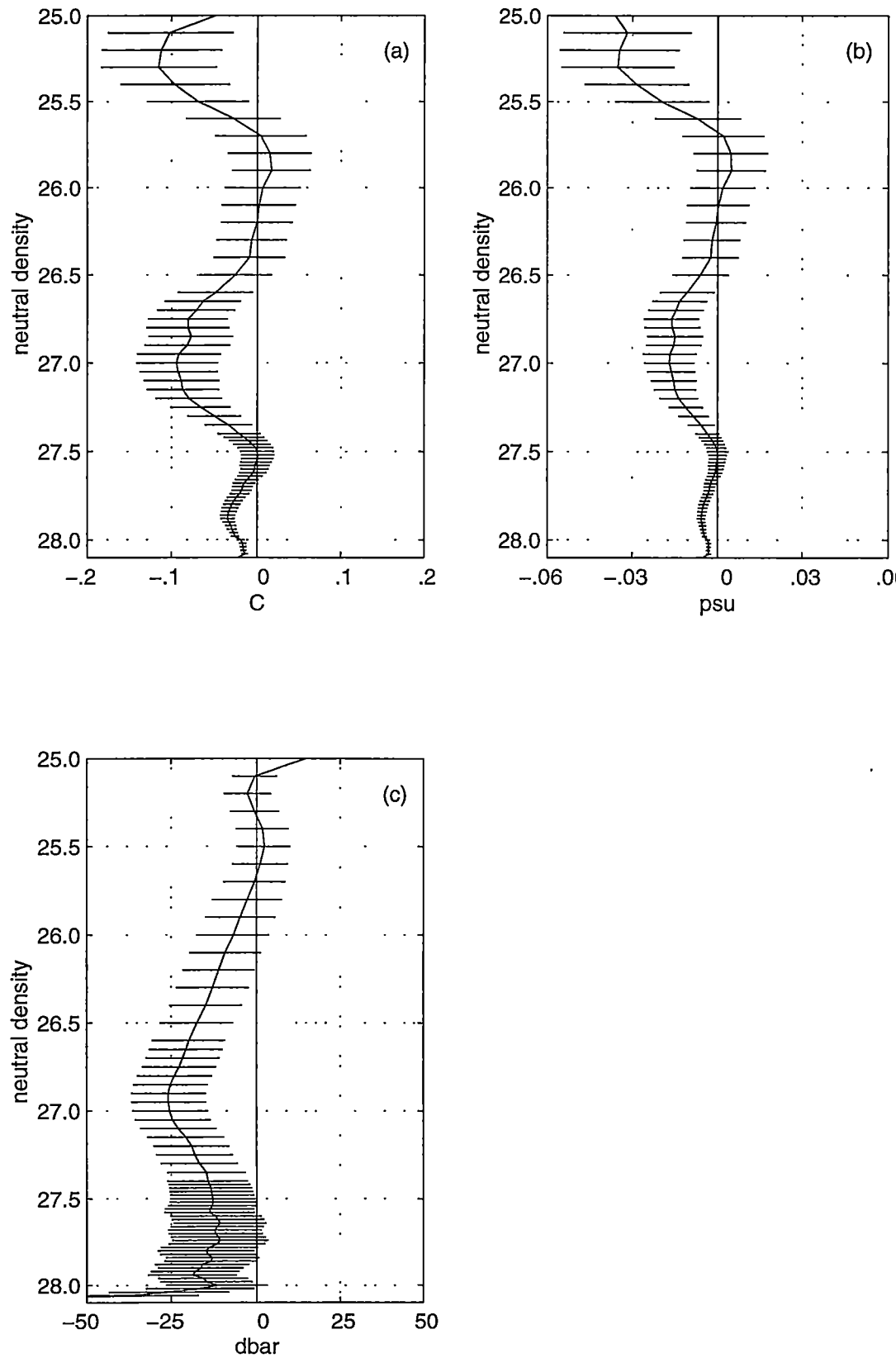

Figure 4.26: Sectional averages between 130°E and 235°E along P3. The error bars indicate 90% confidence intervals. (a) $\overline{\theta'|_n}$, (b) $\overline{S'|_n}$, and (c) $\overline{N'}$.

Observed temporal changes on isobars

Figure 4.27 shows the changes of temperature and salinity on isobars along P3. Below 2000 dbar, changes are negligible and so are not shown. It is obvious that mesoscale eddies have a strong influence on the differences on isobars, making a spatially disorganised picture of negative differences alternating with positive differences. To obtain the mean state of change on isobars for the two upper-layer water masses: the SSM and NPSTMW, spatial averages have been taken over their zonal extents along P3: from 130°E to 160°E for NPSTMW (Figure 4.28 a,b), and from 224°E to 235°E for the SSM (Figure 4.28 c,d). Note that confidence intervals have not been calculated for these averages, because the number of data points is small relative to the *a priori* noise, that the resulting confidence intervals (described in Appendix C) are too large for the averaged differences to be statistically meaningful.

These averages show that NPSTMW (at 200 to 300 dbar) has undergone temperature and salinity decrease on isobars, while the SSM (surface to 300 dbar) has experienced temperature increase on isobars. The top part of the SSM above 150 dbar has experienced some salinity decrease on isobars, while the bottom part of the SSM from 150 to 300 dbar has experienced some salinity increase. For the rest of the transect between 160°E and 210°E, averaged changes on isobars show general freshening and warming between 150 and 230 dbar ($\approx$ 25.0 to 25.5 γ^n).

Qualitatively, the observed cooling and freshening on isobars in NPSTMW, where $R_\rho > 1$, with the corresponding changes on neutral surfaces being $\theta'|_n > 0$ and $S'|_n > 0$, are therefore consistent with the *pure cooling* scenario. In the SSM layer, the slope of the θ-S curve changes from $R_\rho > 1$ to $R_\rho = \infty$. There, the observed warming on isobars, combined with $\theta'|_n < 0$ and $S'|_n < 0$, are in accord with the *pure warming* scenario. For the rest of the transect between 160°E and 210°E, the combined observations suggest that the water mass between 25.0 and 25.5 γ^n has undergone either *pure warming* and/or *pure freshening.*

Below 500 dbar, at the level of the NPIW layer, the entire transect displays freshening on isobars, and general temperature increase (Figure 4.28 e,f). In the NPIW layer, the slope of the θ-S curve changes from $R_\rho > 1$ to $R_\rho = \infty$, then to $R_\rho < 0$. The freshening and warming on isobars observed in the NPIW layer, combined with the observed changes on neutral surfaces being $\theta'|_n < 0$ and $S'|_n < 0$, therefore suggest that the NPIW layer along P3 has mainly undergone *pure freshening*, and *pure warming* above the salinity minimum.

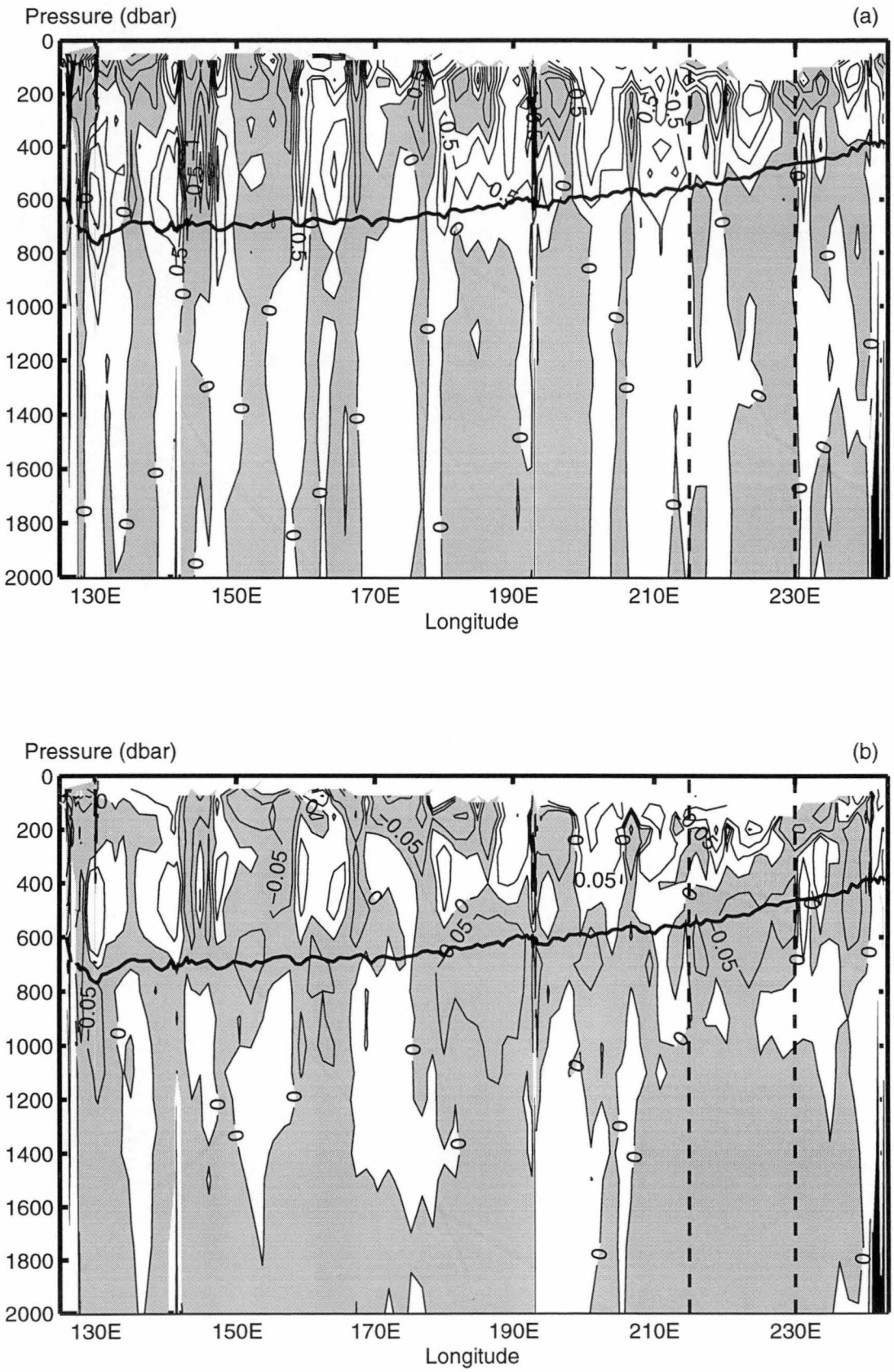

Figure 4.27: (a) $\theta'|_z$ (°C), and (b) $S'|_z$ (pss) for the upper 2000 dbar along P3. Shaded parts indicate, respectively, areas with temperature decrease and salinity decrease on isobars. The solid line marks the average depth of the 26.95 γ^n surface, which is the core density of the NPIW layer.

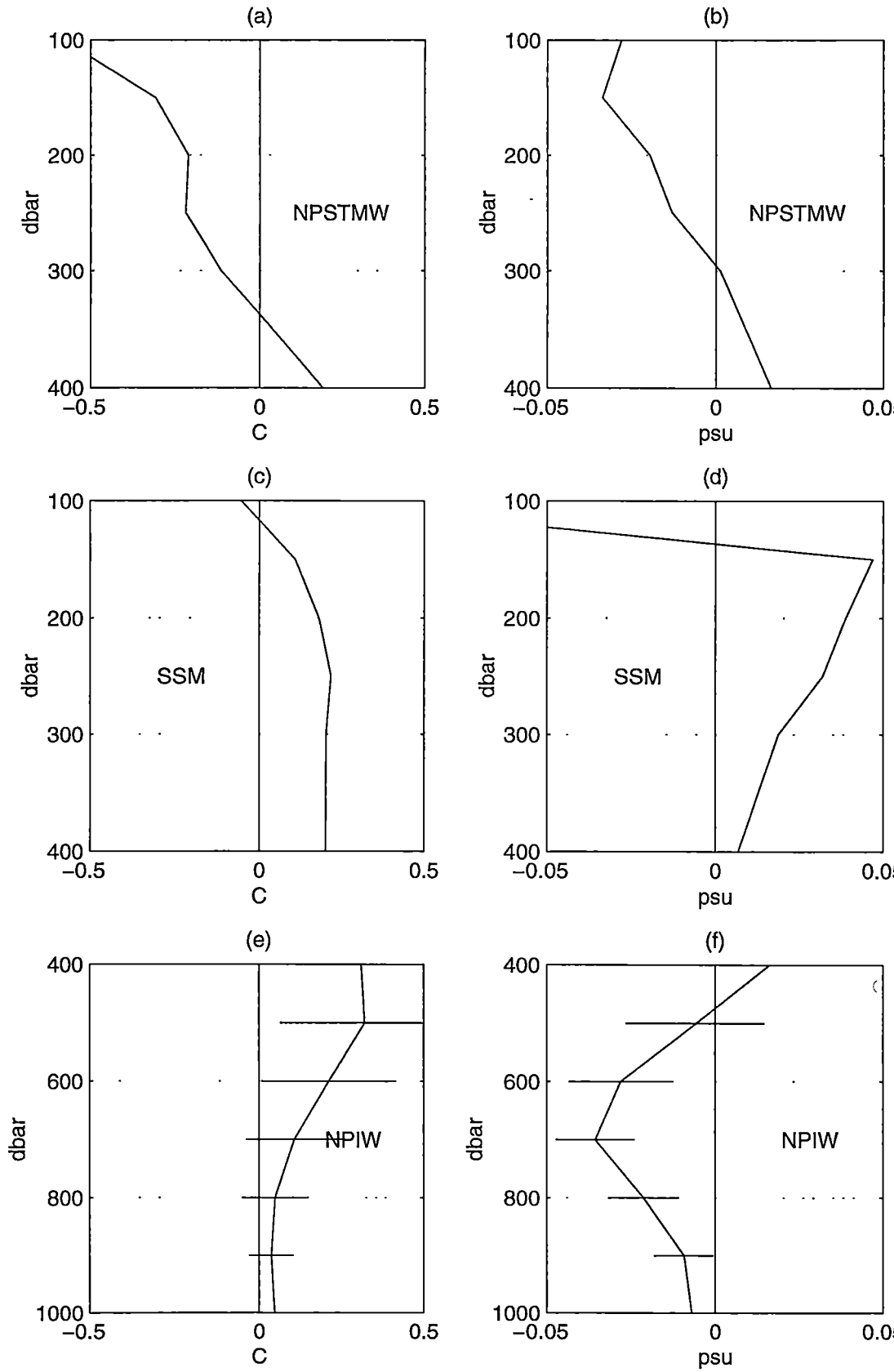

Figure 4.28: (a) and (b) $\overline{\theta'|_z}$ and $\overline{S'|_z}$, averaged between 130°E and 160°E. (c) and (d) $\overline{\theta'|_z}$ and $\overline{S'|_z}$, averaged between 224°E and 235°E. (e) and (f) $\overline{\theta'|_z}$ and $\overline{S'|_z}$, averaged between 130°E and 235°E. The horizontal bars indicate 90% confidence intervals.

Solutions to the inverse problem

In this section, the combined observations on neutral surfaces and on isobars along the WOCE P3 section are decomposed quantitatively into three components due to the three ventilation processes. Figure 4.29 shows the sectionally-averaged solutions to both the under- and the over-determined problems, averaged along the entire length of P3, but excluding the western and eastern boundaries.

For densities between 25.0 to 25.5 γ^n, *pure freshening* and *pure warming* are both responsible in causing the observed changes (Figure 4.29 a). *Pure freshening* accounts for more than 50% of the data variance, while *pure warming* explains more than 90%. From 25.5 to 26.5 γ^n, *pure downward heave* explains a greater percentage of the data variance (over 90%) than the other two ventilation scenarios (Figure 4.29 b).

Figures 4.30 and 4.31 show the solutions for two particular water masses in the 25.5 - 26.5 γ^n range: NPSTW and the SSM. For NPSTMW, which resides on the 25.5 γ^n surface, *pure cooling* and *pure upward heave* are the dominant processes, and explain more than 90% of the data variance. At the SSM (26.1 - 26.4 γ^n), *pure warming* is the dominant process and explains more than 70% of the data variance. Some effect of *pure freshening* is present around 26.1 γ^n.

In the NPIW density range, 26.4 - 27.2 γ^n, *pure freshening* and *pure warming* are the two processes responsible for the observed changes (Figure 4.29 a). *Pure warming* accounts for more than 80% of the data variance between 26.4 and 26.9 γ^n (i.e. above the salinity minimum), while *pure freshening* accounts for more than 60% of the data variance between 27.0 and 27.4 γ^n (i.e. below the salinity minimum) (Figure 4.29 b). In addition, the entire NPIW layer along P3 has been affected by *pure downward heave.*

Between 27.4 and 27.65 γ^n, *pure downward heave* accounts for more than 90% of the variance. Below 27.65 γ^n ($\approx$ 1200 dbar), *pure freshening* dominates the solution, but as discussed previously, the temperature and salinity decreases on neutral surfaces associated with the *pure freshening* solution are more likely due to historical data inadequacy at those depths.

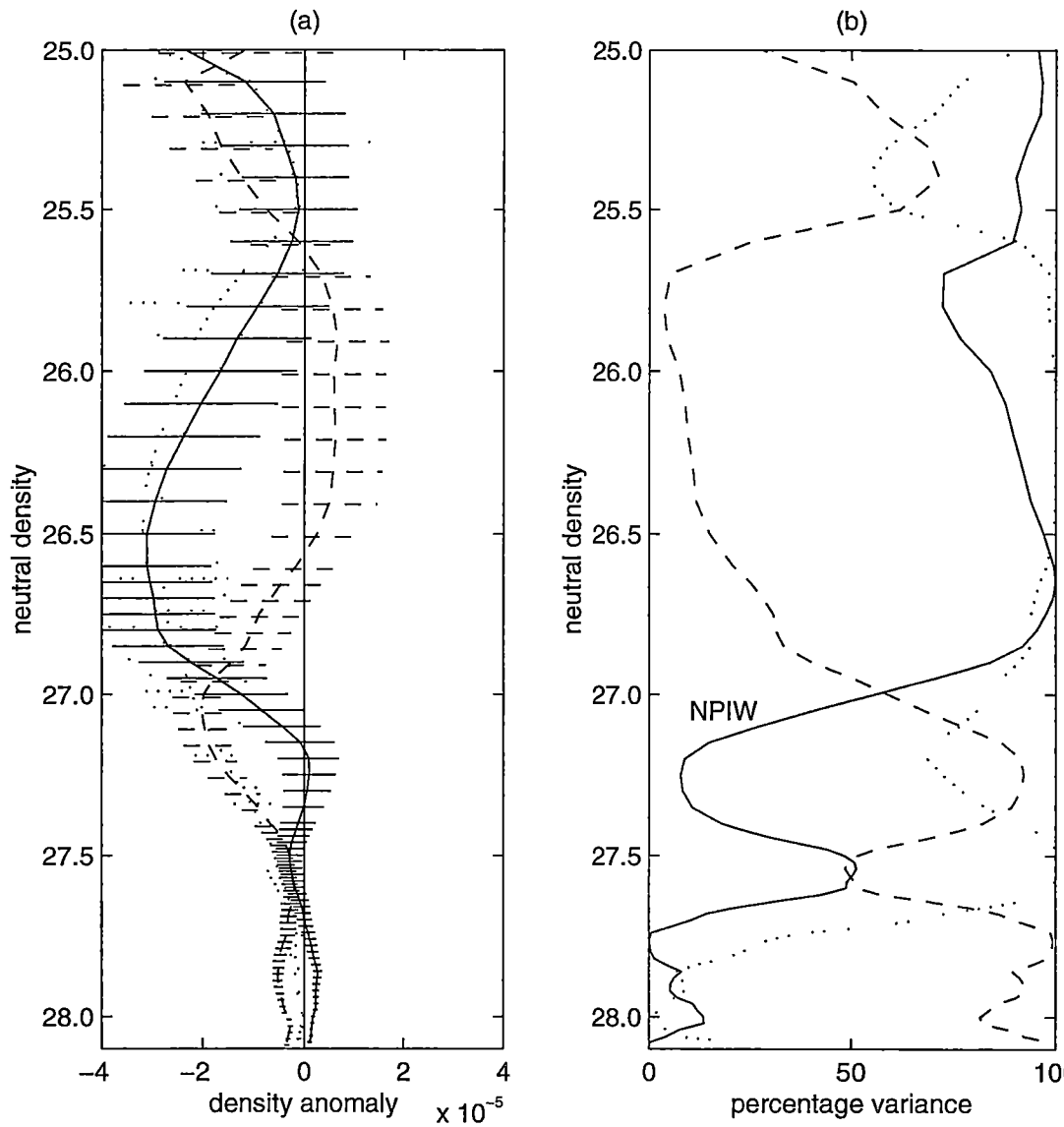

Figure 4.29: (a) Density anomaly $\rho^{-1}\rho'|_z$ contributed by each "pure" process: solution to the under-determined problem, and (b) percentage of variance of the data explained by a single process: solution to the over-determined problem. — denotes $\overline{\rho^{-1}\rho'|_z A^w}$, - - - denotes $\overline{\rho^{-1}\rho'|_z A^f}$, and .... denotes $\overline{\rho^{-1}\rho'|_z A^h}$. Negative anomalies indicate pure warming, pure freshening and pure downward heave respectively. Solutions are averaged from 130°E to 235°E. Horizontal bars mark the 90% confidence intervals.

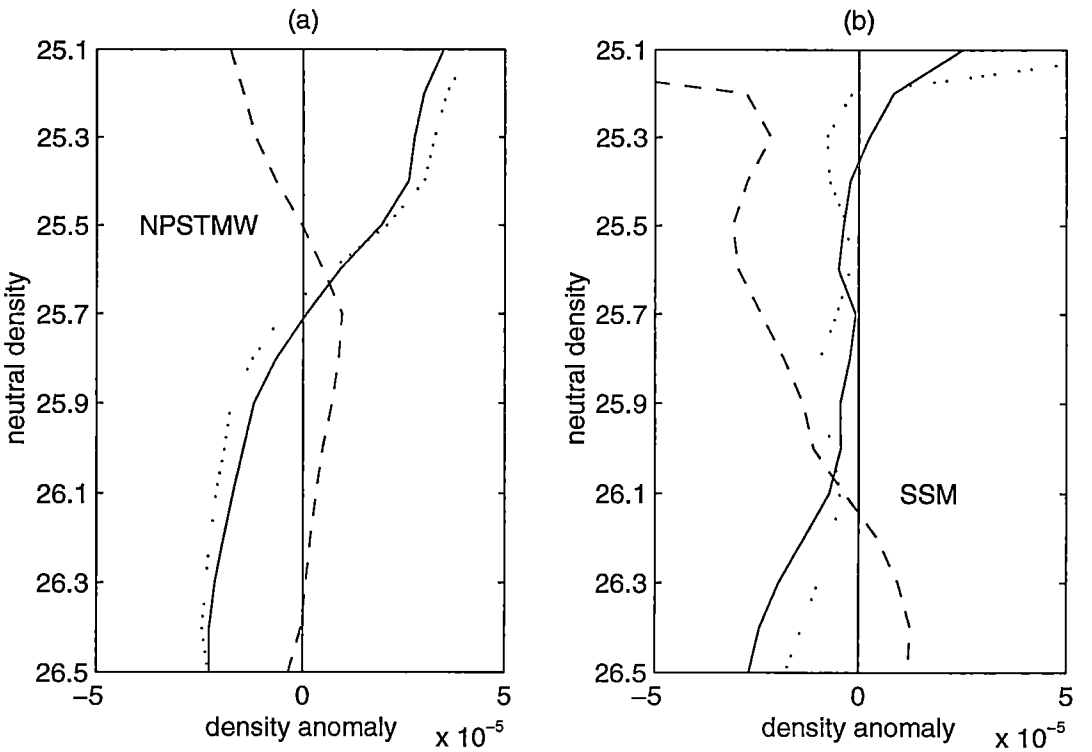

Figure 4.30: Solution to the under-determined problem, (a) averaged from 130°E to 160°E, and (b) averaged from 224°E to 235°E. As in Figure 4.29 (a).

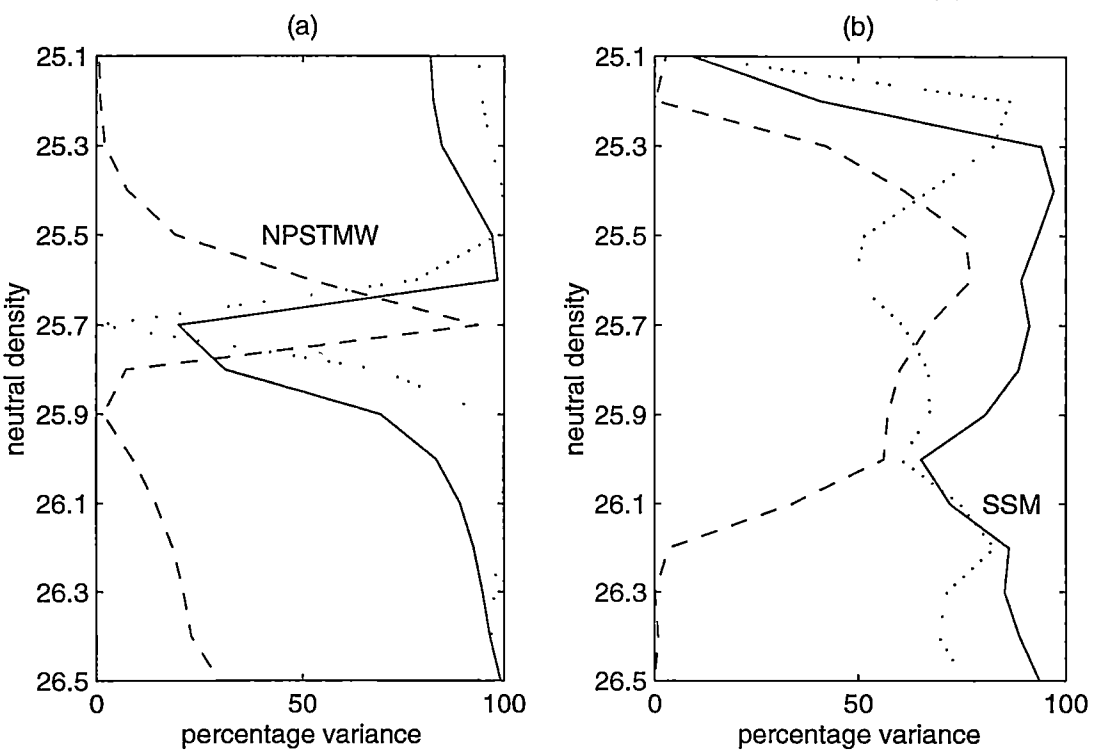

Figure 4.31: Solution to the over-determined problem, (a) averaged from 130°E to 160°E, and (b) averaged from 224°E to 235°E. As in Figure 4.29 (b).

Discussion

On the whole, P3 presents a complex distribution of temporal changes. To facilitate discussion, the water column is divided into 4 layers: (a) from 25.0 to 25.5 γ^n, (b) from 25.5 to 26.4 γ^n, (c) the intermediate layer from 26.4 to 27.5 γ^n, and (d) the deep layer below 27.5 γ^n. Lastly, the general deepening of isopycnals along P3 is discussed.

(a) 25.0 to 25.5 γ^n ($\approx$ 150 to 230 dbar)

In the North Pacific, densities between 25.0 and 25.5 γ^n outcrop at a narrow zonal band between 30°N and 35°N, and at the west coast of North America (Levitus 1982). Because water within the 25.0 - 25.5 γ^n range along P3 has a salinity of approximately 34.8, it is concluded that this water mass has its origin along the zonal band between 30°N and 35°N, and west of 220°E, but not at the west coast of North America. The inverse solutions of *pure warming* and *pure freshening* at the 25.0 - 25.5 γ^n range along P3 therefore suggest a possible increase in sea surface temperature and surface precipitation at the latitude band between 30°N and 35°N. The sea surface temperature increase implication contradicts the surface temperature anomalies map of Parker et al. (1994).

(b) 25.5 to 26.4 γ^n ($\approx$ 230 to 450 dbar)

The two distinct water masses in the 25.5 - 26.4 γ^n range along P3: NPSTMW and the SSM, have both shown significant θ-S changes.

NPSTMW

NPSTMW is formed from deep wintertime convection, at the narrow region between the Kuroshio Extension and the Subtropical Front ($\approx$ 26°N), and between approximately 140°E and 180°E. After formation, NPSTMW is advected to a wide area in the western part of the subtropical gyre south of Japan, by the clockwise Kuroshio recirculation system (Hanawa and Suga 1995). During the large-meander periods of the Kuroshio, no substantial southwestward advection of NPSTMW occurs, whereas during non large-meander periods, the Kuroshio system forms a single anticyclonic gyre and enables more southwestward advection of NPSTMW (Suga and Hanawa 1995). Bingham et al. (1992) reported NPSTMW to be thicker and more geographically confined during 1938-42 than during 1978-82. The greater

thickness was attributed to stronger wintertime cooling in the western North Pacific during 1938-42, and the smaller geographical extent was thought to be the result of a weaker subtropical gyre during 1938-42. Suga et al. (1989) also noticed that less NPSTMW was observed along the 137°E section during the large-meander periods of the Kuroshio, and that the NPSTMW salinity along the 137°E section showed a decreasing trend before 1981, increased considerably during 1981, and has shown a decreasing trend since 1981.

Along 24°N, NPSTMW exhibits temporal changes that are consistent with *pure cooling*. This suggests colder wintertime conditions over the western North Pacific during 1985, than the 1965-76 period, when the majority of the historical data west of 180°E (see Figure 4.18) was sampled.

the SSM

Yuan and Talley (1992)'s study on shallow salinity minima in the North Pacific confirmed Tsuchiya (1982)'s deduction on the SSM, that it is created by downward Ekman pumping of low salinity water in winter, in the area east of 160°W, between 35°and 50°N. It is spread southeastward by the California Current, and turns southwest around 25°N. As this low-salinity water moves away from its source region, its salinity gradually increases, and so does its density. As the SSM in the North Pacific is ventilated directly by Ekman pumping, its properties are set by those in the mixed layer in its source region (Talley 1985).

From our results along 24°N, the changes observed in the SSM along P3 are consistently explained by *pure warming*, with some effect of *pure freshening* present. Roemmich (1992) also found that, off the coast of southern California, temperatures have risen significantly in the top 300 m of the water column between 1950 and 1991. Part of this water could be the SSM, according to Reid (1973)'s map of the shallow salinity minima of the Pacific. These results suggest that the source region of the SSM, which is the northeastern Pacific, has experienced an increase in sea surface temperature and surface precipitation.

These implications agree with several other regional observation studies. The surface temperature anomalies map for 1981-90, relative to 1951-80, constructed by Parker et al. (1994), and the distribution map of the first EOF of SST by Tanimoto et al. (1993), both show recent warming off the west coast of North America and over the Gulf of Alaska. In addition, Freeland and Whitney (1997) reported that both warming and freshening trends have been

observed over the northeast Pacific, based on surface data from four ocean stations off the Pacific coast of Canada.

(c) the intermediate layer (26.4 to 27.5 γ^n, $\approx$ 450 to 1000 dbar)

The dominant water mass within this intermediate layer is NPIW, characterised as a salinity minimum layer spanning densities 26.4 to 27.2 γ^n. Talley (1993) concluded that NPIW is formed at the mixed water region between the Oyashio Extension at about 42°N, and the Kuroshio Extension at about 36°N. There, cold, fresh subpolar waters mix with warmer, more saline subtropical waters. The sinking of the resultant cold, fresh layer beneath the saltier surface layers creates the salinity minimum of NPIW. The cold, fresh subpolar waters attain their characteristics in the subarctic gyre by general vertical diffusion (Reid 1965), and in the Okhotsk Sea through vertical mixing as a result of sea ice formation (Talley 1991). Furthermore, waters with densities 27.2 to 27.5 γ^n also owe their properties to local vertical mixing in the Okhotsk Sea (Talley 1991).

At 24°N, temperature and salinity on neutral surfaces within the NPIW layer increase southward. For example, on the 27.0 γ^n surface, the meridional gradient of salinity along 24°N has been estimated from the historical data to be roughly 0.01 pss per 1°latitude. Hence the observed salinity decrease on the 27.0 γ^n surface along P3 could be due to a less than 2°latitude, or roughly 200 km, southward excursion of the water mass. A southward excursion of the water mass will also be consistent with the observed deepening of the neutral surfaces.

On the other hand, the changes observed in NPIW along P3 (26.4 - 27.2 γ^n) can also be explained by *pure freshening* and *pure warming*, while changes from 27.2 - 27.5 γ^n are consistent with *pure freshening*. These results therefore suggest an increase in precipitation and sea surface temperature over the subarctic gyre and over the Okhotsk Sea. Note that this conclusion is slightly different for waters in similar densities along P1 at 47°N. The conclusion from P1 points to some freshening, but mainly cooling, over the Okhotsk Sea region based on observed temporal changes to the west of 210°E (see Table 4.1).

(d) the deep layer (> 27.5 γ^n, > 1000 dbar)

Below 27.5 γ^n along 24°N, temperature and salinity on neutral surfaces have shown significant decreases. Standard Seawater Batch P96 was used for

bottle salinity measurements during both P1 and P3, and Talley et al. (1991) have commented that an addition of 0.003 pss to P1 bottom salinity values would match those of Mantyla and Reid (1983). Hence, there is probably a 0.003 pss systematic difference between the historical salinity values and those from WOCE P3. After adding 0.003 pss to the sectionally-averaged $S'|_n$, only the levels between 27.8 and 28.0 γ^n remain freshened above the 90% confidence levels. However, examination of the objectively mapped salinity field shows that anomalies exist in the estimates below 2000 dbar ($\approx 27.9\,\gamma^n$), that could be due to historical data inadequacy at those depths. Therefore, only the salinity decreases on neutral surfaces between 27.8 and 27.9 γ^n along P3 are considered as real changes.

The density range of 27.8 to 27.9 γ^n corresponds to an average pressure range of 1500 to 2000 dbar along P3, and is between the oxygen minimum, found at 27.5 γ^n (about 1000 dbar), and the silicate maximum, residing at densities deeper than 27.9 γ^n (greater than 2000 dbar). Hence waters in the 27.8 - 27.9 γ^n range are definitely below the level of any North Pacific ventilation. Because the amount of time needed to renew these waters is much longer than the roughly 15 years between the historical and the WOCE measurements, detection of water mass property change in these waters is not expected in this study.

A recent WOCE transect along 149°E in the western Pacific reveals that the zonal flow, dominated by a complex set of gyres, at this level is more energetic than the meridional flow, and that there are oceanic fronts located near 24°N, that extend to the bottom of the ocean (Wijffels et al. 1998). Furthermore, Qiu and Joyce (1992) have observed along the 137°E meridian, that in the 1500 - 2500 m layer, there have been north-south movements of water mass across 24°N of up to 3°latitude, in the past two decades, that are associated with the Kuroshio meander. Hence the observed salinity decrease on the 27.8 - 27.9 γ^n surfaces are likely to be the result of a southward excursion of the water mass, that is associated with frontal movements, or with the Kuroshio meanders. A meridional section that intersects P3 will help to resolve some of these uncertainties.

General deepening of neutral surfaces along 24°N

Lastly, sectional averages show that all neutral surfaces from 25.7 γ^n to the deepest surface have become deeper along 24°N. Inverse solutions show that *pure downward heave* is a strong process from 25.7 γ^n ($\approx$ 270 dbar) to 27.6 γ^n ($\approx$ 1120 dbar). Lie and Endoh (1991) have noted that in the zonal band between 15°N and 35°N in the North Pacific, seasonal changes in wind stress curl over the region could induce vertical displacements of the thermocline depth. However, the effect of seasonally-induced heaving should be minimal in our results, because the historical data used in this comparison were most frequently sampled in May, which is the same month as when WOCE P3 was carried out. Hence the general deepening of neutral surfaces observed along P3 suggests long-term changes over the entire subtropical gyre in the past decades.

Significant long-term changes have been observed over the North Pacific in recent decades that could have caused a deepening of the subtropical gyre. Tanimoto et al. (1993)'s study of North Pacific SST shows that, after the mid-1970s, the mid-latitude region of the North Pacific experienced a shift in SST anomaly: SST north of 25°N became colder. This cooling is accompanied by the previously-mentioned warming over the far northeast Pacific, off the west coast of the American continent. The same pattern can be seen in Parker et al. (1994)'s surface temperature anomalies map for 1981-90, relative to 1951-80. The 1976-77 shift can also be seen in the space-time evolution study of the decadal subsurface temperature variability by Zhang and Levitus (1997).

This post-1970s mid-latitude cold SST trend is accompanied by subsurface temperature differences: between 1966-75 and 1976-85, the subsurface thermal field along the longitude band 170-180°E north of 25°N has cooled (averaged over the upper 400 m), while the top 400 m between 10°N and 25°N has warmed (Watanabe and Mizuno 1994). Shuto (1996) also found that the subsurface (to 1000 dbar) temperature along the 137°E meridian between 14°N and 26°N, which covers most of the North Equatorial Current, was warmer from 1977 to 1985, than from 1970 to 1976. Our sectional averages show that temporal θ and S changes on neutral surfaces along 24°N are not statistically significant between 25.6 γ^n ($\approx$ 250 dbar) and 26.5 γ^n ($\approx$ 450 dbar) (Figure 4.26 a,b). It is therefore likely that these changes in the temperature field, observed by Watanabe and Mizuno (1994) and Shuto (1996), are caused by downward movements of the isotherms, and are not due to changes in the θ-S relationship of the water masses. Hence the distribution of these SST-related subsurface

temperature anomalies implies a deepening of the subtropical gyre after the mid-1970s.

Furthermore, Qiu and Joyce (1992) found that along the 137°E meridian, from 1967 to 1988, the transports of both the Kuroshio Current and the North Equatorical Current displayed a gradual increase, that is accompanied by a steady increase in magnitude of the North Pacific subtropical wind gyre. Whether it is SST-related or wind-related, our result of the general deepening of neutral surfaces in the top 1000 dbar along 24°N is consistent with the other observations that the North Pacific subtropical gyre has been gradually deepening since the mid-1960s.

4.3 Differences along the WOCE P4 section

The final zonal transect in the North Pacific which has been used to study temporal changes is WOCE P4, located within the cyclonic tropical gyre of the North Pacific. The cruise track of P4 runs from the Philippines to Costa Rica, along the nominal latitude of 9.5°N. Figure 4.32 shows a schematic diagram of the tropical gyre (adapted from Tomczak and Godfrey (1994), p.119, and Wijffels et al. (1995)), and the location of WOCE P4.

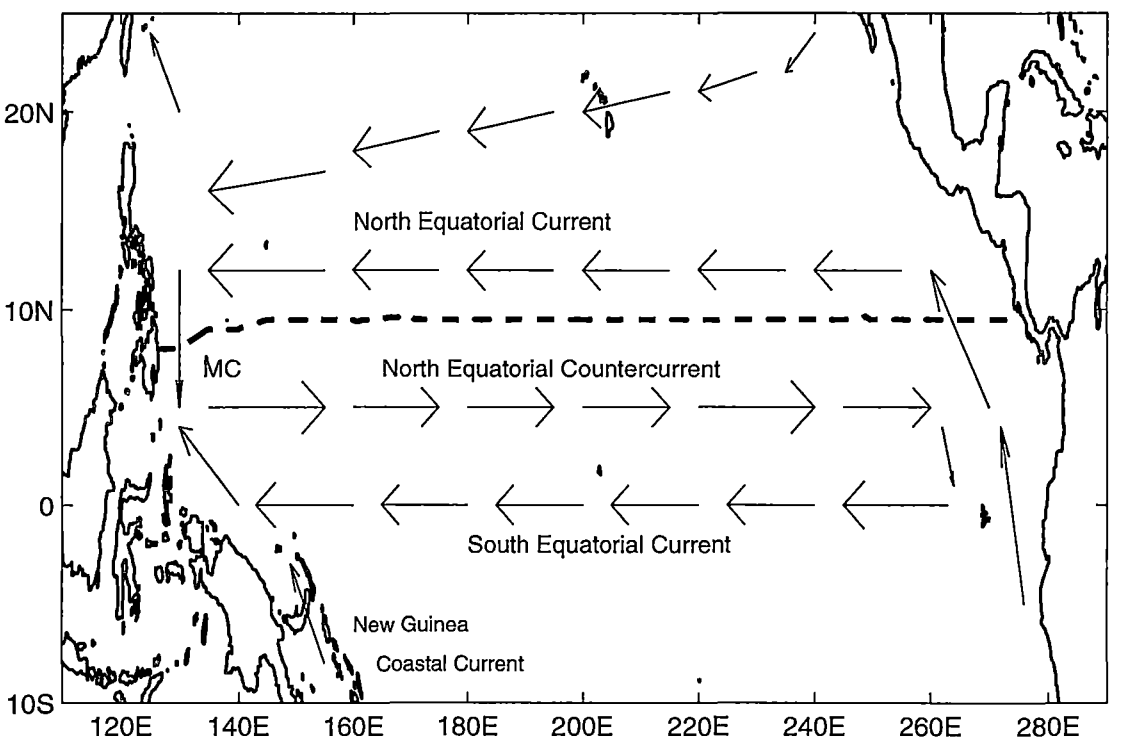

Figure 4.32: Schematic diagram of the North Pacific tropical gyre. The dashed line marks the cruise track of P4. MC = Mindanao Current.

The WOCE P4 data set consists of 213 CTD casts. For mapping to the coordinates of P4, 400 historical casts from the Reid and Mantyla North Pacific data set that are located south of 17°N and north of the equator have been used (Figure 4.33). These historical casts were sampled between 1947 and 1979 (Figure 4.34 a), with the mean year of sampling being 1969 and the standard deviation being 6 years. The median year of sampling is also 1969. Since WOCE P4 was sampled during 1989, any temporal changes along P4 can be treated as 20 ± 6 years differences. The most frequent month of sampling for the historical casts is June (Figure 4.34 b), but overall their seasonal distribution is more

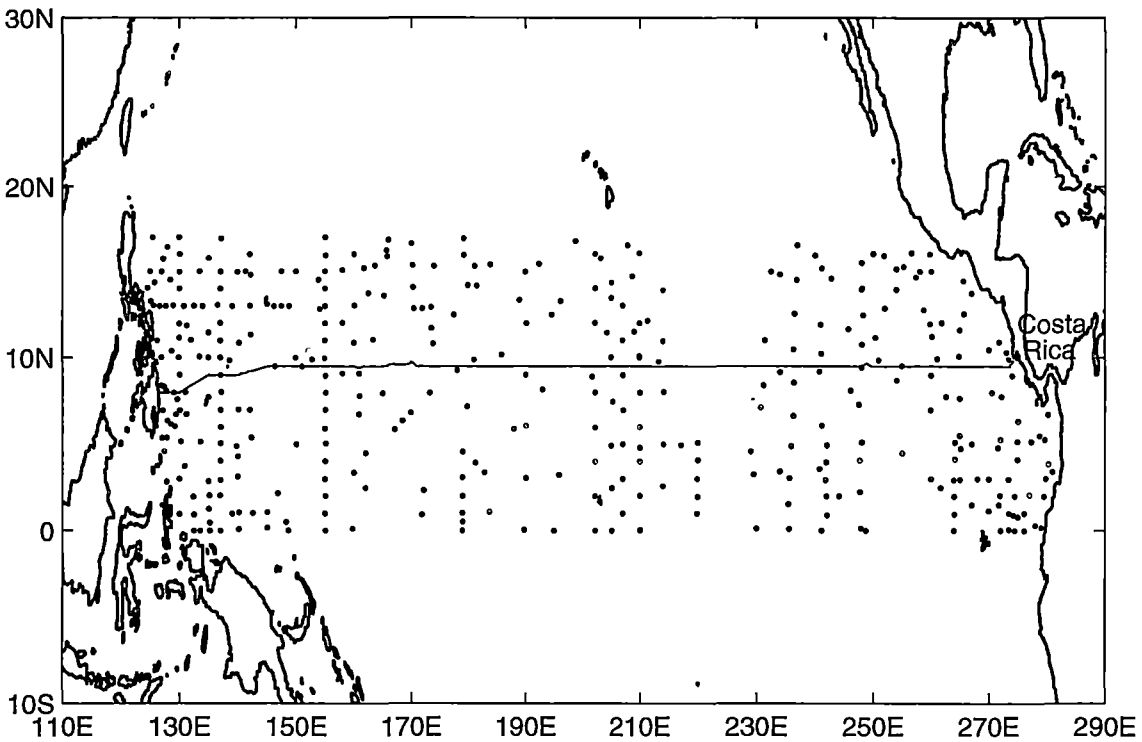

Figure 4.33: The cruise track of the WOCE P4 section, and the distribution of the 400 historical data points that have been used in the mapping to the coordinates of WOCE P4.

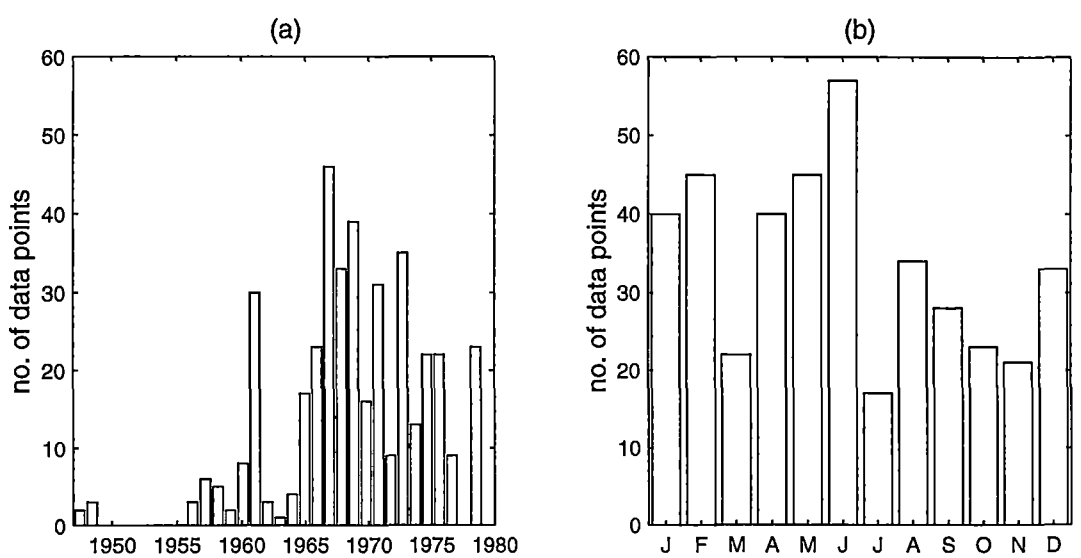

Figure 4.34: (a) The year distribution and (b) the month distribution, of the 400 historical data points in the mapping to the coordinates of the WOCE P4 section.

uniform than the selection of historical casts for P1 and P3. Because the WOCE P4 section was carried out from February till May, there is the possibility of seasonal aliasing in the results along P4. On the other hand, 1989 is not an El Niño year, so any observed differences should not contain El Niño effects.

The vertical temperature structure along P4 is a simple picture of monotonic decrease with depth. In contrast, the salinity distribution along P4 is complex. Figure 4.35 shows the vertical section of salinity along P4 based on the WOCE CTD data. To the west of 210°E, salinity increases with depth from the surface till, at around 150 dbar, a maximum is reached where salinity exceeds 34.90. This is the saltiest water mass along P4 and has an origin at the subtropical evaporative cell. It is also seen in the top 200 dbar along P3 at 24°N, and is called North Pacific Subtropical Water (NPSTW). Along 10°N, it has $20°C < \theta < 25°C$, and core density of less than 24.5 γ^n.

From the level of NPSTW, salinity decreases with depth, until a minimum is reached where $S < 34.54$. This is the same shallow salinity minimum (SSM) as that along P3, only here along 9.5°N, its salinity and density have increased slightly from mixing with more saline water while being advected westward by the North Equatorial Current (Reid 1973). It enters the 9.5°N latitude at approximately 100 dbar (25.5 γ^n) at 220°E. At the western end of the P4 section, its core density has increased to 26.5 γ^n ($\approx$ 300 dbar). Wijffels et al. (1996) called it Northeast Pacific Intermediate Water. In order to be consistent with the terminology used for P3, the name "shallow salinity minimum (SSM)" is retained here.

To the east of 230°E, the top 100 dbar consists of equatorial low salinity surface water, but no subtropical water masses. Consequently the term "the shadow zone of the North Pacific subtropical gyre" has been used to describe the eastern part of the tropics, since no subtropical waters is advected to this area (Wijffels et al. 1996). Below 100 dbar, a salinity maximum is present between 26.0 and 27.0 γ^n. This salinity maximum has salinity between 34.65 and 34.90, and θ ranging from 8°C to 14°C. It extends from the eastern end of the transect westward, beneath the SSM, to roughly 170°E. Because this water mass shares similar θ-S characteristics as the 13°C thermostad in the eastern tropical Pacific, Wijffels et al. (1996) have referred to it as 13°C Water.

A deeper salinity minimum is found at about 750 dbar ($\approx$ 27.3 γ^n). This water mass has $\theta \approx 6°C$ and $S < 34.54$. Because it is much denser than NPIW, this deep salinity minimum along P4 is identified as a derivative of Antarctic Intermediate Water (AAIW) from the south, and will hereafter be referred to as

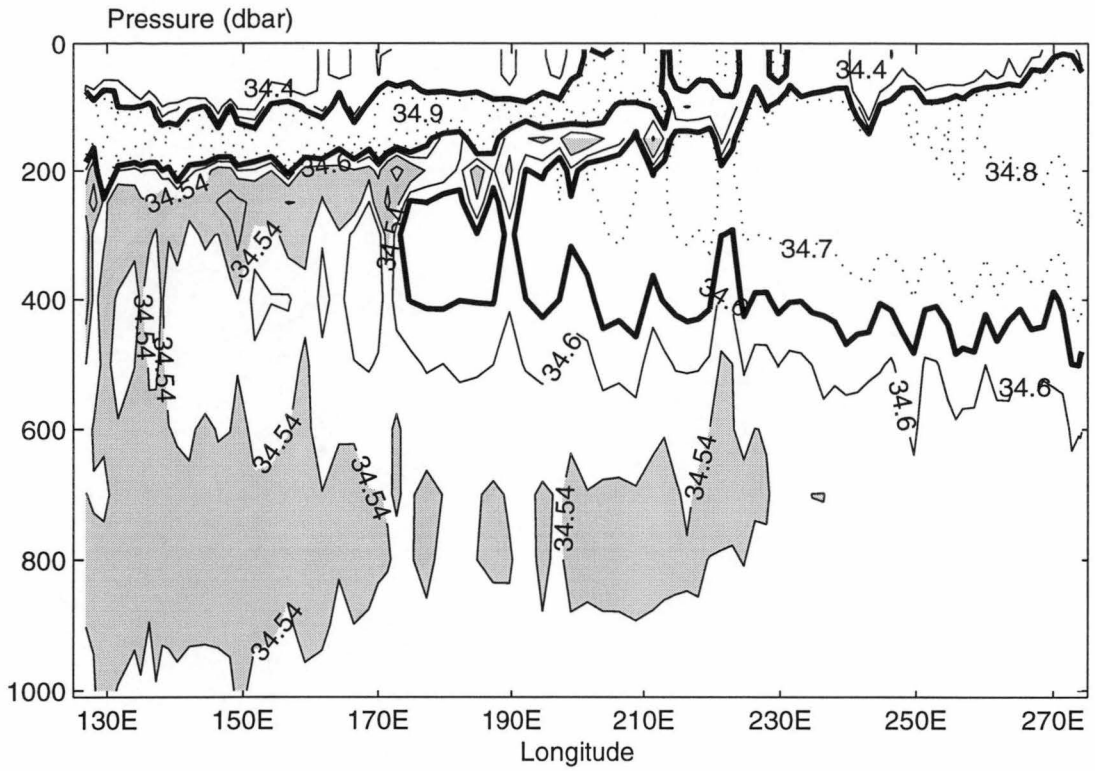

Figure 4.35: Profile of salinity (pss) for the upper 1000 dbar along 9.5°N, based on CTD data from the WOCE P4 section. The thick line marks the 34.65 contour and encloses two salinity maxima: NPSTW, and 13°C Water. The shaded area represents two salinity minima: the SSM, and modified AAIW.

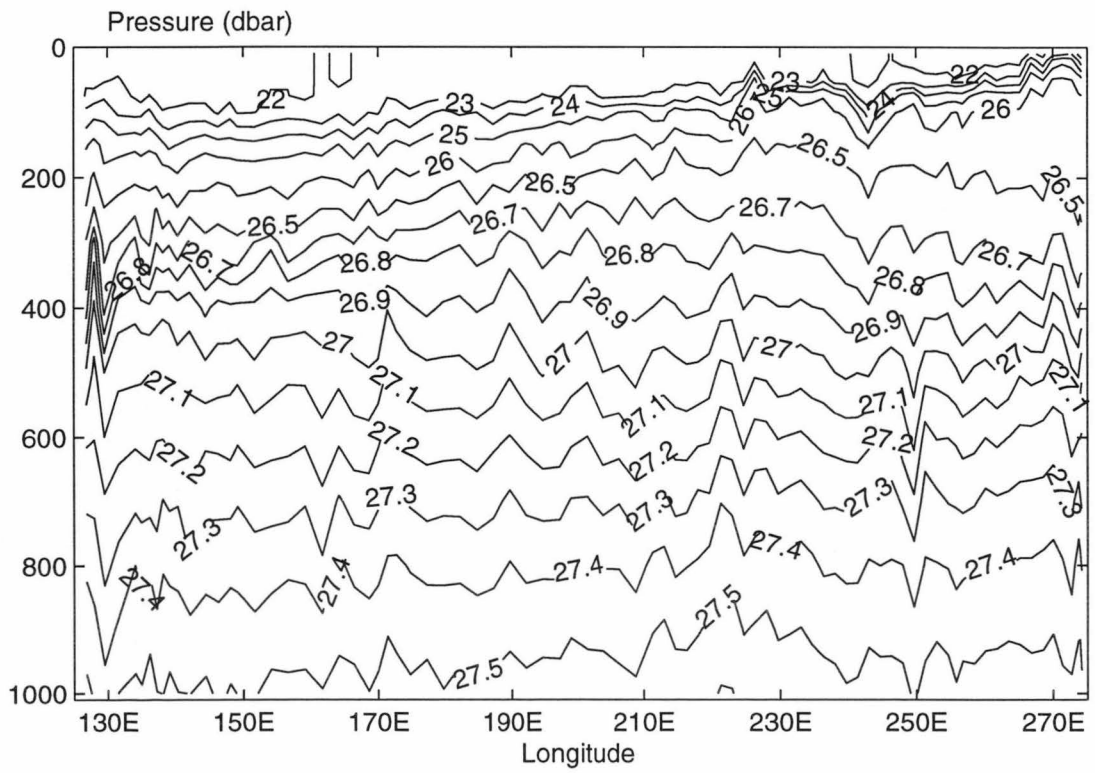

Figure 4.36: Profile of neutral density (kg m^{-3}) along 9.5°N, as in Figure 4.35.

modified AAIW. Below 1000 dbar, salinity increases monotonically with depth, and is not shown in Figure 4.35.

Figure 4.36 shows the neutral density profile for the upper 1000 dbar along P4. West of 230°E, isopycnals slope upward from west to east, indicating general southward flow relative to a deep reference level. To the east of 230°E, there is a reverse in isopycnal slopes, indicating general northward flow across the eastern part of the transect.

Because of the complexity of the vertical salinity structure along P4, the picture of the stability ratio is one of layers of $R_\rho > 1$ alternating with layers of $R_\rho < 0$, separated by regions of $R_\rho = \infty$ at the salinity minima/maxima. This layered structure is illustrated in Figure 4.37. The shaded regions are the parts of the water column where salinity increases with depth (for example, the deep waters below modified AAIW); hence $R_\rho < 0$. The non-shaded regions are where salinity decreases with depth; hence $R_\rho > 1$. The boundaries between the shaded regions and the non-shaded regions are where the slope of the θ-S curve changes sign. Consequently, they mark the salinity extrema along P4.

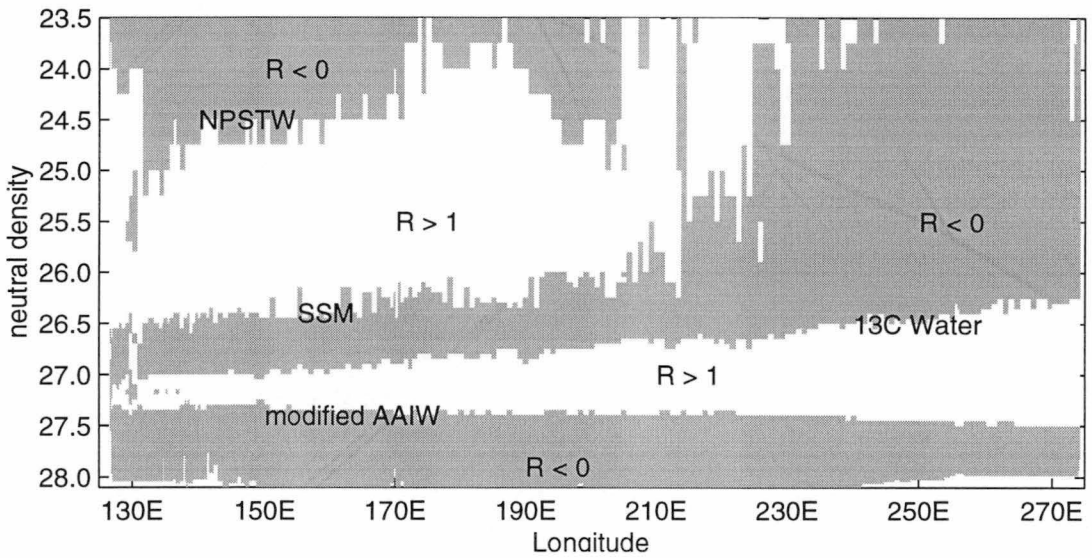

Figure 4.37: Profile of stability ratio R_ρ along P4.

The θ-S diagram of the historical data after objectively mapped to the coordinates of P4 is compared with that from the WOCE 1989 section in Figure 4.38. The objective estimates on levels below 23.5 γ^n ($\approx$ 90 dbar) preserve the neutral surface definition to within instrumental error (see Equation 3.1 in Chapter 3). The ratios of the standard deviation of the

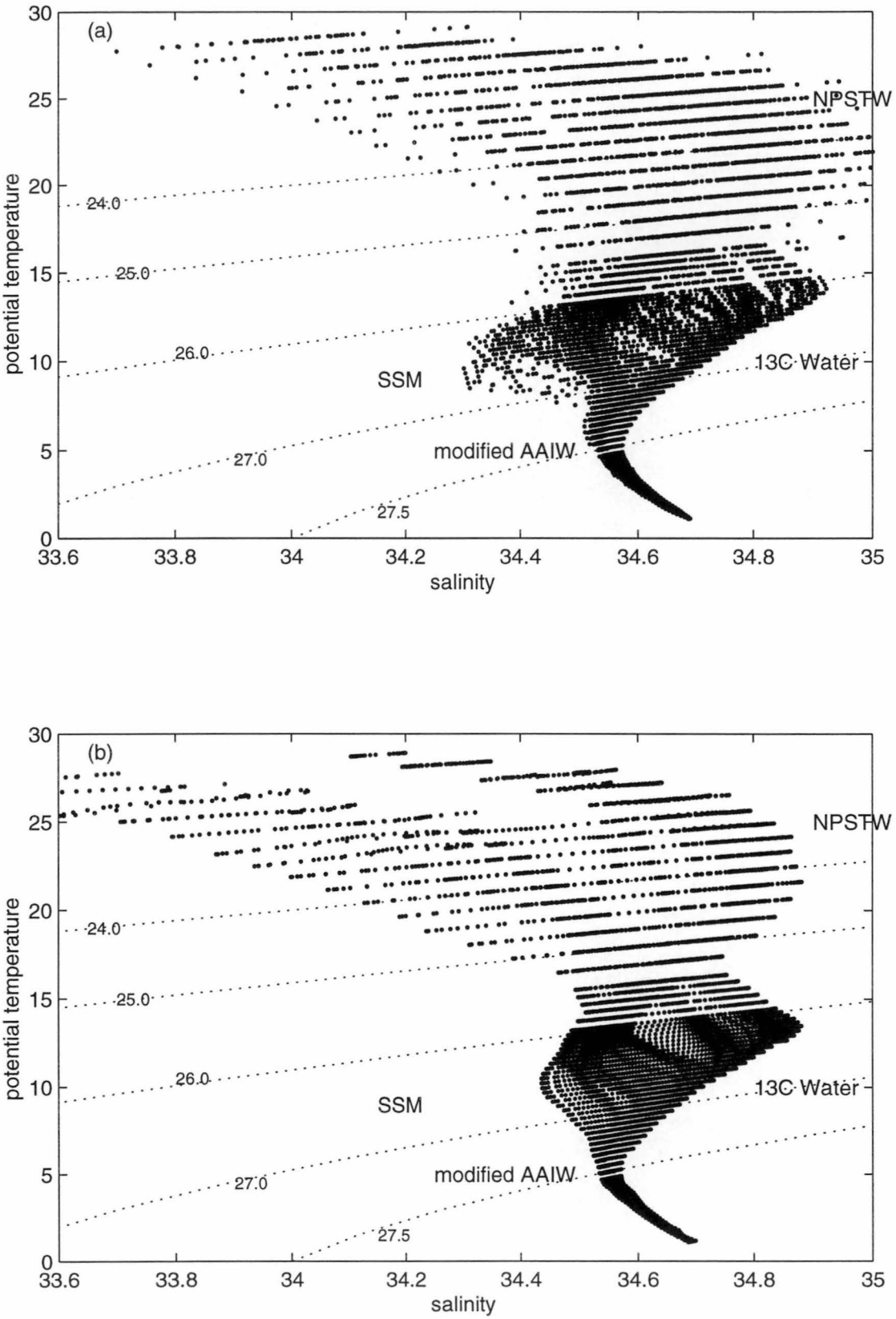

Figure 4.38: θ-S diagram on neutral surfaces along P4, (a) from the WOCE 1989 section, and (b) from the historical data objectively mapped to the coordinates of P4. Lines of constant neutral density are superimposed.

mapping residuals to that of the *a priori* noise, on neutral surfaces below 23.5 γ^n, are between 0.8 and 0.9, indicating good length scales fit in the mapping procedure (see Equation B.3 in Appendix B). However, although the historical data are well-mapped, Figure 4.38 shows that the salinity maximum which marks NPSTW, and the salinity minimum which marks the SSM, are not as prominent in the historical data as they are in the WOCE 1989 data. The salinity maximum of NPSTW has lower salinities in the historical data, while the SSM is fresher during WOCE P4.

Observed temporal changes on neutral surfaces

Figures 4.39, 4.40 and 4.41 show the temporal differences in potential temperature, salinity and pressure on neutral surfaces (i.e. $\theta'|_n$, $S'|_n$ and N') along P4, below 23.5 γ^n. Two dashed lines enclose the area between 215°E and 230°E, where pointwise mapping errors for θ, S and P are greater than the rest of the transect at the same depth levels, reflecting the relative sparsity of historical data in this area (see Figure 4.33).

Above 26.5 γ^n, the water column to the east of 220°E displays extensive temperature and salinity increase on neutral surfaces that are above the pointwise mapping errors at these levels. Averages taken from 220°E to 270°E show that these mean temperature and salinity increases are above the 90% confidence levels, and are not accompanied by statistically significant isopycnal movements (Figure 4.42 b,d,f).

The spatial picture to the west of 220°E, on the other hand, is less coherent. Zonal averages taken between 130°E and 220°E (Figure 4.42 a,c) show that between 24.0 and 25.5 γ^n, which encompasses NPSTW, there have been mean temperature and salinity increases that are significant above the 90% confidence levels, and which can also be seen in the θ-S diagrams (Figure 4.38). NPSTW is also present at 24°N, but its objective estimates along P3 are not reliable and so its temporal changes along the WOCE P3 section have not been discussed.

Still to the west of 220°E, densities from 25.5 to 26.5 γ^n, which include the SSM, show insignificant mean θ and S changes on neutral surfaces, but significant downward movement of isopycnals (Figure 4.42 a,c,e). For comparison, the SSM along 24°N has shown θ-S property changes that are consistent with *pure warming*, with some effect of *pure freshening*.

It can be seen from Figures 4.39 and 4.40, that between 26.5 and 27.0 γ^n,

the spatial pattern of temporal change flips from basin-wide temperature and salinity increase on neutral surfaces, to basin-wide temperature and salinity decrease, across a diagonal line that stretches from about 27.0 γ^n at the western end of the transect, to about 26.5 γ^n at the eastern end. This diagonal line marks the position where R_ρ values along P4 change from negative, to positive, around the salinity maximum of 13°C Water (Figure 4.37). As will be seen later, this is a perfect illustration of the *pure warming* scenario, where a water mass that has experienced a temperature increase on isobars, actually displays different changes on isopycnals, depending on the slopes of its θ-S curve.

Below 27.0 γ^n, all neutral surfaces show basin-wide cooling and freshening that are above the 90% confidence levels. Figure 4.43 shows $\overline{\theta'|_n}$, $\overline{S'|_n}$, and $\overline{N'}$, averaged between 130°E and 270°E along P4. The maximum sectionally-averaged temperature and salinity decrease of 0.06°C and 0.01 pss occur at 27.2 γ^n, just above the core of the modified AAIW layer. Below 27.9 γ^n ($\approx$ 2000 dbar), sectionally-averaged salinity decreases are less than 0.003 pss, and can be regarded as systematic salinity errors similar to that discussed for P1 and P3.

All isopycnals from the sea surface to 27.8 γ^n have become deeper on average between the historical and the WOCE 1989 observations, with the maximum sectionally-averaged difference of 33 dbar occurring at 26.85 γ^n. In particular, within the intermediate salinity minimum layer of modified AAIW (27.2 - 27.5 γ^n), isopycnal movements are not uniform with depth. The 27.2 γ^n surface ($\approx$ 610 dbar) has deepened by 28.9 dbar, while the 27.5 γ^n surface ($\approx$ 950 dbar) has deepened by 16.8 dbar. This means that the modified AAIW layer along 9.5°N has reduced in thickness by 12.1 dbar, or 3.6%, over the roughly 20-year period between the historical measurements and the WOCE sampling.

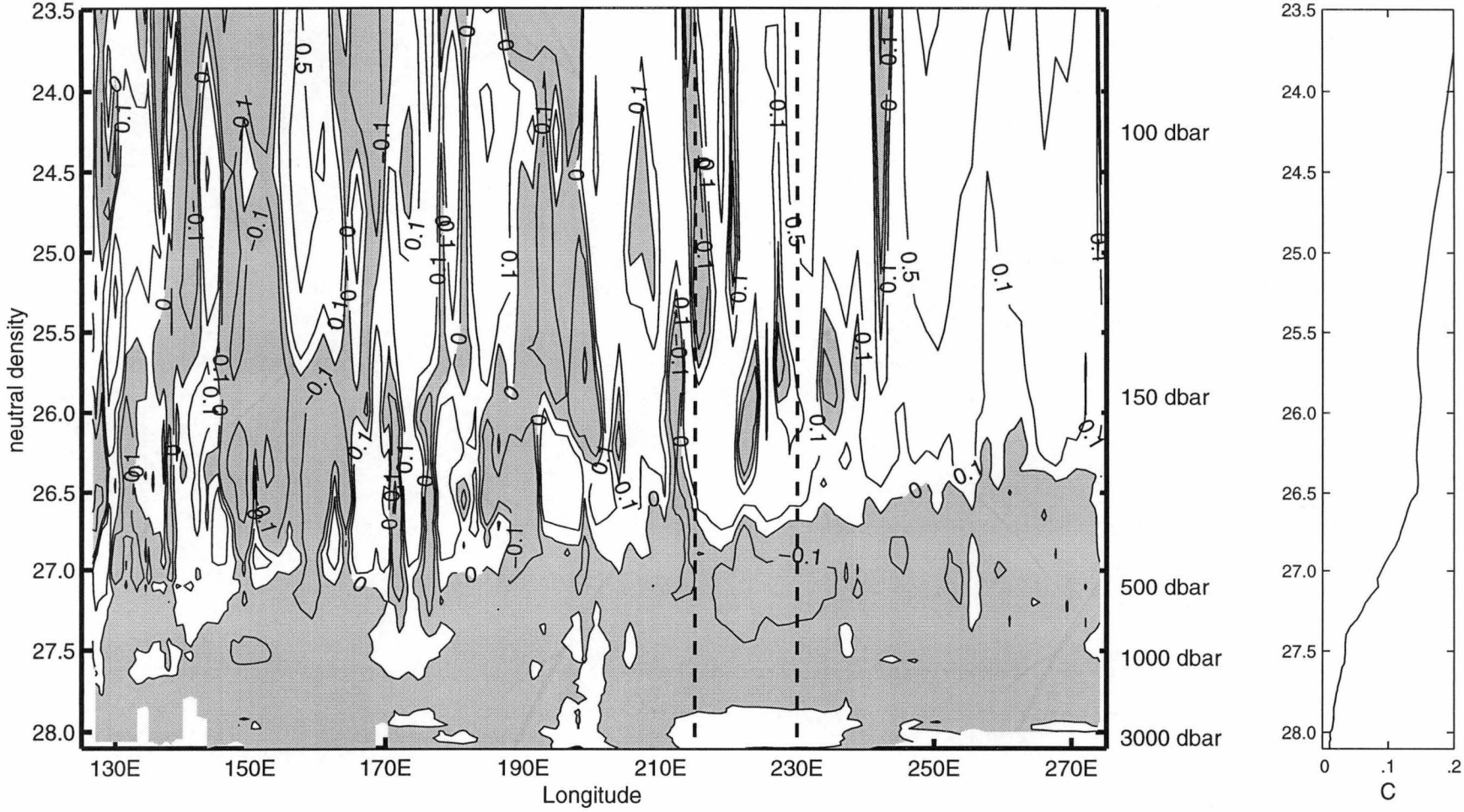

Figure 4.39: (Left) $\theta'|_n$ (°C) along P4. The shaded parts indicate areas with a temperature decrease on neutral surfaces. The average pressures of the neutral surfaces are shown in the right-hand y-axis. (Right) The right-hand panel shows the average pointwise mapping errors for θ, as a function of neutral density γ^n.

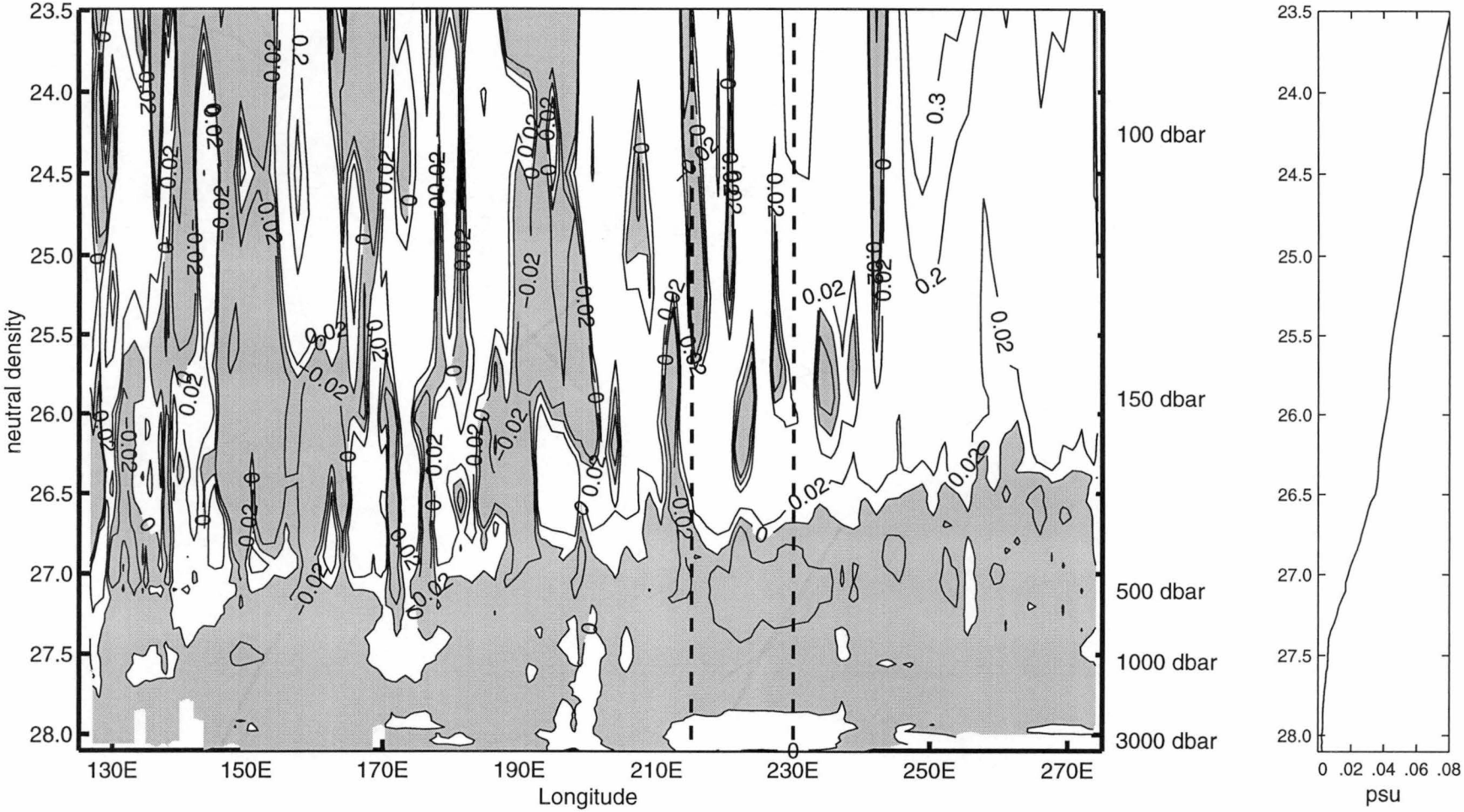

Figure 4.40: (Left) $S'|_n$ (pss) along P4. The shaded parts indicate areas with a salinity decrease on neutral surfaces. The average pressures of the neutral surfaces are shown in the right-hand y-axis. (Right) The right-hand panel shows the average pointwise mapping errors for S, as a function of neutral density γ^n.

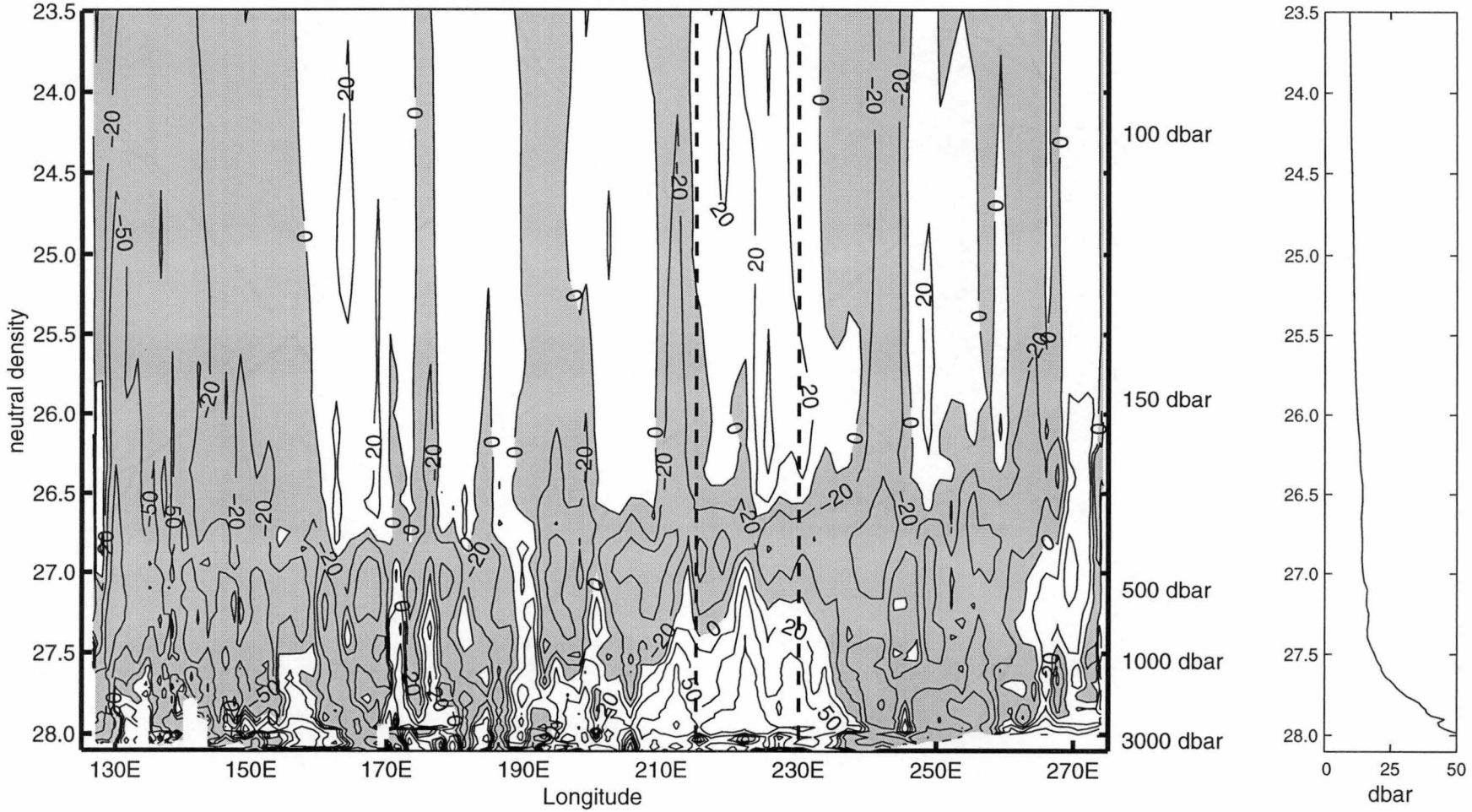

Figure 4.41: (Left) N' (dbar) along P4. The shaded parts indicate a deepening of neutral surfaces. The average pressures of the neutral surfaces are shown on the right-hand y-axis. (Right) The right-hand panel shows the average pointwise mapping errors for P, as a function of neutral density γ^n.

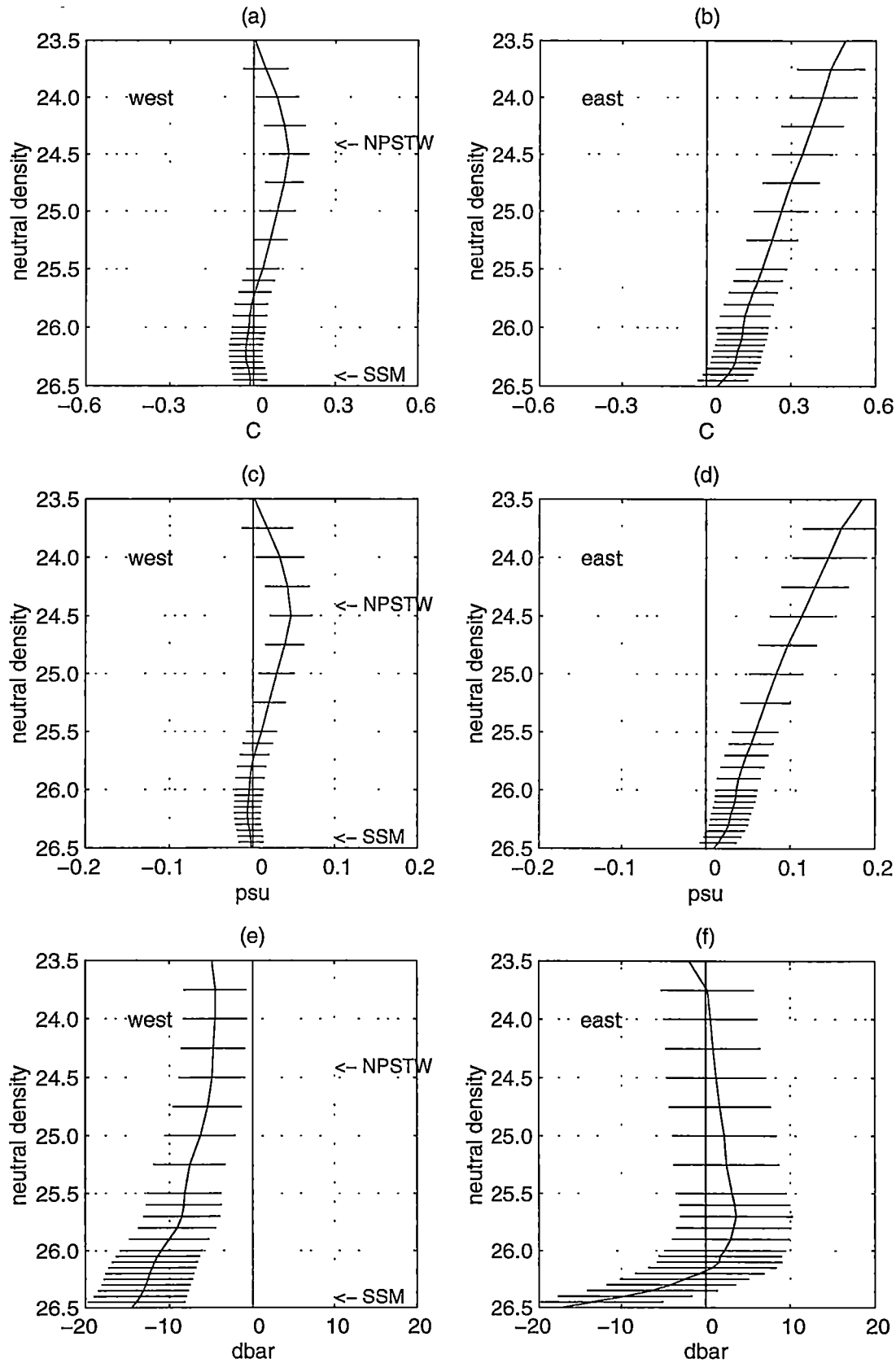

Figure 4.42: Sectional averages along P4, between 130°E and 220°E ('west'), and between 220°E and 270°E ('east'), on neutral surfaces above 26.5 γ^n. The error bars indicate 90% confidence intervals. (a) and (b) $\overline{\theta'|_n}$, (c) and (d) $\overline{S'|_n}$, and (e) and (f) $\overline{N'}$.

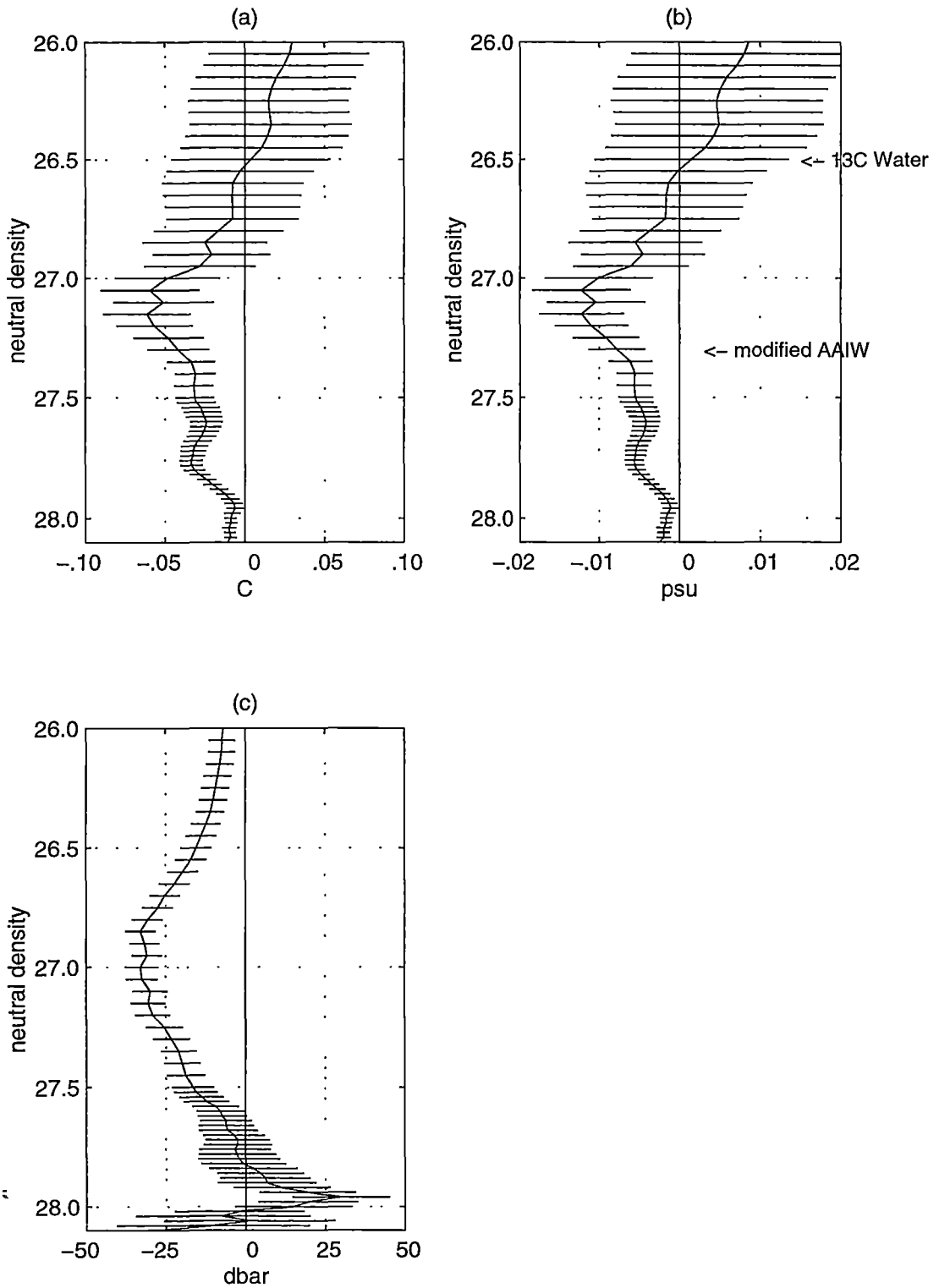

Figure 4.43: Sectional averages between 130°E and 270°E along P4, on neutral surfaces below 26.0 γ^n. The error bars indicate 90% confidence intervals. (a) $\overline{\theta'|_n}$, (b) $\overline{S'|_n}$, and (c) $\overline{N'}$.

Observed temporal changes on isobars

Figure 4.44 shows the temporal changes on isobars, for the upper 2000 dbar along P4. West of 190°E, between 100 and 200 dbar, temporal changes are dominated by increase in salinity, with some increase in temperature. This is the area where the shallow salinity maximum of NPSTW is found. Because the slope of the θ-S curve of NPSTW changes from negative to positive around the salinity maximum, the combined changes on neutral surfaces ($\theta'|_n > 0$) and on isobars are consistent with the *pure warming* scenario only for the part of NPSTW above 24.5 γ^n, where $R_\rho < 0$ (see Figure 4.37), while *pure salinification* fits the observations for the entire NPSTW layer.

Below NPSTW, the shallow salinity minimum layer (at roughly 200 to 400 dbar, also west of 190°E) displays an increase in temperature but a decrease in salinity on isobars. However, the temporal changes within the SSM are not significant on neutral surfaces. Hence the observed changes on isobars are most likely due to downward excursions of isopycnals within the SSM.

Within the deeper salinity minimum layer of modified AAIW, roughly between 600 and 1000 dbar, and to the west of 230°E, temporal changes are dominated by a decrease in salinity, and an increase in temperature on isobars. Because the slope of the θ-S curve changes from positive to negative around a salinity minimum, and because $\theta'|_n < 0$ for the entire modified AAIW layer, the combined observations suggest that modified AAIW along P4 has undergone *pure freshening*, and *pure warming* for the portion above the salinity minimum.

Between 200 and 600 dbar, the water column shows temperature and salinity increase on isobars. This depth range encompasses the entire layer of 13°C Water, whose θ-S curve changes from having a negative slope, to a positive slope, around the salinity maximum. As seen in Figures 4.39 and 4.40, $\theta'|_n$ and $S'|_n$ also change from having negative values, to positive values, around the salinity maximum. The combined observations therefore suggest that the entire layer of 13°C Water along P4 has undergone *pure warming*.

Below 1000 dbar, Figure 4.45 shows that sectionally-averaged temperature and salinity decrease on isobars are significant above the 90% confidence intervals. Because this part of the water column has $R_\rho < 0$, the combined observations on neutral surfaces ($\theta'|_n < 0$) and on isobars therefore suggest *pure cooling* or *pure freshening* for waters below 1000 dbar along P4.

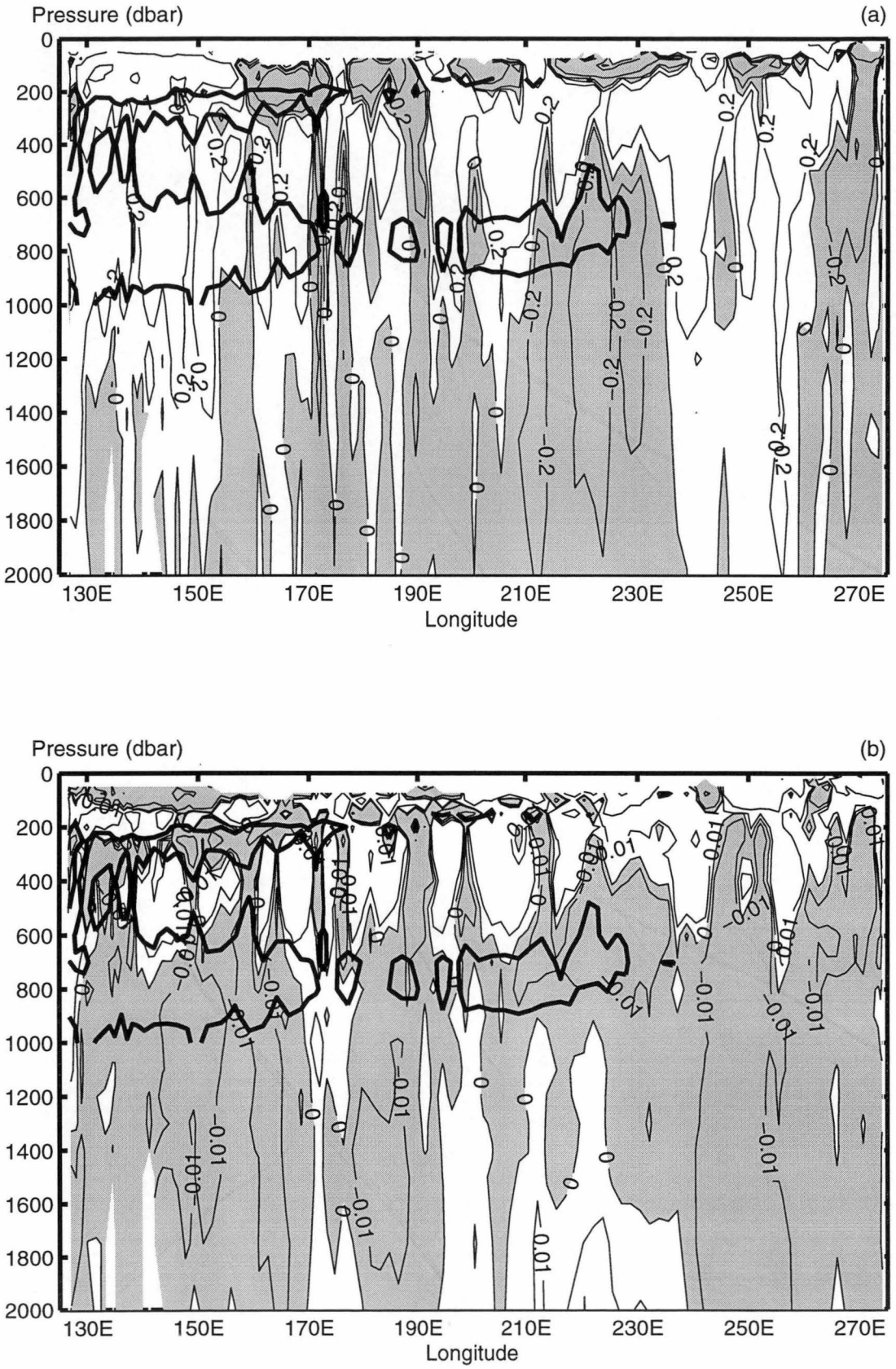

Figure 4.44: (a) $\theta'|_z$ (°C), and (b) $S'|_z$ (pss) for the upper 2000 dbar along P4. Shaded parts indicate areas with temperature and salinity decrease on isobars. The solid line marks the 34.54 pss contour, which encloses the two salinity minima of the SSM, and modified AAIW.

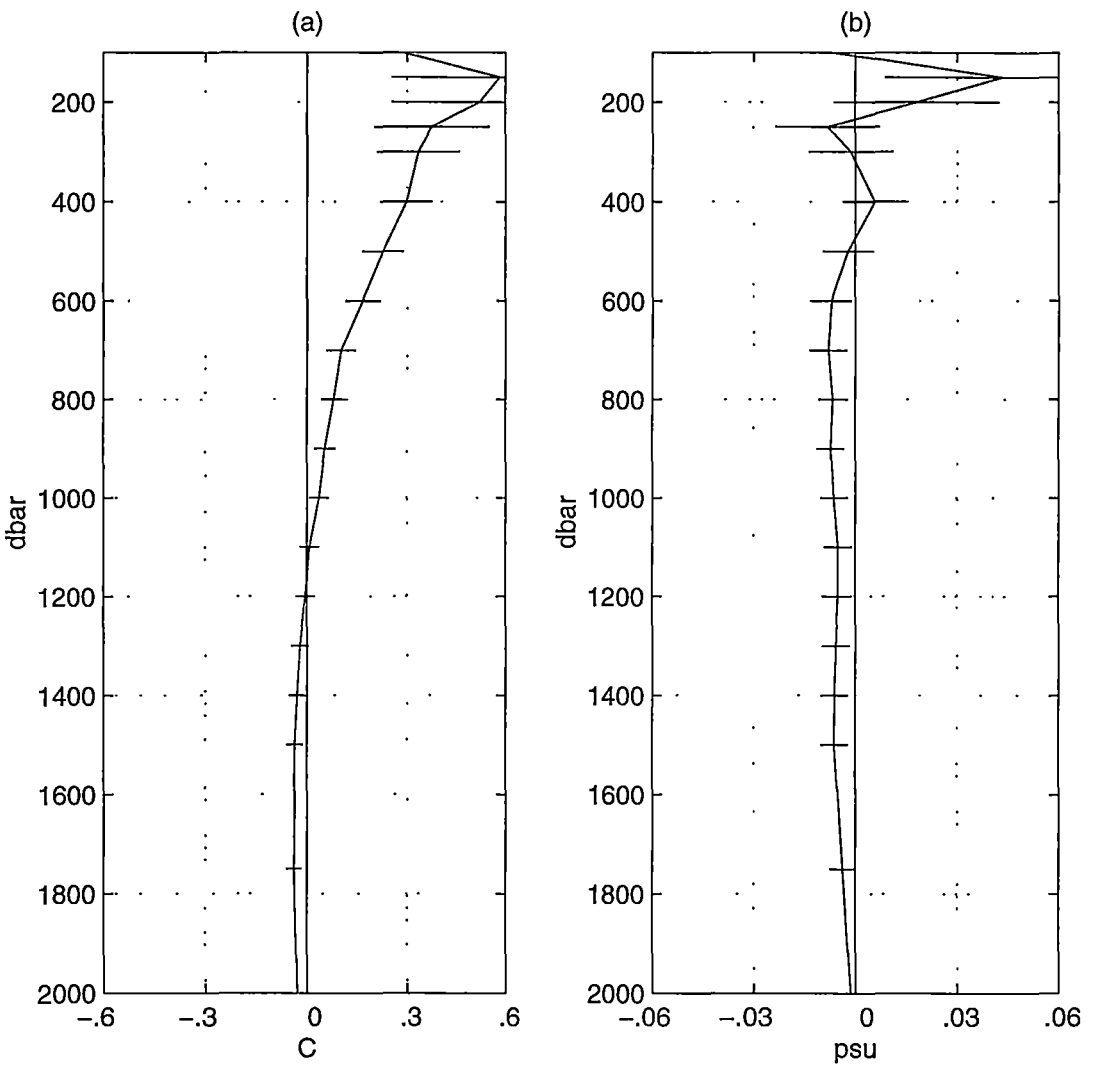

Figure 4.45: (a) $\overline{\theta'|_z}$ (°C), and (b) $\overline{S'|_z}$ (pss), averaged between 130°E and 270°E along P4. The horizontal bars indicate 90% confidence intervals.

Solutions to the inverse problem

In this section, the observations on neutral surfaces and on isobars along P4 are decomposed quantitatively into the three ventilation scenarios. The relative strength of the three "pure" processes in explaining the observations are shown in Figure 4.46 in terms of the inverse solutions. The solutions have been averaged basin-wide, from 130°E to 270°E.

It can be seen that for all densities along P4, the effects of *pure warming* and *pure downward heave* are almost indistinguishable. This is because waters in the tropical Pacific have a relatively narrow salinity range. As a result, the vertical salinity gradients are small, so that our diagnostic method cannot distinguish easily between $\rho^{-1}\rho'|_z A^w$ and $\rho^{-1}\rho'|_z A^h$, but $\rho^{-1}\rho'|_z A^f$ is well-resolved (see Chapter 2).

From the surface to 27.4 γ^n, *pure warming* and *pure downward heave* are the dominant processes. In particular, they explain more than 90% of the data variance in the density range 26.0 - 27.2 γ^n, which includes the salinity maximum layer of 13°C Water.

The effect of *pure salinification* is present from the surface to 26.5 γ^n, and is especially prominent between 24.0 and 25.5 γ^n, which is the density range of NPSTW. Below 26.5 γ^n, the effect of *pure freshening* becomes stronger, and is above the 90% confidence levels below 27.0 γ^n. Within the modified AAIW layer (27.2 - 27.5 γ^n), *pure freshening* accounts for more than 40% of the data variance.

Below the modified AAIW layer, the strength of *pure freshening* dominates to 27.9 γ^n. Some effect of *pure cooling* can be seen below 27.7 γ^n. Below 27.9 γ^n ($\approx$ 2000 dbar), any observed temporal changes are considered to be due to systematic errors.

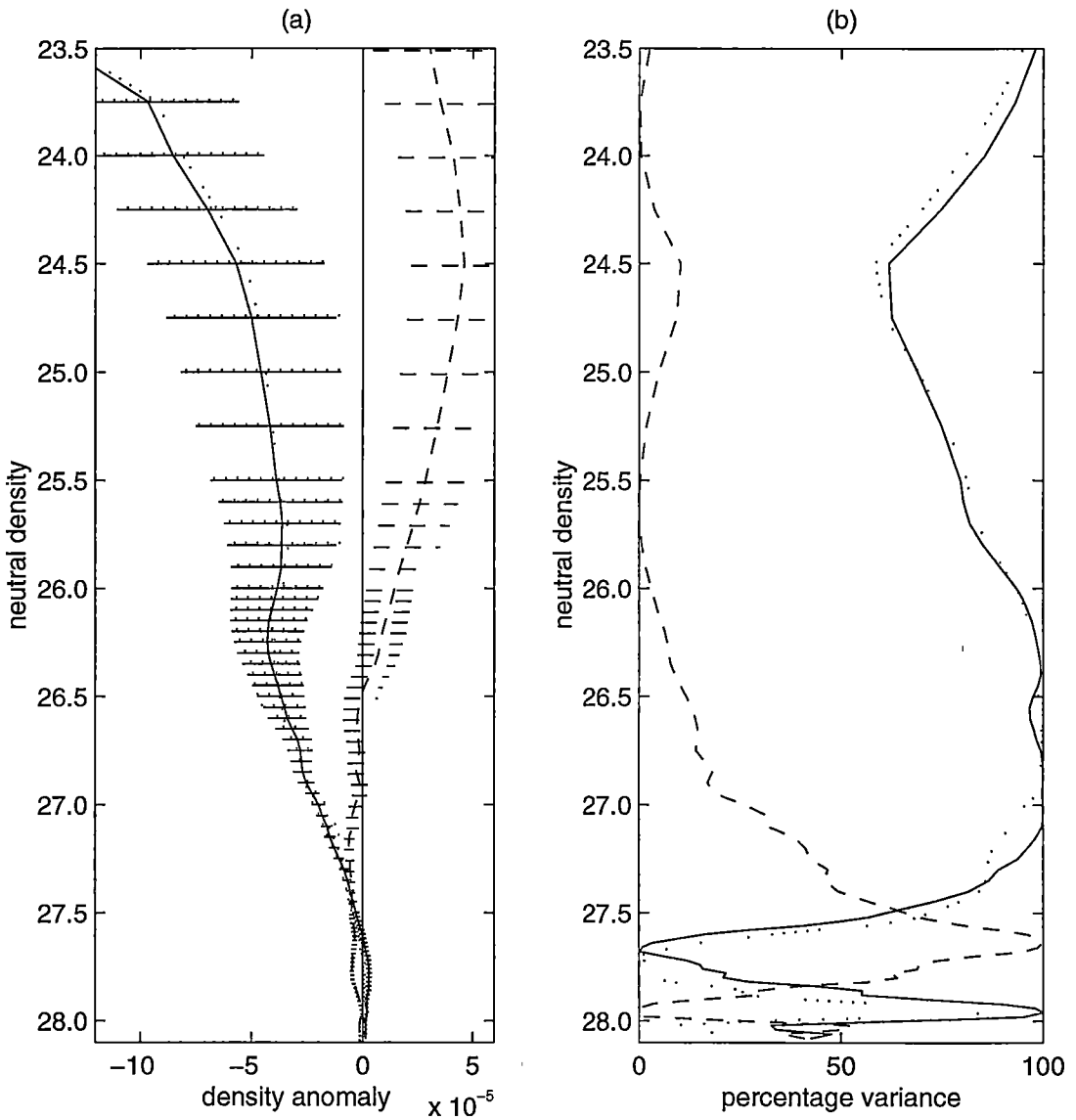

Figure 4.46: Inverse solutions averaged basin-wide from 130°E to 270°E along P4. (a) Solution to the under-determined problem: density anomaly $\rho^{-1}\rho'|_z$ contributed by each "pure" process. — denotes $\overline{\rho^{-1}\rho'|_z A^w}$, - - - denotes $\overline{\rho^{-1}\rho'|_z A^f}$, and .... denotes $\overline{\rho^{-1}\rho'|_z A^h}$. Negative anomalies indicate pure warming, pure freshening and pure downward heave respectively. Horizontal bars mark the 90% confidence intervals. (b) Solution to the over-determined problem: percentage of variance of the data explained by a single process.

Discussion

The implications of these observed temporal changes are discussed below in terms of the water masses in the top 1000 dbar, and then all waters below 1000 dbar. In the top 1000 dbar along P4, four major water masses are found: NPSTW, the SSM, 13°C Water, and modified AAIW.

(a) NPSTW

The shallow salinity maximum of NPSTW along P4 is formed below the high evaporative cell in the central North Pacific (Tsuchiya 1968), where high salinity surface water is subducted into the thermocline and advected southward (Wijffels et al. 1996). NPSTW is also seen as a surface salinity maximum along P3 at 24°N, but is not discussed along P3 because the mapped property fields there do not form the required neutral surfaces.

The North Pacific high evaporative cell is found roughly between 15°N and 30°N (Tomczak and Godfrey (1994), p.13). Furthermore, Levitus (1982)'s winter sea surface salinity map shows that the highest surface salinity in the North Pacific (> 35.0 pss) is found between 20°N and 30°N, and from 140°E to 230°E.

For NPSTW along P4 (24.0 - 25.5 γ^n), significant changes on neutral surfaces have been observed that are most consistent with the *pure salinification* scenario, and implies an increase in sea surface salinity in the zone between 20°N and 30°N in the central subtropical Pacific. One possible cause of this sea surface salinity increase is through an increase in evaporation minus precipitation rate in the high evaporative cell of the central North Pacific.

(b) the SSM

According to Reid (1973), the shallow salinity minimum along 10°N is the continuation of the SSM that originated at the high latitudes of the northeast Pacific, which has been advected equatorward by the California Current. At roughly 25°N, the flow turns southwest, and the SSM is subsequently spread westward following the path of the North Equatorial Current, so that in the zonal band between 10°N and the equator, the SSM can be found from roughly 230°E all the way westward to the western boundary. Yuan and Talley (1992) suggested that the shallow salinity minimum at 10°N (which they termed "tropical salinity minimum") may not be simply a continuation of the SSM, but could be a mixture of the SSM and NPIW. In any case, what is significant is that the shallow salinity minimum along the WOCE P4 section at 10°N is

related to the SSM along the WOCE P3 section at 24°N.

For the SSM along P4, no significant θ and S changes has been observed on neutral surfaces, but significant downward movements of neutral surfaces have occurred (see Figure 4.42). Inverse solutions averaged over the spatial extent of the SSM along P4 (not shown) reveal that *pure downward heave* explains more than 95% of the data variance within the SSM layer from 25.5 to 26.5 γ^n.

This result is different from that observed along the WOCE P3 section. Note that WOCE P4 was carried out 4 years after WOCE P3. Along P3, the SSM shows significant θ-S property changes that are most consistent with the *pure warming* ventilation scheme. The fact that no significant θ-S property change has been observed in the SSM along P4 could be due to the fact that the signal of surface warming has been eroded by the time the SSM is advected south to 10°N, which is where this water mass is furthest away from its source region.

(c) 13°C Water

The intermediate high salinity tongue that is seen to extend westward along 10°N from the eastern boundary of the Pacific has been referred to as 13°C Water by Wijffels et al. (1996) because of its afffinity with the equatorial 13°C thermostad. By studying maps of properties on the 160 cL t^{-1} surface (the core thermosteric anomaly of the equatorial 13°C Water), Tsuchiya (1981) deduced that the original high-salinity characteristic of 13°C Water is formed by winter convection and vertical mixing in the Tasman Sea, and at the region northeast of New Zealand, between 35°and 40°S. The saline characteristic is then advected to the eastern equatorial Pacific via a meandering path: it is first circulated in an anticlockwise manner around the South Pacific subtropical gyre, till it reaches the northeastern coast of Australia, where it flows north before reaching the equator, and is then advected to the east via the Equatorial Undercurrent and the South Equatorial Countercurrent. The subsurface countercurrents, found on either side of the equator in the Pacific, are also a vehicle of eastward advection of salinity (Johnson and Moore 1997). The high salinity tongue along 10°N represents the westward return flow. On the other hand, Toggweiler et al. (1991) found Tsuchiya (1981)'s origin for 13°C Water to be inconsistent with prebomb Δ^{14} C distribution in the Pacific, and proposed that the Equatorial 13°C Water, along with other less dense features of the South Pacific thermocline, may originate as part of a single subduction process

in the subantarctic region of the southwest Pacific.

The combined observations on isopycnals and on isobars suggest that the entire 13°C Water layer along P4 (26.0 to 27.0 γ^n) has undergone θ-S property changes that are most consistent with the *pure warming* ventilation scheme. This result therefore suggests surface warming over the southwest Pacific region. This agrees with Parker et al. (1994)'s surface temperature anomalies map for 1981-1990, relative to 1951-1980, which shows positive anomalies over the southwest Pacific region. Recent work by Holbrook and Bindoff (1997) also found long-term warming trend in the southwest Tasman Sea between 1955 and 1988.

(d) modified AAIW

The intermediate salinity minimum at the western part of P4 has been identified as modified AAIW because its density is in the range of AAIW in the South Pacific. The low salinity characteristic of AAIW is generally attributed to the excess of precipitation over evaporation over the subantarctic zone, where this water mass is renewed (McCartney 1977). Its subsequent northward spreading into the South Pacific subtropical gyre and across the equator has been studied by Tsuchiya (1991), who concluded that AAIW is entrained into the subtropical gyre in the eastern Pacific, then follows the anticlockwise circulation to reach lower latitudes ($\approx$ 20°S), and is then carried across the equator by the New Guinea Coastal Undercurrent in the far western Pacific.

Along the WOCE P4 section, modified AAIW (27.2 - 27.5 γ^n) shows temperature and salinity decreases on neutral surfaces that are above the 90% confidence levels. At 10°N, salinity values on a neutral surface decrease northward. For example, on the 27.5 γ^n surface, the meridional gradient has been estimated from historical data to be approximately 0.05 pss per 8°latitude. Hence the average salinity decrease of about 0.005 pss observed on the 27.5 γ^n surfaces can be accounted for by shifting the water mass southward by about 0.8°latitude, or approximately 90 km. A southward water mass shift would also explain the observed deepening of the neutral surfaces.

On the other hand, the observed salinity decrease in modified AAIW along P4 can also be due to θ-S property change induced at the sea surface. The combined observations on neutral surfaces and on isobars suggest that modified AAIW along P4 has consistently undergone *pure freshening* and *pure warming.* This suggests that the formation area of AAIW, which is the subantarctic zone in the Southern Ocean, has experienced an increase in surface precipitation

minus evaporation rate, and an increase in sea surface temperature. Bindoff and Church (1992) and Johnson and Orsi (1997) have also observed subsurface θ and S changes that suggest surface freshening and warming in the southern high latitudes.

(e) below 1000 dbar

From 27.5 to 27.9 γ^n, temperature and salinity on neutral surfaces have shown significant decreases. Waters in similar density range along the WOCE P3 section have also shown salinity decreases on neutral surfaces, but they are thought to be more likely due to southward movements of the water mass, than due to θ-S property change. Along P4, the observed salinity decrease on neutral surfaces can also be explained by a southward shift of the water mass.

The density range 27.5 - 27.9 γ^n along 10°N corresponds approximately to 1000 to 2000 dbar, and lies above the silica maximum that marks North Pacific Deep Water. Waters in the 27.5 - 27.9 γ^n range along P4 have potential temperature between 4.5°and 2.0°C, and salinity between 34.56 and 34.65 pss. The salinity and temperature decreases observed in these waters are consistent with the *pure freshening* and the *pure cooling* ventilation schemes. The 27.5 - 27.9 γ^n range along 10°N corresponds roughly to layers 11 and 12 in the inverse calculations of Wijffels et al. (1996), and their results show that this density range spans the transition level of the mid-depth meridional overturning cell: above layer 11, intermediate waters flow northward; below layer 12, deep waters return southward. If it is assumed that the salinity and temperature decreases observed in these waters are the result of θ-S property changes, and are not due to southward movements of the gyre, then these changes could be explained by a colder and fresher northward flow from the South Pacific. Again, a meridional section that intersects P4 would help to determine whether these deep changes are due to θ-S changes, or are the results of lateral movements of water masses.

Below 27.9 γ^n, the observed changes are small and are considered to be due to systematic errors.

4.4 Summary and Discussion for the North Pacific Ocean

Summary of observed temporal changes

This chapter has compared three modern WOCE CTD zonal sections with objectively mapped historical data, in order to study water mass changes in the North Pacific Ocean. Temporal differences of θ and S have been observed on neutral surfaces as well as on isobars, so that changes in water mass properties have been separated from the effects of vertical heavings of isopycnals.

The relative importance of surface temperature change and surface salinity change in causing the observed temporal water mass differences have then been quantified, by using the idealised ventilation model of Bindoff and McDougall (1994). It has been found that significant changes have occurred along all three latitudes in the North Pacific Ocean: 47°N, 24°N and 10°N, over the roughly 20-year period between the late 1960s and the late 1980s. Table 4.2 summarizes the observed changes in the major water masses along the three zonal sections in the North Pacific, and lists the surface processes that most consistently explain the observed temporal changes. The formation regions of the respective water masses are also listed.

Along the WOCE P1 section at 47°N, statistically significant θ and S changes have occurred in the density range 25.5 - 27.3 γ^n ($\approx$ 40 to 530 dbar). These changes are predominantly temperature and salinity decreases on neutral surfaces. The combined observations on neutral surfaces and on isobars suggest that the surface conditions over the northwest Pacific (including the Okhotsk Sea, and the areas around Kamchatka and the Kuril Islands) have cooled and freshened. Moreover, an east-west difference in the temporal changes has been observed which might be caused by the disparate sampling years in the historical data, and fits the cyclic temperature anomaly around the subarctic Pacific, first noted by Zhang and Levitus (1997).

Along the WOCE P3 section at 24°N, θ and S changes have occurred in the water masses in the density range 25.0 - 27.5 γ^n ($\approx$ 150 to 1000 dbar). Waters in the density range 25.0 - 25.5 γ^n have warmed and freshened. In North Pacific Subtropical Mode Water (NPSTMW), θ and S changes that are consistent with *pure cooling* have been observed. In the shallow salinity minimum (SSM), θ and S changes are consistent with *pure warming* and *pure freshening*, and imply surface warming and freshening over the northeastern

γ^n range	P1 (47°N)	P3 (24°N)	P4 (10°N)
< 25.0 to 25.5		• - pure freshening - pure warming *30°N to 35°N (central Pacific)*	• NPSTW - pure salinification *20°N to 30°N, 140°E to 230°E* *(central Pacific)*
25.5 to 26.0	• east of 205°E - pure freshening *north of 45°N, east of 200°E* *(northeast Pacific)*	• NPSTMW - pure cooling *26°N to 35°N, 140°E to 180°E* *(western Pacific)*	
26.0 to 26.5	• east of 205°E - pure cooling *north of 40°N, west of 200°E* *(northwest Pacific)*	• the SSM - pure warming - pure freshening *35°N to 50°N, east of 200°E (northeast Pacific)*	• the SSM - pure downward heave
26.5 to 26.8	• west/east of 205°E - pure cooling & freshening/salinification *Kamchatka, Kuril Islands, Okhotsk Sea*	• NPIW - pure freshening - pure warming *subarctic gyre, Okhotsk Sea*	• 13°C Water - pure warming *southwest Pacific*
26.8 to 27.2	• west/east of 205°E - pure cooling/warming *Kamchatka, Kuril Islands, Okhotsk Sea*		
27.2 to 27.5		• - pure freshening *Okhotsk Sea*	• modified AAIW - pure freshening - pure warming *subantarctic zone in the Southern Ocean*
27.5 to 27.9			• - pure freshening - pure cooling *northward flowing water from* *the South Pacific*

Table 4.2: Summary of water masses along the WOCE P1, P3 and P4 sections, and the ventilation scenarios that most consistently explain their observed temporal changes. Their respective formation regions are marked in italics.

Pacific. In the North Pacific Intermediate Water (NPIW) layer, the effects of the *pure warming* and *pure freshening* ventilation schemes are present, and suggest warmer and fresher conditions over the subarctic gyre. Below the NPIW layer, waters in the density range 27.2 - 27.5 γ^n show signs of *pure freshening.*

Along the WOCE P4 section at 10°N, water masses in the density range 24.0 - 27.9 γ^n ($\approx$ 100 to 1950 dbar), except for the SSM, have shown θ and S changes. North Pacific Subtropical Water (NPSTW), which originates under the high evaporative cell in the central Pacific, has shown signs of salinity increase. 13°C Water has warmed. Modified AAIW shows signs of *pure warming* and *pure freshening*, and suggests warmer and fresher conditions over the subantarctic zone in the Southern Ocean. From 27.5 to 27.9 γ^n, waters have become cooler and fresher.

Apart from θ and S changes, vertical displacements of neutral surfaces have also indicated significant changes to the major gyral structures in the North Pacific. Northward transport between 27.3 γ^n and 27.9 γ^n across 47°N is seen to have increased. The isopycnals along 24°N have deepened. Similar deepening of isopycnals can also be seen along 10°N.

Discussion

In general, these results from the North Pacific Ocean agree with those from Antonov (1993), that deeper than 500-600 m, temperature changes in the North Pacific from 25°N to 60°N are negligibly small. For example, along the WOCE P1 section at 47°N, temperature and salinity changes are only significant to about 530 dbar. This lack of deep water property changes reflects the lack of formation, and hence ventilation, of deep waters in the North Pacific, relative to the North Atlantic.

Equatorward of 25°N, temperature and salinity changes have been observed at greater depths. For example, along the WOCE P3 section at 24°N, changes are significant to about 1000 dbar. Along the WOCE P4 section at 10°N, changes are significant to about 2000 dbar, and reflects the influence on the deeper waters of the equatorial Pacific by the Southern Ocean. Below 2000 dbar, no significant θ and S changes has been observed. This is consistent with the long time-scales required for ventilating waters below 2000 dbar in the North Pacific, when compared with the relatively short average time difference of roughly 20 years between the historical data and the WOCE sampling.

In the shallow layers, in the density range 25.5 to 26.0 γ^n along P1, and in

the SSM along P3, the observed differences are most consistent with the ocean's response to known changing atmospheric forcings over the formation area: specifically, surface warming and freshening over the northeastern Pacific, off the west coast of North America and over the Gulf of Alaska, that have been documented independently by Roemmich (1992), Tanimoto et al. (1993), Parker et al. (1994) and Freeland and Whitney (1997).

Lastly, the most coherent large-scale signature of temporal change in the North Pacific comes from the intermediate waters. Figure 4.47 shows the changes in the mean θ-S curves along the three zonal WOCE lines: P1, P3 and P4. The mean values have been obtained by taking zonal averages on neutral surfaces along the transects, but excluding the western and eastern boundaries, as discussed in previous sections. The differences seen in Figure 4.47 are therefore basin-wide averages and do not show the subtle east-west divisions in water mass structures.

Along all three sections, it can be seen that intermediate waters from 26.5 to 27.5 γ^n, which include NPIW along P3 and modified AAIW along P4, have experienced a shift in the θ-S curve towards lower temperature and salinity on neutral surfaces. The decreases in the shallower layers above the salinity minima ($\approx$ 26.9 γ^n along P3, $\approx$ 27.3 γ^n along P4) can be explained by a combination of surface warming and surface freshening, but the decreases at and below the salinity minima can only be explained by surface freshening at the source regions of NPIW and AAIW. A distinct salinity minimum is absent from P1, and the results there are slighly more puzzling: the temperature and salinity decreases along P1 can be explained by a combination of surface freshening and surface cooling.

The pressures of the neutral surfaces in the intermediate waters have also changed (Figure 4.48). However, their changes are not uniform with depth, and so the thickness of the two intermediate water masses have altered. Along P3, the NPIW layer (26.4 - 27.2 γ^n) has thickened by about 1.4%, but along P4, the modified AAIW layer (27.2 - 27.5 γ^n) has thinned by about 3.6%.

Hence although different surface temperature conditions seem to have affected the intermediate waters of the North Pacific, their salinity properties are seen to have been affected by one surface salinity condition: that of surface freshening at the source regions. Because the low salinity characteristics of NPIW and AAIW are believed to be derived generally from the subarctic gyre and the subantarctic region respectively, the freshening of intermediate waters result therefore implies an increase in precipitation minus evaporation rates over

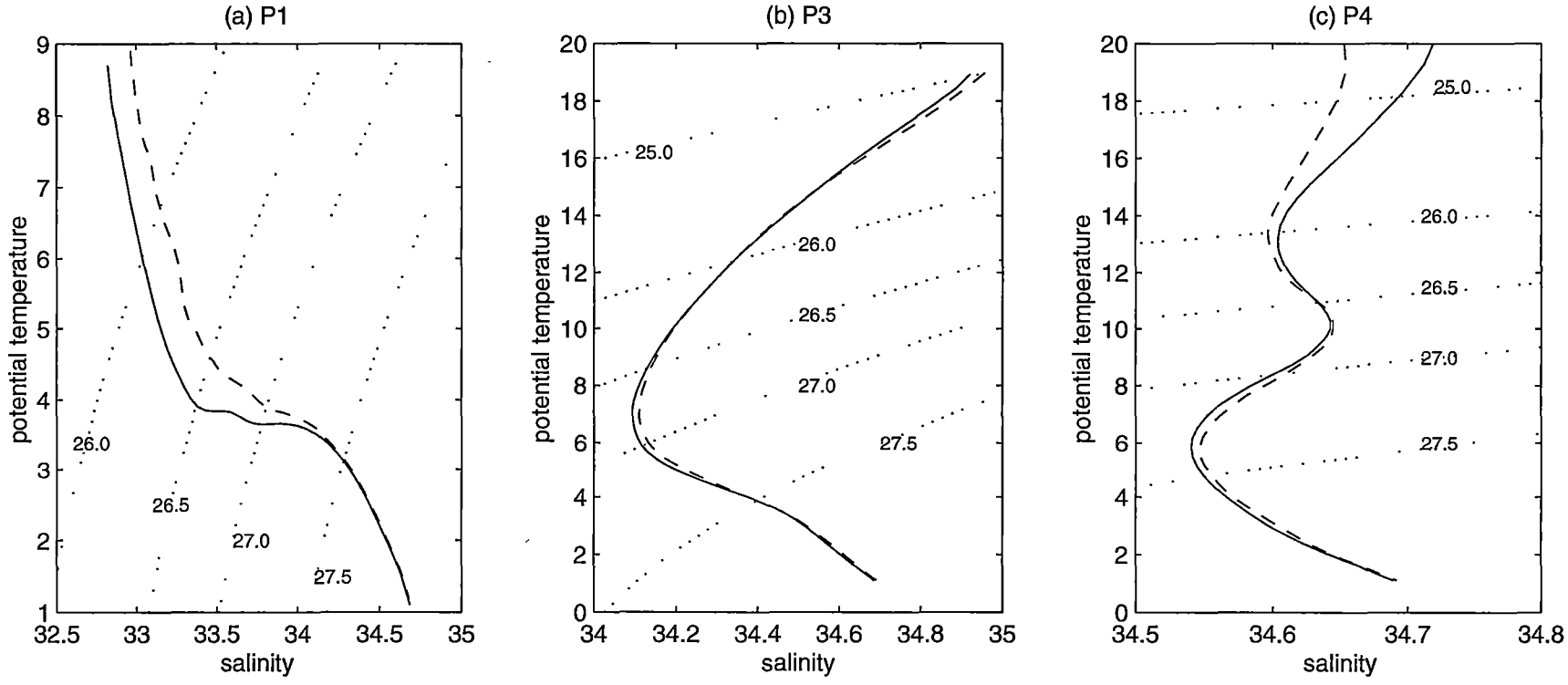

Figure 4.47: Zonally-averaged (along neutral surfaces) θ-S curves along the three North Pacific sections: (a) P1 (47°N), (b) P3 (24°N) and (c) P4 (10°N). Solid lines are from the WOCE data from the late 1980s. Dashed lines are from the objectively mapped historical data, from the late 1960s on average. Lines of constant neutral density are superimposed.

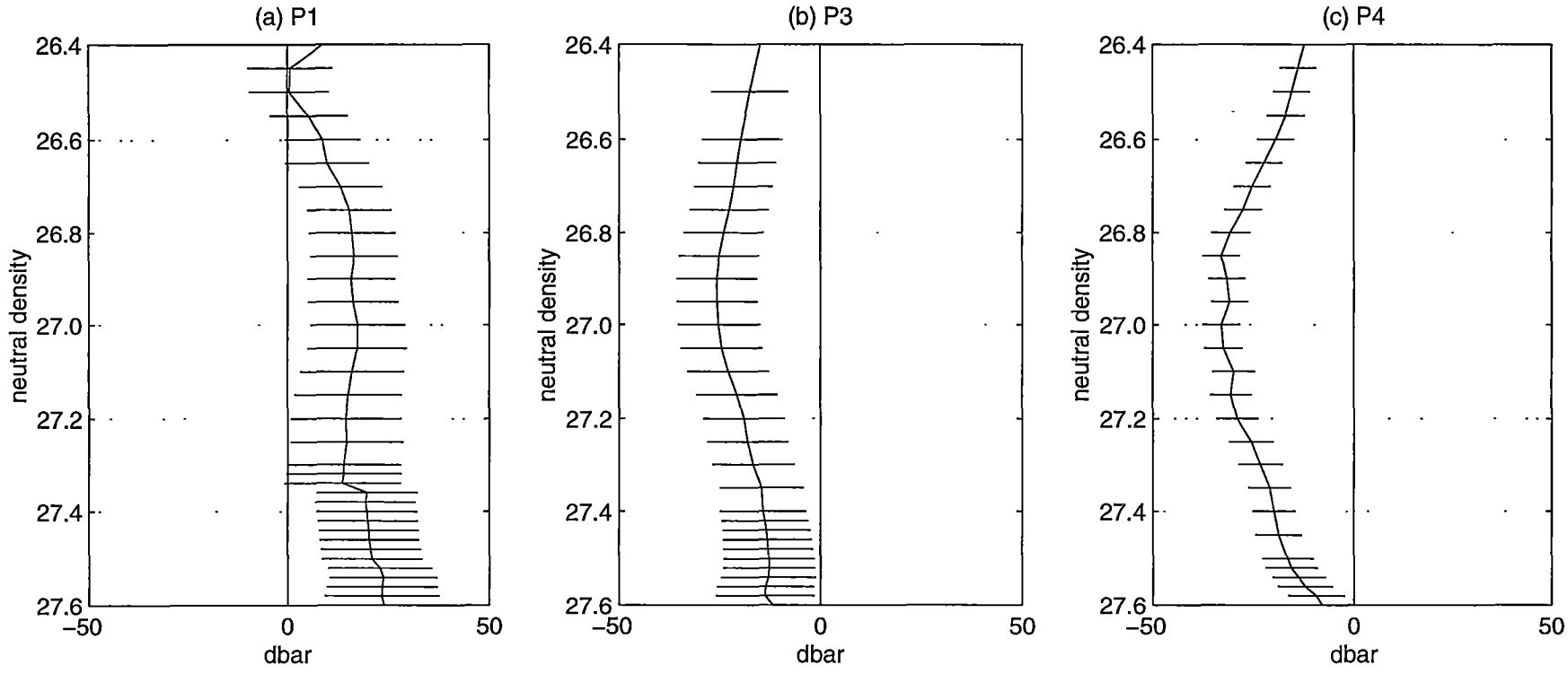

Figure 4.48: Zonally-averaged pressure differences of the neutral surfaces in the 26.5 - 27.5 γ^n range along the three North Pacific sections: (a) P1 (47°N), (b) P3 (24°N) and (c) P4 (10°N). Negative values indicate a deepening of neutral surfaces. Horizontal bars mark the 90% confidence intervals.

the subpolar regions of the North and South Pacific oceans.

Interestingly, the high-salinity water mass that is derived from the high evaporative cell in the central North Pacific, NPSTW, has experienced *pure salinification*, seen in Figure 4.47 (c) as a shift towards higher temperature and salinity on neutral surfaces in the θ-S curve, from surfaces shallower than 25.0 γ^n, down to about 26.0 γ^n. This implies an increase in evaporation minus precipitation rates over the subtropical gyre of the North Pacific. The combination of increased evaporation over the mid-latitudes, and increased precipitation over the high-latitudes, therefore suggests a strengthening of the hydrological cycle over the North Pacific Ocean.

In the next chapter, temporal changes in the South Pacific Ocean are discussed along a zonal transect at 17°S and a meridional transect at 210°E. It will be seen that this signature of freshening of intermediate waters coupled with salinification of subtropical waters is also present in the South Pacific Ocean.

Chapter 5

Observed changes in the South Pacific Ocean

This chapter discusses subsurface temporal changes observed along two WOCE transects in the South Pacific Ocean. These are P21 along 17°S and P16 along 210°E.

5.1 Differences along the WOCE P21 section

The cruise track of WOCE P21 runs along the nominal latitude of 17.5°S, from Iquique, Chile, to New Caledonia, then southwestward to Brisbane, Australia. Hence it lies near the northern boundary of the anticlockwise South Pacific subtropical gyre. The preliminary data set (pers. comm. H. Bryden) contains 294 CTD casts. 706 historical data points that are located between 1°S and 40°S have been selected from the Reid and Mantyla South Pacific data set for mapping to the coordinates of P21 (Figure 5.1).

These 706 historical casts span the years from 1947 to 1980 (Figure 5.2 a). The mean and median year of sampling are both 1967 for the historical data, with the standard deviation being 5 years. As WOCE P21 was undertaken in 1994, any observed temporal changes along P21 can be regarded as 27 ± 5 years differences. Although the most frequent month of sampling for the historical data is July, the distribution of sampling months is fairly uniform (Figure 5.2 b). However, WOCE P21 was sampled between April and June, and so there is the possibility of seasonal aliasing in the comparisons. Note that 1994 is an El Niño year, hence any observed differences along the WOCE P21 section might contain some El Niño effects. Bindoff and Wunsch (1992) have compared a synoptic section which has been sampled in 1987 with a climatologically

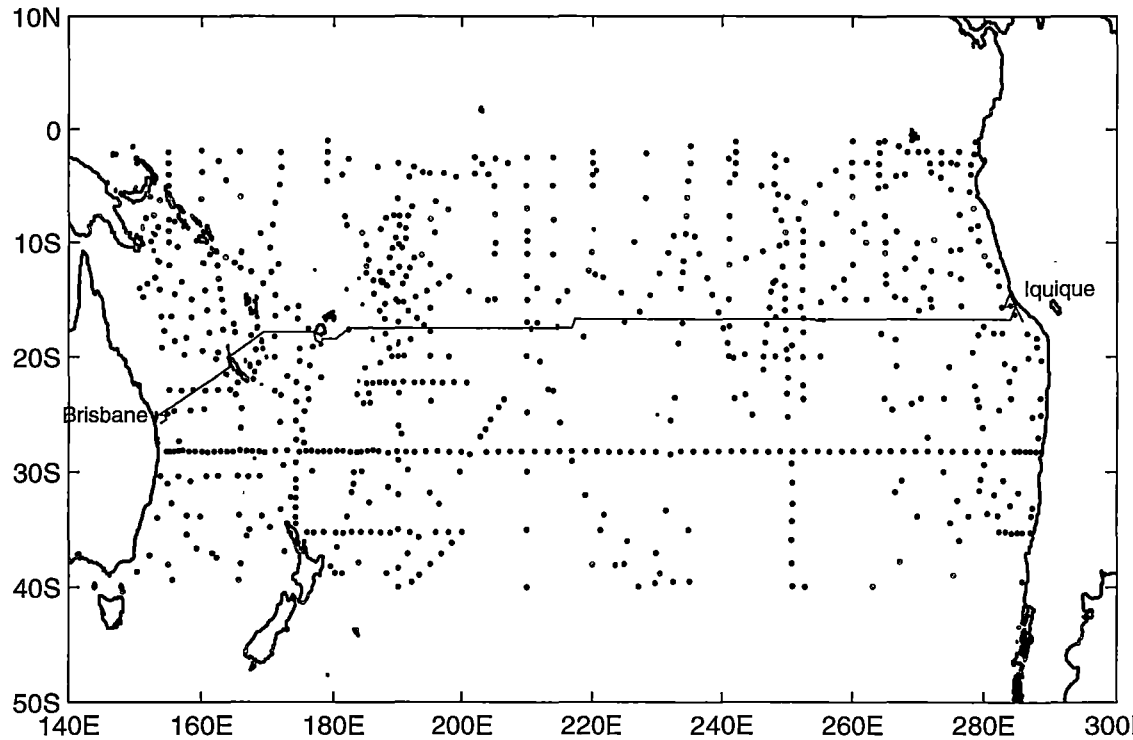

Figure 5.1: The cruise track of the WOCE P21 section, and the distribution of the 706 historical data points that have been used in the mapping to the coordinates of WOCE P21.

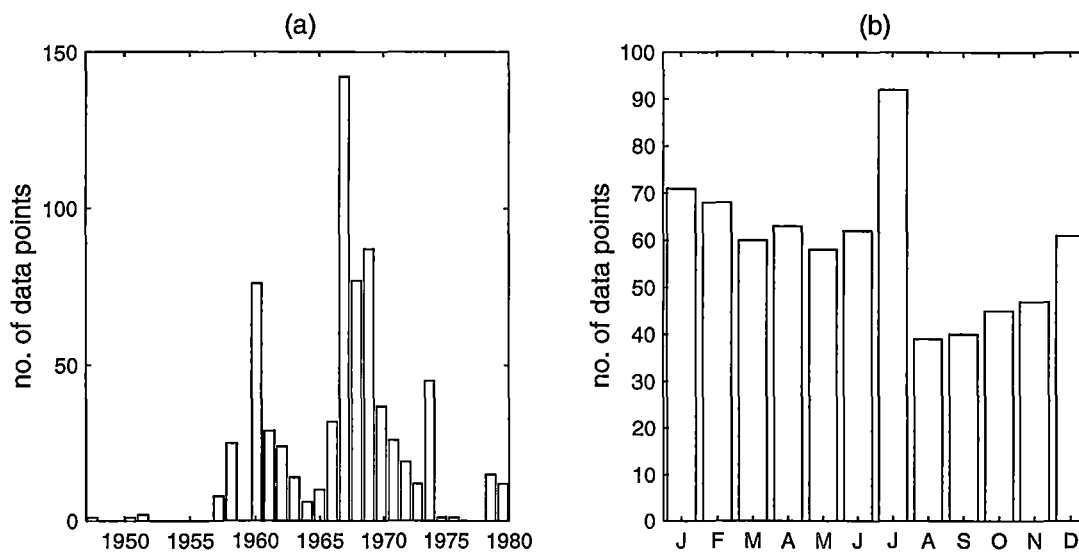

Figure 5.2: (a) The year distribution and (b) the month distribution, of the 706 historical data points in the mapping to the coordinates of the WOCE P21 section.

mapped section along 15°S in the South Pacific, and found significant differences in the temperature and salinity fields above 300 dbar that are related to the 1987 El Niño event.

The vertical section of salinity above 1500 dbar along P21, based on the WOCE CTD data, is shown in Figure 5.3. Below 1500 dbar, there is a weak salinity maximum near 190°E, below about 3600 dbar. It has $S \approx 34.71$, and density $\approx 28.1\ \gamma^n$. Except for this weak maximum, salinity increases monotonically with depth below 1500 dbar along P21, and so is not shown in Figure 5.3.

Salinity distribution in the top 100 dbar shows a marked difference between the eastern and the western part of the transect, due to different surface precipitation-evaporation balance. West of about 200°E, salinity in the top 100 dbar is less than 35.5, with potential temperature greater than 25.0°C. The low surface salinity and warm surface temperature are due to the fact that west of 200°E, P21 passes under the South Pacific Convergence Zone, which is an area of high P-E values and high surface temperatures (Tomczak and Godfrey (1994), p.150-152). East of 200°E, the WOCE P21 section passes under the high evaporative cell of the South Pacific. There, evaporation exceeds precipitation, and waters in the top 100 dbar attain high salinity values that exceed 36.0 in general. This surface salinity maximum along P21 east of 200°E is often called South Pacific Subtropical Water (SPSTW). Its northern equivalent is naturally North Pacific Subtropical Water (NPSTW), and has been discussed along the WOCE P4 section along 10°N.

East of 220°E, careful examination of the θ-S curves reveals slight deflections towards lower salinities at the potential temperature range of 11°C to 13°C (roughly 200 to 400 dbar). This is a subtle manifestation of the South Pacific shallow salinity minimum (the SSM), which is analogous to the North Pacific shallow salinity minimum (Reid 1973). Along 17.5°S, the South Pacific SSM is near the end of its advection path from its formation area near South America, and is no longer obvious as a vertical salinity minimum in Figure 5.3. The SSM along P21 has salinity between 34.6 and 34.8.

The SSM along P21 is underlain by a slight salinity maximum, which has been observed to have a northern origin, from the recent WOCE P19 transect along the 88°W meridian (Tsuchiya and Talley 1998). Again the salinity maximum below the SSM is not obvious from Figure 5.3, but the halostad with salinity values between 35.0 and 34.6 at the eastern end of the transect perhaps indicates its presence.

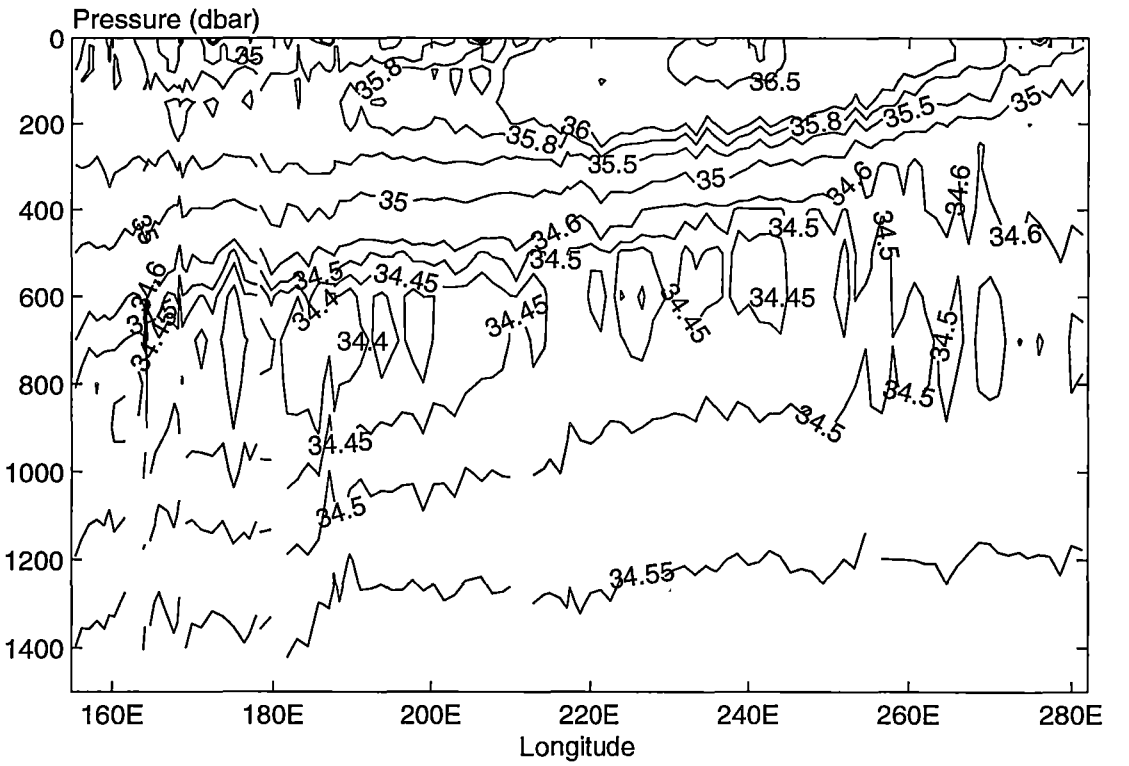

Figure 5.3: Profile of salinity (pss) for the upper 1500 dbar along 17.5°S, based on CTD data from the WOCE P21 section.

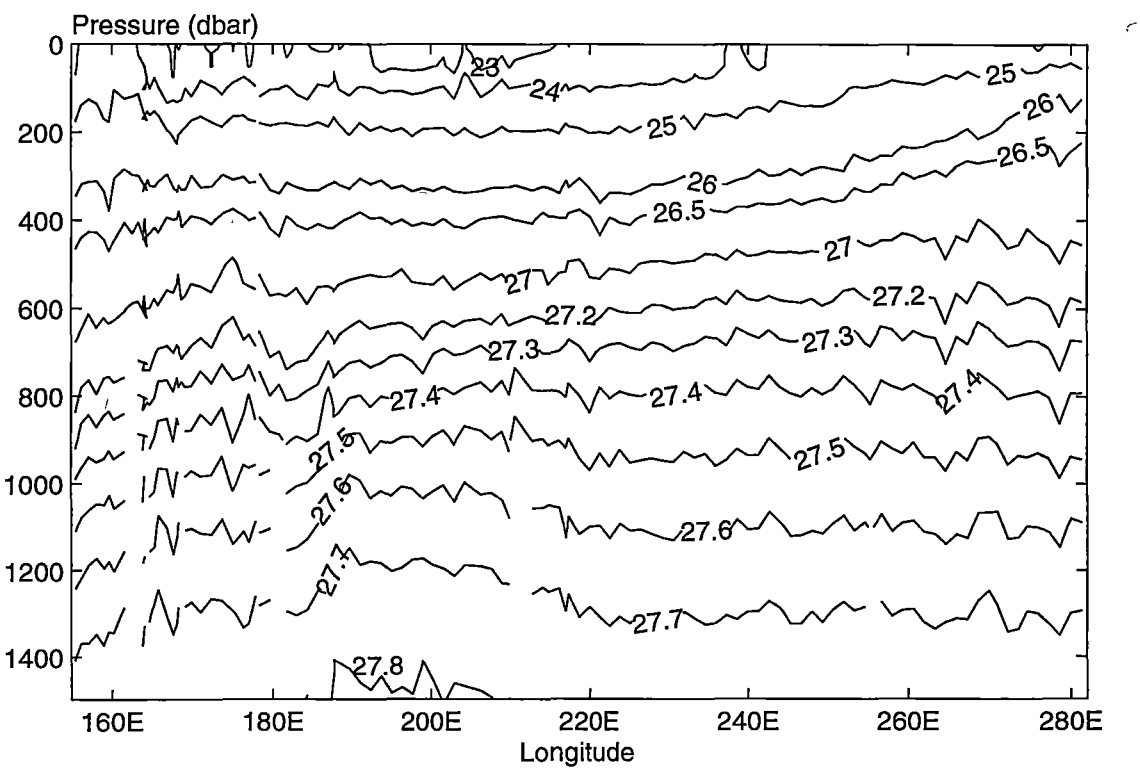

Figure 5.4: Profile of neutral density (kg m^{-3}) along 17.5°S, as in Figure 5.3.

A deeper and more prominent salinity minimum is present between 27.0 and 27.5 γ^n ($\approx$ 600 and 1000 dbar) along the entire length of P21. This is Antarctic Intermediate Water (AAIW). It has salinity values lower than 34.5, and potential temperatures between 4.0°C and 8.0°C along P21.

The vertical distribution of temperature along P21 (not shown) is one of monotonic decrease with depth. Because the WOCE P21 section lies north of the area where Subtropical Mode Water and Subantarctic Mode Water are found, no thermostads (or pycnostads) associated with these two mode waters are found along 17.5°S.

Figure 5.4 shows the vertical profile of neutral densities in the top 1500 dbar along P21. At the eastern end of the transect, the upward-sloping isopycnals from west to east above 400 dbar signifies the northward-flowing Peru Current. The narrow area east of 281°E, as well as the western boundary west of 154°E, are prone to pressure inversions in the mapped pressure field on neutral surfaces. Hence along the WOCE P21 section, discussion of temporal changes is limited to the area between 154°E and 280°E.

Because the vertical temperature distribution along P21 is relatively featureless compared to the vertical salinity distribution, the stability ratio R_ρ reflects the salinity characteristic of the various water masses better than their temperature characteristic. Figure 5.5 shows the vertical profile of R_ρ between 26.0 γ^n ($\approx$ 250 dbar) and 28.0 γ^n ($\approx$ 2700 dbar) along P21. From 26.0 γ^n, salinity decreases with depth, until the salinity minimum of AAIW is reached, whose core density is at roughly 27.2 - 27.3 γ^n along 17.5°S. From the salinity minimum of AAIW, salinity increases with depth to the bottom (except for the weak salinity maximum near 190°E, $>$ 28.0 γ^n). Hence from 26.0 γ^n to the salinity minimum of AAIW, R_ρ are positive; below the AAIW salinity minimum, the rest of the water column has negative R_ρ values.

To the east of 220°E, a large part of the water column above the AAIW layer displays large stability ratios (typically greater than 5) that are associated with the large positive slopes in the θ-S curves above salinity minima. The isopleth in Figure 5.5, which separates the region with $R_\rho < 5$ (the white area) from the region with $R_\rho > 5$ (the light-shade area), stretching from 26.2 γ^n at the eastern end of the transect ($\approx$ 200 dbar), to 26.6 γ^n at 230°E ($\approx$ 400 dbar), therefore marks the core densities of the South Pacific SSM along P21. Note that the slight salinity maximum which underlies the SSM is also obvious in Figure 5.5 as a small part of the water column centred at 26.4 γ^n, roughly to the east of 270°E, with $R_\rho < 0$.

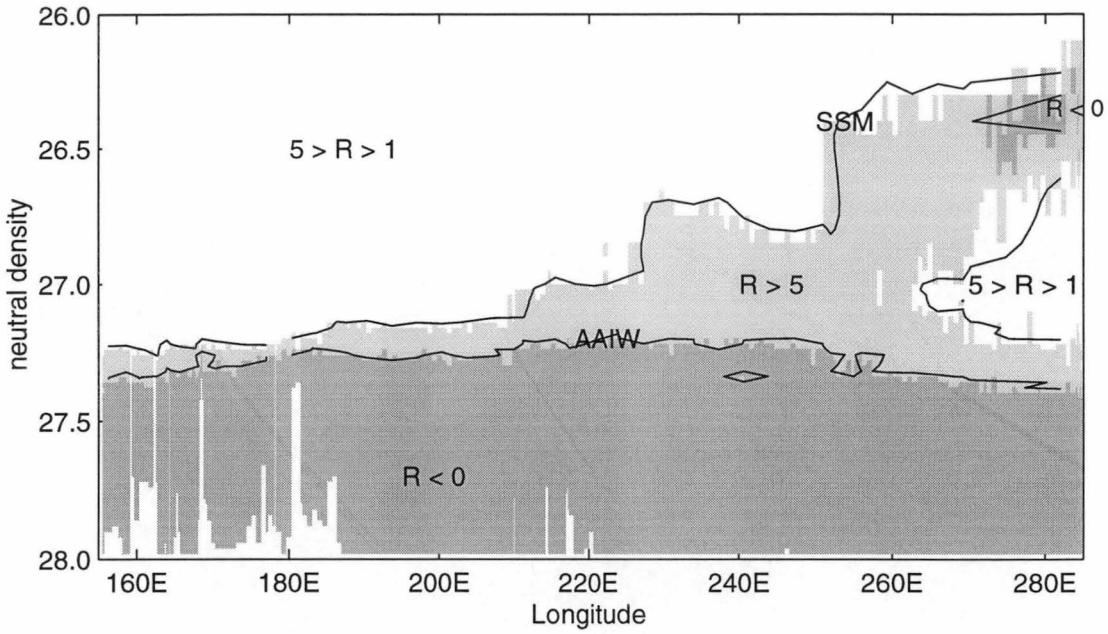

Figure 5.5: Profile of stability ratio R_ρ between 26.0 and 28.0 γ^n along P21.

The θ-S diagrams of the water masses along P21, from the WOCE sampling in 1994, and from the objectively mapped historical data, are shown in Figure 5.6. The mapped property fields on neutral surfaces shallower than 24.0 γ^n to the west of 246°E ($\approx$ 100 dbar), and on neutral surfaces shallower than 25.5 γ^n to the east of 246°E ($\approx$ 200 dbar), do not accurately form the required neutral surfaces. These shallow densities correspond to the surface layers that are affected by high surface precipitation to the west, and high surface evaporation to the east, and so are subject to great seasonal variabilities. Hence waters within these shallow parts of the water column are excluded from the ensuing discussion.

Below these surface layers, the objective estimates of θ, S and P preserve the neutral surface definition to within instrumental error. The ratios of the standard deviation of the mapping residuals to that of the *a priori* noise, for all three mapped fields θ, S and P, are between 0.8 and 1.0, indicating good length scales fit in the mapping procedure (see Equation B.3 in Appendix B).

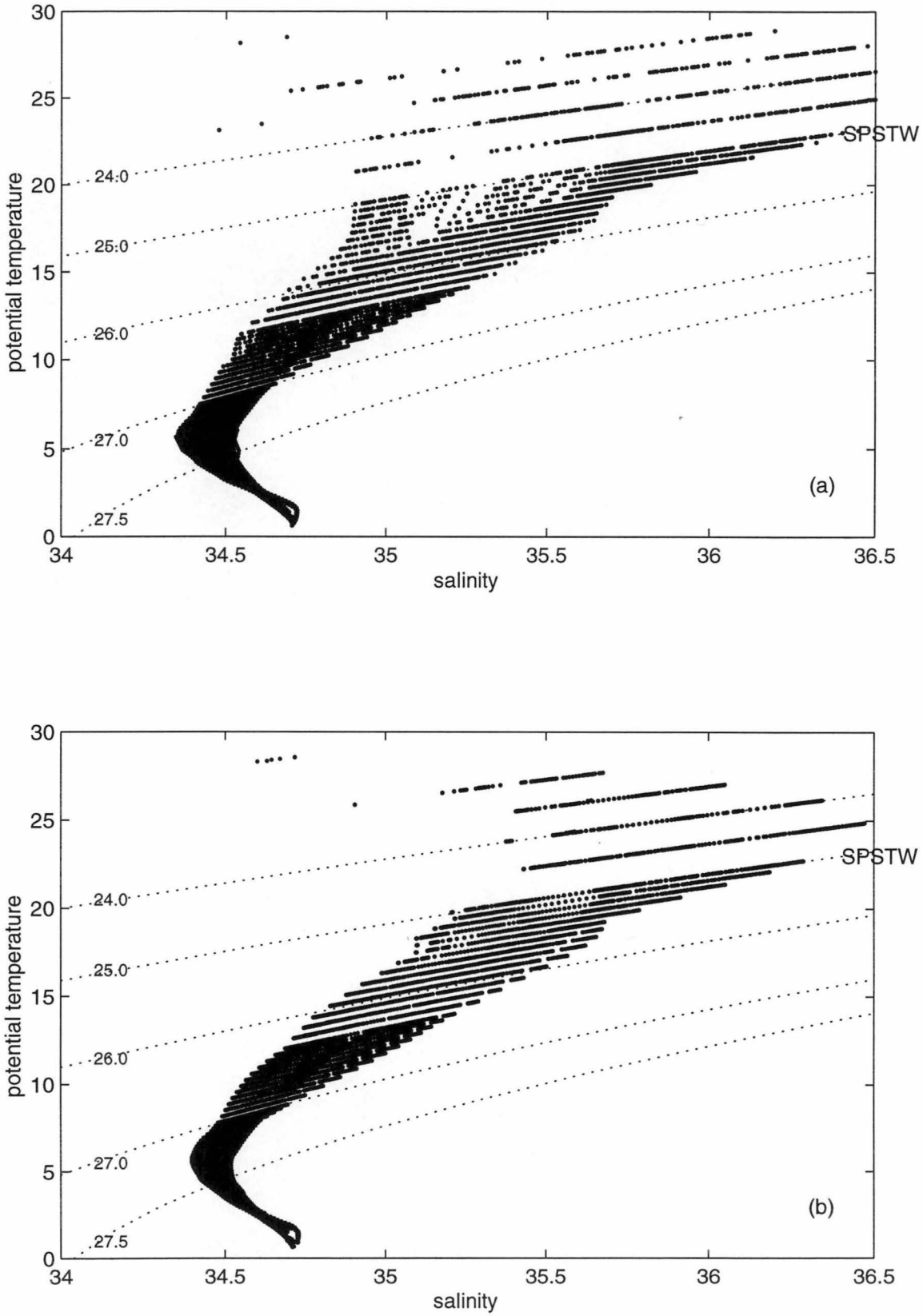

Figure 5.6: θ-S diagram on neutral surfaces along P21, (a) from the WOCE 1994 section, and (b) from the historical data objectively mapped to the coordinates of P21. Lines of constant neutral density are superimposed.

Observed temporal changes on neutral surfaces

Figures 5.7, 5.8 and 5.9 show the differences in potential temperature, salinity and pressure on neutral surfaces (i.e. $\theta'|_n$, $S'|_n$ and N') along the WOCE P21 section. The dashed line marks the level below which the objective estimates of θ, S and P satisfy Equation 3.1.

West of 240°E, waters between 24.0 and 25.0 γ^n ($\approx$ 100 to 200 dbar) display general temperature and salinity increase on neutral surfaces, punctuated by cooled and freshened patches. Temporal θ and S changes in the 24.0 - 25.0 γ^n range are generally less than the pointwise mapping errors at those levels. Below 25.0 γ^n, a large area stretching from roughly 170°E to 240°E show temperature and salinity increase on neutral surfaces down to 26.5 γ^n. Temperature and salinity changes that exceed 0.2°C and 0.05 pss respectively are common in the 25.0 - 26.5 γ^n range, and are above the pointwise mapping errors at those levels.

East of 240°E, the water column between 25.5 and 26.7 γ^n, which encompasses the South Pacific SSM, is dominated by temperature and salinity decreases on neutral surfaces. Zonal averages taken between 240°E and 281°E (Figure 5.10 c,d) reveal that only the averaged temperature and salinity changes on neutral surfaces below 26.2 γ^n are significant above the 90% confidence intervals.

From about 26.7 to 27.5 γ^n, the temporal pattern of change is dominated by basin-wide decreases in temperature and salinity on neutral surfaces that are mostly above the pointwise mapping errors at those levels. When averaged from 154°E to 281°E, $\overline{\theta'|_n}$ and $\overline{S'|_n}$ are greatest at 27.1 γ^n, being 0.13°C and 0.026 pss respectively (Figure 5.11 a,b). 27.1 γ^n is near the core density of AAIW along P21. Note that decreases in temperature and salinity on neutral surfaces have also been observed in the modified AAIW layer along P4 (10°N) in the North Pacific (see Chapter 4). The magnitude of the decrease along P21 is twice that along P4, in terms of temperature and salinity units of °C and pss.

Below 27.7 γ^n ($\approx$ 1300 dbar), $\overline{\theta'|_n}$ are less than 0.01°C and $\overline{S'|_n}$ are less than 0.002 pss (Figure 5.11 a,b). These salinity differences (and the corresponding temperature differences) are within the systematic errors that are expected between the historical data and the modern CTD data (as explained in earlier chapters).

The spatial pattern of temporal differences in pressure on neutral surfaces (Figure 5.9) shows a slight zonal variation above 26.0 γ^n. Neutral surfaces have shaoled to the west of 220°E, and have deepened to the east of 220°E. This

east-west variation might be an indication that the South Pacific subtropical gyre has weakened, or it might be an effect of the 1994 El Niño, which resulted in an uplifting of the thermocline in the western Pacific, and eastward movements of warm water causing a deepening of the thermocline in the eastern Pacific.

Below 26.0 γ^n, general upward displacements of isopycnals have been observed. Sectionally-averaged pressure differences are above the 90% confidence intervals between 26.2 and 27.0 γ^n (Figure 5.11 c). Below 27.0 γ^n, the pattern of N' becomes less spatially coherent, and the sectionally-averaged differences are below the 90% confidence levels.

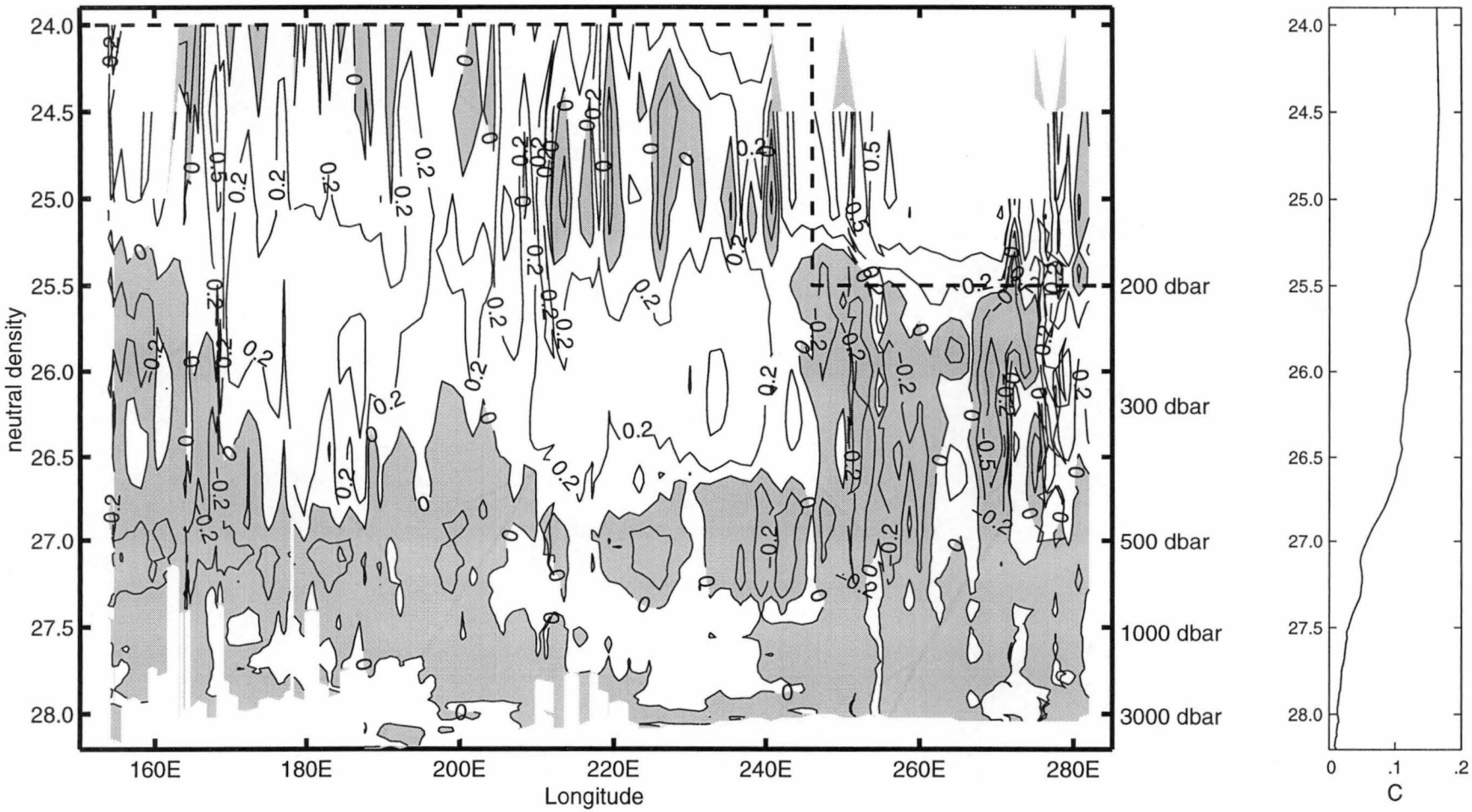

Figure 5.7: (Left) $\theta'|_n$ (°C) along P21. The shaded parts indicate areas with a temperature decrease on neutral surfaces. The average pressures of the neutral surfaces are shown in the right-hand y-axis. (Right) The right-hand panel shows the average pointwise mapping errors for θ, as a function of neutral density γ^n.

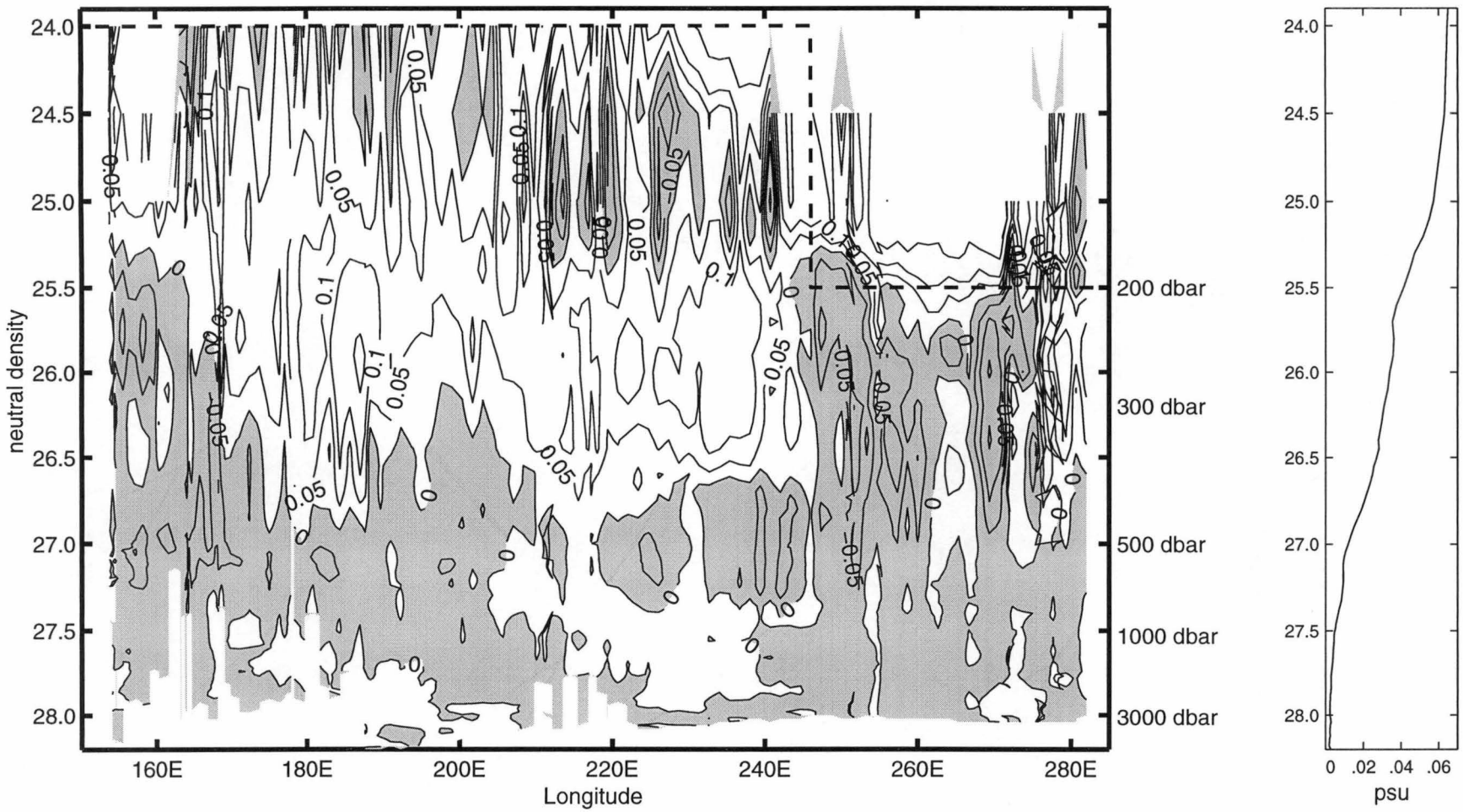

Figure 5.8: (Left) $S'|_n$ (pss) along P21. The shaded parts indicate areas with a salinity decrease on neutral surfaces. The average pressures of the neutral surfaces are shown in the right-hand y-axis. (Right) The right-hand panel shows the average pointwise mapping errors for S, as a function of neutral density γ^n.

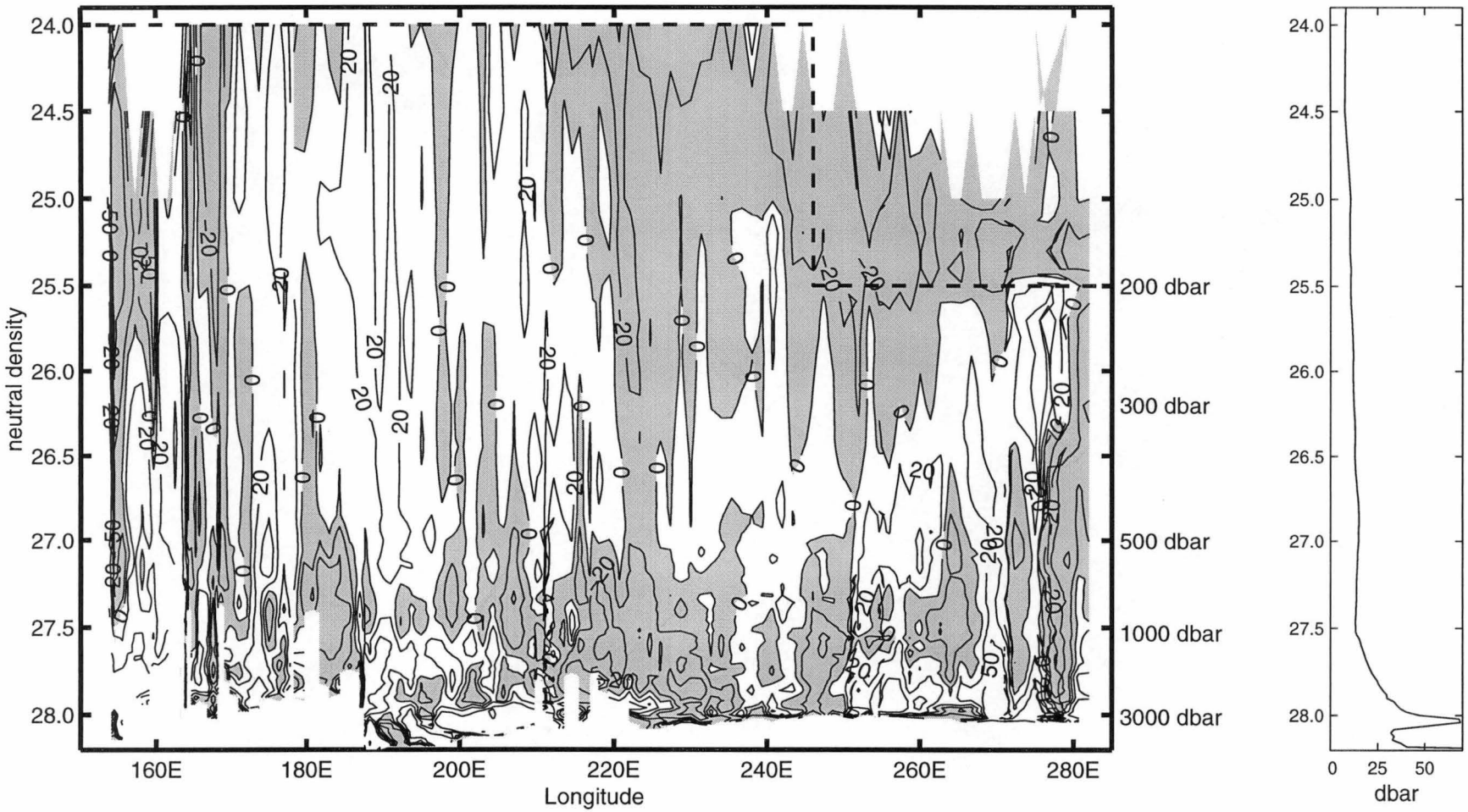

Figure 5.9: (Left) N' (dbar) along P21. The shaded parts indicate a deepening of neutral surfaces. The average pressures of the neutral surfaces are shown on the right-hand y-axis. (Right) The right-hand panel shows the average pointwise mapping errors for P, as a function of neutral density γ^n.

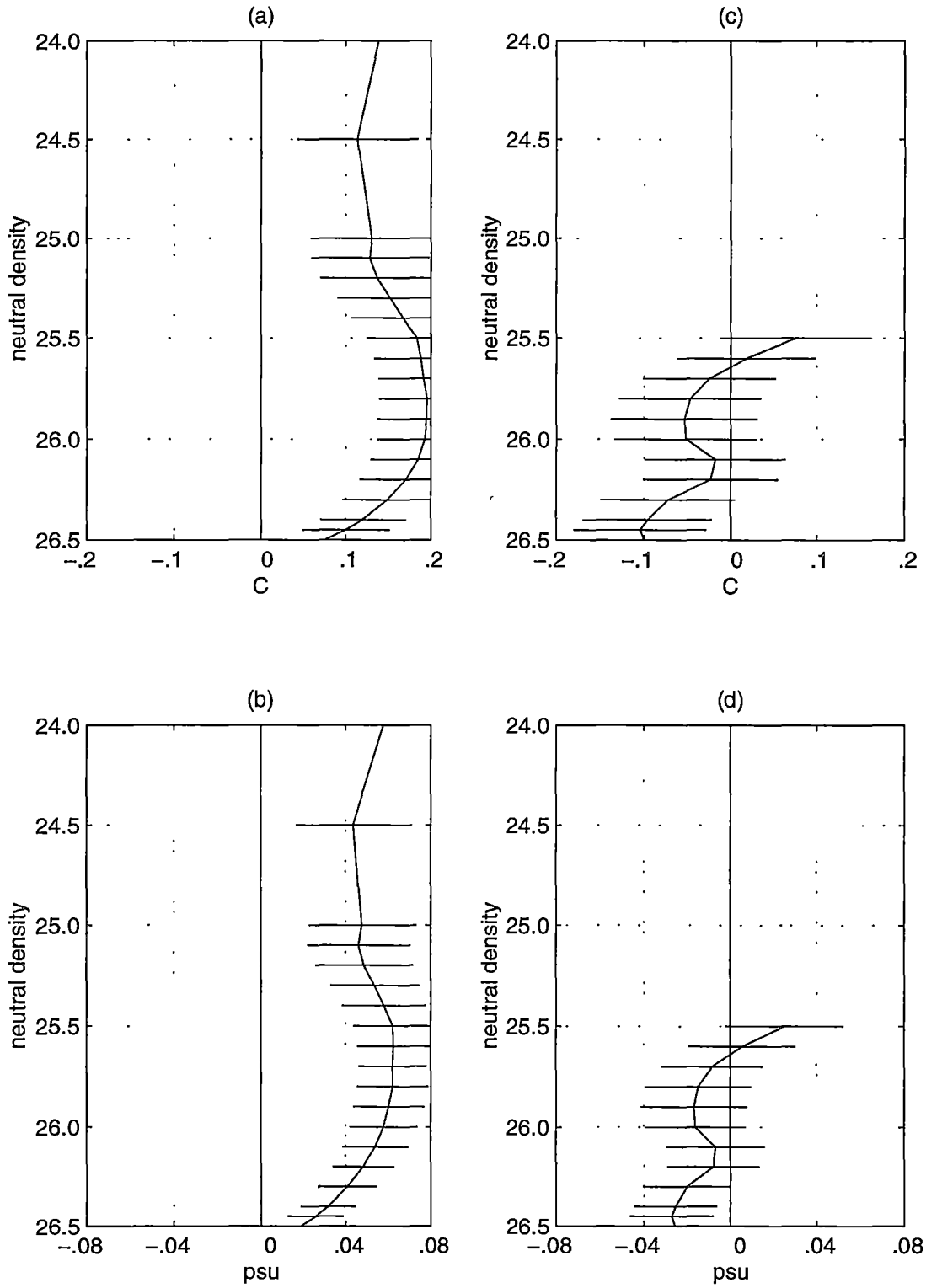

Figure 5.10: (a) and (b) $\overline{\theta'|_n}$ and $\overline{S'|_n}$ respectively, averaged over the western part of the P21 section, between 154°E and 240°E. (c) and (d) $\overline{\theta'|_n}$ and $\overline{S'|_n}$ respectively, averaged over the eastern part of the P21 section, between 240°E and 281°E. Horizontal bars indicate 90% confidence intervals.

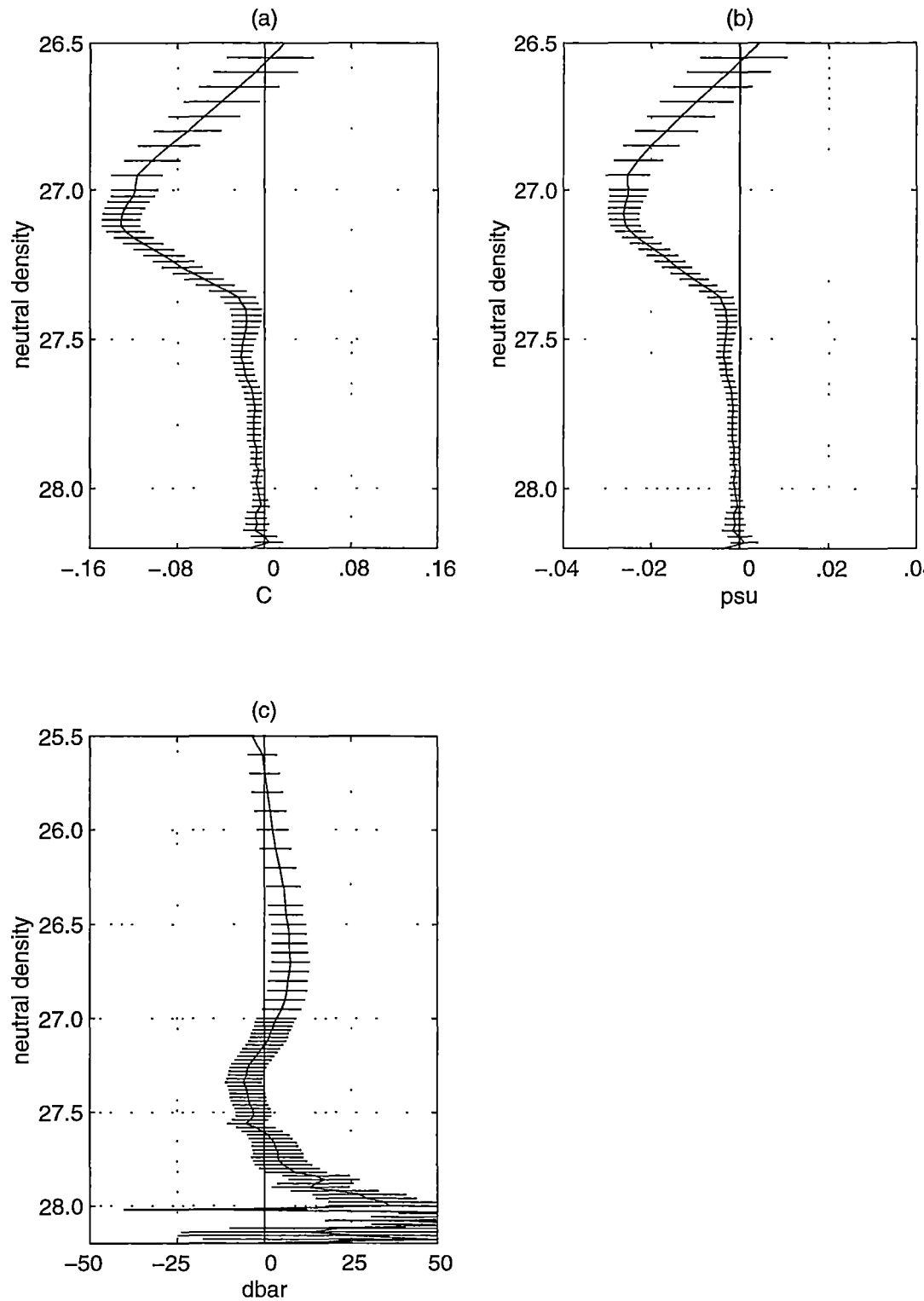

Figure 5.11: Sectional averages between 154°E and 281°E along P21. Horizontal bars indicate 90% confidence intervals. (a) and (b) $\overline{\theta'|_n}$ and $\overline{S'|_n}$ respectively, from 26.5 γ^n to 28.2 γ^n. (c) $\overline{N'}$, from 25.5 γ^n to 28.2 γ^n.

Observed temporal changes on isobars

Temporal changes in temperature and salinity on isobars, for the upper 1400 dbar along the WOCE P21 section, are shown in Figure 5.12. Temperature changes in the top 300 dbar of the water column reflect the possible 1994 El Niño effect that has been observed in pressure changes of the neutral surfaces. To the west of 220°E, cold anomalies dominate, while to the east of 220°E, warm anomalies are present.

This east-west variation is not present in salinity differences in the top 300 dbar, where the majority of the water column shows salinity increases. Between 300 and 400 dbar, cooling on isobars dominate. At the levels of the South Pacific SSM along P21, which stretch from 200 dbar at the eastern end, westward and downward to about 400 dbar at 230°E, temperature and salinity decreases on isobars have been observed.

Above the AAIW layer, the majority of the water column along P21 has a positive stability ratio. To the west of 240°E, the combined observations of salinity increase on isobars above 300 dbar, as well as on neutral surfaces, suggest temporal water mass changes that are consistent with the *pure salinification* scenario (see Table 2.1). In addition, the dominant temperature decrease on isobars between 300 and 400 dbar, accompanied by temperature increase on neutral surfaces above 26.5 γ^n ($\approx$ 400 dbar), suggest *pure cooling* for the waters between 300 and 400 dbar. At the levels of the SSM, the combined observations of salinity decrease on isobars, as well as on neutral surfaces, suggest that the SSM has undergone *pure freshening.*

Below 400 dbar, temporal changes on isobars are dominated by basin-wide cooling and freshening. Averages along the P21 section from 154°E to 281°E (Figure 5.13) show that $\overline{S'|_z}$ are significant above the 90% confidence intervals to 1000 dbar, while $\overline{\theta'|_z}$ are significant above the 90% confidence intervals only to 600 dbar.

The values of the stability ratio change from positive to negative around the salinity minimum of AAIW, which, along 17.5°S, is at approximately 800 dbar. However, $\theta'|_n$ and $S'|_n$ along P21 do not display a change of sign around the salinity minimum (see Figures 5.7 and 5.8). Hence the observed salinity decreases on isobars and on neutral surfaces, in the AAIW layer along P21, are consistent with AAIW having undergone *pure freshening.*

The relative strengths of each of the three *pure* processes in causing the observed temporal changes, are discussed quantitatively in the following section in terms of the inverse solutions.

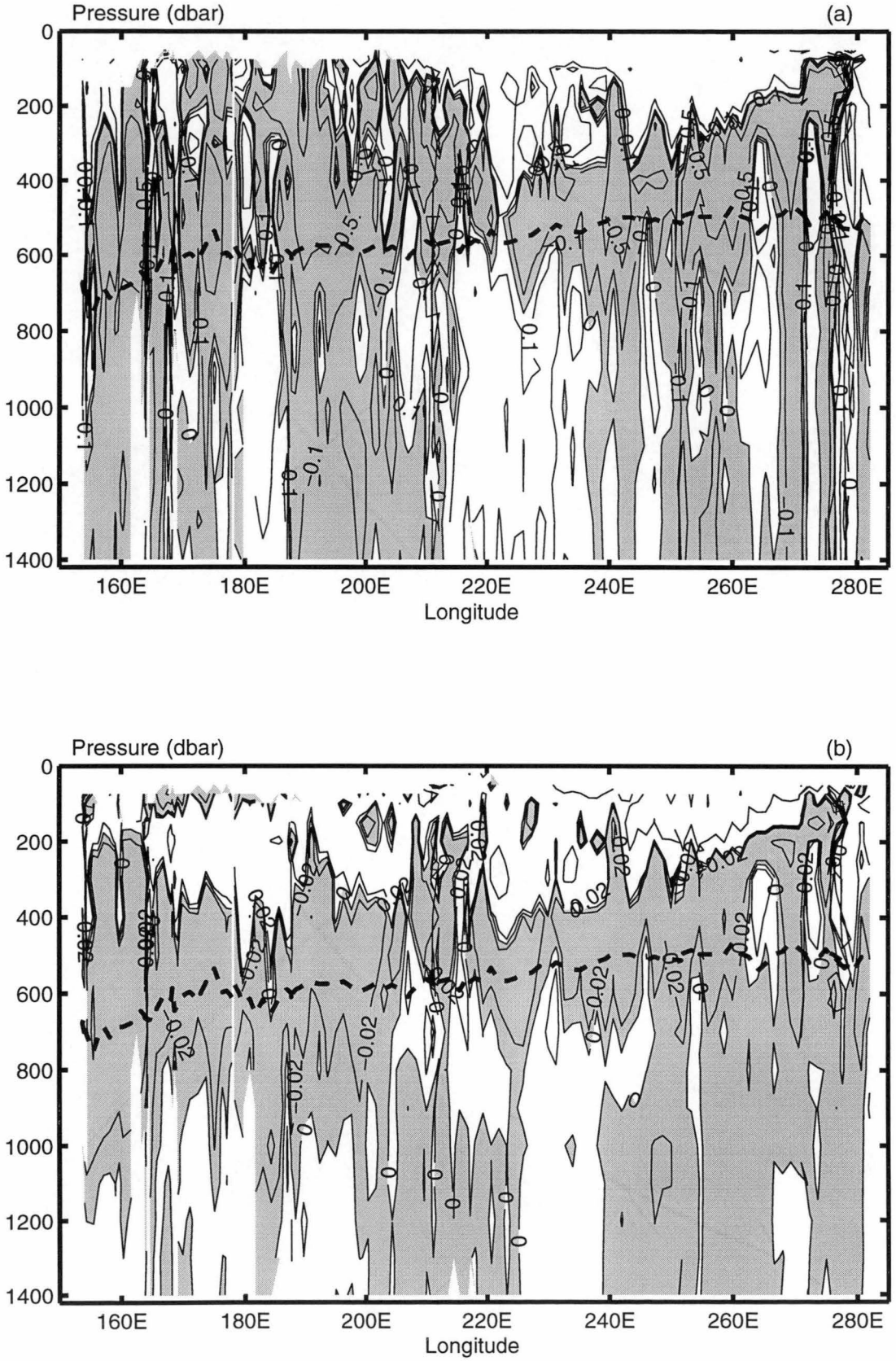

Figure 5.12: (a) $\theta'|_z$ (°C), and (b) $S'|_z$ (pss) for the upper 1400 dbar along P21. Shaded parts indicate areas with temperature and salinity decrease on isobars. The solid line marks the level of 27.1 γ^n, which is the surface that shows the largest $\overline{\theta'|_n}$ and $\overline{S'|_n}$.

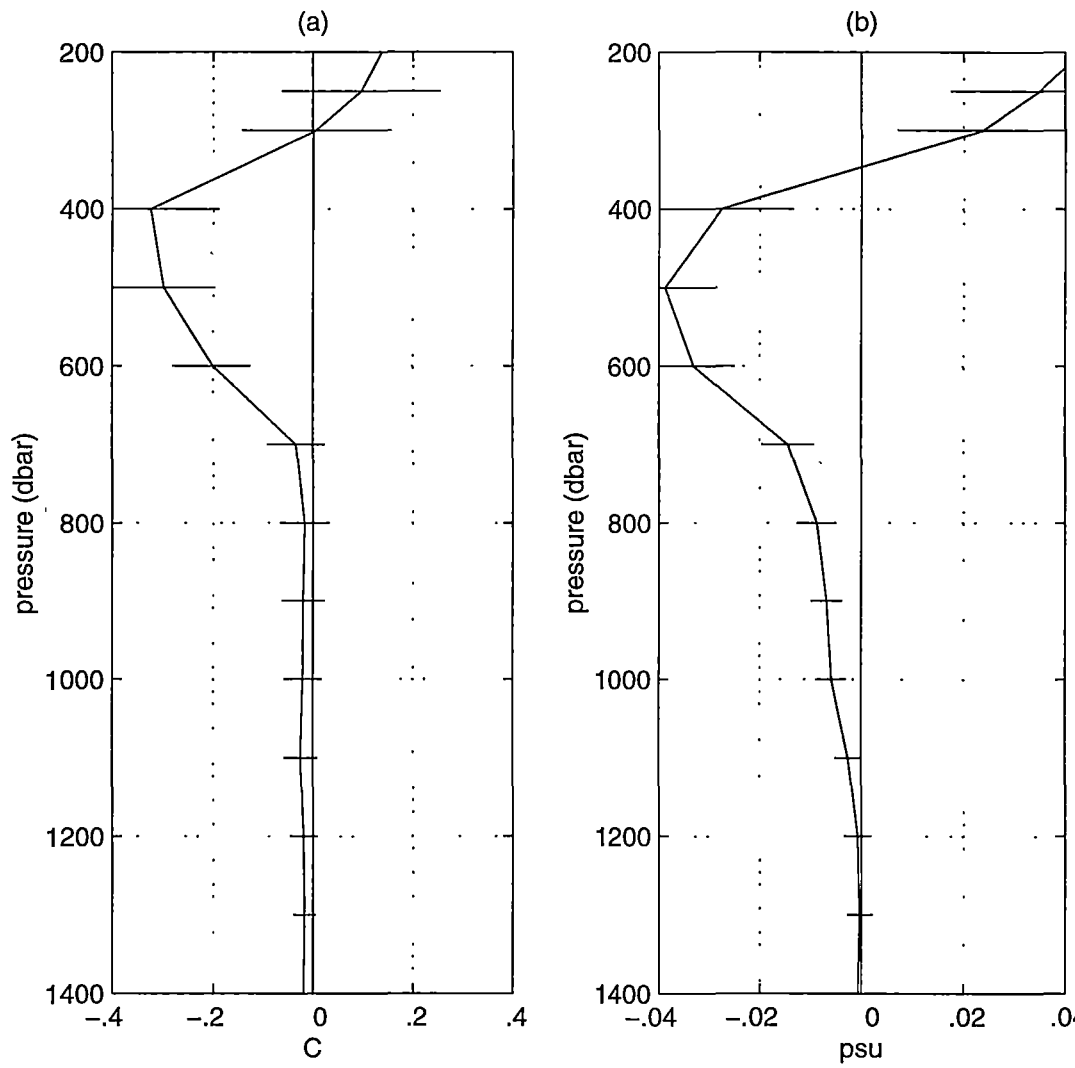

Figure 5.13: (a) $\overline{\theta'|_z}$ (°C), and (b) $\overline{S'|_z}$ (pss), averaged between 154°E and 281°E along P21. Horizontal bars indicate 90% confidence intervals.

Solutions to the inverse problem

The solutions to the inverse problem are discussed first for the top 200 dbar of the water column, i.e. above 25.5 γ^n. The solutions are shown in Figure 5.14 and have been averaged from 154°E to 240°E. It can be seen that the effect of *pure salinification* is present from 24.0 to 25.5 γ^n, but is strongest between 24.5 and 25.5 γ^n. Within this density range is the surface salinity maximum of SPSTW, which has its origin under the South Pacific high evaporative cell.

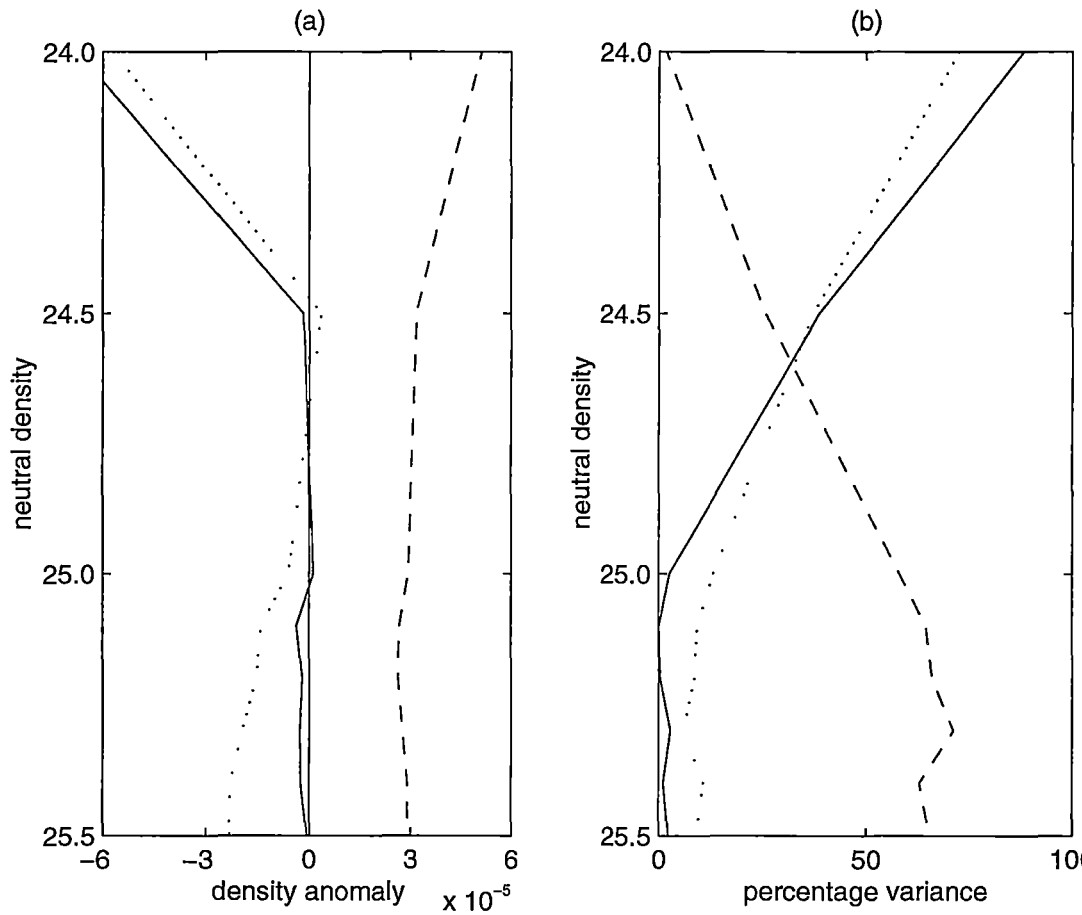

Figure 5.14: Inverse solutions averaged from 154°E to 240°E. (a) Solution to the under-determined problem. (b) Solution to the over-determined problem. See Figure 5.15 for notations.

On a basin-wide scale, *pure salinification* is seen to be statistically significant in causing the observed changes from 25.5 to 26.2 γ^n ($\approx$ 200 to 350 dbar) (Figure 5.15). This agrees with the combined observations of salinity increase on isobars and on neutral surfaces above 300 dbar. From 26.5 γ^n ($\approx$ 400 dbar) to 27.7 γ^n, Figure 5.15 shows that the effect of *pure freshening* is

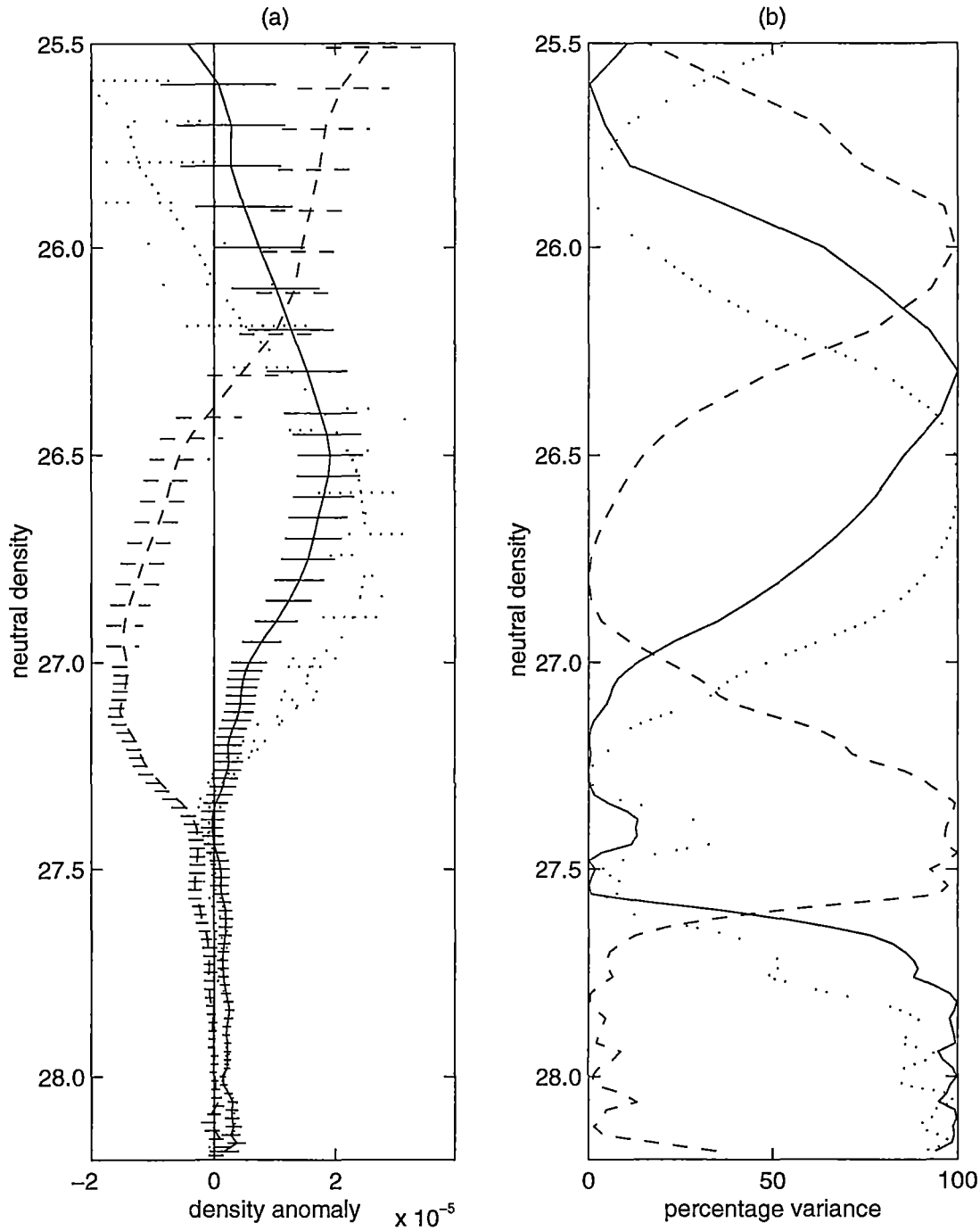

Figure 5.15: Inverse solutions averaged basin-wide from 154°E to 281°E along P21. (a) Solution to the under-determined problem: density anomaly $\rho^{-1}\rho'|_z$ contributed by each "pure" process. — denotes $\overline{\rho^{-1}\rho'|_z A^w}$, - - - denotes $\overline{\rho^{-1}\rho'|_z A^f}$, and .... denotes $\overline{\rho^{-1}\rho'|_z A^h}$. Negative anomalies indicate pure warming, pure freshening and pure downward heave respectively. Horizontal bars mark the 90% confidence intervals. (b) Solution to the over-determined problem: percentage of variance of the data explained by a single process.

present. In particular, this ventilation process explains more than 90% of the data variance in the 27.3 - 27.5 γ^n range, which encompasses the deeper part of AAIW. In the layer from 26.2 to 26.5 γ^n, solutions averaged from 220°E to 281°E (not shown), which is the extent of the South Pacific SSM, show that the SSM has undergone *pure freshening.*

The water column is seen to have been affected by *pure cooling* and *pure upward heave* from 26.1 to 27.3 γ^n (Figure 5.15 a). However, *pure upward heave* is the more significant solution from 26.5 to 27.3 γ^n. The effect of *pure cooling* is also present between 27.5 and 27.7 γ^n. Below 27.7 γ^n, temporal changes can be attributed to systematic errors.

Discussion

The implications of these temporal changes observed along the WOCE P21 section are discussed in this section in terms of five density ranges: (a) 24.5 to 26.2 γ^n; (b) 26.2 to 26.5 γ^n; (c) 26.5 to 27.0 γ^n; (d) 27.0 to 27.5 γ^n; and (e) 27.5 to 27.7 γ^n.

(a) 24.5 to 26.2 γ^n ($\approx$ 100 to 300 dbar)

Along 17.5°S, waters in the 24.5 - 26.2 γ^n range have salinity greater than 35.0 pss, and include the surface salinity maximum of SPSTW. According to Levitus (1982)'s sea surface density map for August, September and October (the austral winter months), isopycnals in the 24.5 - 26.2 γ^n range ($\approx$ 24.5 - 26.1 σ_θ) in the South Pacific outcrop along a wide zonal band between 25°S and 40°S, and at a large part of the eastern South Pacific, extending from the equator to the southern-most tip of the South American continent. However, not all sea surface salinity values in these outcropping areas exceed 35.0. The area where the 24.5 - 26.2 γ^n surfaces outcrop in the South Pacific, and where sea surface salinity exceeds 35.0, stretches from the east coast of Australia, between 25°S and 40°S, eastward and northward to the west coast of South America, between the equator and 20°S (Figure 5.16 b). This saline band of surface water is under the high evaporative cell of the South Pacific, and is considered as the origin of waters in the 24.5 - 26.2 γ^n range along P21.

Along P21, waters in the 24.5 - 26.2 γ^n range have experienced temperature and salinity increases on neutral surfaces that are consistent with the *pure salinification* ventilation scheme. This result therefore indicates an increase in sea surface salinity over their formation region. A possible cause of

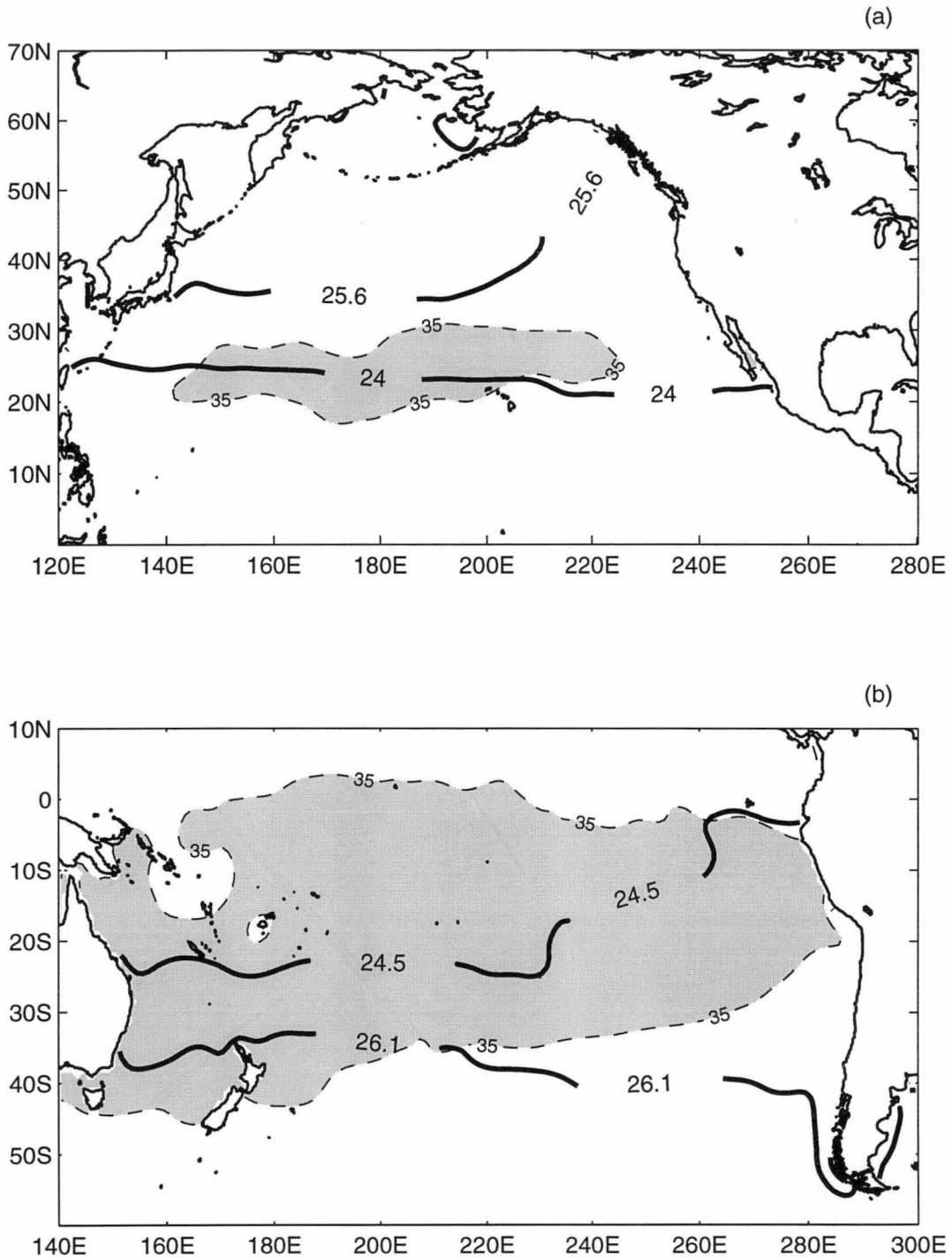

Figure 5.16: - - - Mean winter sea surface salinity (pss), and — mean winter sea surface σ_θ (kg m^{-3}), based on the dataset by Levitus (1982) for (a) northern hemisphere winter (February to April), and (b) southern hemisphere winter (August to October). The shaded regions are where mean winter sea surface salinity values exceed 35.0 pss.

this sea surface salinity increase is through an increase in E-P rate in the high evaporative cell of the South Pacific.

Note that the North Pacific equivalent of this band of saline subtropical surface water ($S > 35.0$) is of a much smaller areal extent, occupying only a narrow zonal band between 20°N and 30°N, from 140°E to 220°E (Figure 5.16 a). Along the WOCE P4 section at 10°N, waters in the 24.0 - 25.6 γ^n range, which include the shallow salinity maximum of NPSTW, have also shown temperature and salinity increases on neutral surfaces that are consistent with *pure salinification*, and which in turn suggest an increase in E-P rate in the high evaporative cell of the North Pacific. Hence there appears to be consistency between the high evaporative cells of the North and South Pacific, with the *pure salinification* signature stronger along P21 (sampled during 1994) than along P4 (sampled during 1989).

(b) 26.2 to 26.5 γ^n ($\approx$ 300 to 360 dbar)

The larger areal extent and the higher salinity of the South Pacific high evaporative cell also restrict the equatorward and westward extent of the South Pacific SSM. The shallow salinity minima of the North and South Pacific are formed in the high latitudes where surface salinity values are low. They are then carried equatorward by the eastern boundary currents: the California Current in the North Pacific, and the Peru-Chile Current in the South Pacific, before turning west along the equatorial currents. Along their advection paths, vertical mixing with the overlying layers increases their salinities, until their characteristics as shallow vertical minima are finally eliminated. Because of the weaker contribution of high-salinity waters from the North Pacific high evaporative cell, the θ-S characteristics of the North Pacific SSM are spread more westward and more equatorward than its South Pacific counterpart. The northern SSM can be observed all across the Pacific between the equator and 10°N, while the southern SSM extends westward only to about 200°E, between 8°S and 16°S (Reid 1973).

Along P21, the South Pacific SSM has experienced temperature and salinity decreases on neutral surfaces that are consistent with *pure freshening*. This indicates an increase in surface P-E rate over its source region, which is at roughly 35°S in the eastern South Pacific, off the west coast of the South American continent (north of where McCartney (1977) proposed to be the formation area of the southeast Pacific type of Subantarctic Mode Water).

Recall from Chapter 4, that the North Pacific SSM shows a strong *pure*

warming signature along P3 (24°N), but a much weakened signature along P4 (10°N). Hence while consistent processes seem to have affected the high salinity cells of the North and South Pacific, as discussed previously, the shallow salinity minima of the two oceans appear to have undergone separate θ-S property changes.

(c) 26.5 to 27.0 γ^n ($\approx$ 360 to 510 dbar)

Sectional averages show that upward displacements of neutral surfaces are statistically significant above 27.0 γ^n along P21, and the inverse solution shows that *pure upward heave* accounts for more than 50% of the data variance between 26.5 and 27.0 γ^n. In the southwest Pacific west of 180°E, between 10°S and 30°S, Ridgway and Godfrey (1996) have observed cooling of the water column on isobars above 450 dbar, between 1975-79 and 1985-89, and have interpreted this temperature decrease on isobars as due to shallowing of thermocline waters. Using MBT and XBT casts during the period between 1955 and 1988, Holbrook and Bindoff (1997) also observed cooling of the water column above 450 dbar in the same region, since the mid-1970s, that has been accompanied by a decrease of steric sea level.

By our observations along P21, the upward heave phenomenon observed previously in the southwest Pacific has continued to 1994, and extends down the water column to 500 dbar along 17.5°S. In addition, the upward heave scenario is not restricted to the southwest Pacific, but is a basin-wide phenomenon in the 26.5 - 27.0 γ^n range, at least along P21. No significant zonal variation in heave has been observed in this density range, implying that changes in the strength of the meridional transport at this level is negligible.

(d) 27.0 to 27.5 γ^n ($\approx$ 510 to 950 dbar)

In the 27.0 - 27.5 γ^n range along the WOCE P21 section is the salinity minimum layer of AAIW. Numerous theories have been proposed on the formation of AAIW. Sverdrup et al. (1946) (p.619-620) proposed that AAIW was formed circumpolarily when low-salinity surface water sank at the Polar Front and consequently mixed with the surrounding waters as it spread north. Reid (1965)'s study shows that the 80 cl/ton surface (which lies close to the AAIW salinity minimum) outcrops throughout the year between 55°S and 65°S in the South Pacific. Hence some part of AAIW may derive its characteristics from direct contact with the atmosphere, as well as from vertical diffusion of

surface properties, in the region from 55°S to 65°S (approximately where the Polar Frontal Zone is in the South Pacific). McCartney (1977) has suggested that for the South Pacific variety of AAIW, the initial formation involves cooling and overturning of Subantarctic Mode Water in the southeast Pacific. The low salinity characteristic of AAIW is then renewed within the subantarctic zone, north of the Polar Front, where precipitation exceeds evaporation.

Along P21, the AAIW layer displays statistically significant temperature and salinity decreases on neutral surfaces that are consistent with *pure freshening*. Vertical movements of the isopycnals are statistically insignificant in this density range ($< \pm 6$ dbar), and so the change in thickness of the AAIW layer along P21 is negligible.

The magnitude of the freshening is such that the observed differences on neutral surfaces could be the result of lateral "wobble" of the water mass. From the central part of the P21 section, temperature and salinity on neutral surfaces decrease southward. For example, on the 27.1 γ^n surface, where the maximum $\overline{\theta'|_n}$ and $\overline{S'|_n}$ (being 0.13°C and 0.026 pss respectively) have been observed, the meridional gradient of salinity on the neutral surface has been estimated from the historical data to be approximately 0.012 pss per 1° latitude. Thus the maximum observed freshening could be explained by a 2° latitude, or approximately 200 km, northward excursion of the water mass. However, shifting the water mass northward by 2° latitude should cause the 27.1 γ^n surface to deepen by about 25 dbar, which is inconsistent with the observation.

If the observed changes are due to altered sea surface conditions, then the result along the WOCE P21 section suggests a decrease in sea surface salinity at the formation region of South Pacific AAIW, which is the subantarctic zone, in particular the southeast Pacific, and maybe also from the region as far south as 65°S. A possible cause of sea surface salinity decrease is through an increase in P-E rate over the South Pacific subantarctic zone. Note that modified AAIW along the WOCE P4 section at 10°N has also freshened. The magnitude of freshening at 17°S is twice that at 10°N, which is consistent with the fact that at 17°S, AAIW is closer to its source than at 10°N.

AAIW in other locations of the South Pacific has also been observed to have freshened between the 1960s and the 1990s. Bindoff and McDougall (1994) found freshening in the AAIW layer along 43°S in the Tasman Sea between 1967 and 1989/90. Johnson and Orsi (1997) found freshening in AAIW along 190°E in the southwest Pacific between 1968/69 and 1990/91. Hence the signature of freshening of AAIW appears to be a large-scale phenomenon that

extends throughout the South Pacific.

On a larger scale, both intermediate salinity minima of the North and South Pacific, NPIW and AAIW, have experienced the same θ-S property changes. This reflects possible symmetric decadal or longer term changes in the precipitation patterns over the Pacific Ocean at the high latitudes in both hemispheres.

(e) 27.5 to 27.7 γ^n ($\approx$ 950 to 1300 dbar)

Waters in the 27.5 - 27.7 γ^n range along P21 have shown temperature and salinity decreases on neutral surfaces that are consistent with both *pure cooling* and *pure freshening*. Although the magnitudes of the sectionally averaged changes are within systematic errors ($\overline{\theta'|_n} < 0.018$°C, $\overline{S'|_n} < 0.003$ pss), they are statistically significant at the 90% confidence level. In the North Pacific, waters in similar density range along the WOCE P4 section at 10°N have also displayed temperature and salinity decreases on neutral surfaces that are consistent with *pure cooling* and *pure freshening*. A colder and fresher southern source could lead to the observed cooling and freshening in this density range along both P21 and P4.

5.2 Differences along the WOCE P16 section

This section discusses temporal changes observed along the final section used in this thesis: the WOCE P16 section. WOCE P16 is a meridional one-time Pacific survey whose cruise track intersects those of P21 at 17°S and P4 at 10°N. The entire P16 line consists of four sections that combine to occupy the nominal latitude of 209.5°E (150.5°W), from 60°N to 62°S. Hence the WOCE P16 section cuts through the central subtropical gyres of the North and South Pacific. At the time of writing of this thesis (July 1998), the northern-most section of the WOCE P16 line, that which runs from 60°N to 20°N, has not yet become publicly available. Hence this thesis discusses only that part of the WOCE P16 data set which stretches from 20°N to 62°S, and which consists of three sections: P16 C, P16 S and P16 A.

P16 S was carried out on board the RV *Thomas Washington* during August 1991. Its cruise track runs from 37.5°S northward to 17.5°S, and terminates at Papeete, Tahiti. It is followed immediately by P16 C during September 1991 on board the same ship. P16 C continues northward from Papeete to 19°N, and terminates at Honolulu, Hawaii, at 20°N. One year later, P16 A was carried out on board the RV *Knorr* during October 1992. The cruise track of P16 A runs from 37.5°S to 62.5°S, along the nominal longitude of 209.5°E (Figure 5.17).

The combined WOCE data set of P16 C, P16 S and P16 A (referred to as simply WOCE P16 from here on) contains 198 CTD casts. For mapping to the coordinates of these WOCE casts, 1041 historical casts that are located between 175°E and 240°E (Figure 5.17) have been selected from two climatological data sets: (1) the Reid and Mantyla Pacific data set between 27°N and 30°S, and (2) the Olbers "clean casts" between 30°S and 70°S.

These 1041 historical casts were sampled between 1928 and 1989, with the majority collected after the mid-1960s (Figure 5.18). The mean year of sampling is 1969, with the standard deviation being 10.2 years. The median year of sampling is 1968. As WOCE P16 was carried out during 1991-92, any observed differences between the mapped historical data and the WOCE data can be treated as approximately 23 $\pm$ 10 years differences.

For the historical casts that are located north of 17.5°S, the most frequent month of sampling is December. Between 17.5°S and 37.5°S, the most frequent month of sampling is also December. While south of 37.5°S, very few historical casts were sampled in the austral winter months of May and June, with the

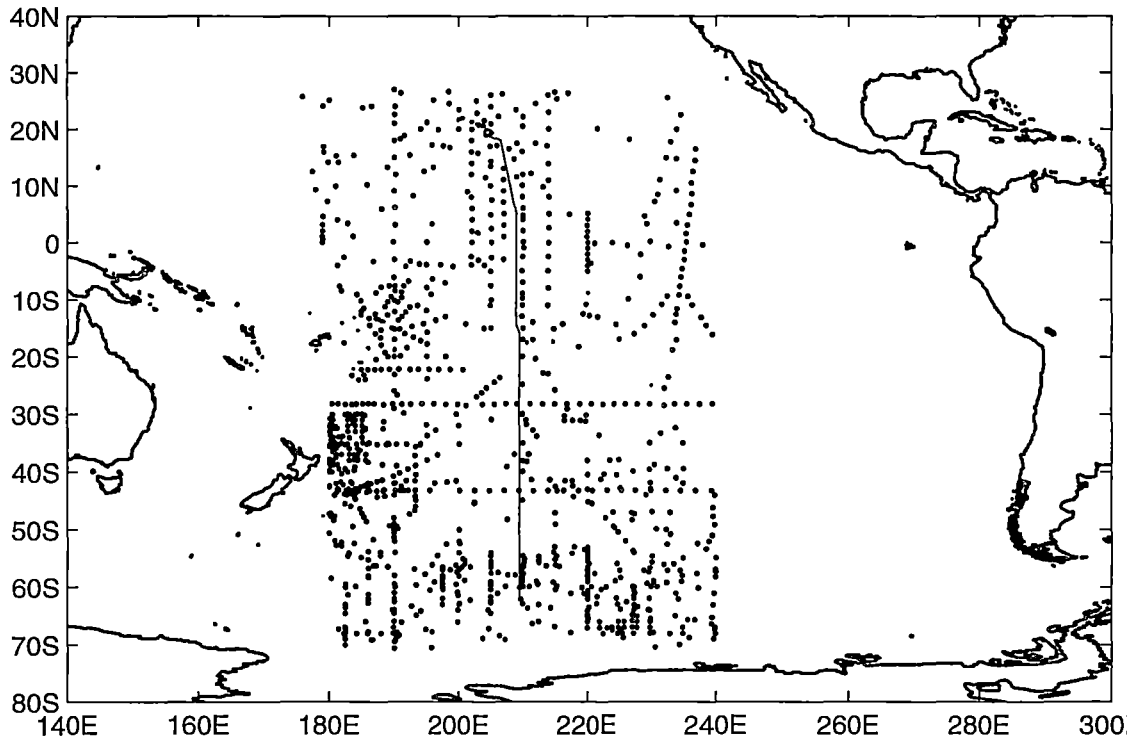

Figure 5.17: The combined cruise track of the WOCE P16 C, P16 S and P16 A sections, and the distribution of the 1041 historical data points that have been used in the mapping to the coordinates of WOCE P16.

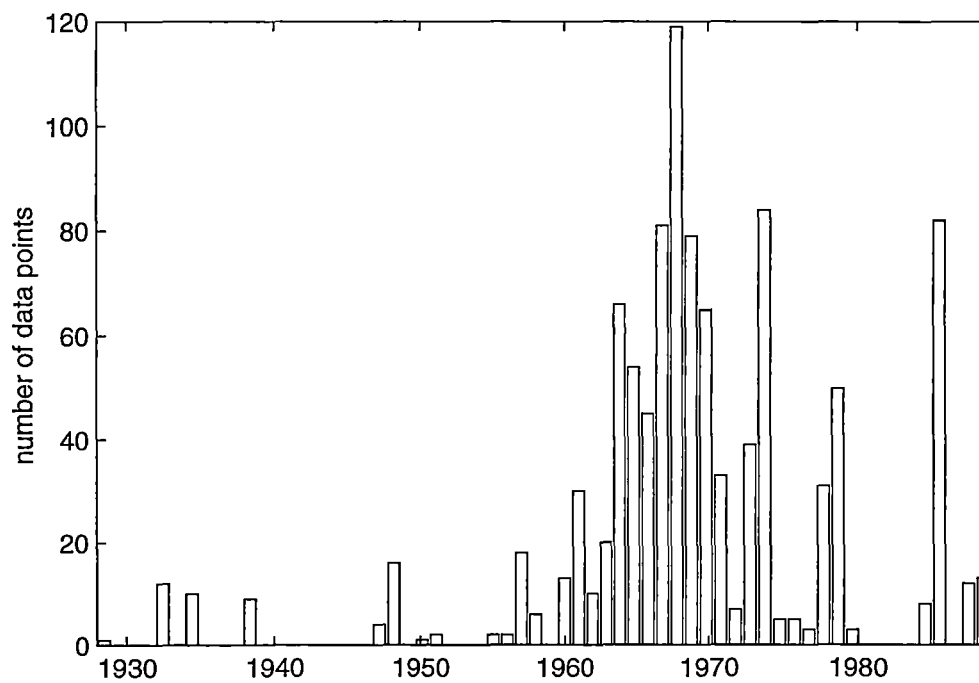

Figure 5.18: The year distribution of the 1041 historical data points used in the mapping to the coordinates of the WOCE P16 section.

most frequent month of sampling being January. Hence along the WOCE P16 section, the observed temporal changes may contain the effects of seasonal aliasing, because WOCE P16 was sampled between August and October.

The vertical salinity structure of the upper 1500 dbar along P16, based on the WOCE CTD data, is shown in Figure 5.19. North Pacific Intermediate Water (NPIW), with salinities below 34.4 (26.0 - 27.2 γ^n), is present from the northern end of the section, to as far south as 15°N. Between 20°N and 20°S, salinity structure in the top 200 dbar is complex. Two salinity maxima can be seen to extend from the sea surface, down to approximately 200 dbar. These two water masses are of subtropical origin (Wyrtki and Kilonsky 1984), formed as a result of excess surface evaporation. The southern salinity maximum, with salinity greater than 36.2, is South Pacific Subtropical Water (SPSTW), previously discussed along the WOCE P21 section along 17°S. Along P16, SPSTW outcrops between 12°S and 20°S, and spreads equatorward as a thin layer centred at 24.0 - 25.0 γ^n. The northern salinity maximum is North Pacific Subtropical Water (NPSTW), previously described as a water mass along the WOCE P4 section. Here along P16, it can be seen as a layer with salinity greater than 34.8, north of 15°N, and spreads equatorward along similar densities as SPSTW.

Wedged between SPSTW and NPSTW is a pool of low-salinity surface water ($S < 34.4$) between approximately 5°N and 15°N. This low-salinity water is a result of high local precipitation under the Intertropical Convergence Zone. Riding beneath this pool of low-salinity surface water are two relatively small-scale salinity features. The first feature is a vertical salinity minimum, centred at 13°N, 140 dbar (Figure 5.19). This is the North Pacific shallow salinity minimum (SSM), previously described as a water mass found along WOCE sections P3 and P4. Here along P16, it has salinity less than 34.4 and density between 26.0 and 26.5 γ^n. Note that the South Pacific SSM, previously described as a water mass along the WOCE P21 section, is not well-defined in Figure 5.19.

The second small-scale salinity feature is the vertical salinity maximum centred at 9°N, 200 dbar, with salinity greater than 34.7 (Figure 5.19) and density between 26.5 and 26.7 γ^n. This is 13°C Water, which is the same intermediate salinity maximum observed along the WOCE P4 section. It has been referred to as 13°C Water by Wijffels et al. (1996) because of its affinity with the 13°C thermostad in the eastern equatorial Pacific. South of the core, the salinity maximum is reduced, but intensifies again from 5°N to the equator,

as indicated by the 34.8 isohaline in Figure 5.19. This alternating pattern in the meridional structure of the intermediate salinity maximum in the equatorial Pacific has also been observed along the WOCE P17 section (Tsuchiya and Talley 1996). It is attributed to the westward recirculation, by the zonal equatorial currents, of the saline 13°C thermostad water from the east. The actual thermostad of the 13°C Water (potential temperature section not shown) is seen as a pool of water with salinity between 34.8 and 35.0, centred at 26.7 γ^n ($\approx$ 300 dbar), about 3°of latitude north and south of the equator.

South of 20°S, three main fronts are encountered along P16. The Subtropical Front, marked by a rapid salinity decrease from 35.0 to less than 34.8, is found at approximately 35 - 38°S, and can be seen to extend down to about 400 dbar. South of the Subtropical Front, surface salinity decreases southward, until a meridional minimum is reached at about 44°S, where salinity is less than 34.3. Surface salinity then increases southward from this meridional minimum, until the Subantarctic Front is reached at about 52°S. The Subantarctic Front can be seen to extend down to about 500 dbar, with salinity across the front decreasing from 34.4 to less than 34.2. Lastly, the Polar Front along P16 can be found at around 56°S.

Between the Polar Front and the Subantarctic Front, low salinity water appears to plunge from the surface layers to form the salinity minimum of Antarctic Intermediate Water (AAIW). AAIW, defined here as the tongue with salinities less than 34.4, has a core depth of about 900 dbar at 50°S, and rises to about 700 dbar at 20°S. The core density decreases from about 27.3 γ^n at 50°S, to about 27.2 γ^n at 20°S. The core potential temperature is approximately 6°C. North of the Subantarctic Front, Subantarctic Mode Water (SAMW) can be seen as a water mass with vertically homogeneous characteristics between 50°S and 30°S, overlying the AAIW layer. Along P16, SAMW has salinity between 34.4 and 34.5, and potential temperature between 7 and 8°C. Its signature pycnostad is in the 27.0 - 27.1 γ^n range, which, along P16, occupies the depths between 400 and 600 dbar.

The salinity maximum of Circumpolar Deep Water (CDW) can be seen in Figure 5.19 as a layer with salinity greater than 34.72 south of the Polar Front. It has potential temperature of less than 2°C, and density around 28.1 γ^n. Its core depth rises from about 3600 dbar at 50°S (not shown in Figure 5.19), to near the surface around Antarctica.

Figure 5.20 shows the vertical profile of neutral density in the top 1500 dbar along P16. The ridge-trough structure of isopycnals in the upper

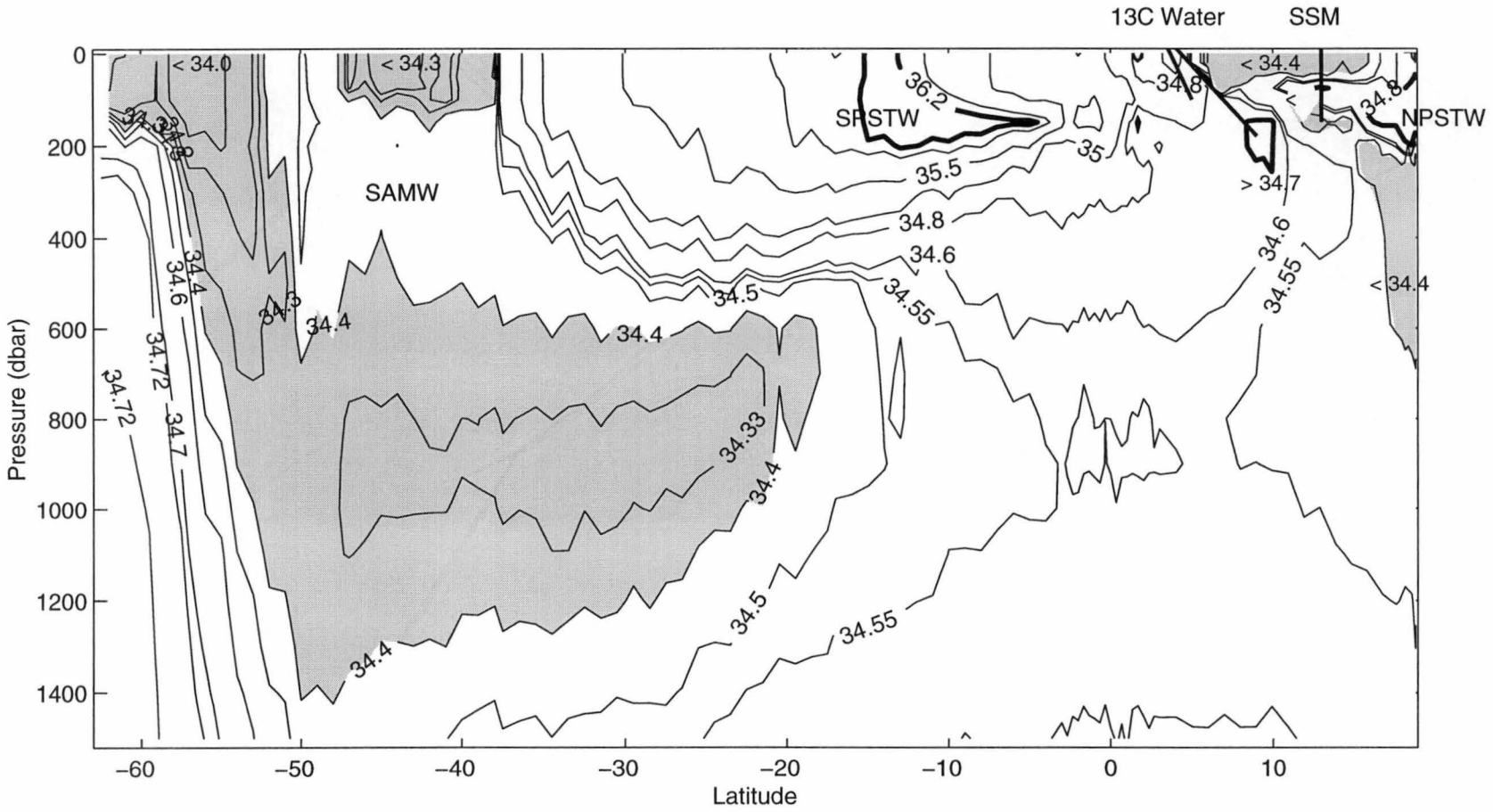

Figure 5.19: Profile of salinity (pss) for the upper 1500 dbar along 210°E, based on CTD data from the WOCE P16 section. The shaded areas are the parts of the water column with salinity less than 34.4 pss.

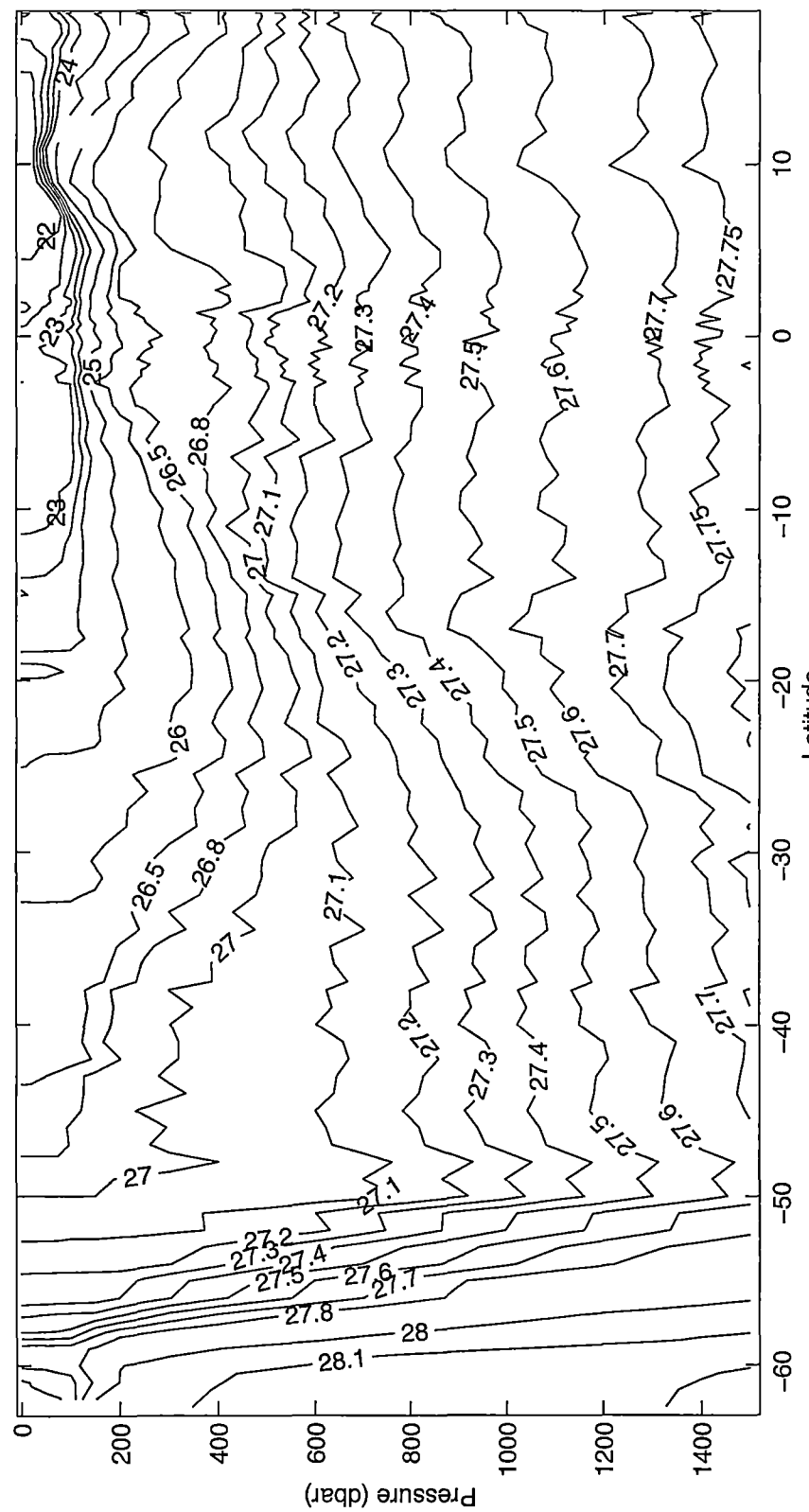

Figure 5.20: Profile of neutral density (kg m^{-3}) along 210°E, as in Figure 5.19.

200 dbar of the equatorial Pacific suggests an array of zonal equatorial currents and countercurrents (Wyrtki and Kilonsky 1984). The crest at 10°N, and the trough at 5°N, mark respectively the northern and southern boundary of the eastward-flowing North Equatorial Countercurrent. The South Equatorial Countercurrent is not as strong as its northern equivalent, and therefore does not display as prominent a ridge-trough system in the isopycnals; nonetheless, it spans the latitudes from about 5°S to 12°S along P16. North of 10°N and south of 15°S, the deepening of isopycnals are the signatures of the westward-flowing North Equatorial Current and South Equatorial Current respectively.

Along the equator, in the narrow band between 5°N and 5°S, a complex system of currents is present. The pycnostad between 200 and 400 dbar signifies the eastward-flowing Equatorial Undercurrent. Below 400 dbar, the Equatorial Intermediate Current flows west, and is flanked to the north and south respectively by the North and South Subsurface Countercurrents, both flowing east (Wyrtki and Kilonsky 1984).

South of 30°S, the pycnostad (27.0 - 27.1 γ^n) of SAMW is seen to be "wedged between the overlying primary pycnocline, which deepens equatorward, and the underlying secondary pycnocline, which shoals equatorward" (c.f. WOCE P17 section, Tsuchiya and Talley (1996)). South of 50°S, isopycnals along P16 slope downward from south to north, marking the eastward-flowing Antarctic Circumpolar Current.

North of the Polar Front, the distribution of temperature along P16 (not shown) is one of monotonic decrease with depth, with its structure closely resembling that of neutral density. The stability ratio R_ρ along P16 north of the Polar Front therefore largely reflects the vertical salinity structure. North of the equator, the presence of multiple vertical salinity minima/maxima means that the stability ratio flips between values of $R_\rho < 0$ (below a salinity minimum), and $R_\rho > 1$ (below a salinity maximum). Between the equator and the Subtropical Front, the stability ratio has a simpler structure. From the surface down to the salinity minimum of AAIW, salinity decreases with depth, so $R_\rho > 1$. Below AAIW, except for the influence of CDW at depth, salinity increases with depth to the bottom, so $R_\rho < 0$. Between the Subtropical Front and the Subantarctic Front, this simple pattern remains, with the only exception being that the presence of the meridional surface salinity minimum creates a patch at the surface (between 37°S and 47°S) where $R_\rho < 0$.

South of the Polar Front, surface temperatures are generally below 0°C. For example, at the southern-most stations along the P16 section, potential

temperature is less than -1.5°C at the surface, but increases with depth and reaches above 0°C at about 150 dbar. In the same depth range, salinity increases with depth. Hence south of the Polar Front, waters in the top 150 dbar has stability ratio $0 < R_\rho < 1$. Below this surface layer, temperature decreases with depth, while salinity increases with depth to the salinity maximum of CDW, giving $R_\rho < 0$. Antarctic Bottom Water (AABW) is seen as a cold (< 1°C), fresh bottom layer extending from the southern-most end of the P16 section, north to about 30°S, where its northward spread is blocked by a deep sea rise. Because AABW is fresher than the overlying CDW, stability ratio from the CDW layer down to the AABW layer has values $R_\rho > 1$.

Figure 5.21 shows the θ-S diagram of the water masses along P16, from the WOCE sampling during 1991-92 (Figure 5.21 a), and from the objectively mapped historical data (Figure 5.21 b). Two surface water masses show notable differences between the two time periods. The first is the surface salinity maximum of SPSTW. In the WOCE 1991-92 data, SPSTW has salinity greater than 36.2 ($\theta \approx 25.0$°C, density $\approx 24.0\,\gamma^n$, see Figure 5.21 a); in the objectively mapped historical data, the salinity of SPSTW does not reach greater than 36.2. The second is the surface salinity minimum between the Subtropical Front and the Subantarctic Front (marked by 'B' in Figure 5.21). In the WOCE 1991-92 data, this surface salinity minimum has salinity less than 34.3 (θ less than 10.0°C, density $\approx 26.5\,\gamma^n$); in the objectively mapped historical data, the salinity of this surface minimum is greater than 34.3.

There are several places along P16 where the mapped property fields fail to accurately form the required neutral surfaces between adjacent station pairs (see Chapter 3, Section 3.2.2, Equation 3.1), and where vertical inversions in the mapped pressure field are common. The most extensive area, where the mapped property fields are unrealistic, is the top 800 dbar of the water column between about 55.5°S and the Subantarctic Front ($\approx$ 52°S). Moving north away from the Subantarctic Front, the objective mapping technique provides better estimates. For example, at 49°S, inaccurately mapped property fields are found in the top 400 dbar; at 47°S, they are found in the top 200 dbar; at 43°S, only the mapped properties on neutral surfaces in the top 100 dbar are unsatisfactory. North of 42°S, except for the top 200 dbar between 27°S and 18°S, the objective estimates preserve the neutral surface definition to within instrumental error. Hence the changes observed in SPSTW (see Figure 5.21) are realistic, while the changes observed in the meridional surface salinity minimum (marked by 'B' in Figure 5.21) may not be realistic. South of 46°S, neutral surfaces below 28.0 γ^n

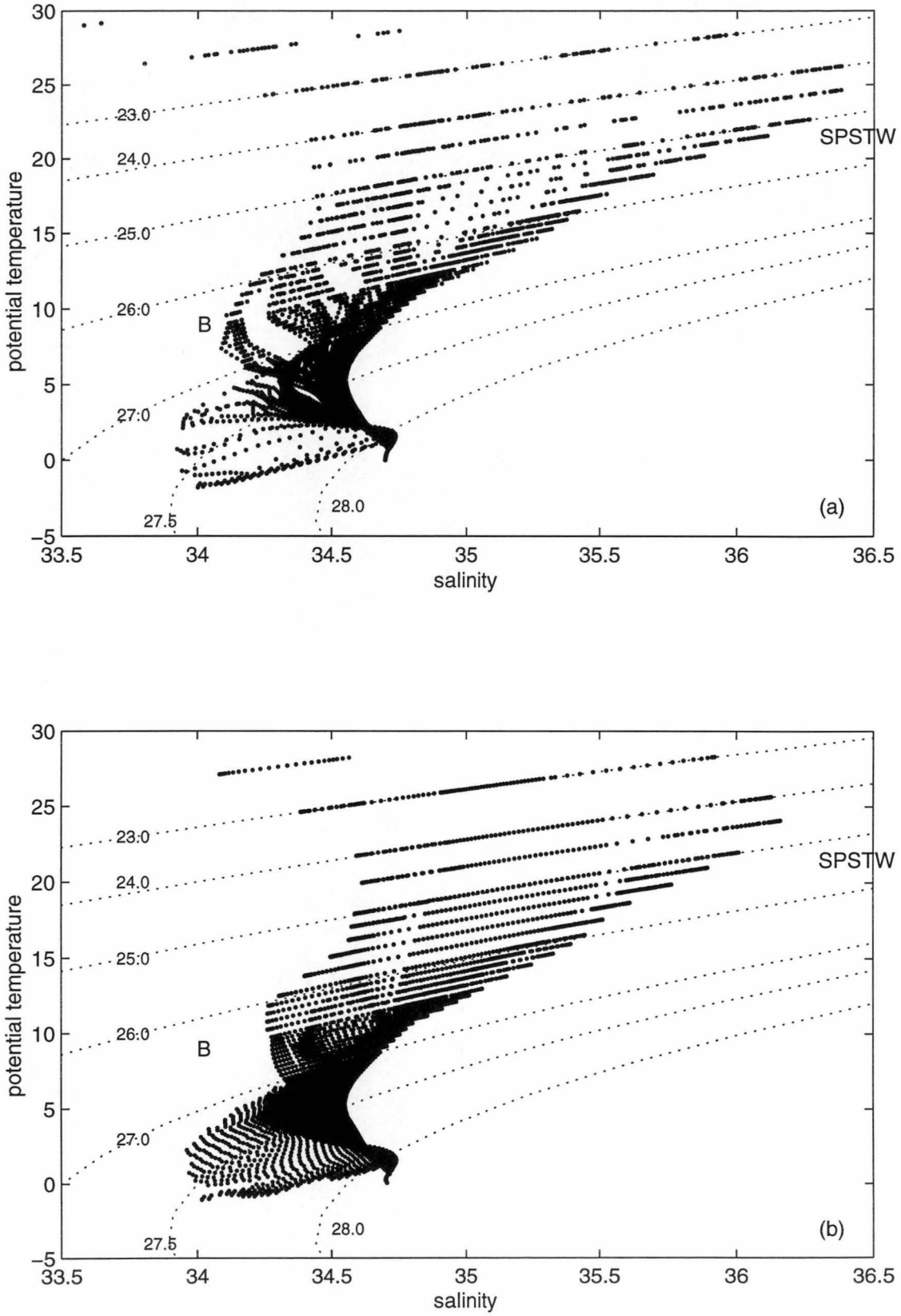

Figure 5.21: θ-S diagram on neutral surfaces along P16, (a) from the WOCE 1991-1992 section, and (b) from the historical data objectively mapped to the coordinates of P16. Lines of constant neutral density are superimposed.

(2000-3000 m, close to the bottom of the ocean there) are also prone to having vertical inversions in the mapped pressure field.

These unsatisfactory neutral surfaces are excluded from the ensuing discussion. Along the density surfaces where the objective estimates preserve the neutral surface definition to within instrumental error, the ratios of the standard deviation of the mapping residuals to that of the *a priori* noise are between 0.8 and 1.1, indicating good length scales fit in the mapping procedure.

Observed temporal changes on neutral surfaces

Figures 5.22, 5.23 and 5.24 show the differences in potential temperature, salinity and pressure on neutral surfaces (i.e. $\theta'|_n$, $S'|_n$ and N') along P16. The dashed line marks the level below which the objective estimates of θ, S and P are realistic.

North of the equator, from the surface down to 26.5 γ^n, temporal changes are dominated by temperature and salinity decrease on neutral surfaces that are above the pointwise mapping errors. South of the equator to 26°S, waters from the surface down to 26.5 γ^n, which include the surface salinity maximum of SPSTW, show temperature and salinity increase on neutral surfaces that are mostly above the pointwise mapping errors at those levels. Zonal averages taken between the equator and 17°N (Figure 5.25 a,b), and between the equator and 26°S (Figure 5.25 c,d), show that these temporal changes above 26.5 γ^n are significant at the 90% confidence levels.

South of 26°S, waters from the surface down to 27.1 γ^n, which include SAMW, show temperature and salinity decrease on neutral surfaces that are mostly above the pointwise mapping errors at those levels. In the 27.0-27.1 γ^n range (the bounding densities for SAMW), the average temperature decrease is 0.06°C, and the average salinity decrease is 0.013 pss.

On a basin-wide scale, below 27.1 γ^n, which include AAIW, the temporal pattern of change is dominated by temperature and salinity decrease on neutral surfaces, along almost the entire length of P16. The major exception is a warmed, salty patch of water that can be seen in Figures 5.22 and 5.23 to extend from the southern end of P16 northward to about 44°S, along the 27.1-27.5 γ^n range. Sectional averages between 60°S and 17°N (Figure 5.26 a,b) show that this warm, salty patch causes $\overline{\theta'|_n}$ and $\overline{S'|_n}$ to be positive between 27.3 and 27.4 γ^n, while for all other neutral surfaces below 27.0 γ^n, $\overline{\theta'|_n}$ and $\overline{S'|_n}$ are negative. 27.1-27.5 γ^n are near-surface densities at the high southern

latitudes, hence the warm, salty anomaly could be a seasonal signal, or could be an artifact of the mapping procedure, due to the sparse historical data around 50°S (see Figure 5.17). Sectionally-averaged salinity changes are statistically significant to 27.8 γ^n.

Most θ and S temporal differences in the 27.1-27.7 γ^n range are greater than the pointwise mapping errors at those levels south of 10°S. North of 10°S, almost all θ and S changes below 26.8 γ^n are below the pointwise mapping errors at those levels.

Temporal differences in pressure on neutral surfaces (N') form an incoherent spatial picture below 27.0 γ^n (Figure 5.24). Sectional averages of N' between 60°S and 17°N show that from 27.0 to 27.6 γ^n (the density range which encompasses SAMW and AAIW), the neutral surfaces have deepened, and the differences are significant at the 90% confidence levels (Figure 5.26 c). However, the temporal pressure changes are not uniform with depth. The 27.1 γ^n surface ($\approx$ 564 dbar) has deepened by 15.5 dbar, while the 27.6 γ^n surface ($\approx$ 1109 dbar) has only deepened by 2.3 dbar. This means that the AAIW layer has thinned by 13.2 dbar over the roughly 20-year period between the WOCE sampling and the mean historical period.

Above 27.0 γ^n, three spatially consistent areas of N' can be seen in Figure 5.24. From 16°N to 8°N, where the westward-flowing North Equatorial Current is found, the depths of the neutral surfaces have become shallower. From 8°N to 11°S, where the eastward-flowing North and South Equatorial Countercurrents are found, neutral surfaces have become deeper. From 11°S to 26°S, where the westward-flowing South Equatorial Current is found, neutral surfaces have again become shallower, just as its northern hemisphere counterpart.

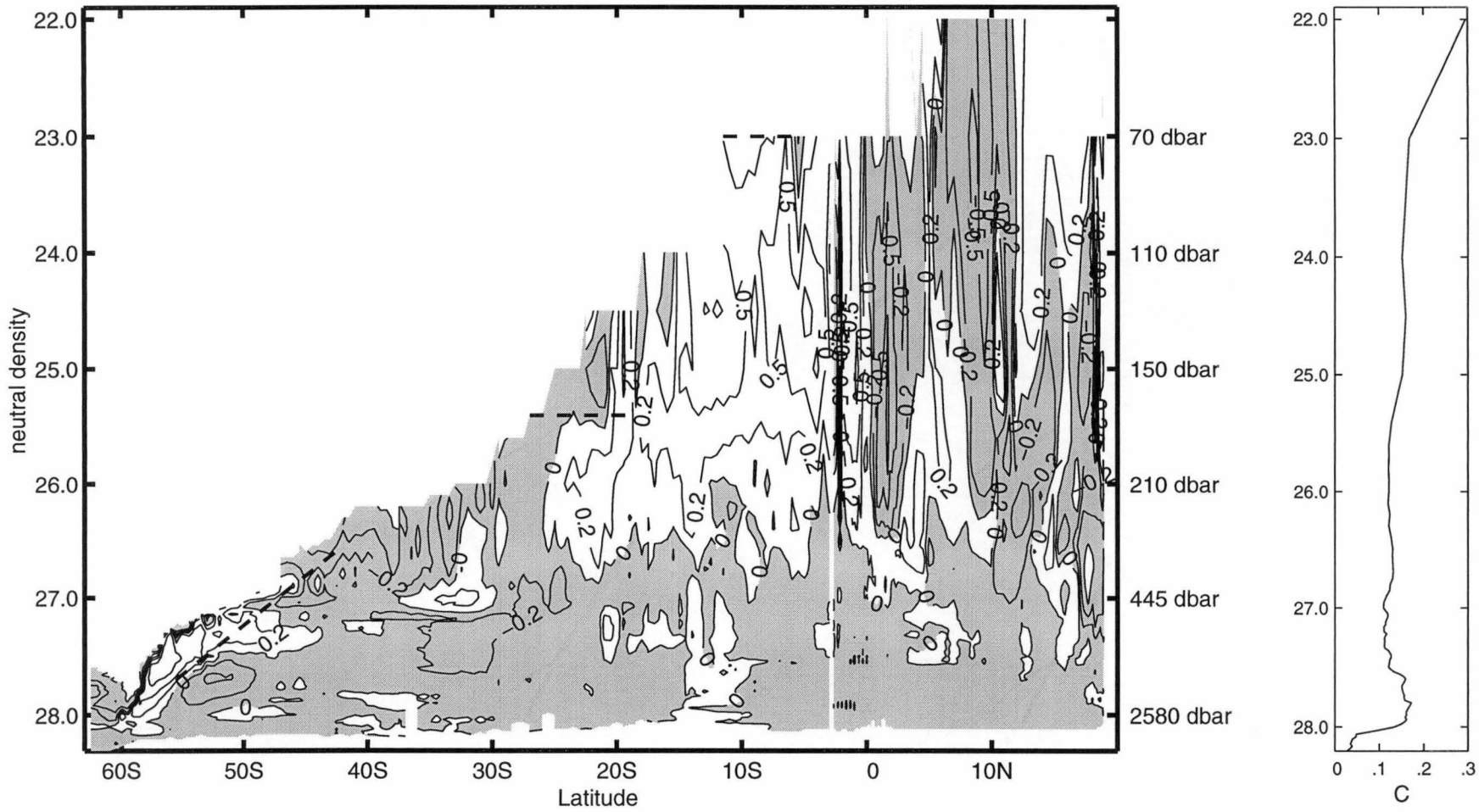

Figure 5.22: (Left) $\theta'|_n$ (°C) along P16. The shaded parts indicate areas with a temperature decrease on neutral surfaces. The average pressures of the neutral surfaces are shown in the right-hand y-axis. (Right) The right-hand panel shows the average pointwise mapping errors for θ, as a function of neutral density γ^n.

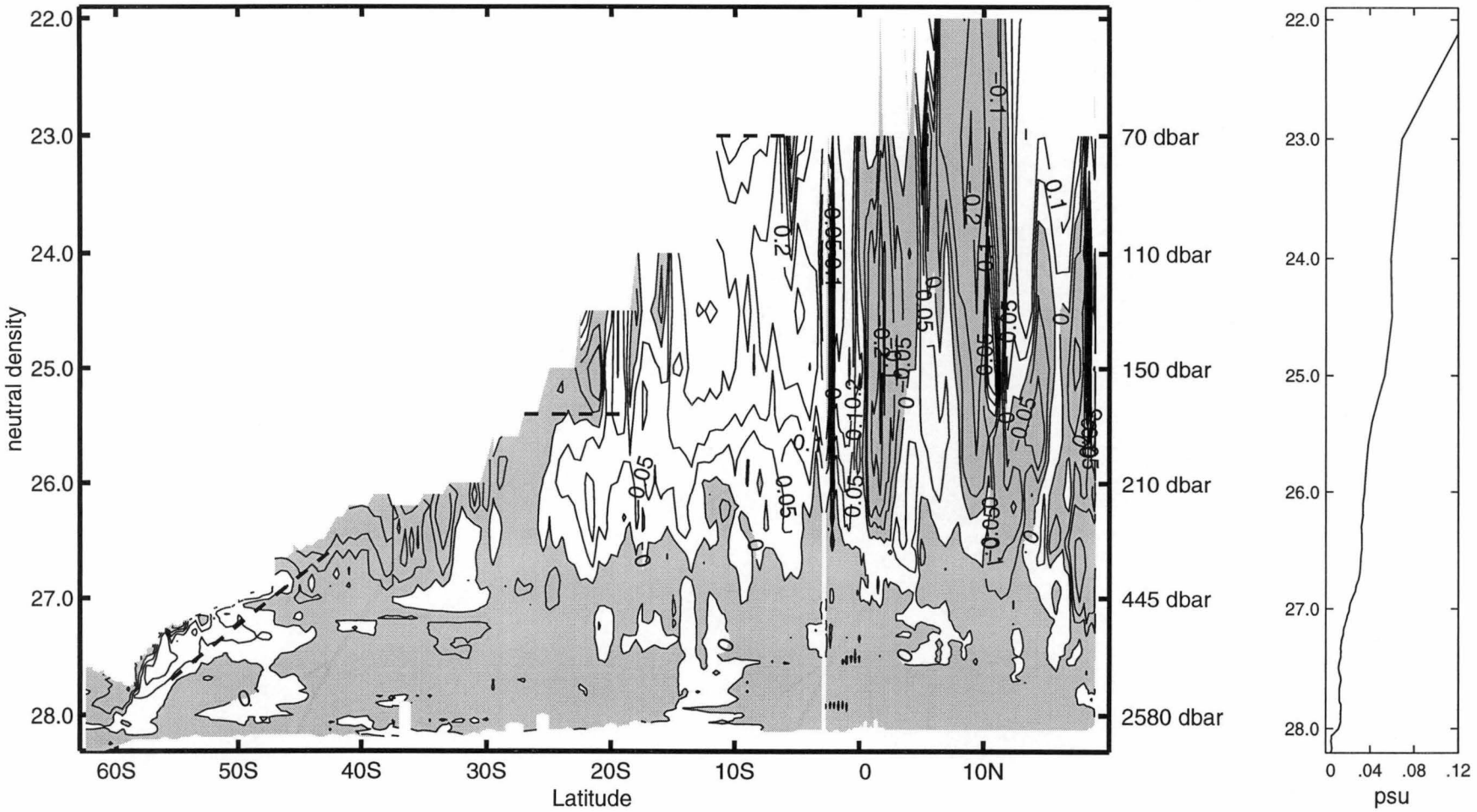

Figure 5.23: (Left) $S'|_n$ (pss) along P16. The shaded parts indicate areas with a salinity decrease on neutral surfaces. The average pressures of the neutral surfaces are shown in the right-hand y-axis. (Right) The right-hand panel shows the average pointwise mapping errors for S, as a function of neutral density γ^n.

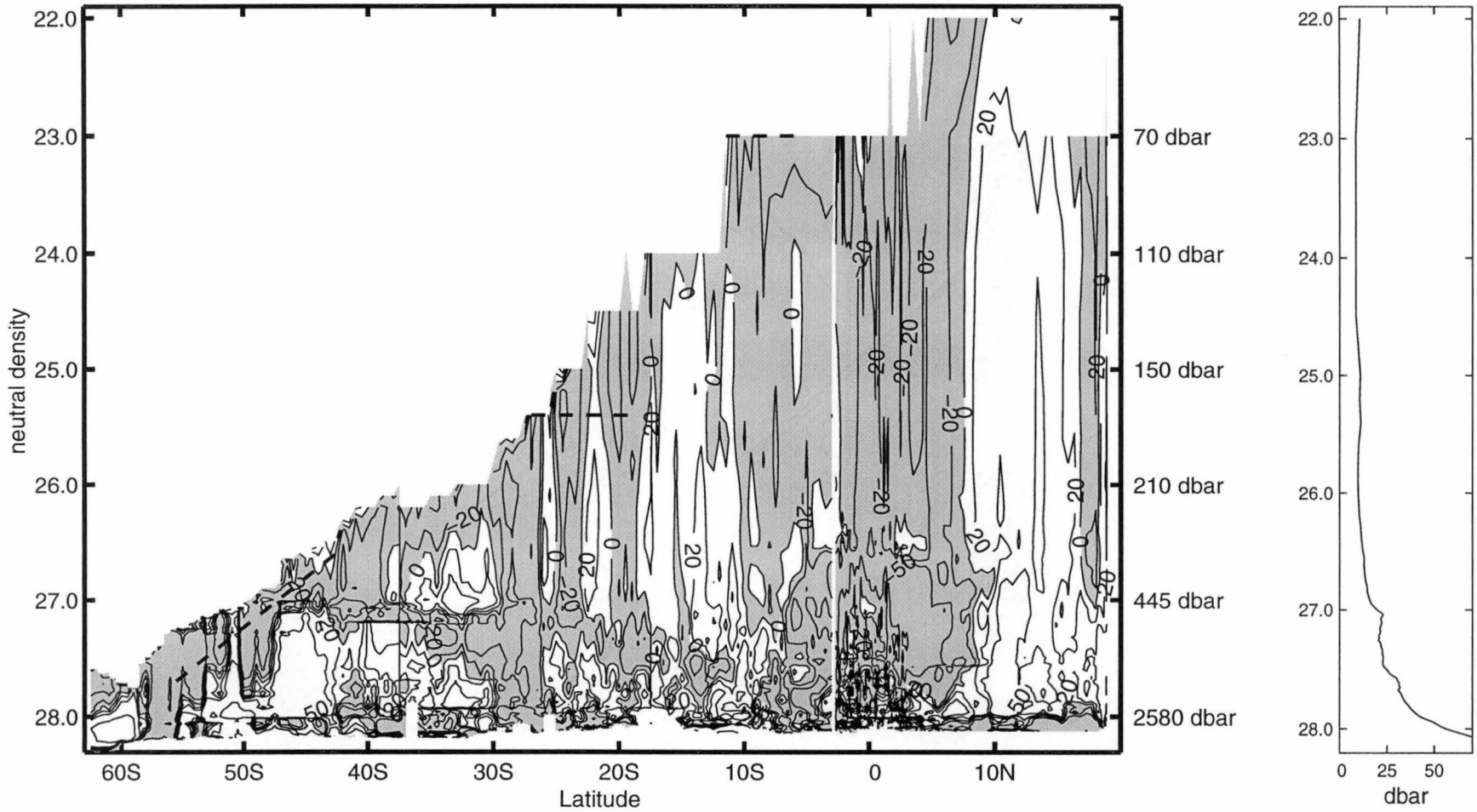

Figure 5.24: (Left) N' (dbar) along P16. The shaded parts indicate a deepening of neutral surfaces. The average pressures of the neutral surfaces are shown on the right-hand y-axis. (Right) The right-hand panel shows the average pointwise mapping errors for P, as a function of neutral density γ^n.

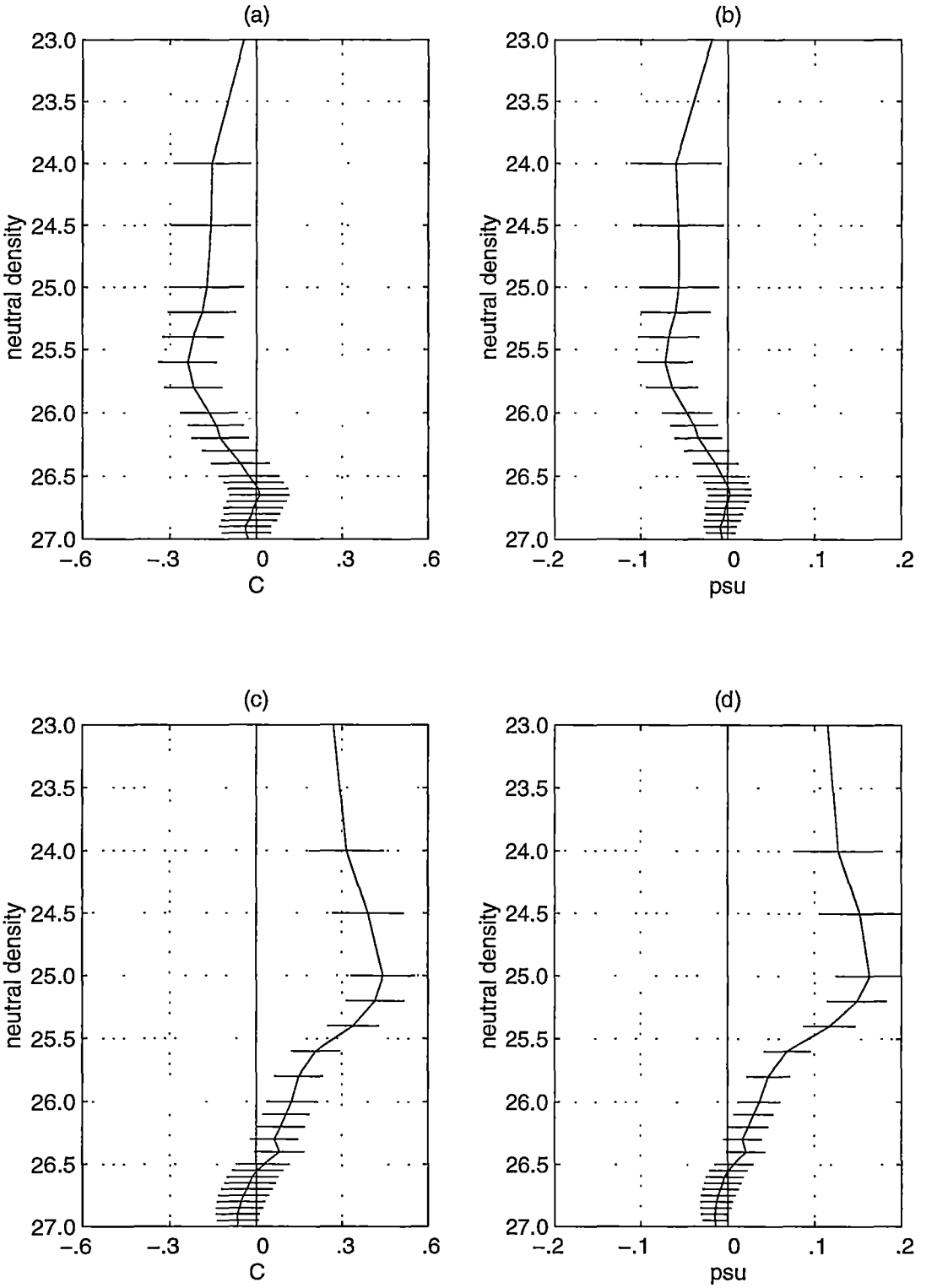

Figure 5.25: (a) and (b) $\overline{\theta'|_n}$ and $\overline{S'|_n}$ respectively, averaged along the P16 section north of the equator, from 0° to 17°N. (c) and (d) $\overline{\theta'|_n}$ and $\overline{S'|_n}$ respectively, averaged along the P16 section south of the equator, from 0° to 26°S. Horizontal bars indicate 90% confidence intervals.

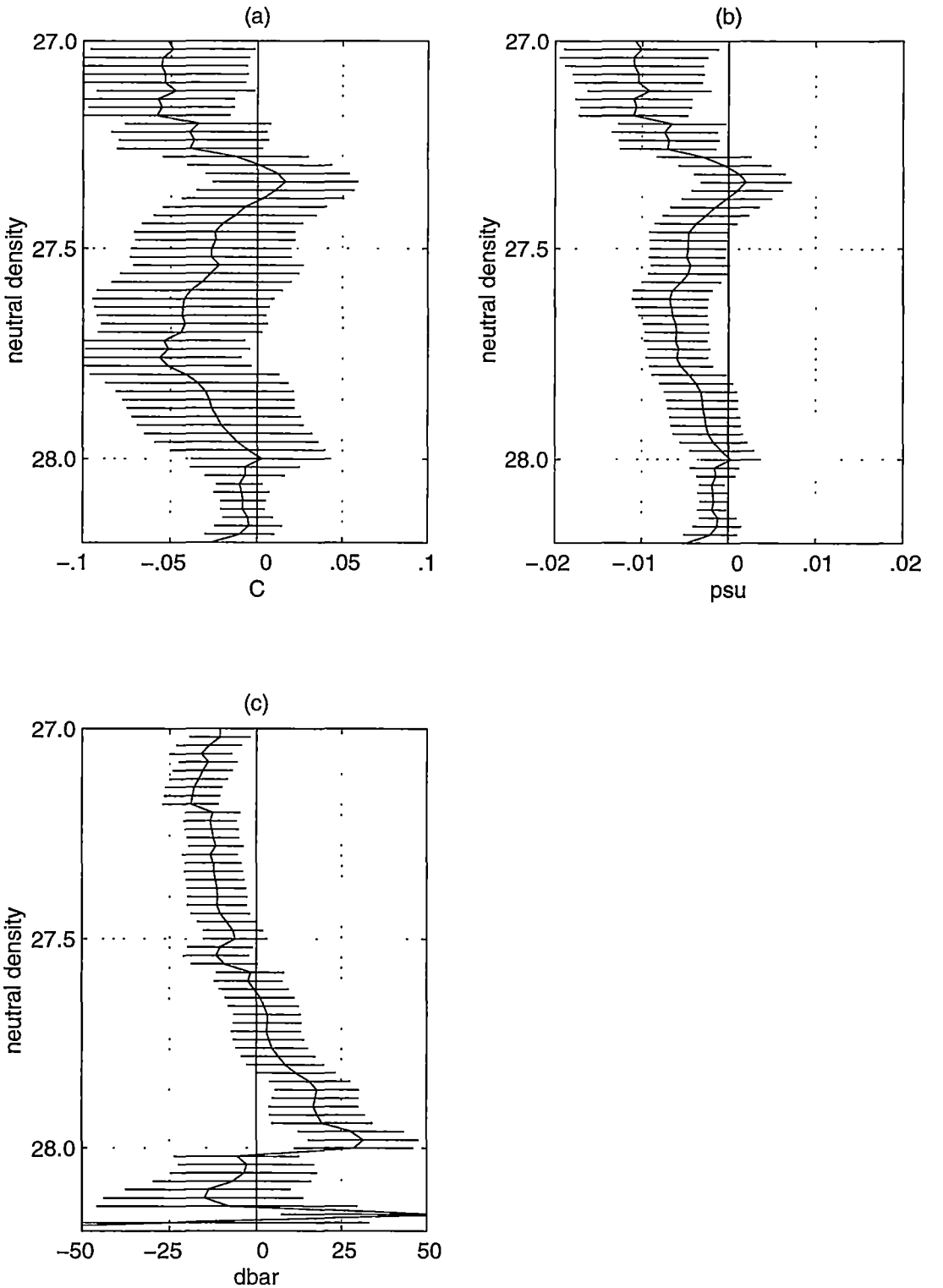

Figure 5.26: Sectional averages between 60°S and 17°N along P16. Horizontal bars indicate 90% confidence intervals. (a) $\overline{\theta'|_n}$, (b) $\overline{S'|_n}$, and (c) $\overline{N'}$.

Observed temporal changes on isobars

Temporal changes in temperature and salinity on isobars (i.e. $\theta'|_z$ and $S'|_z$), for the upper 1500 dbar along P16, are shown in Figure 5.27. Between 200 and 700 dbar, the spatial pattern of temperature change on isobars ($\theta'|_z$) resembles that of pressure change of neutral surfaces (N'). From 16°N to 8°N, and from 11°S to 26°S, where neutral surfaces are seen to have become shallower, cooling on isobars is evident (Figure 5.27 a). Between 8°N and about 11°S, where neutral surfaces have deepened, warming on isobars can be seen. On a basin-wide scale, sectional averages on isobars from 60°S to 17°N show that the top 1000 dbar of the water column along P16 has warmed in general, and are mostly above the 90% confidence levels (Figure 5.28 a). This average warming on isobars corresponds to the average deepening of neutral surfaces to 27.6 γ^n (Figure 5.26 c).

The spatial pattern of salinity change on isobars is more akin to the water mass distribution along P16. South of the equator to 26°S, the top 200 to 400 dbar show salinity increase on isobars. This part of the water column encompasses the surface salinity maximum of SPSTW, and so has stability ratio greater than 1. Therefore the combined observations of salinity increases on neutral surfaces and on isobars suggest that SPSTW along P16 has undergone θ-S changes that are consistent with the *pure salinification* scenario.

North of about 8°N, the top 600 dbar of the water column exhibits freshening and cooling on isobars. Here, four water masses are found: the surface salinity maximum of NPSTW, the North Pacific SSM, 13°C Water, and NPIW. When combined with the observation of salinity decrease on neutral surfaces, these changes are consistent with these four water masses, identifiable as salinity extrema, having undergone *pure freshening.*

From approximately 30°S to 50°S, SAMW occupies the water column from about 300 to 600 dbar. Freshening on isobars can be seen in Figure 5.27 (b) to dominate the SAMW area, which has stability ratio greater than 1. The combined observations of salinity decreases on neutral surfaces and on isobars in SAMW are therefore consistent with it having undergone *pure freshening.* Moreover, the average warming on isobars in this area (average plot not shown) suggests that SAMW along P16 has undergone *pure warming* as well.

On a basin-wide scale, sectional averages from 60°S to 17°N show that from 800 to 1500 dbar along P16, salinity values on isobars have decreased in general, and are significant at the 90% confidence levels (Figure 5.28 b). The 800-1500 dbar depth range ($\approx$ 27.2-27.7 γ^n) encompasses the AAIW layer along

P16. The stability ratio in this depth range flips from greater than 1 above the salinity minimum, to less than 0 below the salinity minimum. Hence the combined salinity decreases on neutral surfaces and on isobars along the entire AAIW layer are consistent with AAIW along P16 having undergone *pure freshening*. Moreover, the basin-wide warming in the top 1000 dbar along P16 suggests that the part of the AAIW layer above the salinity minimum has undergone *pure warming* as well.

South of 50°S, temporal differences on isobars are dominated by cooling of the water column between 1000 to 3000 dbar ($\approx$ 27.86 - 28.3 γ^n, not shown in Figure 5.27). This is the depth range of the CDW layer along P16. Combined with temperature and salinity decrease on the corresponding neutral surfaces, CDW along P16 therefore seems to have undergone changes that are consistent with *pure cooling*.

The relative strengths of each of the three processes in causing the observed temporal changes are discussed in the following section in terms of the inverse solutions.

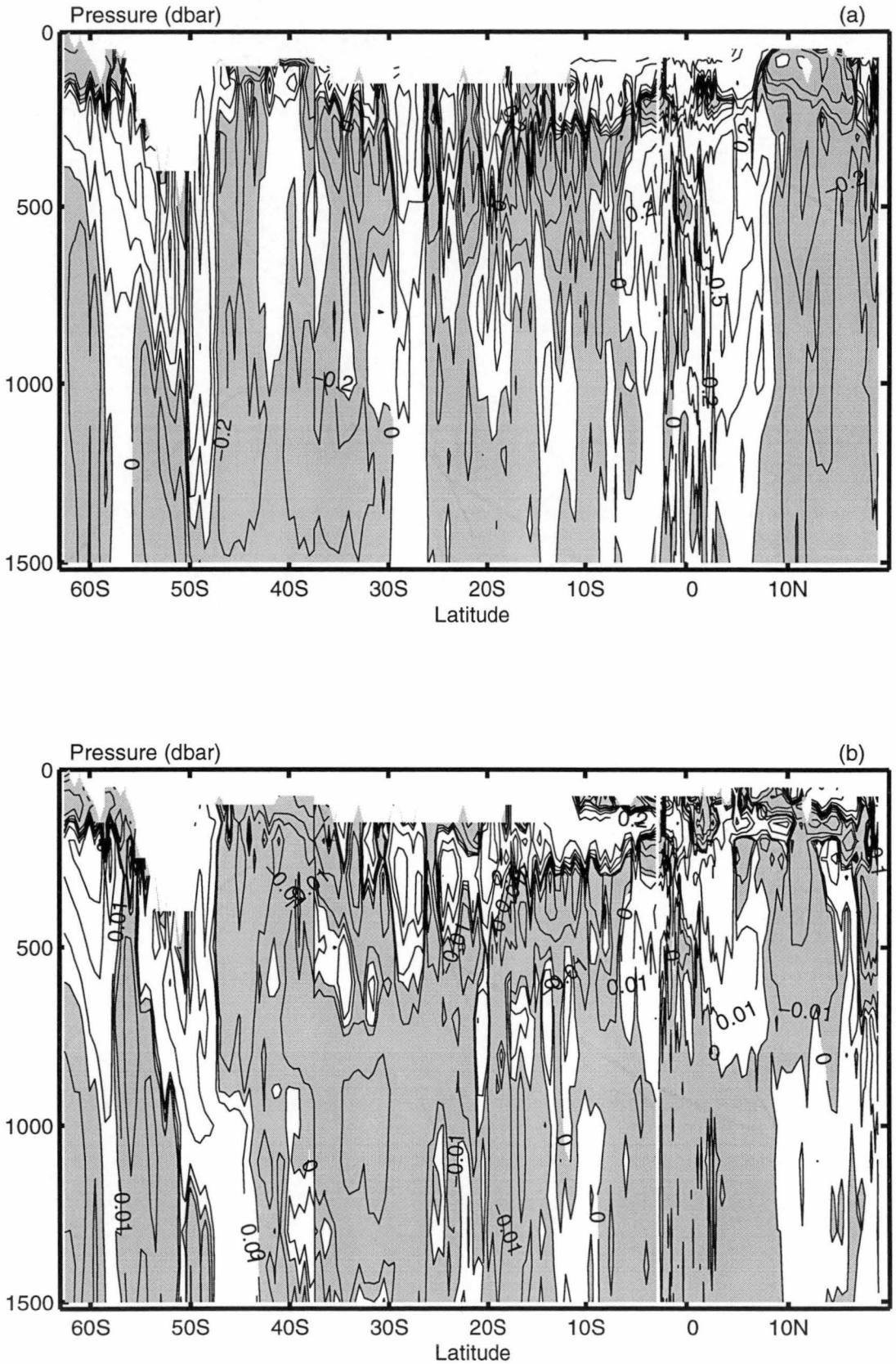

Figure 5.27: (a) $\theta'|_z$ (°C), and (b) $S'|_z$ (pss) for the upper 1500 dbar along P16. Shaded parts indicate areas with temperature and salinity decrease on isobars.

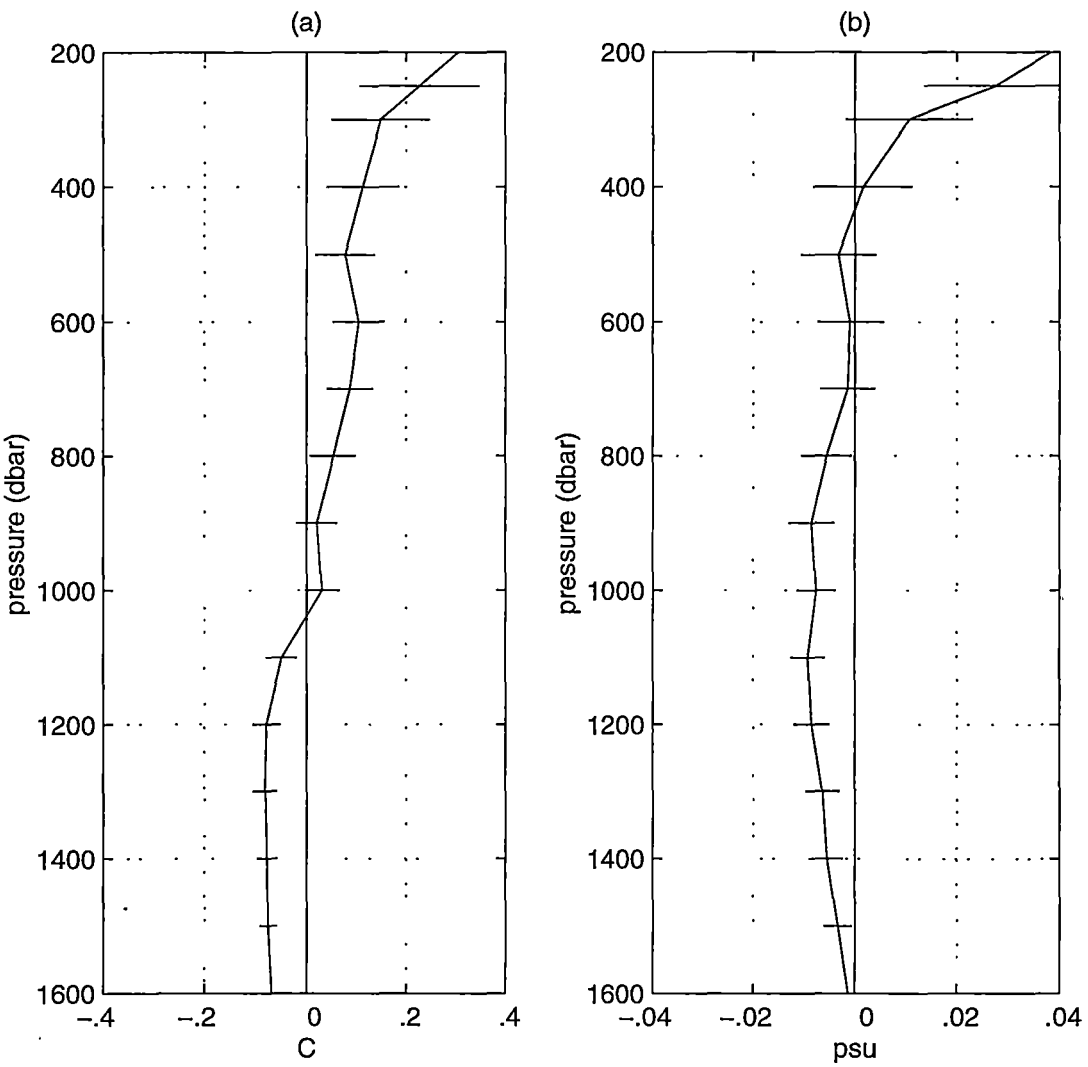

Figure 5.28: (a) $\overline{\theta'|_z}$ (°C), and (b) $\overline{S'|_z}$ (pss), averaged between 60°S and 17°N along P16. Horizontal bars indicate 90% confidence intervals.

Solutions to the inverse problem

Because of the meridional variation in the pattern of temporal changes along the WOCE P16 section in the shallow layers, and because the shallow densities do not extend along the full length of P16, the inverse solutions are discussed first for the water column above 26.5 γ^n. Figure 5.29 shows the inverse solutions that have been averaged over the section north of the equator from 0 to 17°N, and south of the equator from 0 to 26°S.

North of the equator, the presence of multiple vertical salinity maxima/minima in the top 200 dbar ($\approx$ 26.5 γ^n) means that the stability ratio often attains values that approach infinity. Hence the decomposition approach cannot distinguish between *pure cooling* and *pure heave*, i.e. $\rho^{-1}\rho'|_z A^w$ and $\rho^{-1}\rho'|_z A^h$, as is evident in Figure 5.29 (a). Nonetheless, the effect of *pure freshening* is present in the 24.0 - 26.5 γ^n range north of the equator. Within this density range are four water masses: NPSTW, the North Pacific SSM, 13°C Water, and NPIW. For NPIW along P16, the effect of *pure freshening* persists to 27.2 γ^n (not shown).

South of the equator to 26°S, Figure 5.29 (c) shows that the effect of *pure salinification* is present from 24.5 to 26.5 γ^n, which includes SPSTW, but is curiously absent in its contribution to the percentage variance (Figure 5.29 d). On the other hand, *pure downward heave* is a strong process in this density range, and explains more than 80% of the data variance to 26.3 γ^n.

At the SAMW layer along P16, solutions averaged from 26°S to 50°S (not shown) show that *pure warming* and *pure freshening* are the two stronger processes in causing the observed θ-S changes in the 27.0 - 27.2 γ^n range, and explain more than 90% of the data variance.

Along the entire length of P16, Figure 5.30 shows that the AAIW layer (27.1 - 27.6 γ^n) has experienced *pure downward heave*. In addition, *pure warming* is the strongest process in causing the observed changes in the 27.1 - 27.4 γ^n range, while *pure freshening* is the dominant process in the 27.4 - 27.6 γ^n range. From 27.6 to 27.8 γ^n, the effects of *pure freshening* and *pure cooling* are present. Below 27.8 γ^n, temporal changes are not statistically significant and are considered as due to systematic errors.

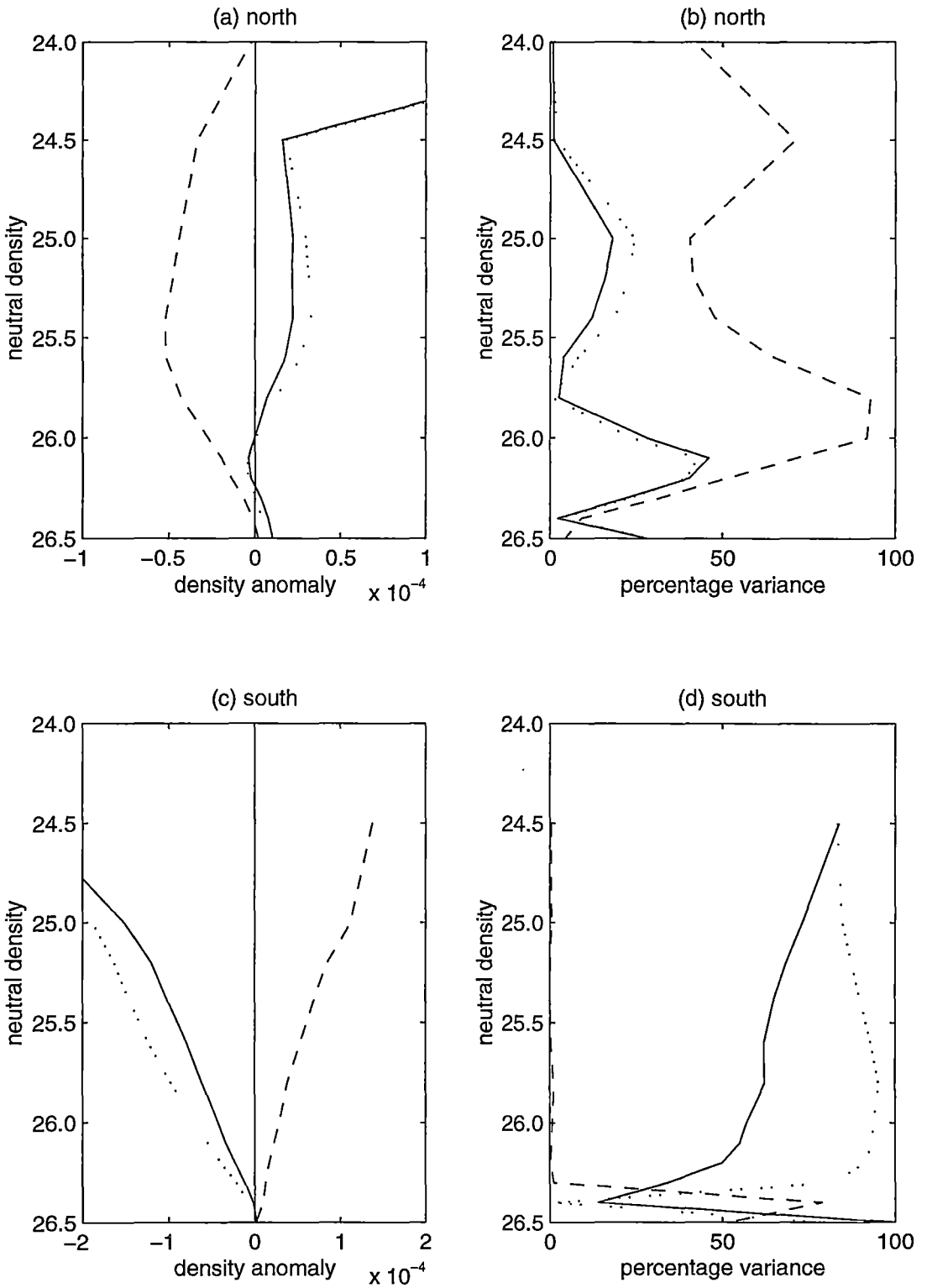

Figure 5.29: Inverse solutions averaged from 0 to 17°N ('north'), and from 0 to 26°S ('south'), along P16. (a) and (c) Solution to the under-determined problem: density anomaly $\rho^{-1}\rho'|_z$ contributed by each "pure" process. — denotes $\overline{\rho^{-1}\rho'|_z A^w}$, - - - denotes $\overline{\rho^{-1}\rho'|_z A^f}$, and .... denotes $\overline{\rho^{-1}\rho'|_z A^h}$. Negative anomalies indicate pure warming, pure freshening and pure downward heave respectively. (b) and (d) Solution to the over-determined problem: percentage of variance of the data explained by a single process.

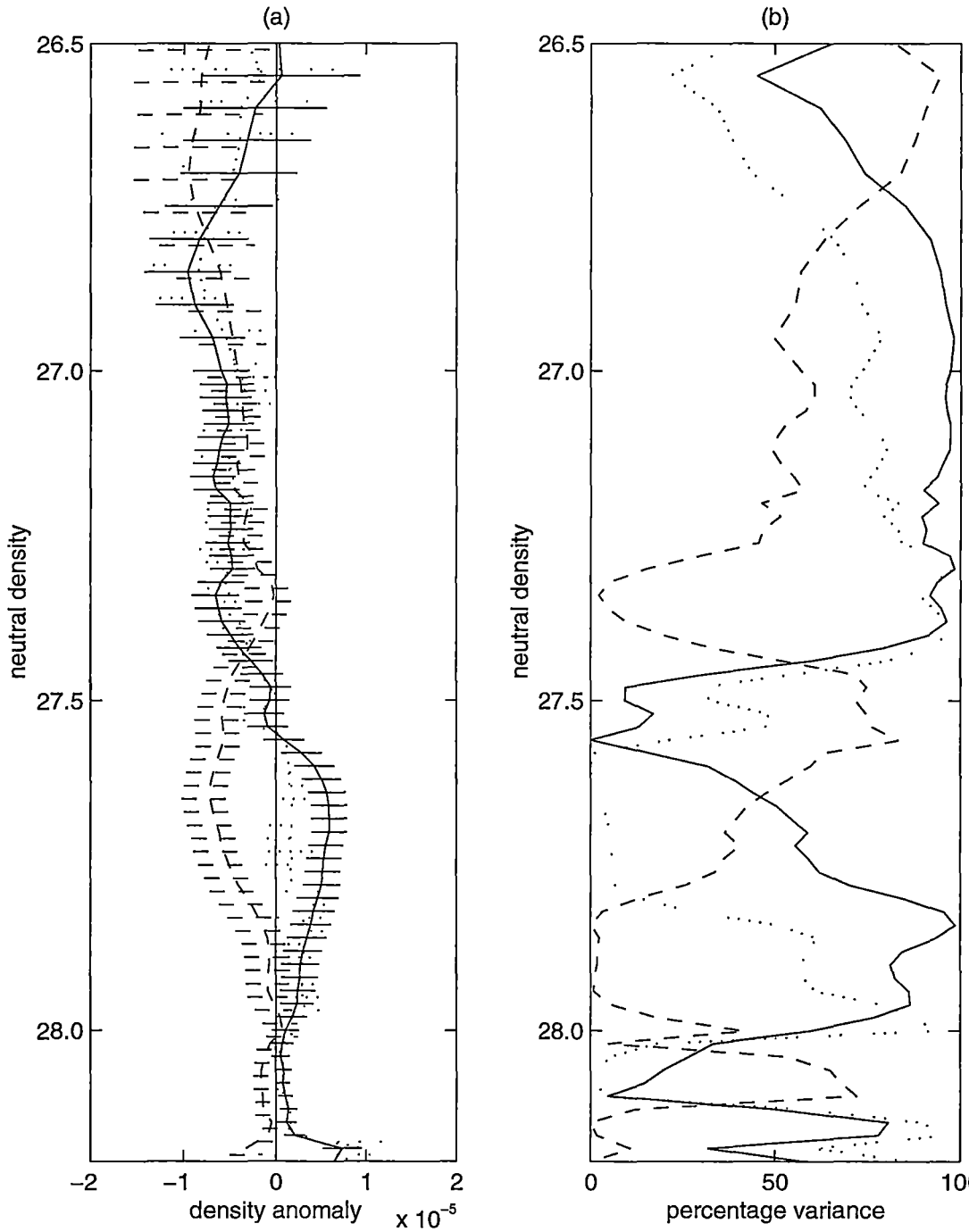

Figure 5.30: Inverse solutions averaged basin-wide from 60°S to 17°N along P16. (a) Solution to the under-determined problem, and (b) solution to the over-determined problem, as in Figure 5.29. Horizontal bars in (a) mark the 90% confidence intervals.

Discussion

The implications of the observed temporal changes along the WOCE P16 section are discussed in this section in five density ranges: (a) 24.0 to 27.2 γ^n north of the equator; (b) 24.5 to 26.5 γ^n south of the equator; (c) 26.5 to 27.1 γ^n south of the equator; (d) 27.1 to 27.6 γ^n; and (e) 27.6 to 27.8 γ^n.

(a) 24.0 to 27.2 γ^n north of the equator ($\approx$ 100 to 650 dbar)

Four water masses that are identifiable as salinity extrema are found in the 24.0 - 27.2 γ^n range north of the equator along the 210°E meridian. They are NPSTW, the North Pacific SSM, 13°C Water, and NPIW. These four water masses are also present along the North Pacific WOCE sections of P3 (24°N) and P4 (10°N). Here along the WOCE P16 section, all four of these water masses display temporal changes that are consistent with *pure freshening.* However, apart from NPIW, this freshening signature along P16 in these water masses do not agree with the observations from P3 and P4.

Temporal changes in NPSTW at 24°N are not discussed because of unreliable objective estimates there, while at 10°N, NPSTW displays changes that suggest *pure salinification.* For the North Pacific SSM along 24°N, *pure warming* is the dominant process in explaining the data, while along 10°N, *pure heave* dominates the observation. 13°C Water is present along 10°N, and shows signs of *pure warming* at that latitude. On the other hand, NPIW has shown consistent temporal changes along 24°N, 10°N, and 210°E. Table 5.1 summarizes these results.

WOCE sections (year)	NPSTW	North Pacific SSM	13°C Water	NPIW
P3 at 24°N (1985)		pure warming		pure freshening
P4 at 10°N (1989)	pure salinification	pure heave	pure warming	pure freshening
P16 at 210°E (1991-92)	pure freshening	pure freshening	pure freshening	pure freshening

Table 5.1: The ventilation processes that best describe the temporal changes observed in the four water masses (all identifiable as salinity maxima) that are common along the WOCE sections of P3, P4 and P16.

A possible explanation for why the results for NPSTW, the North Pacific

SSM, and 13°C Water along P16 are different from those along P3 and P4 is that 1991-92 is an El Niño period, and 1985 and 1989 are not. Because these three water masses are found close to the equatorial region, and in the top 200 dbar of the water column along the 210°E meridian, their temporal changes as observed along P16 are likely to contain the effects of the 1991-92 El Niño event. Indeed, all three water masses: NPSTW, North Pacific SSM, and 13°C Water, show signs of *pure freshening* along P16, which are consistent with increased precipitation in the central equatorial Pacific during an El Niño event. On the other hand, along the 210°E meridian, NPIW is found north of 15°N and below 200 dbar. Hence the temporal θ and S changes observed in NPIW along P16 are not likely to have been affected by the 1991-92 El Niño event, and so agree with the changes observed along P3 and P4.

Between 8°N and 16°N, where the westward-flowing North Equatorial Current (NEC) is found, shoaling of neutral surfaces (or cooling of the water column) have also been observed. However, this observation is not supported by congruous results from P3 and P4. Between 8°N and 11°S, where the Equatorial Undercurrent and the Equatorial Intermediate Current are found, the deepening of neutral surfaces (or warming of the water column) is probably due to interannual variability in the equatorial region.

(b) 24.5 to 26.5 γ^n south of the equator ($\approx$ 150 to 350 dbar)

The surface salinity maximum of SPSTW is found in the 24.5 - 26.5 γ^n range along P16, and is also present along the WOCE P21 section at 17°S. Waters in this density range in both the WOCE P16 (1991-92) and P21 (1994) sections display temporal changes that are consistent with *pure salinification.* Note that both 1991-92 and 1994 are El Niño periods. However, unlike NPSTW, which displays a freshening signature in an El Niño year relative to the historical data, SPSTW shows a consistent salinification signature.

As discussed previously for the WOCE P21 section, waters in this density range have their origin under the high evaporative cell of the South Pacific. The combined results from P16 and P21 therefore reinforce the implication that the high evaporative cell of the South Pacific has undergone an increase in E-P rate. Note that Kessler (in press) has also observed a general rise in salinity in the high salinity tongue on 24.5 σ_t during the 1990s, between 10°N and 10°S, along 165°E, 180°and 155°W. However, the inferred subducted variability from the ventilation region was found to be inconsistent with the oberved downstream salinity changes.

(c) 26.5 to 27.1 γ^n south of the equator ($\approx$ 350 to 600 dbar)

Waters in the 26.5 - 27.1 γ^n range south of the equator along P16 has undergone θ-S property changes that are consistent with *pure freshening* and *pure warming*. A water mass of particular interest here is SAMW (27.0 - 27.1 γ^n). Note that Bindoff and Church (1992) and Johnson and Orsi (1997) have also observed the same θ-S property changes in SAMW in the southwest Pacific. Together these results imply surface warming and freshening in the subantarctic zone, where SAMW is ventilated.

Apart from θ-S property changes, neutral surfaces in this density range between 11°S and 26°S display significant upward movements. This is the area where the westward-flowing South Equatorial Current (SEC) is found, but the affected neutral surfaces reach deeper than the SEC. This shoaling of neutral surfaces has also been observed along the WOCE P21 section at 17°S, and in the southwest Pacific by Ridgway and Godfrey (1996) and Holbrook and Bindoff (1997) as a cooling of the water column.

(d) 27.1 to 27.6 γ^n ($\approx$ 560 to 1110 dbar)

Underlying the SAMW pycnostad along P16 is the salinity minimum of AAIW, occupying the density range 27.1 to 27.6 γ^n. Same as SAMW, temporal differences along P16 show that AAIW has undergone θ-S changes that are consistent with *pure warming* and *pure freshening*.

The AAIW layers along P21 and P4 have also displayed changes that are consistent with *pure freshening*, but those changes could be explained by shifting the water mass northward at 17°S, and southward at 10°N. The results along the 210°E meridian show that the salinity decreases in the AAIW density range observed along P21 and P4 are not restricted to those two latitudes, but extend meridionally through the Pacific from about 50°S to north of the equator. Because this salinity decrease is a coherent basin-wide signature, it is more likely due to long-term θ-S property changes in AAIW, than due to lateral movements of the water mass. Note that freshening in the AAIW layer has also been observed in the southwest Pacific by Bindoff and Church (1992) and Johnson and Orsi (1997). There are therefore strong implication that the source region of AAIW, which is the subantarctic zone in the Southern Ocean, has experienced a decrease in surface salinity, possibly as a result of an increase in P-E rate.

(e) 27.6 to 27.8 γ^n ($\approx$ 1110 to 1490 dbar)

Waters between 27.6 and 27.8 γ^n along P16 show statistically significant salinity decreases on neutral surfaces that are consistent with *pure cooling* and *pure freshening*. Waters in similar density range along P21 and P4 have also displayed the same θ and S changes. Moreover, Swift (1995) has observed cooling of the deep water along the south end of the WOCE P17 meridional section (135°W), and has concluded that this change is not due to a north-south shift in the water masses, but is a θ-S characteristic change that is probably connected to Ross Sea processes. These observations all point to a fresher and colder source of deep water.

5.3 Summary and Discussion for the South Pacific Ocean

Summary of observed temporal changes

This chapter has discussed temporal changes along two modern WOCE CTD sections in the South Pacific Ocean: the zonal P21 section at 17°S, and the meridional P16 section at 210°E. Because P16 intersects P4 (10°N) and P21 (17°S), and has water masses in common with P3 (24°N), it provides added evidence of water mass changes observed along the other transects.

Table 5.2 summarizes the observed changes in the major water masses in the South Pacific Ocean along P21 and P16, and lists the surface processes that most consistently explain the obseved temporal changes. The formation regions of the respective water masses are also listed.

γ^n range	P21 (17°S)	P16 (210°E)
24.0 to 25.0 25.0 to 26.2 26.2 to 26.5	• SPSTW - pure salinification *central S. Pacific* • the SSM - pure freshening *35°S eastern S. Pacific*	• SPSTW - pure salinification *central S. Pacific*
26.5 to 27.0 27.0 to 27.5	• - pure upward heave • AAIW - pure freshening *subantarctic zone*	• SAMW - pure freshening - pure warming • AAIW - pure freshening - pure warming *subantarctic zone*
27.5 to 27.8	• - pure cooling - pure freshening *Southern Ocean*	• - pure cooling - pure freshening *Southern Ocean*

Table 5.2: Summary of water masses along the WOCE P21 and P16 sections, and the ventilation scenarios that most consistently explain their observed temporal changes. Their respective formation regions are marked in italics.

Along the WOCE P21 section, statistically significant temperature and salinity increases on neutral surfaces have been observed between 24.0 and 26.2 γ^n. The combined observations on neutral surfaces and on isobars suggest that the observed salinity increases are due to surface salinification at the source region of these waters, which is in the central South Pacific Ocean under the high evaporative cell. Below 26.5 γ^n, statistically significant temperature and salinity decreases on neutral surfaces have been observed down to 27.7 γ^n. These decreases have been attributed to a surface freshening at the source

region of AAIW, which is the subantarctic zone in the Southern Ocean, and to a colder and fresher deep water source from the Southern Ocean.

Along the WOCE P16 section north of the equator, waters above the 27.2 γ^n surface have undergone θ and S changes that are consistent with *pure freshening*. However, apart from NPIW, this freshening result does not agree with observations from the WOCE P3 and P4 sections, and so the freshening is thought to contain the effect of the 1991-92 El Niño event. South of the equator, waters from 24.0 to 26.5 γ^n show significant temperature and salinity increases on neutral surfaces that suggest an increase in surface salinity at the source region, which is the central South Pacific, under the high evaporative cell. Below the 26.5 γ^n surface, θ and S changes are dominated by decreases on neutral surfaces to 27.8 γ^n. These decreases have been concluded to be the results of surface warming and freshening at the source region of SAMW and AAIW, which is the subantarctic zone in the Southern Ocean. A colder and fresher deep water source from the Southern Ocean is also implied. Similar cooling of the deep waters has been observed by Swift (1995), and has been attributed to changes in Ross Sea processes.

Apart from θ and S changes, neutral surfaces from 26.5 to 27.0 γ^n along P21, and between 11°S and 26°S along P16, have shoaled. Similar upward movements of isopycnals have also been observed by Ridgway and Godfrey (1996) and Holbrook and Bindoff (1997) in the southwest Pacific as a cooling of the water column.

Discussion

In general, the results from the South Pacific Ocean show that deeper than about 1500 dbar ($\approx 27.8\,\gamma^n$), temporal temperature and salinity changes are not statistically significant. This is similar to the finding from the North Pacific Ocean, and is consistent with the long time-scales required for ventilating waters below 1500 dbar in the South Pacific. Note that the bottom layer of Antarctic Bottom Water has a shorter renewal time that the layer of Circumpolar Deep Water above it, but the sparse historical data around the bottom makes it difficult to detect any temporal changes.

There are general agreements between the results from P21 and from P16. Figure 5.31 shows the changes in the mean θ-S curves along these two WOCE sections. The mean values have been obtained by taking averages on neutral surfaces along the sections, from 154°E to 281°E for P21, and from 17°N to

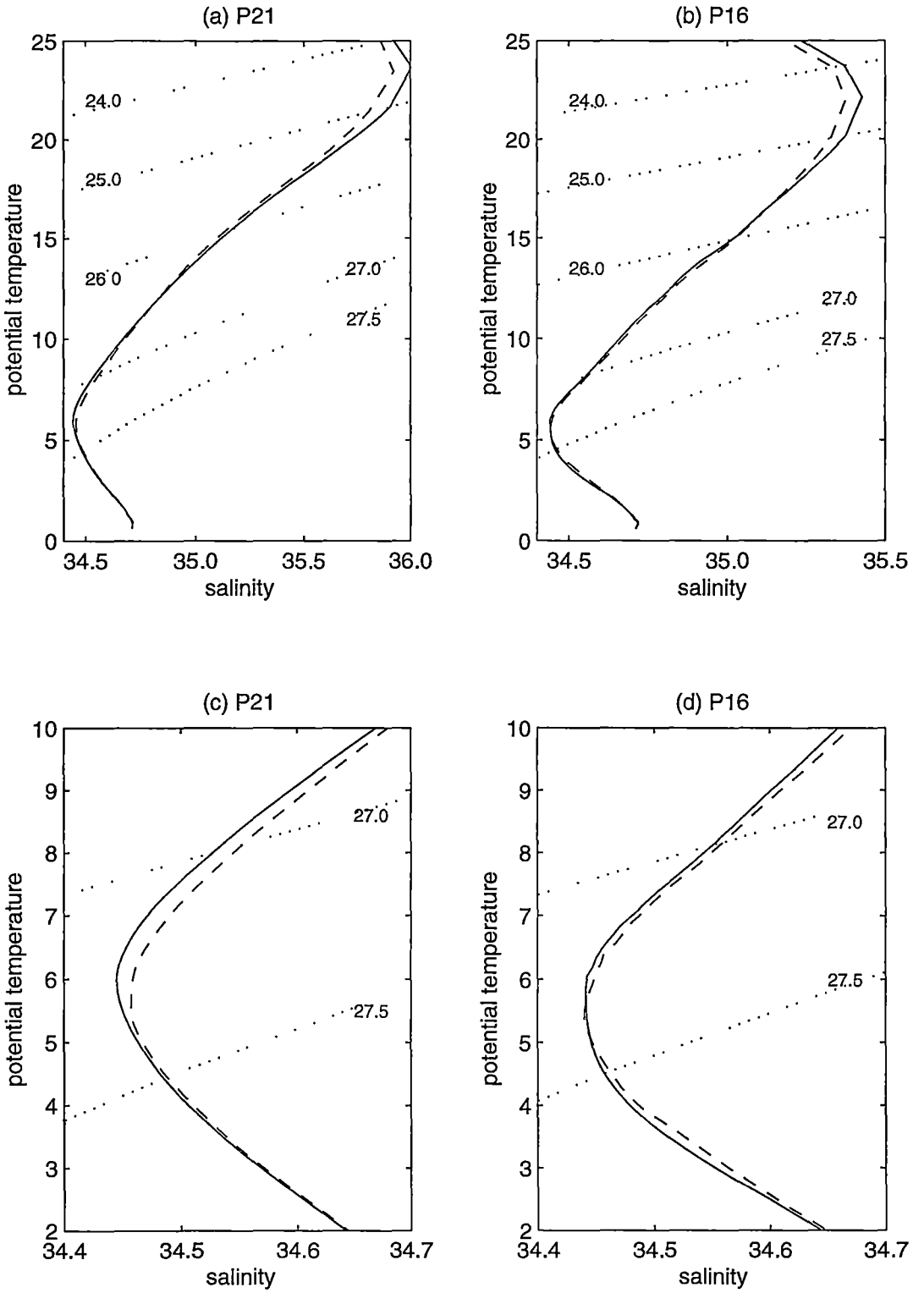

Figure 5.31: Mean (averaged along neutral surfaces) θ-S curves along the two South Pacific sections: (a) and (c) P21 (17°S), (b) and (d) P16 (210°E). Solid lines are from the WOCE data from the early 1990s. Dashed lines are from the objectively mapped historical data, from the late 1960s on average. Lines of constant neutral density are superimposed.

south of the Subantarctic Front at 55°S for P16. Along both sections, the salinity maximum of SPSTW at around 24.5 γ^n shows a shift towards higher temperature and salinity on neutral surfaces. From the SAMW density range of 27.0 - 27.1 γ^n, to the salinity minimum of AAIW at around 27.3 γ^n, and to below 27.5 γ^n, the θ-S curves shift towards lower temperature and salinity on neutral surfaces. Freshening of intermediate waters in the southwest Pacific has also been observed by Bindoff and Church (1992) and Johnson and Orsi (1997).

Combining these results with those from the North Pacific, and recalling that the equatorial P16 results were affected by the 1991-92 El Niño event, it becomes apparent that there is a coherent large-scale salinification signature in the subtropical waters of the Pacific (NPSTW and SPSTW), and a coherent large-scale freshening signature in the intermediate waters of the Pacific (NPIW and AAIW). Because these results suggest a symmetrical increase in evaporation over the mid-latitudes, and a symmetrical increase in precipitation over the high-latitudes, they therefore imply a strengthening of the hydrological cycle over the North and South Pacific oceans.

The symmetrical increase in precipitation over the high-latitudes of both oceans is qualitatively consistent with results from coupled ocean-atmosphere models forced by increasing atmospheric carbon dioxide. For example, Manabe et al. (1990) has shown that in response to carbon dioxide doubling, precipitation increased more than evaporation over the Arctic Ocean of the northern hemisphere and the Southern Ocean of the southern hemisphere, thus reducing the surface salinity of the oceans in the high latitudes. Hence the freshening of intermediate waters signature detected in this thesis might be one of the ocean's manifestation of the enhanced greenhouse effect.

To investigate whether the observed freshening of intermediate waters signature is due to decadal variability or is a response of the ocean interior to atmospheric carbon dioxide doubling, numerical outputs from a coupled ocean-atmosphere model that is forced by increasing atmospheric carbon dioxide is investigated in the next chapter.

Chapter 6

Response of a model ocean to increasing atmospheric CO_2

In Chapters 4 and 5, it has been demonstrated from historical hydrographic data and modern CTD data over the last two decades, that the intermediate waters of the North and South Pacific oceans, NPIW and AAIW, have experienced a decrease in salinity that can be attributed to sea surface freshening at the high latitudes, which in turn suggests an increase in high latitude net precipitation in both hemispheres. In addition, the shallow salinity maxima of NPSTW and SPSTW, which derive their properties from under the high evaporative cells of the North and South Pacific subtropical gyres, have experienced an increase in salinity that implies a possible increase in evaporation at their formation regions.

The North and South Pacific climate systems are known to exhibit interdecadal variability that are observable via sea surface temperature anomalies, and whose spatial signatures are symmetrical about the equator (e.g. Mantua et al. (1997), Garreaud and Battisti (1999)). Although there are insufficient data to determine changes in precipitation patterns related to such interdecadal events, natural variaiblity cannot be ruled out as a possible contribution factor to the inferred symmetrical high latitude precipitation increase. On the other hand, the inferred freshwater increase is also consistent with results from coupled ocean-atmosphere models with increasing atmospheric carbon dioxide forcing (e.g. Manabe et al. (1990)).

This chapter examines the ocean component of a coupled climate model that has been forced by two sets of equivalent atmospheric carbon dioxide levels: one which contains a constant level of CO_2, and another which contains an increasing level of CO_2. The model outputs are examined qualitatively to

identify changes in the model ocean that are more as a result of climate change than of natural variability. Then, the model ocean's response and the observed decadal changes are compared to see if any of the observed changes are qualitatively consistent with the model's response to increasing CO_2.

6.1 Model data

The model output being examined here is the ocean component of the coupled climate model from CSIRO, Australia. The CSIRO coupled model is a comprehensive model that contains atmospheric, oceanic, sea-ice and biosphere sub-models (Gordon and O'Farrell 1997). In particular, the ocean model employs the Gent and McWilliams (1990) scheme in its parameterization of eddy-induced transport (Hirst and McDougall 1996), and has zero explicit horizontal diffusivity. The grid resolution of the ocean model is about 5.6°longitude by 3.2°latitude, and has 21 depth levels.

Two sets of integration outputs from this model are being studied here. The first set, called the c10 control run, contains a constant equivalent atmospheric CO_2 level of 330 ppmv (parts per million by volume), and has been integrated for 1000 years (calendar years 1851 to 2850). The second set, called the r10 transient run, is initialized by fields from the end of the 30th year of the control run, and contains an equivalent atmospheric CO_2 level which increases with time. For the calendar years 1881 to 1990, CO_2 level is varied to give the same radiative forcing change from the total observed greenhouse-gas increase over this period. For the calendar years 1991 to 2082, CO_2 level varies according to the IPCC/IS92a CO_2 scenario. Under this scenario, CO_2 doubling (relative to the 1880 level) occurs around the year 2033, and trebling around 2082. After the year 2082, CO_2 level is held constant at the 3×1880 level, and the integration continues to the year 2700 (Hirst in press). Note that this model does not include aerosols forcing.

The outputs of these two integrations are stored in 10-year averages. Figure 6.1 (a) shows the neutral density on the 100 dbar surface from the control 1966-75 output, which is the decade that best corresponds to the historical observations. It can be seen that the model contains the large-scale wind-driven gyres of the Pacific: the cyclonic subarctic gyre north of 30°N, the anticyclonic subtropical gyres equatorward of 30°N and 30°S, and the eastward-flowing Antarctic Circumpolar Current south of 40°S. A vertical profile of the neutral density field along the 202.5°E meridian shows that these

gyral features exist to about 1500 dbar (Figure 6.1 b).

Figure 6.2 shows the vertical temperature and salinity profiles, also from the control 1966-75 output, along the 202.5°E meridian. The temperature and salinity fields from the model Pacific are poor representations of the real ocean. For example, the thermostad associated with Subantarctic Mode Water is not prominent along this longitude (Figure 6.2 a), where it is usually found at around 50°S, between 7°and 8°C. Secondly, the low salinity tongue ($S < 34.4$, core density $\approx 26.5\ \gamma^n$) associated with North Pacific Intermediate Water is exaggerated (Figure 6.2 b): it reaches deeper and extends more equatorward than in the real ocean. On the other hand, the low salinity tongue ($S < 34.4$, core density $\approx 27.5\ \gamma^n$) associated with Antarctic Intermediate Water is understated in the model and does not extend equatorward (Figure 6.2 b). Lastly, below the intermediate salinity minima, salinity values increase with depth, but do not exceed 34.5 pss, which is lower than observations (typical values for deep waters in the Pacific are about 34.6 to 34.7 pss).

The disparity in water mass structures between the model ocean and the real ocean is most strikingly shown in terms of zonally-averaged θ-S curves. Figure 6.3 shows the θ-S curves along the four latitudes from (a) the modern WOCE CTD data and the objectively mapped historical data, and (b) the transient 1986-95 model output and the control 1986-95 model output. The years 1986-95 being the model decade that best corresponds the WOCE data. It can be seen that along most latitudes, the salinity extrema are not prominent in the model, and the model deep ocean's θ-S properties are wrong relative to the real ocean. Hence while the ocean model contains most of the large-scale circulation features, the mean state of the water mass structure is a poor representation of reality. The unrealistic θ-S curves consequently make comparison with observed changes on neutral surfaces complicated and cumbersome. Therefore, in Section 6.3, the model's response is compared with observed changes at constant depths, so as to eliminate the variations caused by the unrealistic slopes of the model's θ-S curves.

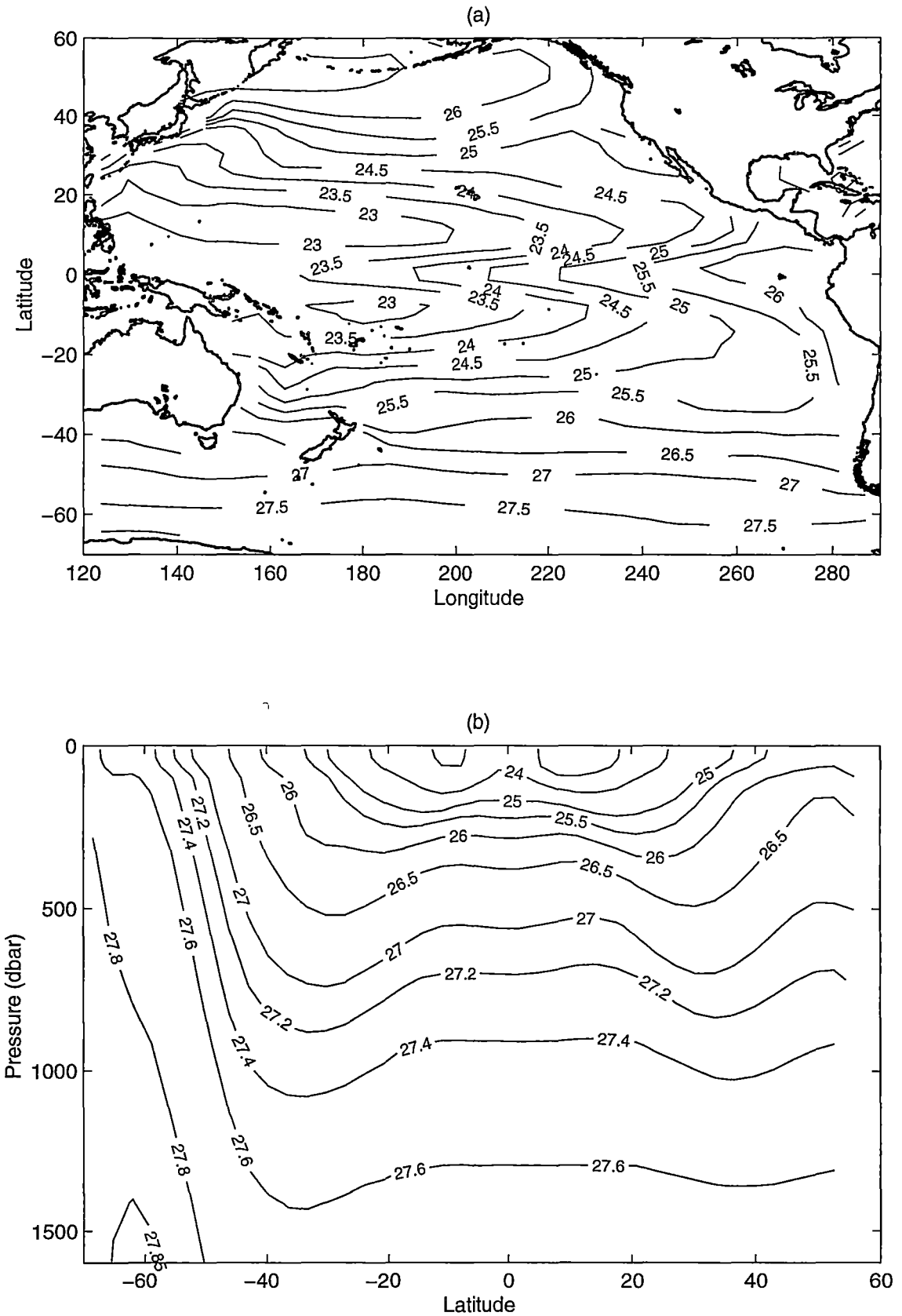

Figure 6.1: Model control run output 1966-75. (a) Neutral density (kg m^{-3}) on the 100 dbar surface. (b) Neutral density (kg m^{-3}) along the 202.5°E meridian.

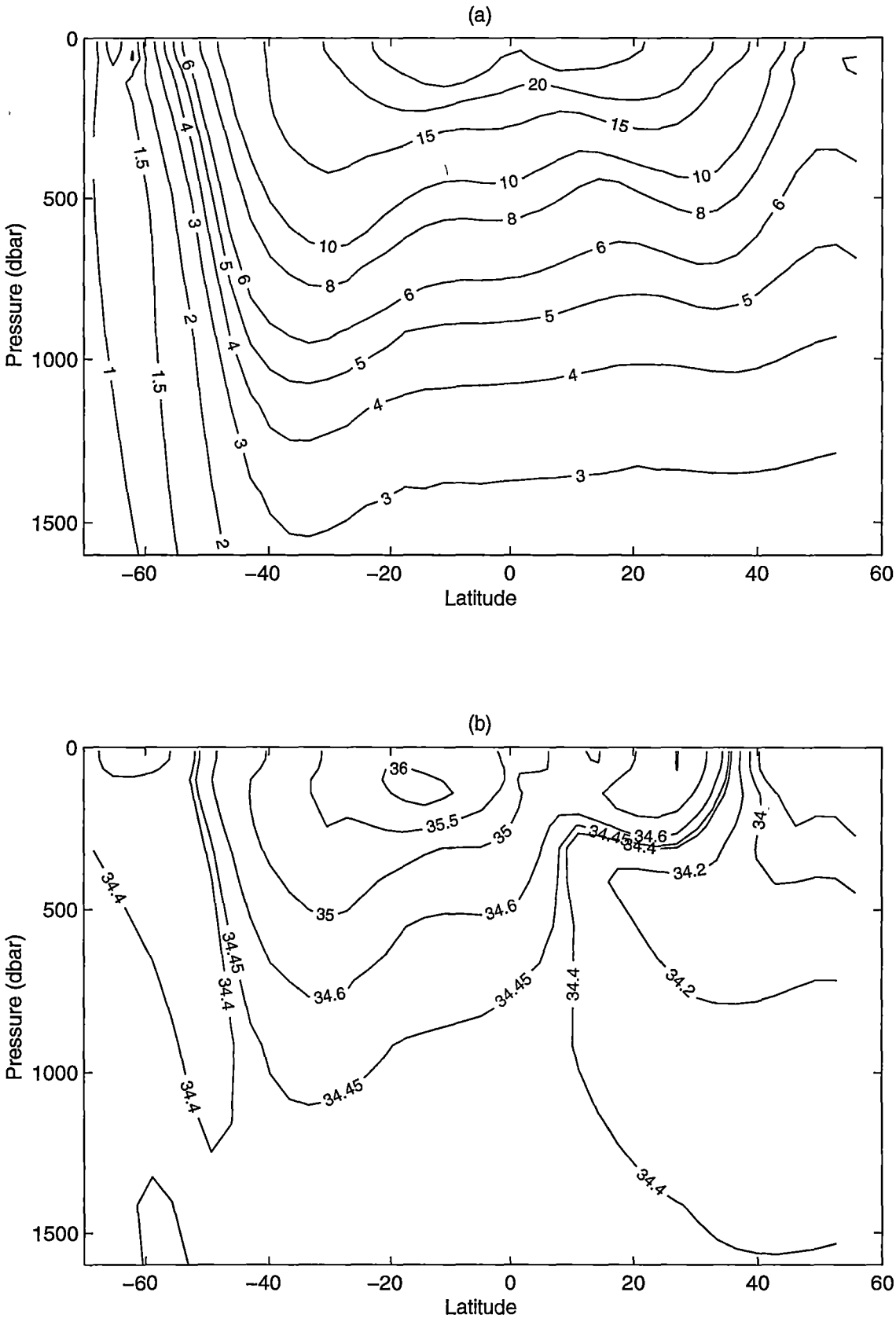

Figure 6.2: Model control run output 1966-75 along the 202.5°E meridian. (a) Potential temperature (°C). (b) Salinity (pss).

Figure 6.3: (the following two pages)

Zonally-averaged (along neutral surfaces) θ-S curves. Lines of constant neutral density are superimposed.

(a) Along the four zonal WOCE sections: (1) P1 at 47°N, (2) P3 at 24°N, (3) P4 at 10°N, and (4) P21 at 17°S. Solid lines are from the modern WOCE data. Dashed lines are from the objectively mapped historical data.

(b) Along four zonal lines in the model ocean that are closest to the four zonal WOCE sections: (1) at 46.2°N, (2) at 23.9°N, (3) at 11.2°N, and (4) at 17.5°S. Solid lines are from the transient 1986-95 output. Dashed lines are from the control 1986-95 output.

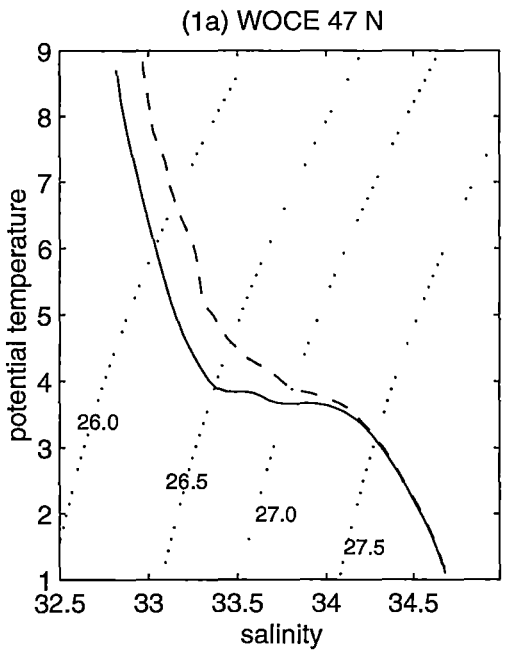
(1a) WOCE 47 N
potential temperature
salinity
26.0
26.5
27.0
27.5

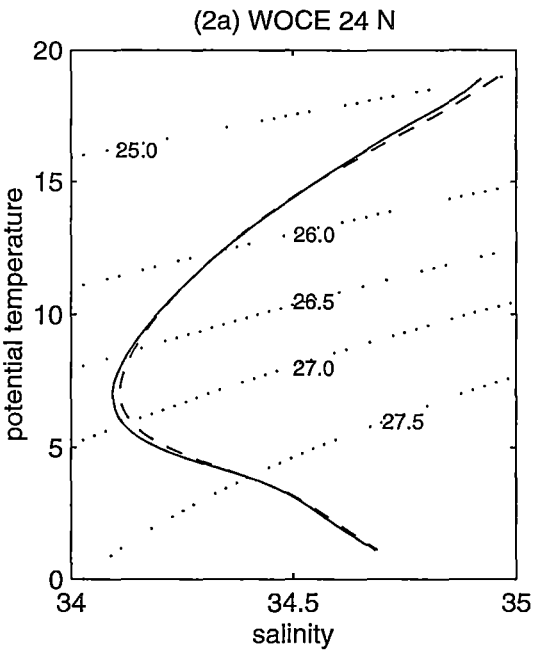
(2a) WOCE 24 N
potential temperature
salinity
25.0
26.0
26.5
27.0
27.5

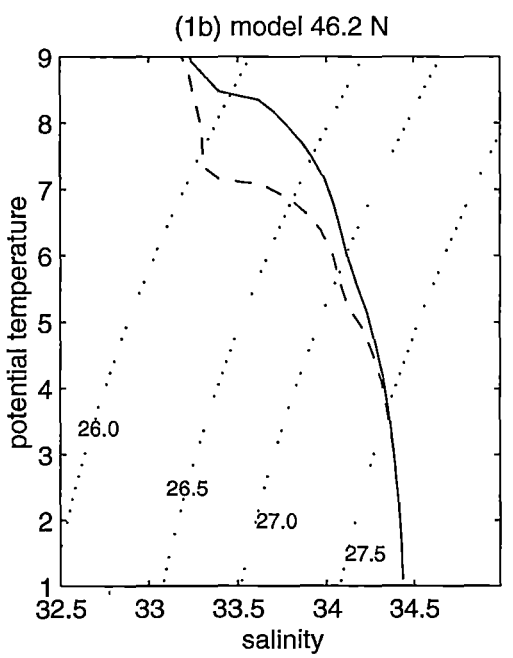
(1b) model 46.2 N
potential temperature
salinity
26.0
26.5
27.0
27.5

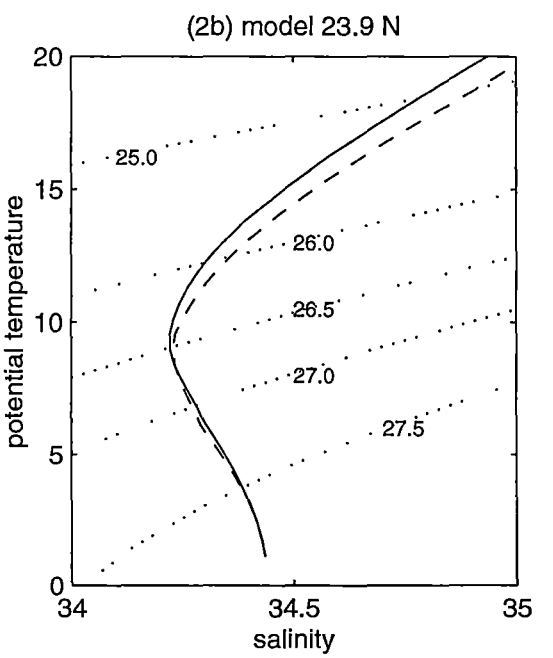
(2b) model 23.9 N
potential temperature
salinity
25.0
26.0
26.5
27.0
27.5

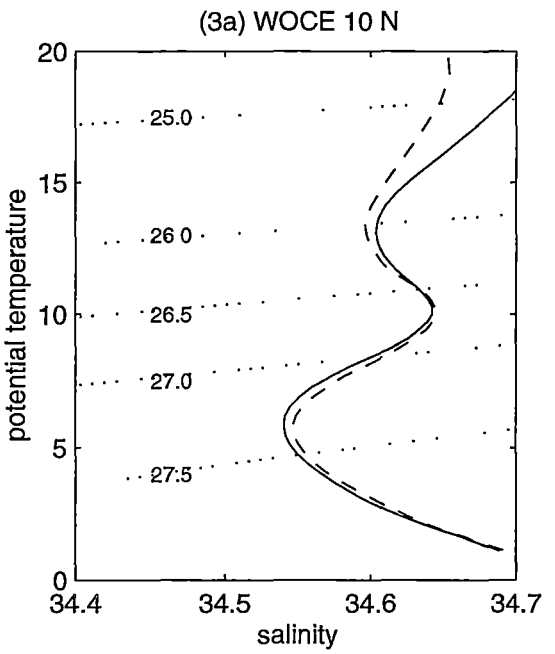
(3a) WOCE 10 N
potential temperature
salinity
25.0
26.0
26.5
27.0
27.5
20
15
10
5
0
34.4
34.5
34.6
34.7

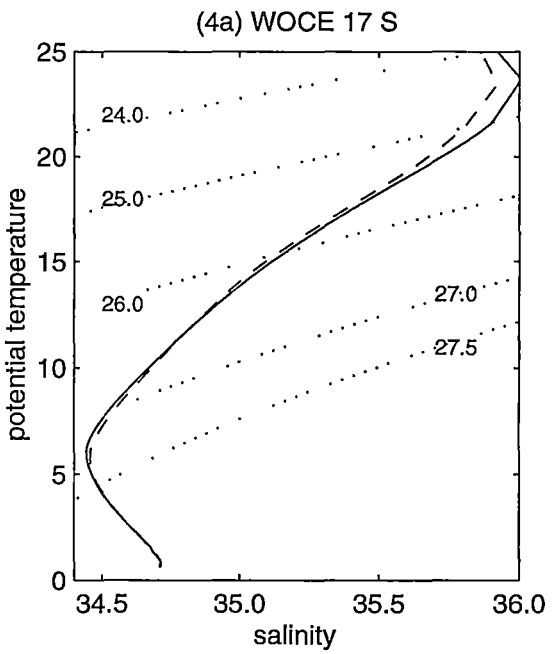
(4a) WOCE 17 S
potential temperature
salinity
24.0
25.0
26.0
27.0
27.5
25
20
15
10
5
0
34.5
35.0
35.5
36.0

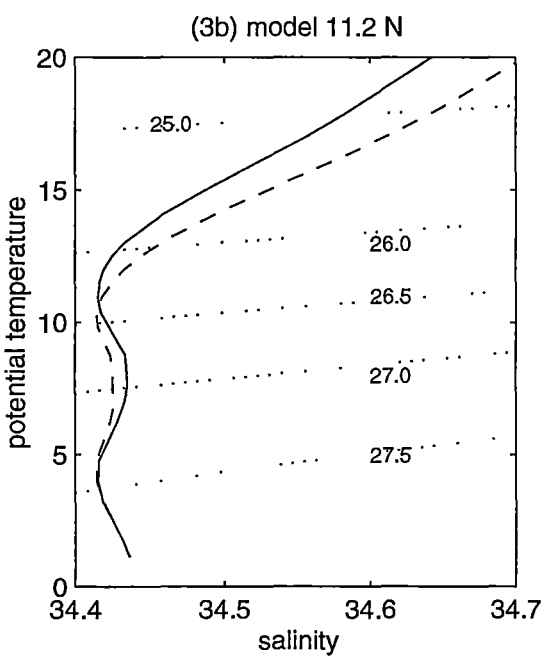
(3b) model 11.2 N
potential temperature
salinity
25.0
26.0
26.5
27.0
27.5
20
15
10
5
0
34.4
34.5
34.6
34.7

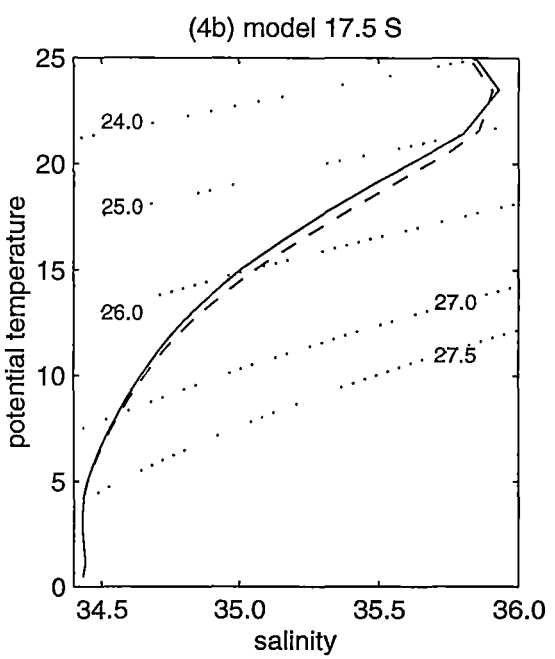
(4b) model 17.5 S
potential temperature
salinity
24.0
25.0
26.0
27.0
27.5
25
20
15
10
5
0
34.5
35.0
35.5
36.0

6.2 The model ocean's response to increasing CO_2

The model ocean's response to an increasing atmospheric CO_2 level is examined by looking at the differences between the transient run and the control run. Both integrations have common inherent changes that are either due to natural variability or due to model drift. Various investigators who have dealt with climate change models have subtracted this common component and defined the climate change signal as the instantaneous difference between the transient run and the control run (e.g. Santer et al. (1995)).

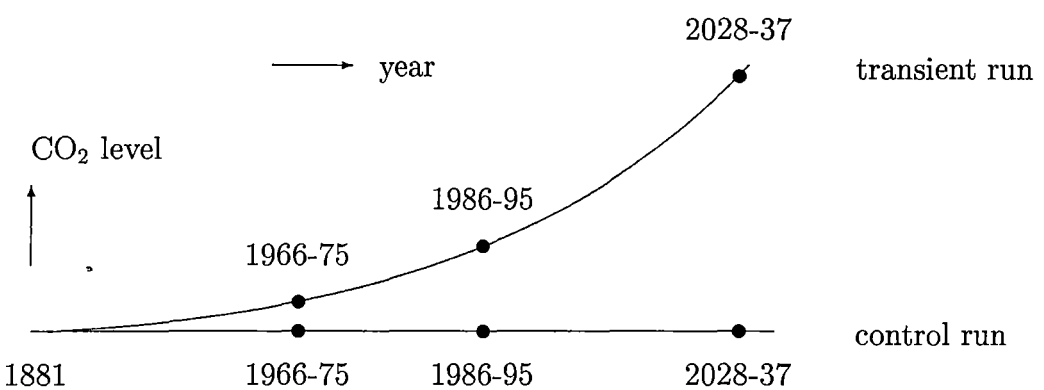

Figure 6.4: Schematic diagram illustrating the two sets of atmospheric CO_2 forcings that have been applied respectively to the control run and the transient run of the CSIRO model, up to the double CO_2 period. The differences being examined are (r8695-r6675) − (c8695-c6675), and (r2x-r6675) − (c2x-c6675).

Two 10-year blocks from the CSIRO model output, 1986-95 and 1966-75, have been selected to represent the Pacific WOCE observation period and the historical data period (mean WOCE year is 1989, mean historical year is 1968). The double CO_2 decade is 2028-37. The differences being examined are the differences between the transient run and the control run, of the changes in the model output at the two time periods: (i) from 1966-75 to 1986-95, and (ii) from 1966-75 to 2028-37 (Figure 6.4). That is, let the 10-year averages from the control run be referred to as c6675, c8695, and c2x, and those from the transient run be referred to as r6675, r8695, and r2x. The differences being examined are

(r8695-r6675) − (c8695-c6675), and (r2x-r6675) − (c2x-c6675). The former will be referred to as the response at the model WOCE time; the latter will be referred to as the response at double CO_2 time. Defined as such, these climate change signals will have excluded the model drift and some natural variability.

The present study focuses on the response of the two intermediate water masses of the Pacific: North Pacific Intermediate Water (NPIW), and Antarctic Intermediate Water (AAIW). Three surfaces have thus been selected on which changes will be examined:

(a) at the 12.5 dbar level, which is the shallowest level in the model ocean;

(b) on the 26.5 γ^n surface, which best represents the model NPIW;

(c) on the 27.5 γ^n surface, which best represents the model AAIW.

Response at the 12.5 dbar level

The 12.5 dbar level is the shallowest level in the model ocean. Changes at this level are examined here to show the relation between the spatial response to increasing CO_2 and the outcropping areas of various isopycnals. The potential temperature and salinity changes at the 12.5 dbar level are shown in Figure 6.5 for the model WOCE time, and in Figure 6.6 for double CO_2 time. The neutral density field on the 12.5 dbar surface is superimposed in Figure 6.7 to show the climate changes at the approximate outcropping regions for the various neutral surfaces. The magnitudes of the θ and S changes are displayed as zonal averages in the right-hand panels in Figure 6.7. The averages are taken from 129.375°E to 258.75°E for the North Pacific, and from 151.875°E to 281.25°E for the South Pacific.

In the North Pacific, the temperature response to an increasing atmospheric CO_2 forcing at the model WOCE time is a broad-scale warming of near-surface water, except for an anomalous cold area at 142°- 170°E, 20°- 30°N in the middle of the subtropical gyre (Figure 6.5, top panel). This cold patch could be part of the decadal natural variability in the North Pacific, such as the cycle of temperature anomaly circulating around the North Pacific, as detailed by Zhang and Levitus (1997), or it could be due to an upward displacement of the thermocline in the subtropical gyre, as a result of ocean thermal expansion (Church et al. 1991). In any case, this cold anomaly disappears by the time double CO_2 is reached (Figure 6.6).

The largest near-surface warming occurs along 46.2°N, where the zonally averaged θ increase is 1.08°C at the model WOCE time (Figure 6.7). This

agrees well with real surface observations such as those presented in Parker et al. (1994), where positive surface temperature anomalies in the 1980s is clearly seen north of 50°N in the North Pacific.

Near-surface warming in the South Pacific is not as marked as in the North Pacific. At the model WOCE time, most of the South Pacific poleward of 40°S actually displays near-surface cooling. However, by the time double CO_2 is reached, almost the entire Southern Ocean, except for a small region around 60°S and 180-200°E (Figure 6.6), shows near-surface temperature increase. Note that the magnitude of increase is less than that in the North Pacific.

In short, near-surface warming in the model South Pacific Ocean is slower and weaker than that in the North Pacific. Similar interhemispheric asymmetry of sea surface temperature responses have been observed in other models (e.g. Stouffer et al. (1989), Manabe et al. (1990)), and is believed to be partly due to the large thermal inertia of the ocean-dominated Southern Hemisphere.

The high latitudes near-surface salinity response is more symmetrical in the two hemispheres than the temperature response. Poleward of 40°N and 40°S, near-surface freshening is widespread, as has also been observed in other models (e.g. Manabe et al. (1990)). The southern high latitudes (south of 40°S), except for a narrow area around Antarctica, show consistent near-surface freshening under an increasing atmospheric CO_2 level. The northern high latitudes (north of 40°N) also show predominantly a freshening response, but there is a persistent salty tongue stretching eastward from the Okhotsk Sea north of Japan to 200°E, 40°N.

Equatorward of 40°N and 40°S, another important interhemispheric asymmetry is noted in the near-surface salinity response. The pattern is not as obvious at the model WOCE time, but is more fully evolved by the time double CO_2 is reached (Figure 6.6). In the South Pacific between the equator and about 40°S, stretching from the east coast of Australia to about 240°E (an area which includes the model's South Pacific high evaporative region), there is predominantly near-surface salinity increase. On the other hand, almost the entire North Pacific subtropical gyre, which includes the model's North Pacific high evaporative region, shows a marked freshening response. This salinity response of the model is contrary to the implied symmetrical (about the equator) P-E decrease over the subtropical gyres, based on observations that the shallow salinity maxima, NPSTW and SPSTW, have undergone increases in salinity.

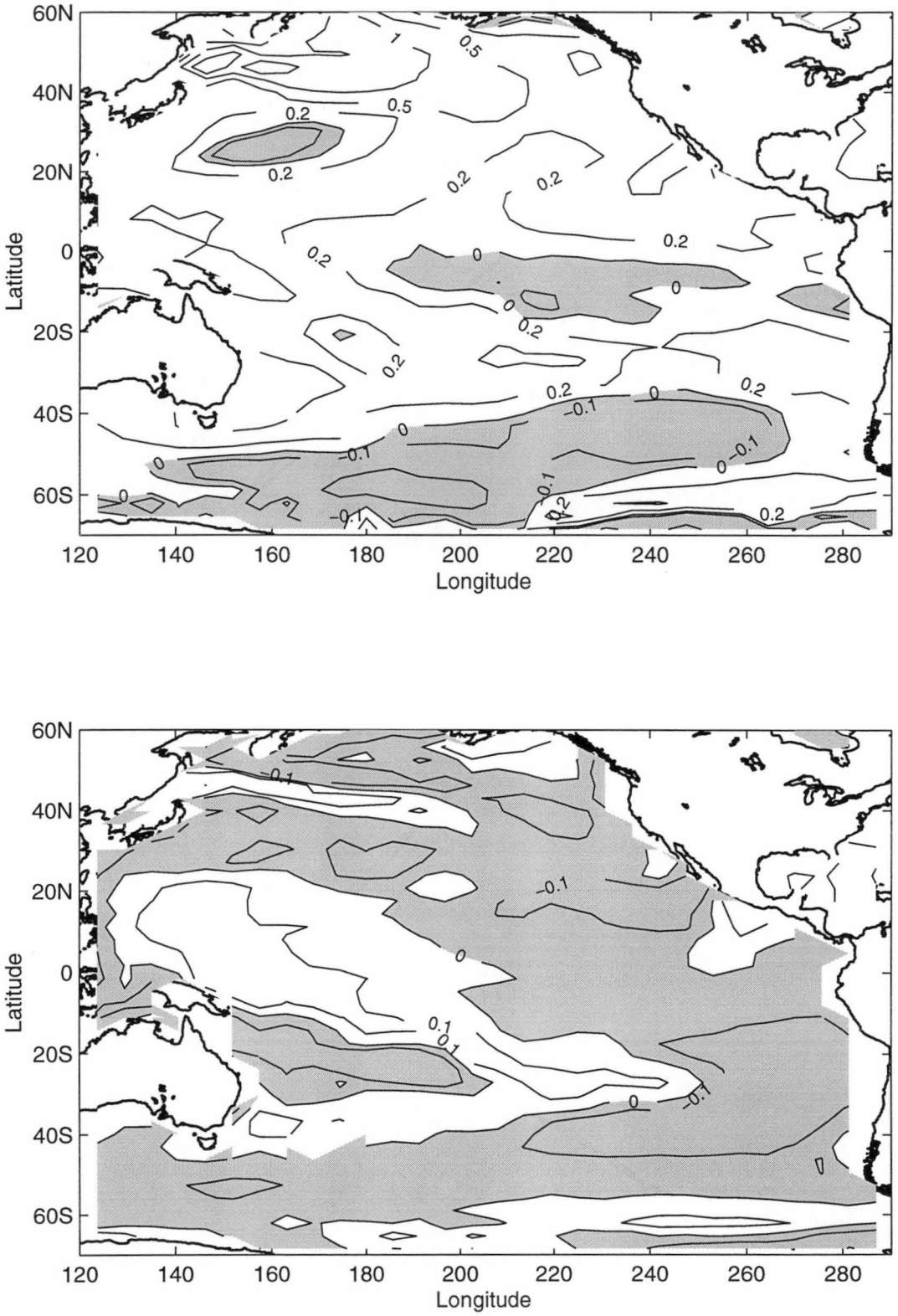

Figure 6.5: Differences in (top panel) potential temperature (°C) and (bottom panel) salinity (pss) at the model WOCE time at the 12.5 dbar level. Shaded parts denote areas of θ and S decreases.

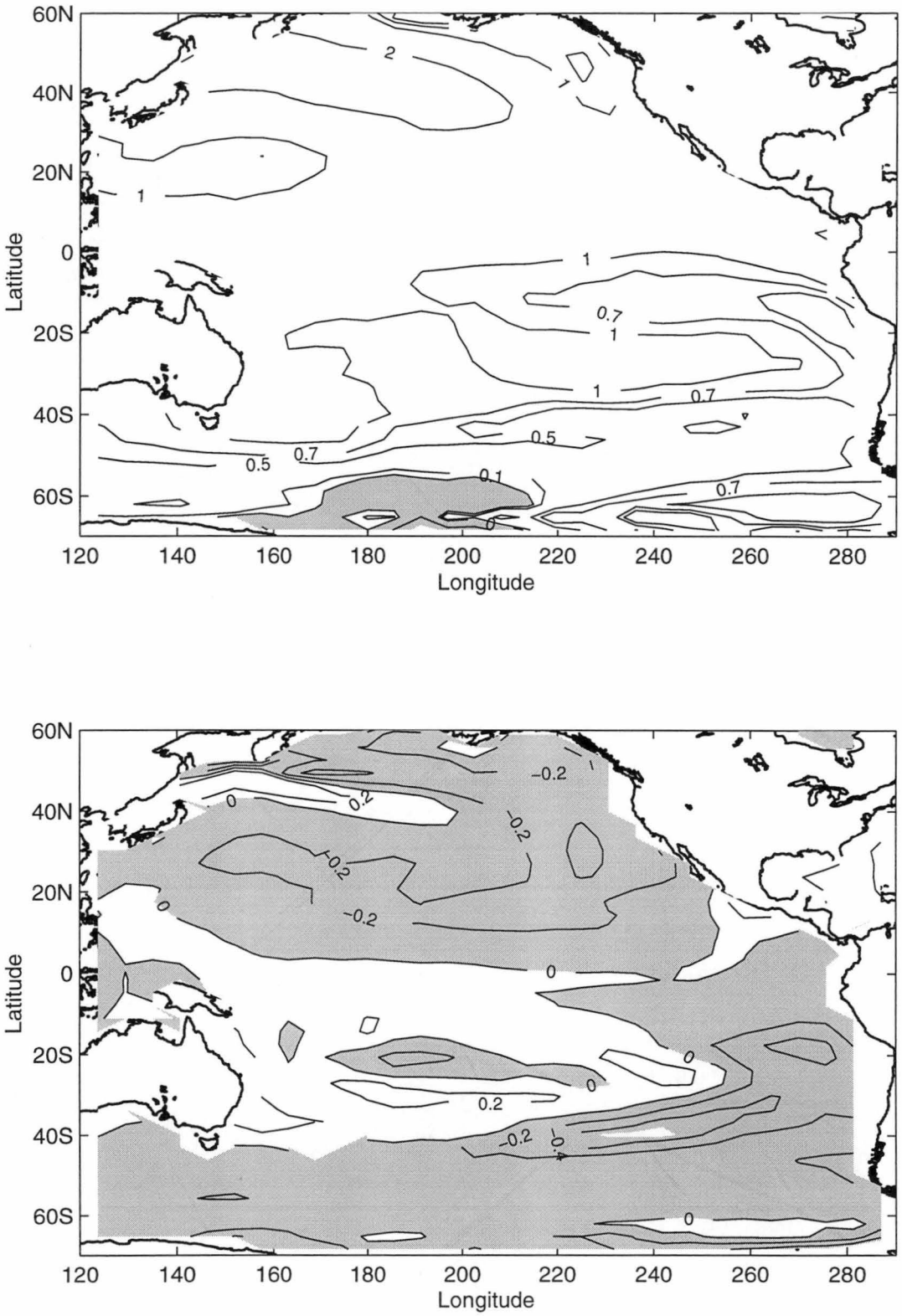

Figure 6.6: As in Figure 6.5, but at double CO_2 time. Note that the contour intervals are different from Figure 6.5.

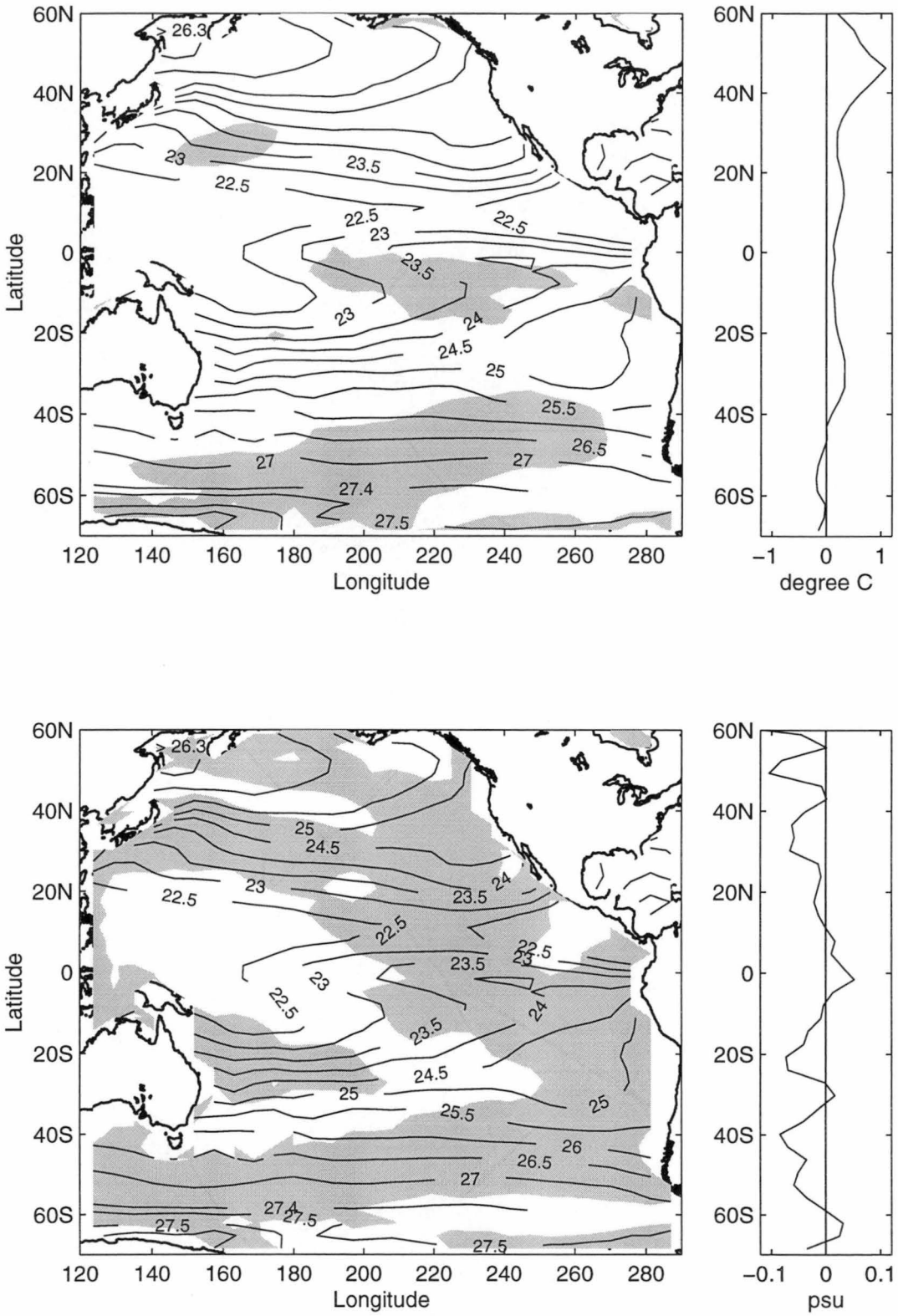

Figure 6.7: As in Figure 6.5, with the addition that the neutral density (kg/m^3) field at the 12.5 dbar level from the control 1966-75 output is superimposed to show the approximate outcropping areas of various isopycnals. The right-hand panels show the zonally averaged θ and S differences (i.e. $\overline{\theta'|_z}$ and $\overline{S'|_z}$).

Response on the 26.5 γ^n surface

As 26.5 γ^n is the approximate core density of NPIW in the model ocean, changes on this surface are examined here as representative of the response of the northern salinity minimum to increasing atmospheric CO_2. Differences on isobars ($\theta'|_z$ and $S'|_z$) have been interpolated to the time-averaged depths of the 26.5 γ^n surface, and are shown in Figures 6.8 and 6.9. Figures 6.10 and 6.11 show the potential temperature and salinity differences on the 26.5 γ^n surface (i.e. $\theta'|_n$ and $S'|_n$). Because a change in temperature on a neutral surface will be accompanied by a corresponding change in salinity on the same neutral surface (and vice versa), the top panel ($\theta'|_n$) and bottom panel ($S'|_n$) in Figures 6.10 and 6.11 will have the same pattern, but they are shown to elucidate the magnitudes of change. The pressure field on this surface is shown in Figure 6.12 to give an indication of the geostrophic circulation.

North Pacific (NPIW)

On isobaric surfaces, Figure 6.8 shows that at the model WOCE time, the North Pacific at the 26.5 γ^n level has warmed everywhere, except for a cold pool in the central Pacific. The subtropical gyre has freshened almost everywhere, except for a small area in the western Pacific, and along a salty tongue stretching from the Sea of Japan, that is also present at the 12.5 dbar level. By the time double CO_2 is reached (Figure 6.9), the cold pool has shrunk, and almost the entire North Pacific has warmed, but the salty tongue remains.

Corresponding to the general freshening and warming on isobars, there is a decrease in temperature and salinity on the 26.5 γ^n surface in the central North Pacific. This is seen as a thick elongated band stretching from about 140°E to about 220°E, and roughly following the circulation path of the subtropical gyre (Figure 6.12). By the time double CO_2 is reached, this band has moved southwestward with the circulation and has almost filled the entire subtropical gyre (Figure 6.11). The magnitude of the differences also seems to decrease towards the centre of the gyre at roughly 160°E, 30°N, which is the most downstream along the ventilation pathway on this surface.

The area covered by the elongated band represents the horizontal extent of the salinity minimum of NPIW according to historical hydrographic data (Talley 1993), and in the model, these waters have a positive θ-S slope. Combining the responses on the neutral surface and on the corresponding isobars therefore suggests that, as a result of increasing CO_2, NPIW in the

model undergoes a change in its θ-S property that is qualitatively consistent with both the *pure warming* and *pure freshening* subduction scenarios. These model ocean interior responses also match the near-surface responses at the model outcropping region near the Sea of Okhotsk. Because the centre of the subtropical gyre does not display *pure cooling* type water mass changes, the cold pool is caused by upward displacements of isopycnals.

Outside the elongated band, the rest of the waters in the North Pacific have a negative θ-S slope on the 26.5 γ^n surface. The temperature and salinity increases on the neutral surface in the rest of the North Pacific (Figures 6.10 and 6.11) are therefore also qualitatively consistent with *pure warming.*

In short, as a result of increasing CO_2, almost all waters in the model North Pacific on the 26.5 γ^n surface, except for a persistant cold pool centred at 30°N (see Figure 6.9), have undergone *pure warming.* The flip in sign that follows the boundary of the North Pacific subtropical gyre (see Figures 6.10 and 6.11), of changes on the neutral surface, is related to the change in slope of the θ-S curve. In addition, the model NPIW experiences both *pure freshening* and *pure warming.* These interior changes are consistent with the responses at the outcropping regions, and seem to follow the geostrophic circulation. Moreover, the centre of the North Pacific subtropical gyre, where waters are most downstream along the ventilation pathway and hence the oldest on this surface, experiences mainly upward heave.

South Pacific

At the model WOCE time, on both isobaric surfaces (Figure 6.8) and the 26.5 γ^n surface (Figure 6.10), a fresh tongue is seen to spread from where the 26.5 γ^n surface outcrops in the Southern Ocean, in an anticlockwise manner around the South Pacific subtropical gyre (Figure 6.12). Temperature changes on isobars along this tongue (Figure 6.8, top panel) is a mixture of warming and cooling. The values of $\beta S'|_z$ are greater than $\alpha\theta'|_z$ along this tongue, indicating that salinity changes are more important here than temperature changes. This fresh anticlockwise tongue of 26.5 γ^n in the South Pacific therefore has undergone θ-S changes that are consistent with the *pure freshening* subduction scenario. Its interior changes also fit the response at its source region at the southeastern Pacific near South America, according to McCartney (1977).

Elsewhere in the South Pacific, especially in the middle of the subtropical gyre near 30°S, 180-200°E, the magnitude of warming on isobars far exceeds that of freshening on isobars in density terms. At the model WOCE time, the

fresh anticlockwise tongue has not yet spread to the middle of the gyre, indicating the longer time needed to ventilate the western South Pacific. At the model WOCE time, most of the warming in the western South Pacific is therefore more likely due to downward displacements of isopycnals as an initial response to increasing CO_2.

By the time double CO_2 is reached, the fresh anticlockwise tongue has spread to the entire South Pacific between the equator and 40°S (Figure 6.11). On isobars (Figure 6.9), warming becomes dominant, except at the southeastern Pacific east of 240°E, where freshening on isobars persists. In the model South Pacific, 26.5 γ^n is above the salinity minimum of AAIW. Hence waters on this surface in the model have a positive θ-S slope, except at the southeastern corner off the west coast of South America, where the stability ratio is negative. So at double CO_2 time, θ-S changes on the 26.5 γ^n surface is predominantly of warming, except at the southeastern Pacific, where both warming and freshening are present.

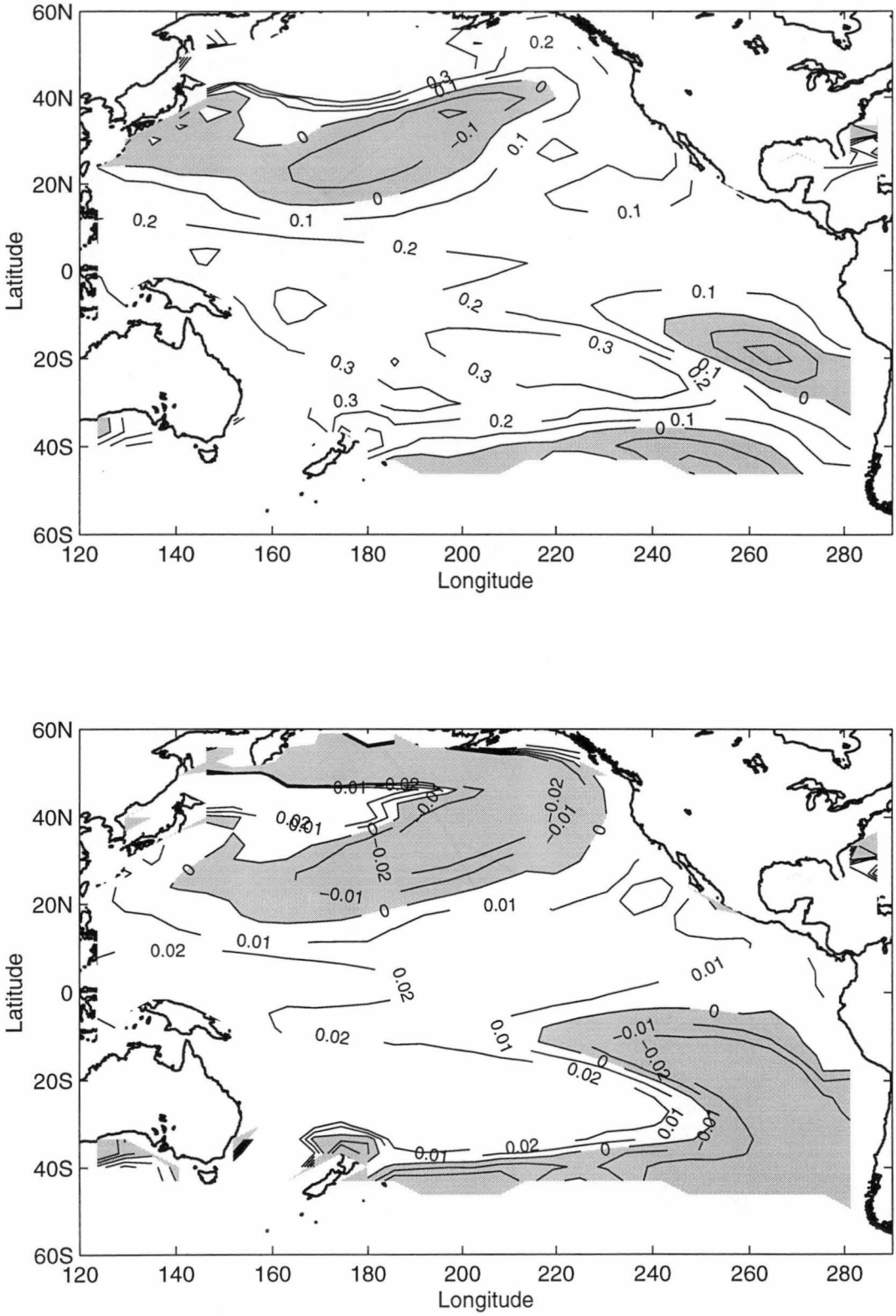

Figure 6.8: Differences in (top panel) potential temperature (°C) and (bottom panel) salinity (pss) at the model WOCE time on isobars, interpolated to the time-averaged depths of the 26.5 γ^n surface. Shaded parts denote areas of negative $\theta'|_z$ and $S'|_z$.

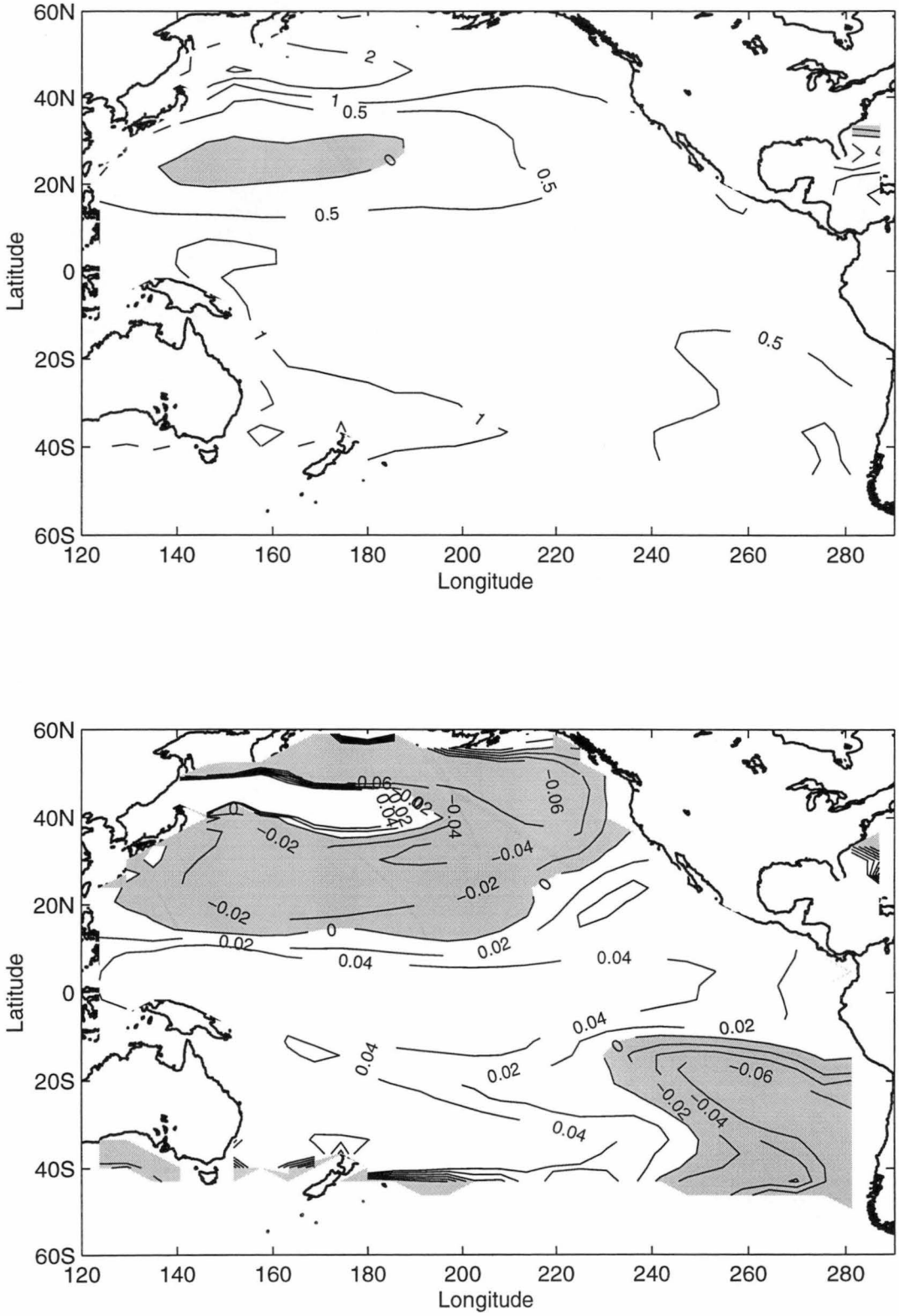

Figure 6.9: As in Figure 6.8, but at double CO_2 time. Note that the contour intervals are different from Figure 6.8.

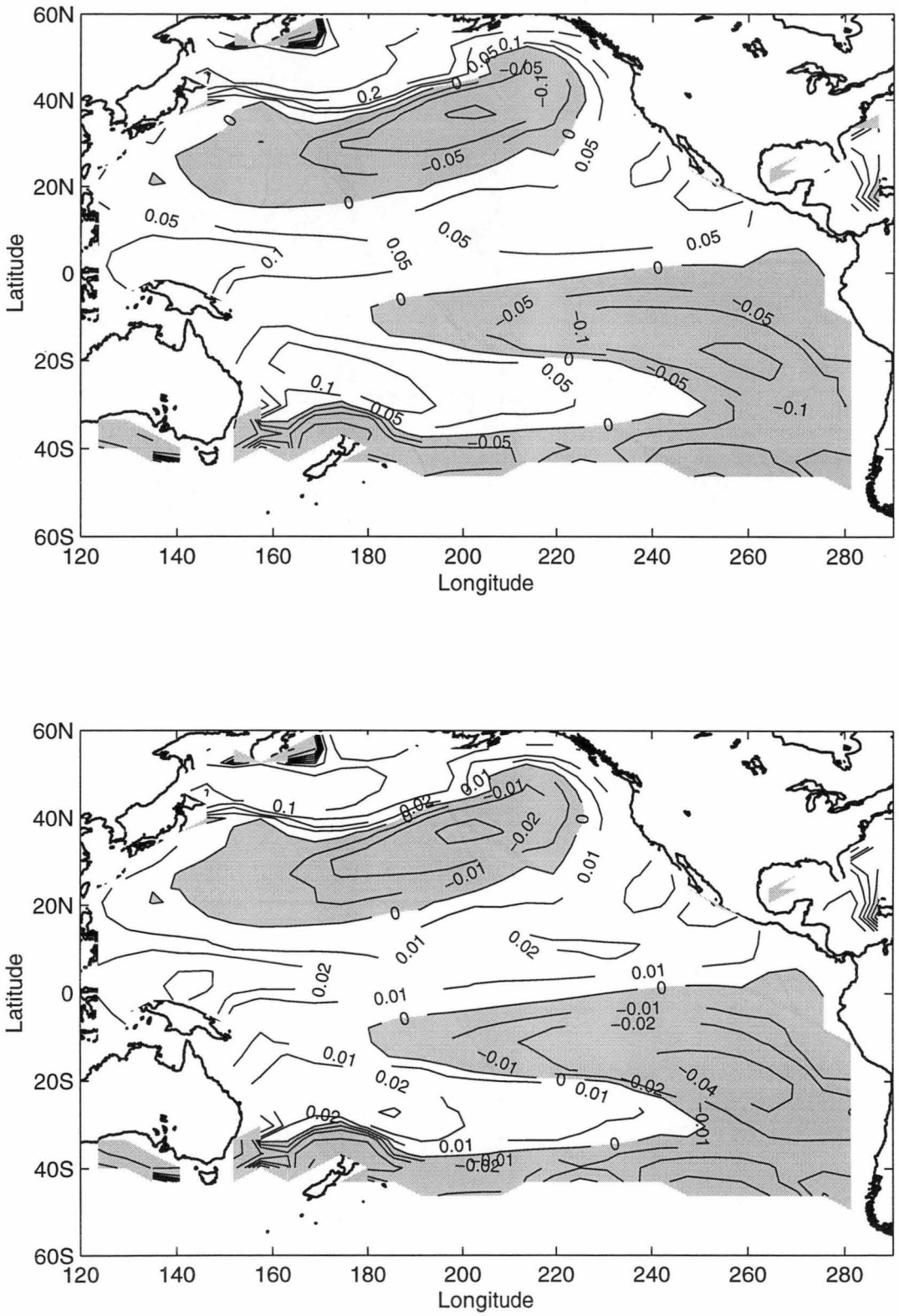

Figure 6.10: Differences in (top panel) potential temperature (°C) and (bottom panel) salinity (pss) at the model WOCE time on the 26.5 γ^n surface. Shaded parts denote areas of negative $\theta'|_n$ and $S'|_n$.

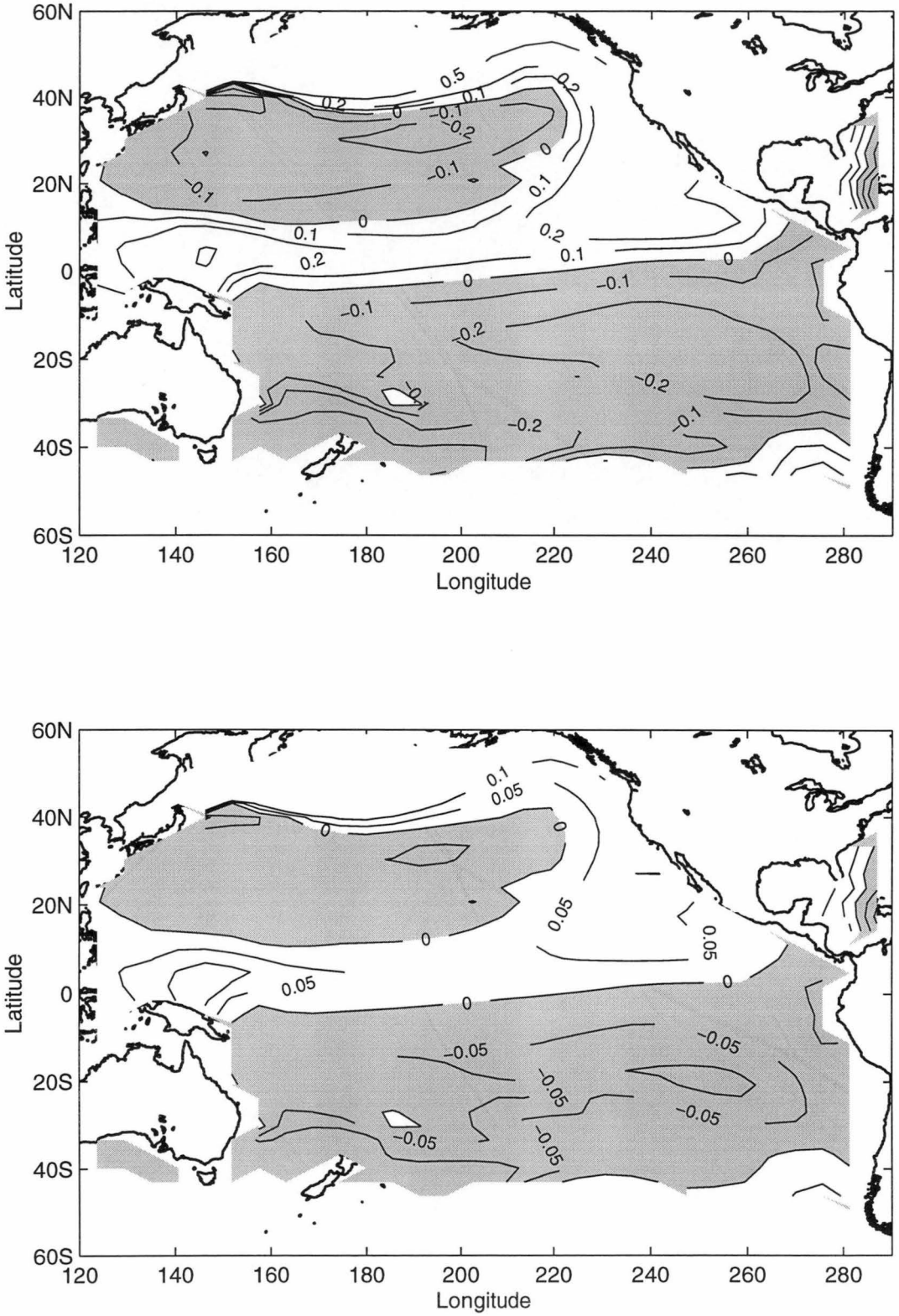

Figure 6.11: As in Figure 6.10, but at double CO_2 time. Note that the contour intervals are different from Figure 6.10.

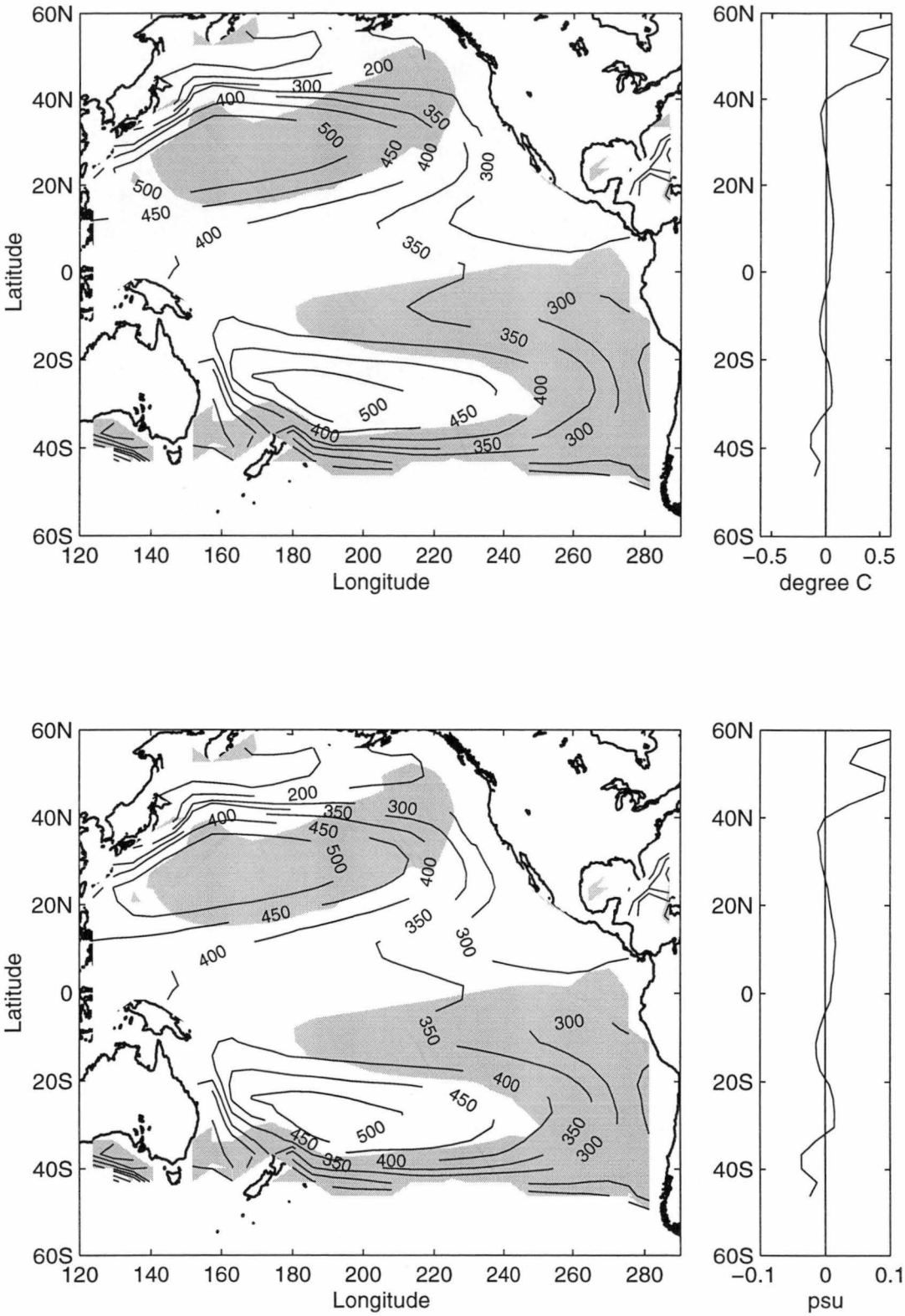

Figure 6.12: As in Figure 6.10, with the addition that the pressure field (dbar) on the 26.5 γ^n surface from the control 1966-75 output is superimposed to give an indication of the geostrophic circulation. The right-hand panels show the zonally averaged θ and S differences (i.e. $\overline{\theta'|_n}$ and $\overline{S'|_n}$).

Response on the AAIW surface (27.5 γ^n)

27.5 γ^n is the approximate core density of AAIW in the model ocean, so changes on this surface are representative of the response of the southern salinity minimum to increasing atmospheric CO_2. The 27.5 γ^n surface outcrops south of 60°S in the model, where the near-surface responses to increasing atmospheric CO_2 are of progressive warming and freshening.

In the South Pacific, interior responses are consistent with those at the outcropping regions. Changes on isobars at the model WOCE time reveal large areas of freshening in the South Pacific, except for a band of salinified water south of 40°S (Figure 6.13). This salinified band is a transient feature and is replaced by freshening by the time double CO_2 is reached (Figure 6.14). Note that there is a corresponding band of saline water around Antarctica at the 12.5 dbar level, which is also a transient feature in the near-surface response. Also in the South Pacific, between 20°S and 50°S, a cold patch exists east of 220°E at the model WOCE time. By the time double CO_2 is reached, the spatial extent of this cold patch is reduced significantly, and the South Pacific is dominated by warming on isobars at the 27.5 γ^n level. Hence this cold patch may be a transient upward heave response of the southeastern Pacific.

On the neutral surface, responses of waters of 27.5 γ^n south of the equator are of decreases in temperature and salinity (Figures 6.15 and 6.16). These waters have a positive θ-S slope on this surface, and so represent the upper layer of AAIW above the salinity minimum. Their combined responses on isobars and on neutral surfaces are therefore consistent with the *pure warming* and *pure freshening* ventilation processes. Moreover, the southeastern Pacific shows the biggest decreases on the neutral surface (Figure 6.17), consistent with the theory that the main region where polar surface waters enter the ocean interior as South Pacific AAIW is in the subantarctic zone in the southeastern Pacific (McCartney 1977).

In the model, the 27.5 γ^n surface does not outcrop anywhere in the North Pacific. Much of the response on isobars in the North Pacific is more due to downward displacements of the isopycnals, and less as a result of θ-S property shifts.

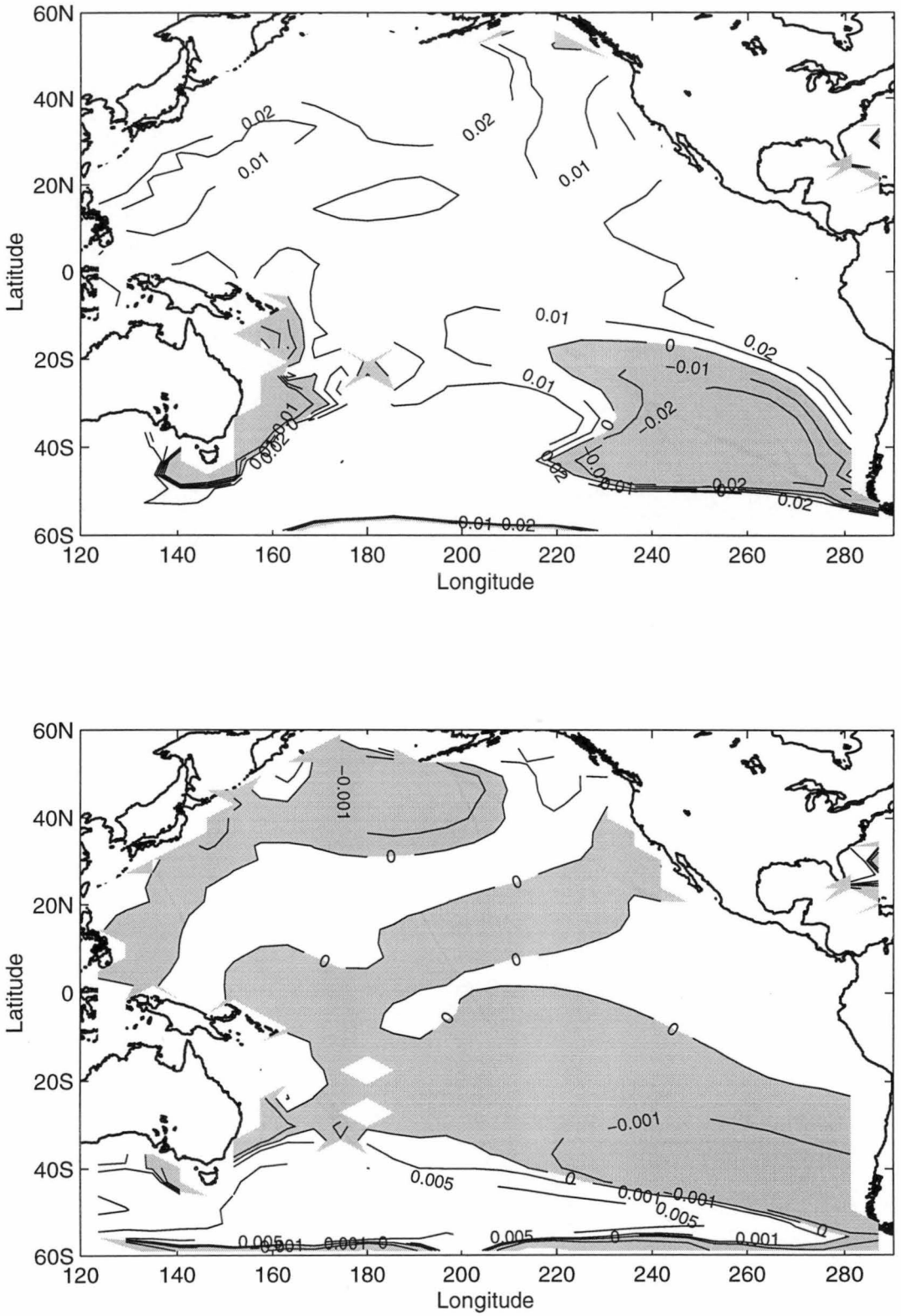

Figure 6.13: Differences in (top panel) potential temperature (°C) and (bottom panel) salinity (pss) at the model WOCE time on isobars, interpolated to the time-averaged depths of the 27.5 γ^n surface. Shaded parts denote areas of negative $\theta'|_z$ and $S'|_z$.

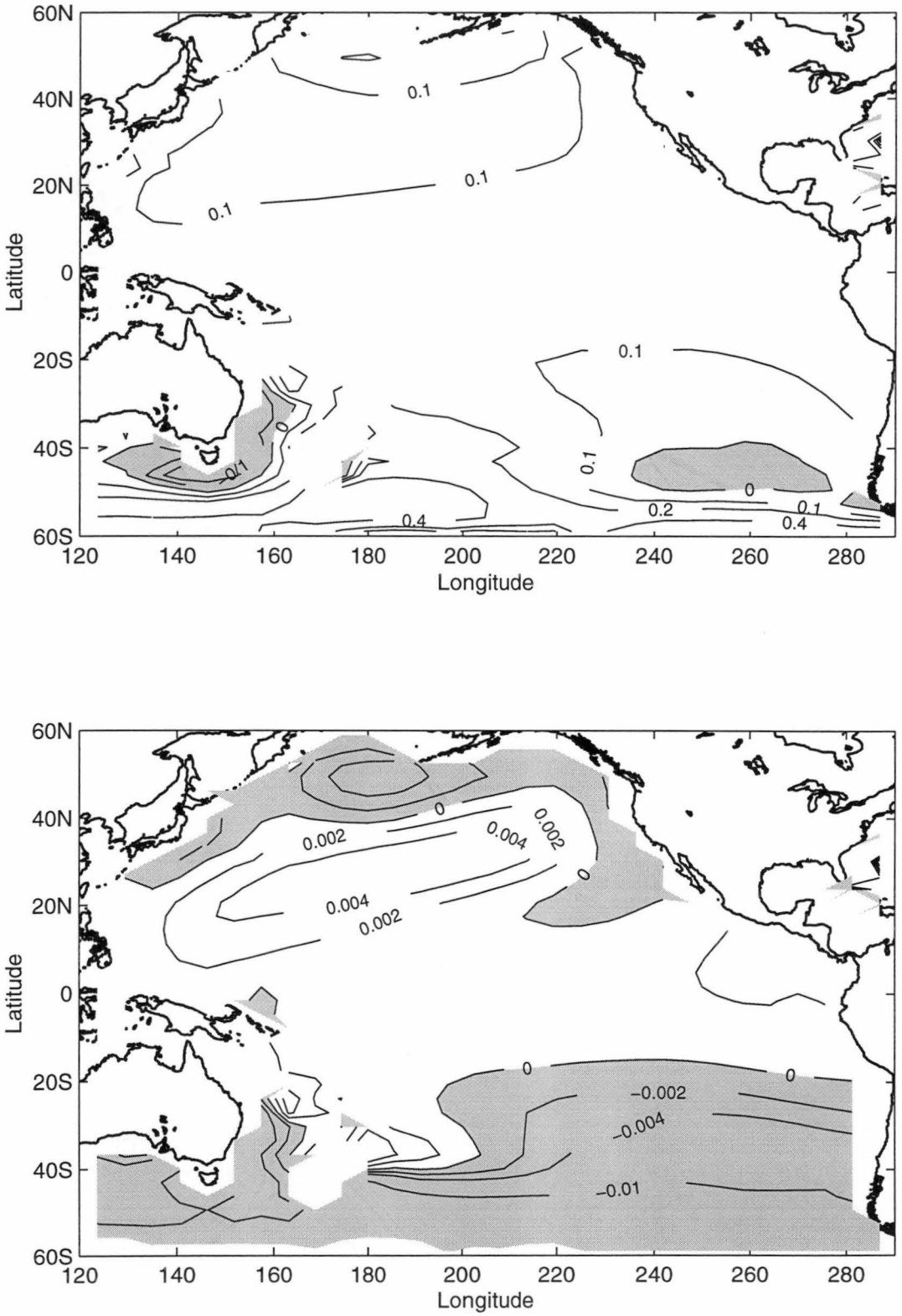

Figure 6.14: As in Figure 6.13, but at double CO_2 time. Note that the contour intervals are different from Figure 6.13.

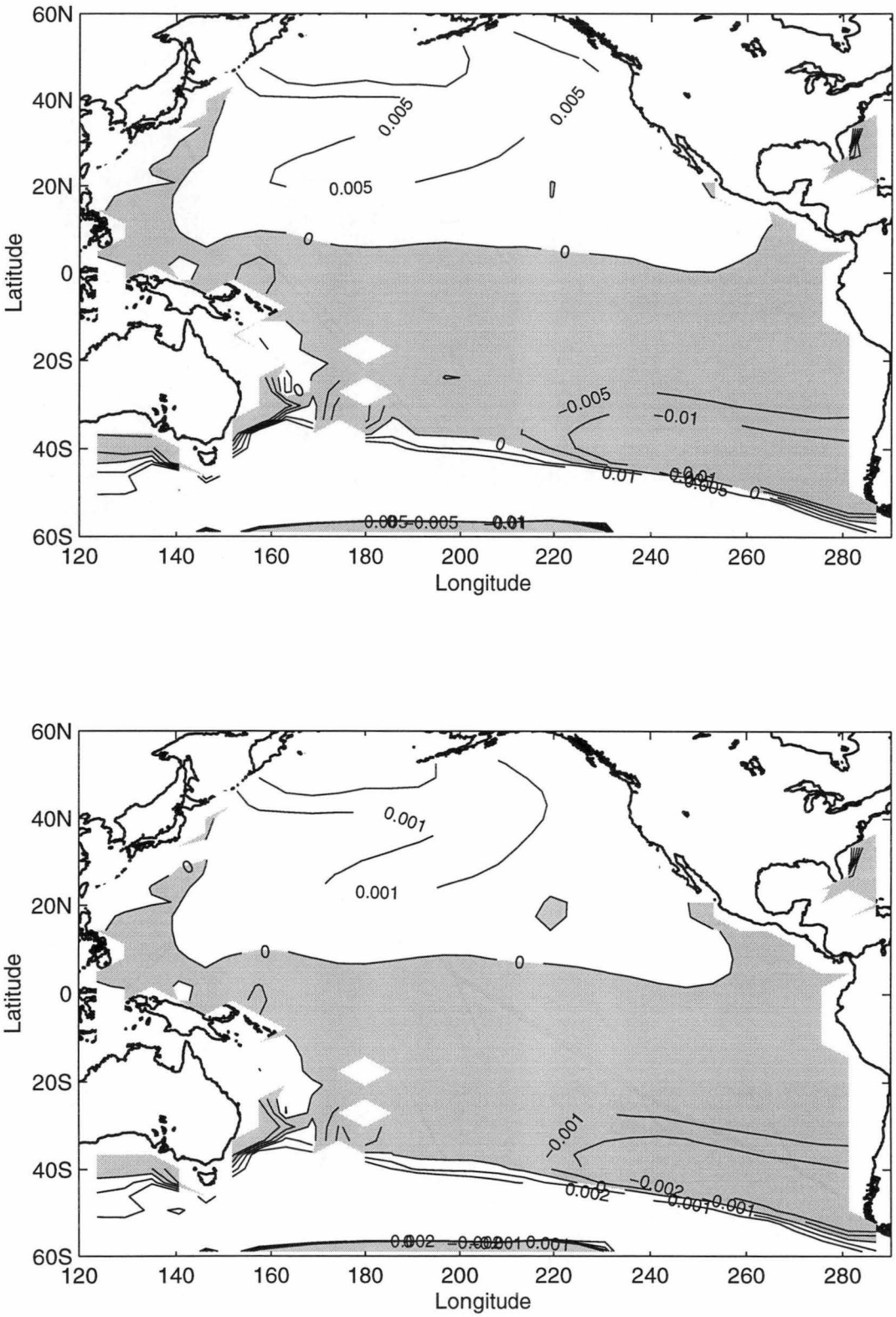

Figure 6.15: Differences in (top panel) potential temperature (°C) and (bottom panel) salinity (pss) at the model WOCE time on the 27.5 γ^n surface. Shaded parts denote areas of negative $\theta'|_n$ and $S'|_n$.

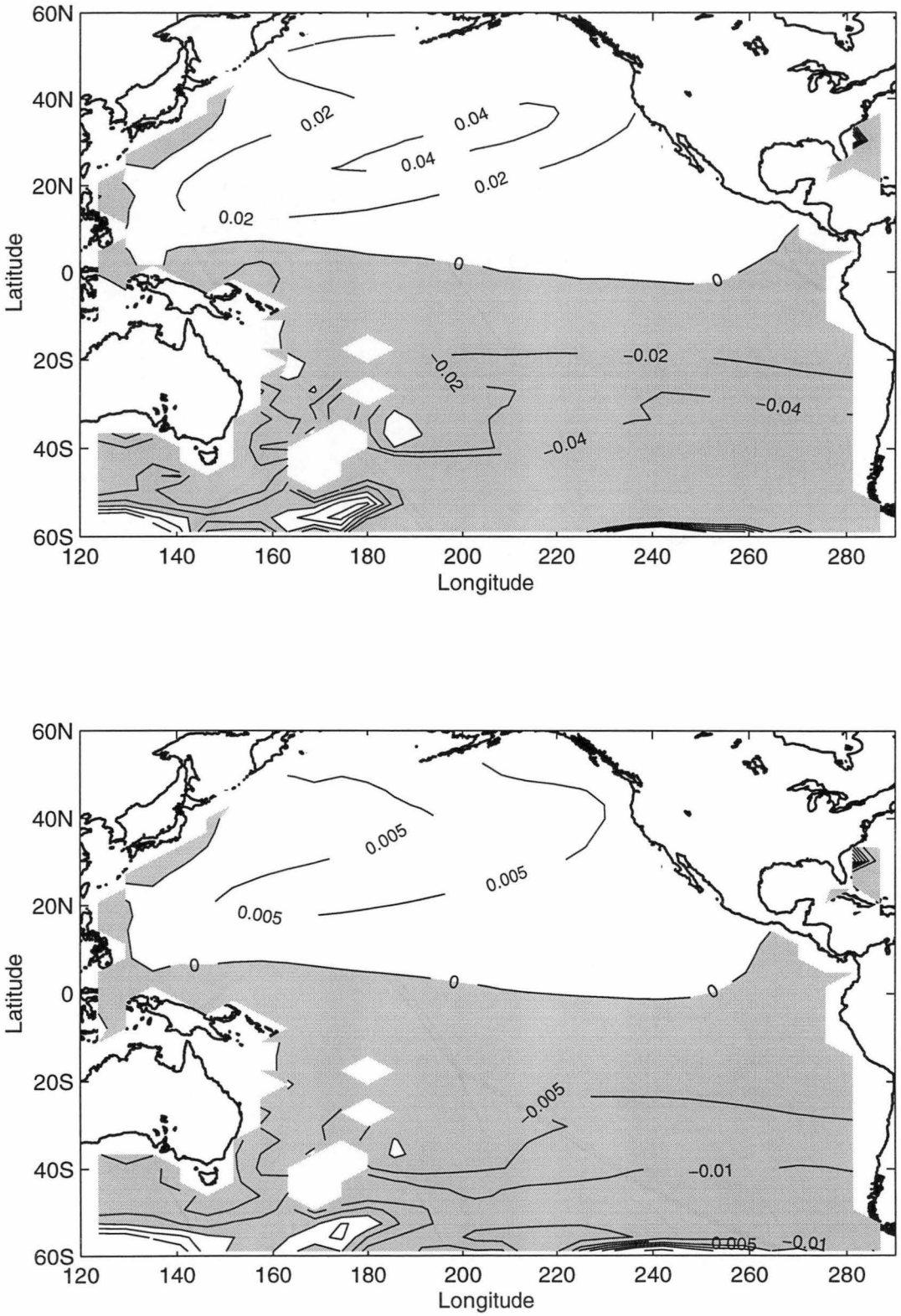

Figure 6.16: As in Figure 6.15, but at double CO_2 time. Note that the contour intervals are different from Figure 6.15.

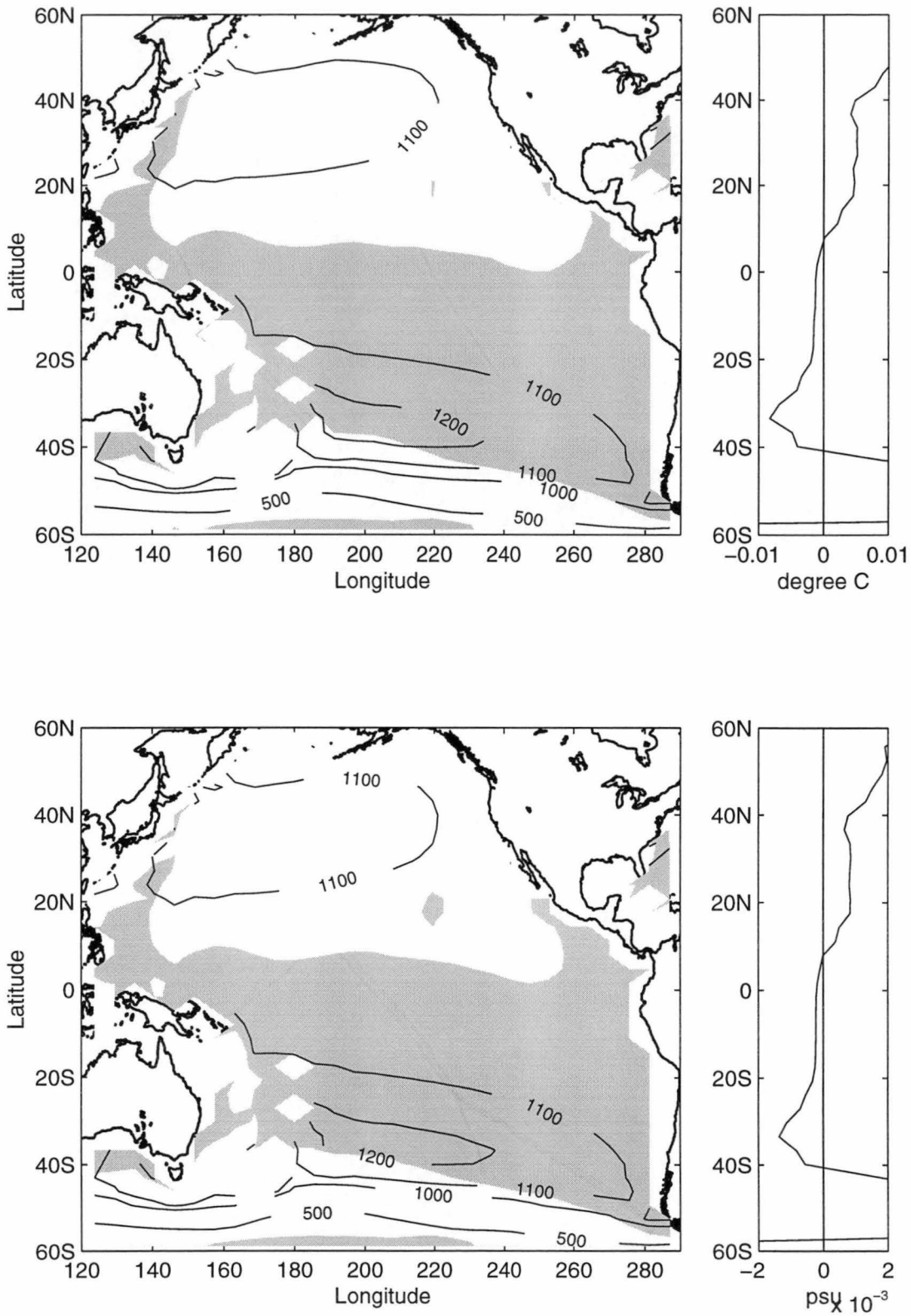

Figure 6.17: As in Figure 6.15, with the addition that the pressure field (dbar) on the 27.5 γ^n surface from the control 1966-75 output is superimposed to give an indication of the geostrophic circulation. The right-hand panels show the zonally averaged θ and S differences (i.e. $\overline{\theta'|_n}$ and $\overline{S'|_n}$).

Scatter plots of responses for NPIW and AAIW

A simple way to show the relative strength of the three processes *pure warming/cooling*, *pure freshening/salinification* and *pure heaving* is by the use of scatter plots of one variable versus another. Figure 6.18 shows the hodographs of $\alpha\theta'|_z/(R_\rho - 1)$ versus $R_\rho\beta S'|_z/(R_\rho - 1)$. These two variables are chosen because within this coordinate system, each of the three processes are represented as vectors with constant directions, with two being orthogonal and the third as a diagonal. The *pure freshening* process lies along the x-axis, the *pure warming* process lies along the y-axis, and the *pure heaving* process is a diagonal. A data point is a linear combination of these processes. Hence a dominant process is easily identified as a cluster of data points along the axes, or along the diagonal.

Figure 6.18 (a) plots the hodograph of the response at the model WOCE time, for the North Pacific Ocean on the 26.5 γ^n surface, which is mostly NPIW. Similarly, Figure 6.18 (b) plots the hodograph of the response at the model WOCE time, for the South Pacific Ocean on the 27.5 γ^n surface, which is mostly AAIW. These two water masses have a positive θ-S slope on these surfaces, hence the vectors for the three processes for when $R_\rho > 1$ are superimposed in Figure 6.18, to ease interpretation of the responses of NPIW and AAIW due to increasing CO_2.

It can be seen that for both NPIW and AAIW in the model, the response to increasing CO_2 at the model WOCE time forms a cluster around the *pure freshening* axis. The dominance of the effect of salinity reduction in these two water masses is therefore evident. In Figure 6.18 (a), the data points that fall around the *pure salinification* axis are from the salty tongue stretching from the Sea of Japan, on the 26.5 γ^n surface, while in Figure 6.18 (b), the data points around the *pure salinification* axis come from the transient saline band south of 40°S on the 27.5 γ^n surface. Note that the strength of the data points on the 26.5 γ^n surface is one order of magnitude larger than on the 27.5 γ^n surface (see the different scales in Figure 6.18 a and b), because surface response signals are attenuated by the time they reach the deeper waters.

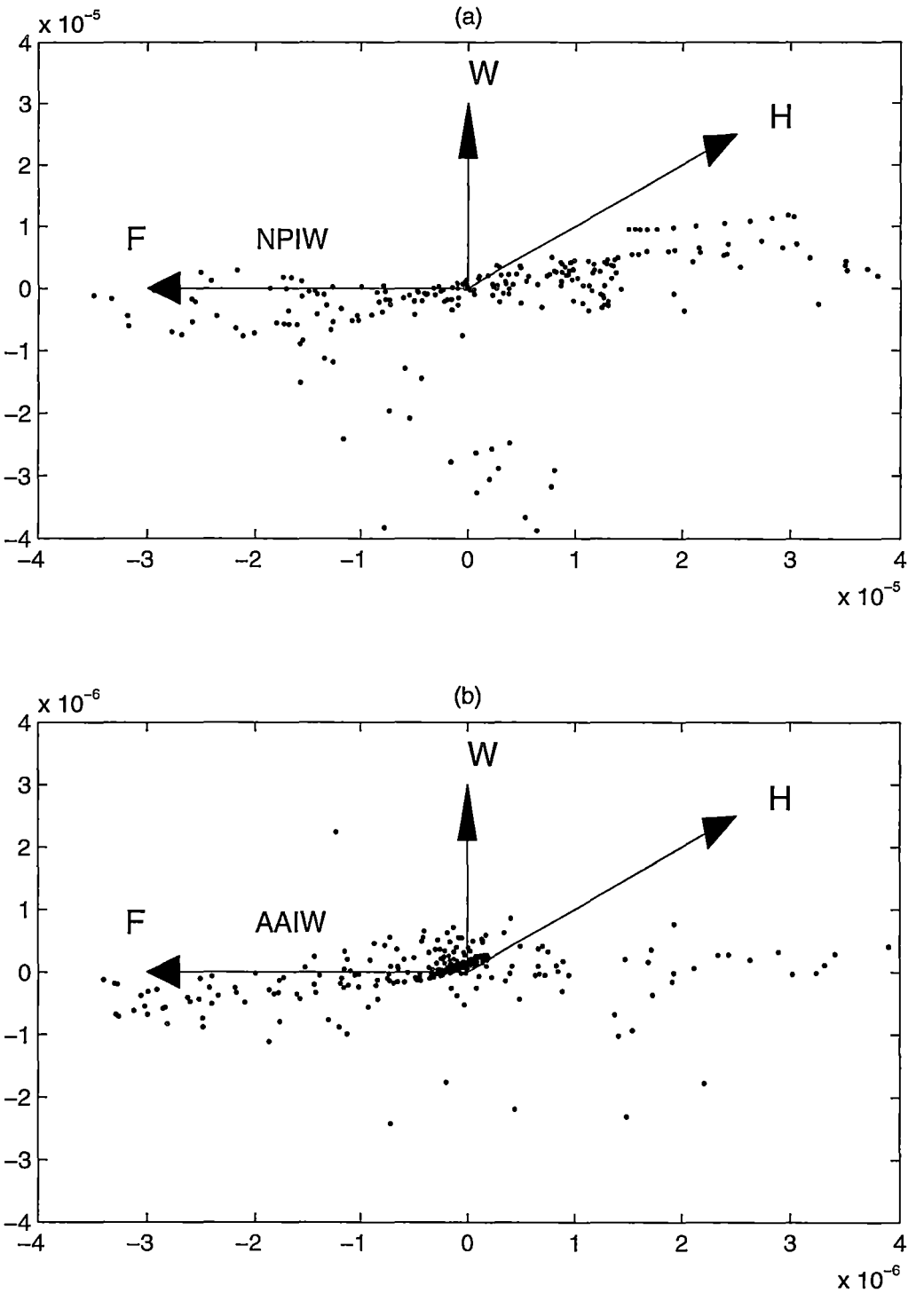

Figure 6.18: Scatter plots of the response at the model WOCE time for (a) the North Pacific on the 26.5 γ^n surface, and (b) the South Pacific on the 27.5 γ^n surface. The x-axis is $R_\rho \beta S'|_z/(R_\rho - 1)$. The y-axis is $\alpha\theta'|_z/(R_\rho - 1)$. The three arrows represent the three processes for when $R_\rho > 1$. 'W' = *pure warming.* 'F' = *pure freshening.* 'H' = *pure heaving.* When $R_\rho < 0$, the *pure warming* arrow is reversed.

6.3 Comparing the model's response with observations

In this section, the model ocean's response to increasing atmospheric CO_2 at the model WOCE time is examined along four latitudinal lines that are closest to the nominal latitudes of the four zonal WOCE sections: P1 at 47°N, P3 at 24°N, P4 at 10°N, and P21 at 17°S. The purpose is to compare more quantitatively the model ocean's response to the observed temporal changes in the North and South Pacific oceans. As has been discussed in Section 6.1 on model data, the model water masses are very different from observations (Figure 6.3). To eliminate the variations caused by the different slopes of the θ-S curves between model and observations, this section will discuss changes on isobars rather than changes on neutral surfaces. As a result, these differences contain the effects of vertical movements of isopycnals.

Figures 6.19 and 6.20 show the changes on isobars from observations and the model response on isobars. Only the top 1500 dbar are plotted because changes below 1500 dbar are invariably small. The top 100 dbar are also omitted to exclude the seasonal mixed layer, where objective estimates are usually unreliable.

Comparing the temperature response

At the model WOCE time, along all four latitudes, the model ocean responds to increasing CO_2 by showing general warming (bottom panels, Figure 6.19), except at the level of NPIW along 23.9°N, where there is a cold pool at the centre of the subtropical gyre. The general warming pattern does not fit the observations along the WOCE P1 section at 47°N, where a combination of cooling and upward heave gives an overall temperature decrease on isobars. There is qualitative consistency between the model output and observations along the WOCE section at 10°N, in that the water column exhibits general warming down to 1000 dbar (Figure 6.19 (3a,b)). Along the WOCE P21 section at 17°S, the model does not show the cooling pattern between 300 and 700 dbar that was noted in the observations, but the upper layer warming between 100 and 300 dbar qualitatively agrees with observations along 17°S.

Hence apart from the subarctic latitude of 47°N, the model ocean's temperature response qualitatively agrees with the general warming of the upper 300 dbar of the ocean from observations.

Comparing the salinity response

The model's salinity response pattern along 46.2°N shows a banded structure of increased salinity above 200 dbar, freshening between 200 and 400 dbar, increased salinity again between 400 and 500 dbar, and freshening below 500 dbar (Figure 6.20 1b). This pattern does not fit the observation along the WOCE 47°N section (Figure 6.20 1a), where apart from surface freshening above 200 dbar, the rest of the water column shows a general increase in salinity that is caused by upward displacements of isopycnals.

In the model, NPIW is found at shallower depths than the observations. Along 23.9°N, where the model NPIW is found at above 500 dbar, zonally-averaged freshening of NPIW (difference > 0.04 pss) is seen to be greater than the freshening observed along the WOCE section at 24°N (difference < 0.04 pss).

Along the other two latitudes at 11.2°N and 17.5°S, there is no salinity minimum of AAIW in the model ocean, and a salinity increase is seen between 200 and 700 dbar, which does not agree with the observations. However, this inconsistency is more due to the model's failure to propagate the southern salinity minimum to these latitudes. As has been discussed in Section 6.2, AAIW in the model, under increasing CO_2, actually shows changes (*pure warming* and *pure freshening*) that are qualitatively consistent with observations. But the *pure freshening* signature, in particular, follows the geostrophic circulation of the subtropical gyre, and, even at double CO_2 time, is confined to south of 20°S (Figure 6.14).

Along all three latitudes at 23.9°N, 11.2°N and 17.5°S, the model's shallow waters ($\approx$ 200 dbar) show a freshening response (bottom panels, Figure 6.20). This does not fit the observations where subtropical surface waters show an increase in salinity that implies increased E-P rates over the subtropics.

Comparing the response below 1500 dbar

Below 1500 dbar (not shown), the differences between the transient output and the control output along the four latitudes are generally less than 0.02°C in potential temperature and 0.002 pss in salinity at the model WOCE time. These differences are smaller than those observed in the deep waters along the WOCE sections. The model therefore exhibits essentially no changes in the deep Pacific.

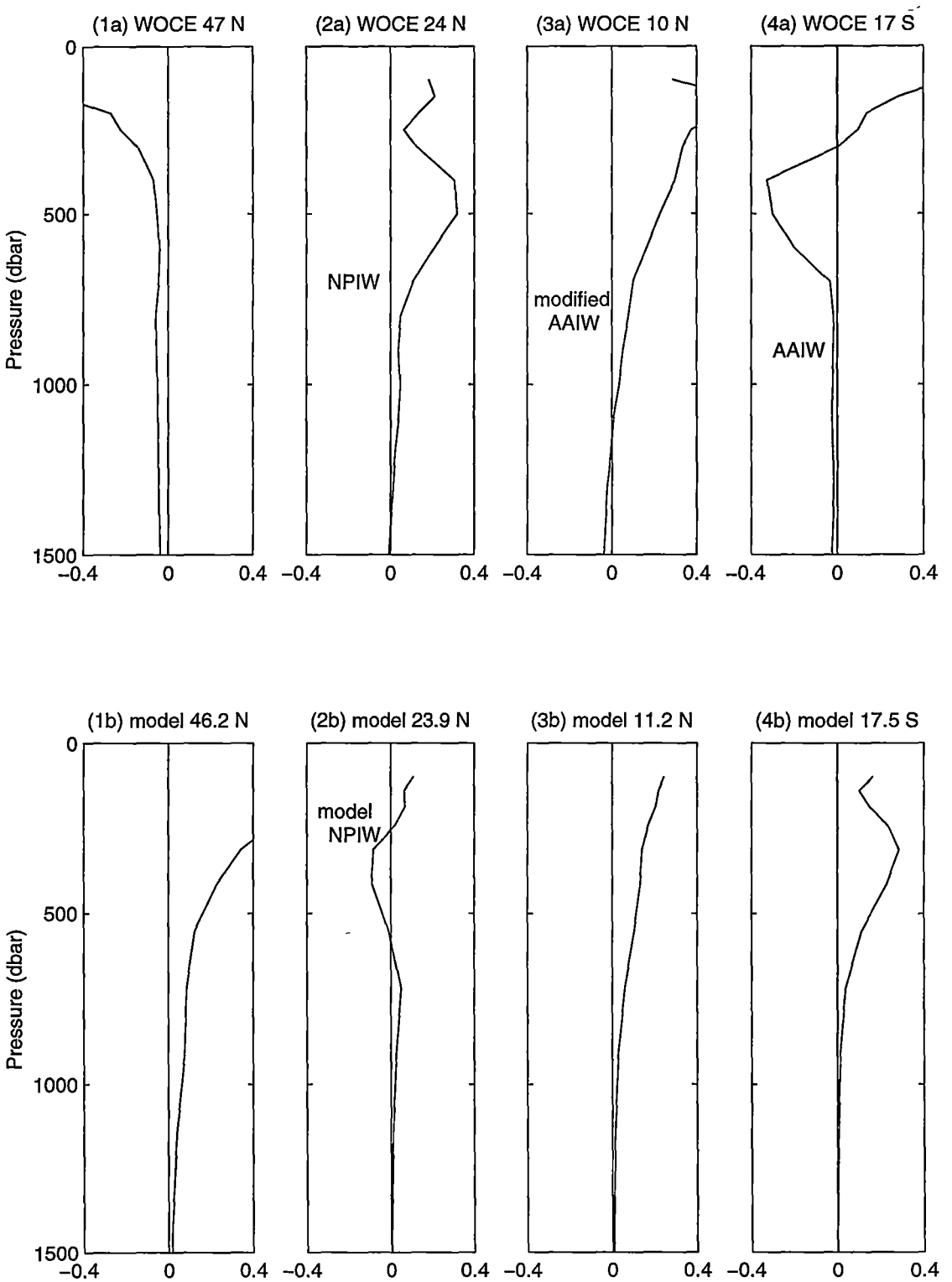

Figure 6.19: Differences in potential temperature (°C) on isobars, (top panel) between the WOCE data and the historical data, (bottom panel) according to the model response at the model WOCE time.

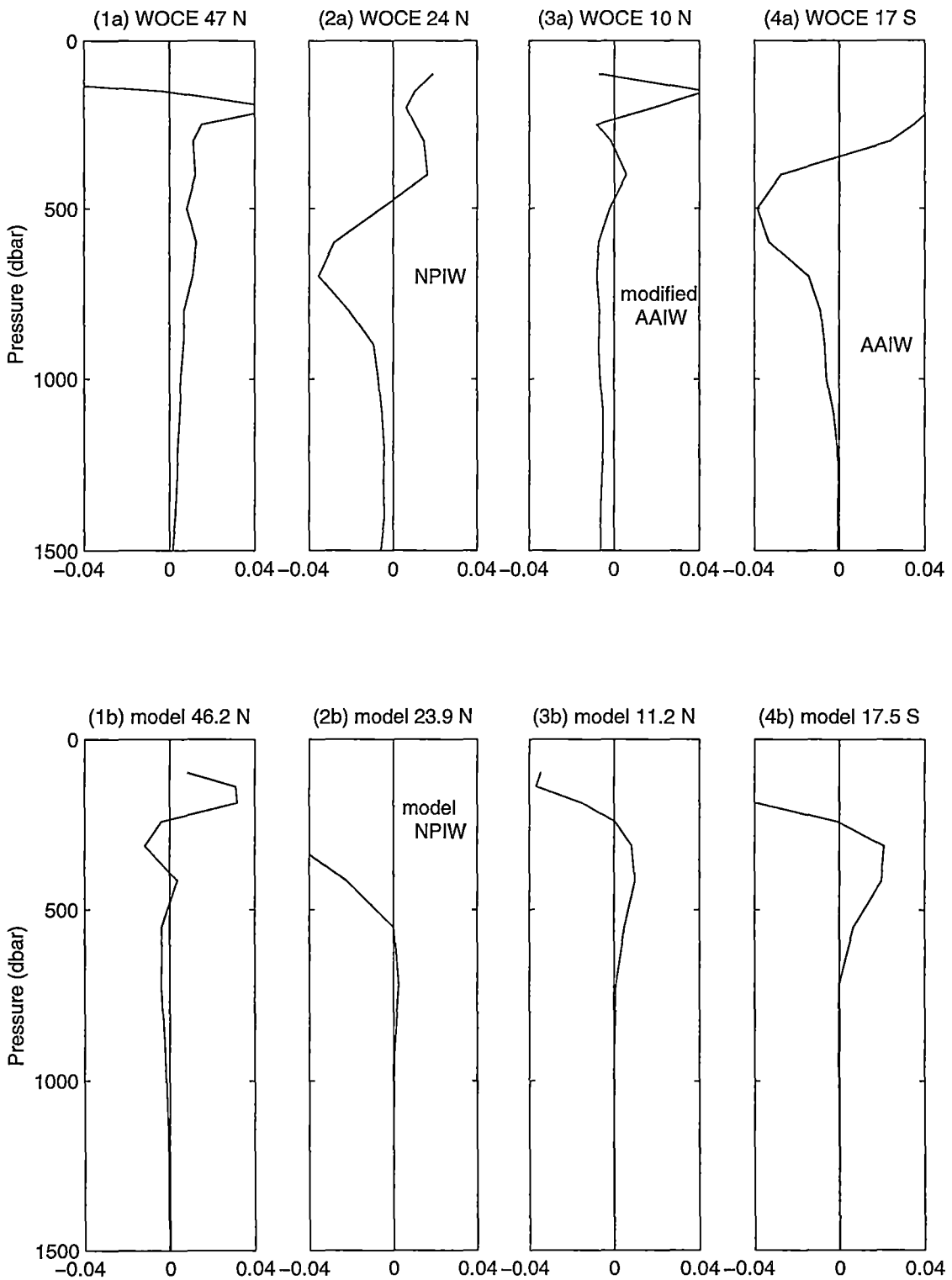

Figure 6.20: Differences in salinity (pss) on isobars, (top panel) between the WOCE data and the historical data, (bottom panel) according to the model response at the model WOCE time.

6.4 Summary

The model is poor in forming water masses, as is evident from the different θ-S curves between the model ocean and observations. However, it contains most of the large-scale wind-driven circulation features of the Pacific. By comparing the transient output with the control output, it is demonstrated that the model ocean responds to increasing atmospheric CO_2 with a general warming near the sea surface and in the ocean interior. In addition, there is a shift towards lower temperature and salinity on neutral surfaces in the subtropical gyres of the North and South Pacific oceans, on the 26.5 γ^n surface and the 27.5 γ^n surface, that is predominately due to a freshening of the water masses.

The 26.5 γ^n and 27.5 γ^n surfaces are the two representative isopycnals of NPIW and AAIW respectively in the model ocean, and their *pure freshening* response (Figure 6.18) corresponds to near-surface freshening at the outcropping areas (Figure 6.7). The spatial distribution of the magnitudes of their θ-S changes is also consistent with the geostrophic circulation, with the strongest changes found close to the source regions, and the weaker changes found downstream of the circulation path. All changes are larger in magnitude at double CO_2 time than at the model WOCE time.

Comparison of the transient integration with the control integration brings out changes in the model that are due to climate change rather than due to natural variability. Hence it is not surprising that the overall model response pattern does not fit all of the temporal differences observed along the WOCE transects. For example, the model does not show the effect of upward heaving and cooling of the water column along 47°N. Also, making zonal comparisons is not representative of the model's spatial response. For example, in the model, AAIW does not penetrate northwards to 17°S and 10°N, hence comparison of zonal averages between the model's transient salinity response and the observations along these two latitudes shows poor agreement (Figure 6.20). Moreover, the model's shallow salinity maxima do not show an increase in salinity, as in the observations.

However, qualitative agreements exist. The model's temperature response in the top 300 dbar agrees with the observed upper ocean warming in the subtropics. In addition, the freshening of the two intermediate salinity minima stands out as the main coherent signature in both the observations and the model response. In the model, the response at the model WOCE time are

similar to that at double CO_2 time, only at double CO_2 time, the spatial pattern of change is more coherent, and the magnitude larger. In other words, in the model, surface signals of increased atmospheric CO_2 have penetrated into the ocean interior already at the model WOCE time. This signature of freshening of the intermediate salinity minima therefore seems to be a fingerprint of the ocean's response to increasing atmospheric CO_2, at least in the Pacific, and the fact that observational data from the past 20 years show similar temporal changes tantalisingly suggests that the North and South Pacific oceans are beginning to show signs of the effect of increasing atmospheric CO_2. Of course, increased CO_2 forcing and natural variability in the Pacific, such as the Pacific Decadal Oscillation (Mantua et al. 1997) and the ENSO-like variability (Garreaud and Battisti 1999), may exhibit similar fingerprints. It remains to be shown, how much of the observed changes are due to natural variability.

Chapter 7

Discussion

In this discussion chapter, temporal differences in temperature and salinity observed along the five modern WOCE sections are integrated to provide an overall view of the freshwater, heat and steric sea level changes in the North and South Pacific oceans between the 1960s and the decade of 1985-94. Integrations are carried out along the four zonal WOCE sections, and area-weighted averages are estimated for the North and South Pacific oceans, which are divided into four zonal boxes around the four zonal lines. Because of this design, the meridional section along 210°E is not used in the overall estimation. These changes are discussed in relation to model responses and observations from other ocean basins, and their global implications are considered.

7.1 Pacific freshwater content change

Overall view of the salinity changes

Amongst all the observed differences between the WOCE data and the historical data, the most spatially coherent large-scale changes are the shift towards lower temperature and salinity on neutral surfaces in the intermediate salinity minima of North Pacific Intermediate Water (NPIW) and Antarctic Intermediate Water (AAIW), that is caused by a large-scale reduction in salinity in these two water masses. This observed ocean interior freshening implies a reduction in sea-surface salinity at areas where the corresponding isopycnals outcrop, which are the high latitudes oceans in the case of NPIW and AAIW. Unfortunately, the lack of sea surface P-E and salinity observations prevents direct verification of this implication. However, the latitudinal variation of the magnitudes of the changes decreasing towards the equator is

broadly consistent with the circulation of NPIW and AAIW, and so lends weight to the theory that this interior freshening is a result of sea-surface reduction of salinity being subducted into the ocean interior.

Figure 7.1 shows the zonally-averaged salinity changes on neutral surfaces ($\overline{S'|_n}$) along the four zonal WOCE sections. They are superimposed on a background of the mean salinity field of the central Pacific to show the magnitudes of the changes relative to the positions of NPIW and AAIW. The corresponding potential temperature changes on neutral surfaces ($\overline{\theta'|_n}$) contain the same spatial information as $\overline{S'|_n}$, and so are not shown.

From Figure 7.1, the shift towards lower temperature and salinity on neutral surfaces is seen to be generally coherent along the direction of movement of NPIW (approx. 26.8 γ^n) and AAIW (approx. 27.2 γ^n). In the North Pacific, although no distinct intermediate salinity minimum is present along 47°N, waters in the NPIW density range along 47°N have also experienced a reduction in salinity on neutral surfaces. The largest salinity reduction in the NPIW range occurs along 47°N, with a smaller reduction along 24°N, consistent with the increased distance of 24°N from the source of NPIW in the Kuril Islands/Kamchatka regions and in the Sea of Okhotsk (Talley (1991), Warner et al. (1996)). In the South Pacific, the main region where renewal of AAIW takes place is in the subantarctic zone in the southeast Pacific (McCartney (1977), Piola and Georgi (1982)). AAIW then flows north around the South Pacific subtropical gyre and crosses the equator in the far western Pacific (Tsuchiya 1991). The fact that freshening in AAIW along 17°S is stronger than that along 10°N is thus qualitatively consistent with the Pacific AAIW circulation pattern. Changes along the meridional WOCE P16 section at 210°E agrees with this overall pattern by displaying coherent freshening north of 44°S, along the AAIW density range.

Other studies in the southwest Pacific Ocean and the Indian Ocean have also shown similar spatially coherent freshening patterns that are consistent with the general circulation (Wong et al. 1999). In the Indian Ocean at 32°S (Bindoff and McDougall in press) and in the Tasman Sea at 43°S (Bindoff and Church 1992), freshening in the AAIW range has been recognised, with the Indian Ocean showing a stronger freshening (0.064 pss at 27.37 γ^n) than the Tasman Sea (0.007 pss at 27.37 γ^n). This is consistent with the Tasman Sea being more distant from the sources of AAIW than the Indian Ocean. In the southwest Pacific Ocean, Johnson and Orsi (1997) have also noted freshening of AAIW that is consistent with its advection, with the largest amplitudes at 48°S,

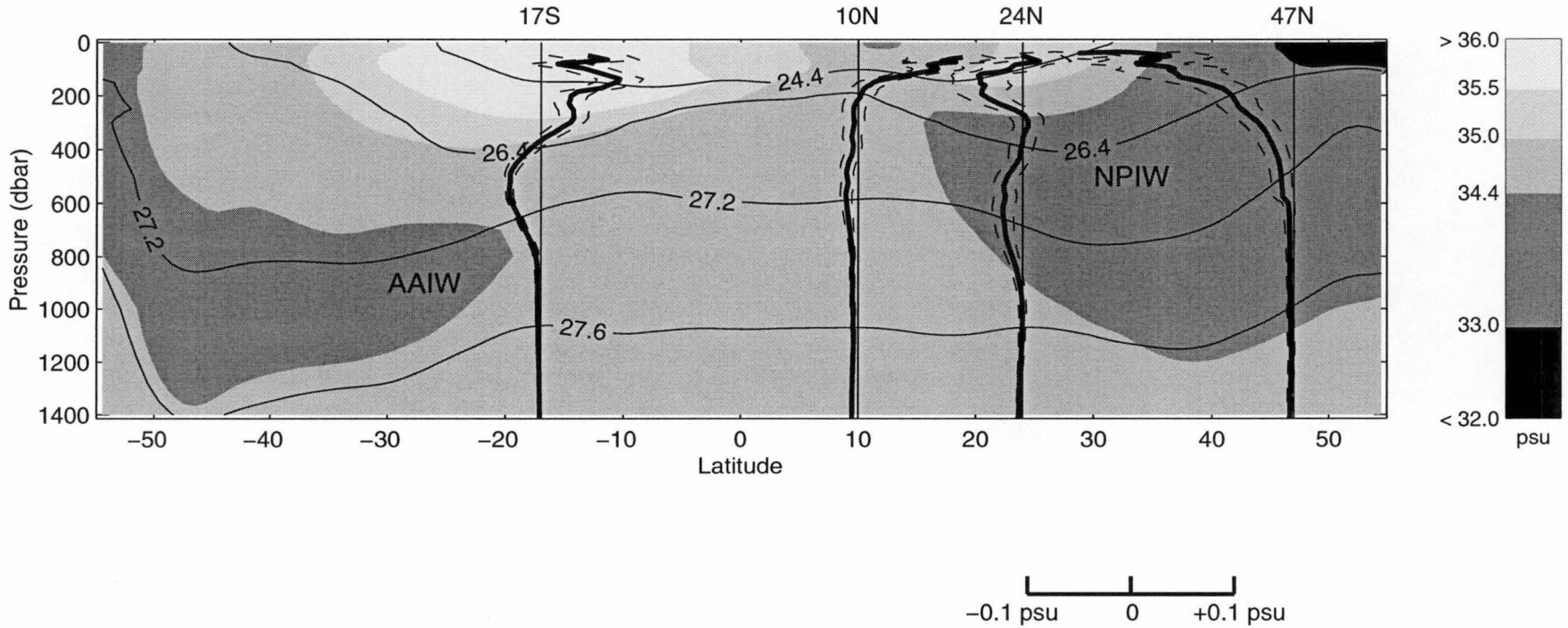

Figure 7.1: Zonally-averaged differences of salinity on neutral surfaces ($\overline{S'|_n}$) along the four zonal WOCE sections at 47°N, 24°N, 10°N, and 17°S (adapted from Wong *et al.* (1999)). Here, the differences on neutral surfaces (solid lines) have been plotted on pressure coordinates. The dashed lines mark the 90% confidence intervals. The background is the salinity field along 200°E in the Pacific Ocean from the Levitus (1982) dataset. Lines of constant neutral density are superimposed.

near where the water mass subducts, and decays in amplitude towards 20°S.

The transient response of a coupled climate model that has been forced by increasing atmospheric CO_2 also shows such a large-scale freshening signal in its ocean component, on the two neutral surfaces that correspond to NPIW and AAIW in the model Pacific (see Chapter 6). Moreover, the model freshening can be traced back to where the isopycnals outcrop, and corresponds to a reduction in sea-surface salinity. The spread of the freshening signature in the model's ocean interior also seems to follow the geostrophic flow of the model subtropical gyres.

The freshening of AAIW observed in the present study, at 10°N, 17°S and along the 210°E meridian, plus similar observations by Bindoff and Church (1992) in the Tasman Sea, by Johnson and Orsi (1997) in the southwest Pacific, and by Bindoff and McDougall (in press) in the Indian Ocean, combine to reveal the strikingly large spatial extent of the salinity reduction in this southern intermediate salinity minimum water. It is thus likely that the freshening of AAIW is not confined to the South Pacific and the Indian Ocean basins, but is circumpolar in extent. The implied increase in high-latitude net precipitation rate would therefore also be circumpolar in nature.

On the opposite side of the globe, NPIW displays the same freshening signature as AAIW. The North Atlantic, on the other hand, does not produce a major intermediate salinity minimum, but produces several deep water masses. One of the water masses that has its origin in the high latitudes of the North Atlantic is Labrador Sea Water (LSW), which is formed by deep wintertime convection in the Labrador Basin. Dickson et al. (1996) have been able to link LSW variability to the North Atlantic Oscillation. A recent study by Joyce et al. (1999) has shown that in the western part of the subtropical gyre between 20°N and 35°N, LSW has become colder and fresher since 1992. Curry et al. (1998) have been able to trace the penetration of this signal from the origin of LSW to the subtropical gyre. In the North Atlantic subtropical gyre, changes in LSW are found at $\approx$ 2000 m. For comparison, changes in NPIW are found at $\approx$ 700 m in the North Pacific subtropical gyre. This shows that sea surface conditions at the North Atlantic are able to translate to deeper waters than in the North Pacific, because of the stronger vertical convective activities in the North Atlantic. Information obtained from this kind of inter-basin comparison is useful for validating the effectiveness of coupled atmosphere-ocean models in transmitting atmospheric forcings to the interior of various ocean basins.

In addition to the large-scale mid-depth salinity decrease, the shallower

waters ($\approx$ 24.4 γ^n) along 24°N, 10°N and 17°S, which originate from the high evaporative regions of the subtropical gyres, have all shown an increase in salinity between the WOCE data and the historical data (Figure 7.1). Results from the meridional WOCE P16 section along 210°E agree with the salinification of the shallower waters south of the equator, but not north of the equator. However, shallow water results along the 210°E meridian are likely to be affected by the 1991-92 El Niño event. The implied net evaporation increase over the subtropics in the Pacific, and the implied net precipitation increase over the polar gyres, suggest a strengthening of the atmospheric hydrological cycle over the study period.

Freshwater content change

Since salt is conserved in the ocean, changes in salinity are the result of addition or removal of freshwater to or from the ocean. For a column of water with 1 m^2 cross-sectional area and H m in depth, changes in its freshwater content and its salinity have the relation:

$$H \cdot \overline{S} = (H + \triangle f) \cdot (\overline{S} + \overline{\triangle s})$$

where H (in metres) is the depth of the water column, $\overline{S}$ is the average salinity of the water column, $\triangle f$ (in metres) is the change in height of the water column due to addition or removal of freshwater, and $\overline{\triangle s}$ is the average resultant decrease or increase in salinity in the water column. Upon expansion, the above equation becomes:

$$\triangle f \cdot \overline{S} + H \cdot \overline{\triangle s} + \triangle f \cdot \overline{\triangle s} = 0$$

Because the last term $\triangle f \cdot \overline{\triangle s}$ is small relative to the other two terms, to first order accuracy, the above equation can be written as:

$$\triangle f = - \frac{H \cdot \overline{\triangle s}}{\overline{S}} \tag{7.1}$$

A positive $\triangle f$ indicates an increase in height of the water column due to addition of freshwater, and results in a negative $\overline{\triangle s}$, indicating a resultant decrease in salinity.

Along a hydrographic section from $cast_a$ to $cast_b$, the overall change in salinity $\overline{\triangle s}$ of the water column bounded by two neutral surfaces γ_x^n and γ_y^n can

be calculated as a sectional area-weighted average, by:

$$\overline{\triangle s} = \frac{1}{area} \sum_{i=x}^{y-1} \triangle s_i \tag{7.2}$$

where

$$\triangle s_i = \int_{\gamma_i^n}^{\gamma_{i+1}^n} \int_{cast_a}^{cast_b} S'|_z \; dl \, dz_\gamma$$

where l (in metres) is the horizontal distance between casts along the hydrographic section, z_γ (in metres) is the vertical distance between the two neutral surfaces, $S'|_z$ is the temporal change in salinity at the time-average depths of respective neutral surfaces at each cast, and $area = \int\int dz_\gamma \, dl$ is the vertical area between the two surfaces along a section.

In other words, $S'|_z$ is first integrated zonally for each neutral density layer, then summed vertically and divided by the total area of the water column to obtain the overall change in salinity $\overline{\triangle s}$. The advantage of calculating $\overline{\triangle s}$ in this manner is that the vertical distribution of $\triangle s_i$ can be examined to show which neutral density layer contributes more to the overall salinity change. Furthermore, H can be calculated as $area/L$, where $L = \int dl$. Note that because differences on isobars $S'|_z$ is used, the overall change in salinity $\overline{\triangle s}$ calculated as such is the combined result of isopycnal heaving as well as water mass property changes.

In the vertical integration, the upper limit γ_y^n has been chosen to exclude the highly variable surface mixed layer where objective estimates are unrealistic. Inclusion of the mixed layer will cause the integration result to vary by as much as 100%. The lower limit γ_x^n represents the deepest surface below which temporal differences cannot be separated from instrumental errors. These levels have been discussed in details in Chapters 4 and 5, and are listed in Table 7.1. In the zonal integration, the western and eastern boundaries have been excluded, as has also been discussed in previous chapters.

	P1 at 47°N	P3 at 24°N	P4 at 10°N	P21 at 17°S
upper limit γ^n level (approx. pressure)	26.6 γ^n (130 dbar)	25.1 γ^n (160 dbar)	23.5 γ^n (85 dbar)	25.5 γ^n (200 dbar)
lower limit γ^n level (approx. pressure)	27.4 γ^n (650 dbar)	27.5 γ^n (990 dbar)	27.9 γ^n (1950 dbar)	27.7 γ^n (1290 dbar)

Table 7.1: Upper and lower γ^n levels for vertical integration.

Figure 7.2 plots the distribution of the area-weighted and zonally-integrated salinity change $\triangle s_i$ for each neutral surface layer, along the four zonal WOCE sections, to show the contribution by each layer to the overall change in salinity. Note that these are differences on isobars, and so are not the same as those shown in Figure 7.1, which are the zonally-integrated (but not area-weighted) salinity differences on neutral surfaces, and so do not contain the effects of vertical movements of isopycnals.

Along all four sections, a clear change in $\triangle s_i$ occurs in the 26.3 to 27.0 γ^n range. These correspond to a change in regime in the water mass thermohaline properties. Along 47°N, the change occurs at the base of the thermocline. Below the thermocline, upward displacements of isopycnals contribute to increases in salinity. Along 24°N, 10°N, and 17°S, where an intermediate salinity minimum exists, the change in sign of $\triangle s_i$ occurs in the transition zone between salty upper waters and low-salinity intermediate waters. The upper waters give an overall salinity increase and the waters below give an overall reduction in salinity. However, this vertical distribution is not balanced, and the salinity decrease in the intermediate and deep waters is greater than the salinity increase in the upper waters. It is estimated that the salinity increases in the upper layers balance the salinity reductions below 26.5 γ^n by 60% along 24°N, by 56% along 10°N, and by only 29% along 17°S.

Most of the water masses in the upper layers along these three sections have a subtropical origin, while those in the intermediate layers acquire their properties near the polar gyres. Extrapolating the overall salinity changes along these three sections to the rest of the subtropical Pacific suggests that there is a net freshwater loss from the subtropics that is not balanced by the freshwater gain in the polar gyres. In other words, the implied increase in evaporation over the subtropics is not balanced by the implied increase in precipitation over the polar gyres. However, the spatial sampling inadequacy means that the extrapolation contains large errors. For example, along the meridional WOCE section at 210°E, south of the equator to about 20°S, in the region where the vertical distribution of $\triangle s_i$ is similar to 24°N, 10°N and 17°S, the overall salinity change is actually a net increase. The exclusion of the mixed layer might also contribute to the freshwater budget imbalance. Although the salinity increase in the shallower waters does not exactly balance the salinity reduction in the deeper waters, the combined observations suggest a strengthening of the atmospheric hydrological cycle over the Pacific between the historical and WOCE periods (Wong et al. 1999).

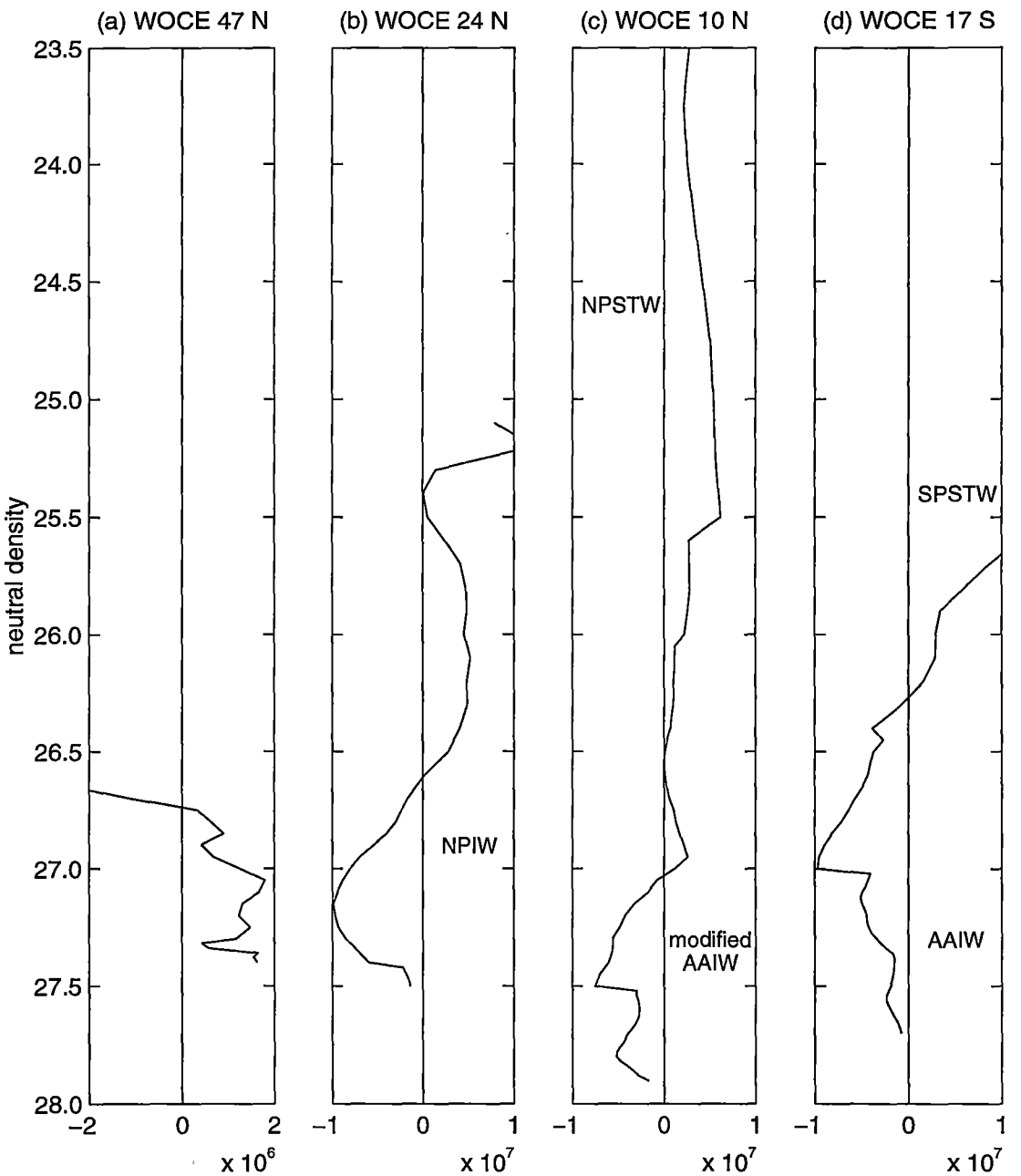

Figure 7.2: The distribution of the area weighted and zonally integrated salinity change $\triangle s_i$ (pss m^2) for each neutral surface layer, along the four zonal WOCE sections. Note that the scale for (a) is different from (b), (c) and (d).

Even though the South Pacific estimate is only based on one section, extrapolating the changes observed in AAIW to the entire South Pacific is useful in providing an estimate for the implied freshwater gain in its source region. This is done by assuming that all sea surface freshwater gain in the outcropping region that is subducted into the mixed layer is advected to the ocean interior without loss to mixing. Despite the inherent errors associated with such extrapolations and assumptions, these estimates are useful in verifying numerical model outputs, especially at the southern high latitudes, where precipitation observations over the ocean are sparse.

Based on observations along the WOCE P21 section at 17°S and the P16 section at 210°E, the average thickness of AAIW in the South Pacific is about 500 m. From the salinity map in Reid (1965), AAIW in the South Pacific is found between approximately 15°S and 55°S (the region bounded by the 34.2 and 34.5 contours on the $\delta_T = 80$ cl/ton surface). Between 150°E and 280°E, this area is approximately 5.24×10^7 km^2. This gives the volume of AAIW in the South Pacific to be about 2.62×10^7 km^3. Based on the average decrease in salinity in South Pacific AAIW being -0.02 pss, then the amount of inferred freshwater gain in the source region of AAIW is 76.38 cm over roughly 25 years, which is equivalent to 31 mm/yr. This calculation is based on the source region of AAIW being the Polar Frontal Zone, which is a circumpolar belt at roughly 60°S $\pm$ 5° latitude (approx. 2×10^7 km^2 in area). According to the precipitation data from GASP (Budd et al. 1995), this estimated 31 mm/yr of freshwater gain is about 8.5% of the annual P-E rate over the ocean south of 55°S.

Coupled climate model experiments indicate that, as a result of atmospheric CO_2 increase, the surface salinity of the ocean in the polar latitudes shows a general freshening that is caused by increases in most components that make up the freshwater flux (P-E, runoff from land, and ice melt). Gordon and O'Farrell (1997) estimated an increase in freshwater flux of 21 mm/yr for the circumpolar ocean south of 60°S, over 70 years to about the time of CO_2 doubling. The 31 mm/yr (over 25 years) freshwater gain in the circumpolar Polar Frontal Zone inferred from observations is therefore 1.5 times larger than these model experiment results for CO_2 doubling. In the absence of direct observations of precipitation over the oceans, especially at the southern high latitudes, it is difficult to confirm the estimated freshwater gain. However, it is the same reason that makes observational studies such as this one invaluable for validating model simulations on climate change and climate variability.

The overall area-weighted salinity change $\overline{\triangle s}$ (Equation 7.2), and the

inferred amount of freshwater input/output $\triangle f$ (Equation 7.1), are listed in Table 7.2. Along the three sections with an intermediate salinity minimum, the overall salinity change is a net loss: -0.0049 pss along 24°N, -0.0016 pss along 10°N, and -0.0068 pss along 17°S. These net results are close to instrumental precisions for salinity observations. The freshwater input/output to/from each section, inferred from the observed salinity change, as given by Equation 7.1, is less than 1 cm/yr (see Table 7.2). Observation of salinity differences in the ocean interior could therefore be a sensitive tool for monitoring changes to surface P-E rates for long time scales.

	P1 at 47°N	P3 at 24°N	P4 at 10°N	P21 at 17°S
$\overline{\triangle s}$ (pss)	0.0038	-0.0049	-0.0016	-0.0068
$\overline{S}$ (pss)	33.8	34.3	34.6	34.7
$\triangle f$ (cm)	-4.8	10.0	8.3	19.1
average time between WOCE and historical data (yr)	19	15	20	27
$\triangle f$ per annum (cm/yr)	-0.25	0.66	0.42	0.71

Table 7.2: Area-weighted averages of the observed temporal salinity change $\overline{\triangle s}$, and the inferred freshwater input/output $\triangle f$, along the four zonal WOCE sections. The depth ranges for integration are listed in Table 7.1. Negative $\overline{\triangle s}$ indicates an overall decrease in salinity, and the inferred $\triangle f$ will be positive, indicating freshwater input into the section.

Along P1 at 47°N, the only WOCE section in this thesis that does not exhibit a distinct salinity minimum, the entire water column below 26.7 γ^n gives an area-weighted increase in salinity that is more the result of upward displacement of isopycnals, resulting in a salinity net gain of 0.0038 pss (Table 7.2).

Overall, the area-weighted salinity change in the North Pacific between 47°N, 24°N and 10°N is a net loss of -0.0014 pss. In the South Pacific, because 17°S is the only zonal section, its average salinity change of -0.0068 pss is taken to be the South Pacific salinity net loss estimate. The meridional P16 section at 210°E qualitatively supports this estimate by showing an overall salinity loss south of 15°S.

7.2 Pacific heat content change

Overall view of the temperature changes

Figure 7.3 shows the zonally-averaged differences of potential temperature on isobars along the four zonal WOCE sections. Along 24°N, 10°N and 17°S, the top 300 dbar of the water column exhibits higher potential temperatures on isobars, that is a combination of warming of the water masses and downward displacements of isopycnals. This observed warming is reproduced in the model's transient response to increasing CO_2. The meridional section along 210°E shows cooling at 10°N and 17°S, but warming in the equatorial region. This disparity may also be due to the 1991-92 El Niño event.

Below 300 dbar, the observed temperature differences do not seem to follow the circulation of water masses (Figure 7.3). In the NPIW density range, cooling has been observed along 47°N, but warming along 24°N. Antonov (1993) found that negative trends in ocean temperature dominated the North Pacific subtropical and subpolar gyres below 300 dbar, between 1957 and 1981. The observed opposite trends in temperature therefore may be part of the Pacific natural variability, such as the cyclic thermal anomaly described by Zhang and Levitus (1997). Similarly, in the AAIW density range, cooling has been observed along 17°S, but warming along 10°N and 210°E.

In general, the observed salinity changes seem to follow the circulation on isopycnals more closely than the observed temperature changes. Nonetheless, the success in detecting the general spatial coherence of the changes shows that the method of using objective mapping to interpolate randomly distributed data is a suitable tool for the type of large-scale comparisons as presented in this thesis. The objective mapping method does not yield satisfactory results in the shallow waters, where seasonal and interannual variability dominates, and in the equatorial region, where the effects of El Niño events are more directly felt. However, for the majority of the ocean basins, this method is very useful in detecting decadal-scale changes.

Heat content change

Unlike salt content of the global ocean, which is a conserved quantity, ocean temperature, or its heat content, is not conserved. The heat content change $\triangle Q$ of a parcel of water which has undergone an average temperature

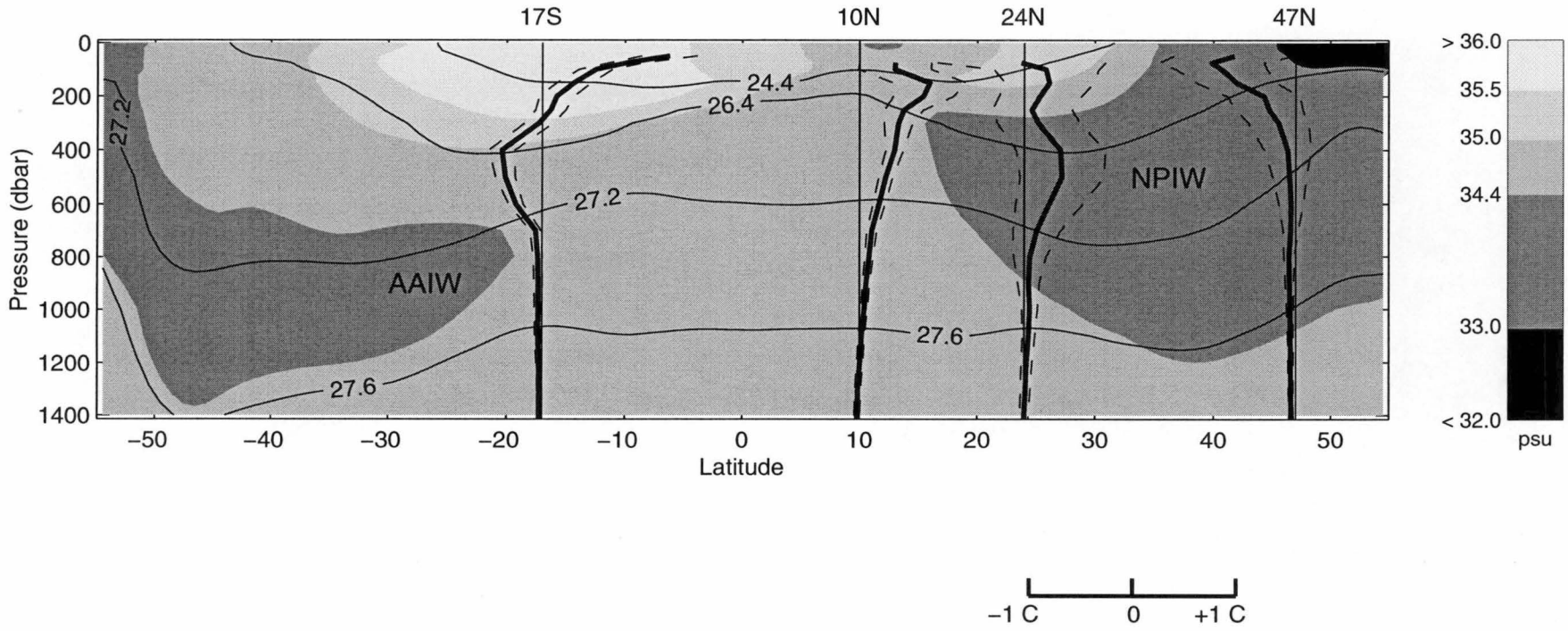

Figure 7.3: Zonally-averaged differences (solid lines) of potential temperature on isobars ($\overline{\theta'|_z}$) along the four zonal WOCE sections at 47°N, 24°N, 10°N, and 17°S. The dashed lines mark the 90% confidence intervals. The background is the salinity field along 200°E in the Pacific Ocean from the Levitus (1982) dataset. Lines of constant neutral density are superimposed.

change of $\overline{\triangle\theta}$ is:

$$\triangle Q = V \cdot \rho \cdot C_p \cdot \overline{\triangle\theta}$$

where V (in m^3) is the volume of the parcel of water, ρ (in kg m^{-3}) is the density of the parcel of water, and C_p (in J K^{-1} kg^{-1}) is the specific heat of the water parcel at constant pressure p. Strictly speaking, $\overline{\triangle\theta}$ in this case is measured in K (Kelvin), although in practice, difference in temperature measured in °C is the same as difference in temperature measured in Kelvin. The resulting heat content change $\triangle Q$ has unit in J (Joules).

Along a hydrographic section, similar to $\overline{\triangle s}$ in Equation 7.2, the overall change in potential temperature $\overline{\triangle\theta}$ can be calculated as:

$$\overline{\triangle\theta} = \frac{1}{area} \sum_{i=x}^{y} \triangle\theta_i \tag{7.3}$$

where

$$\triangle\theta_i = \int_{\gamma_i^n}^{\gamma_{i+1}^n} \int_{cast_a}^{cast_b} \theta'|_z \; dl \, dz_\gamma$$

where $\theta'|_z$ is the temporal change in potential temperature at the time-averaged depths of respective neutral surfaces at each cast, and all other notations are the same as in Equation 7.2. Note again that because differences on isobars $\theta'|_z$ are used, the integrated result combines water mass changes and changes in depths of the isopycnals.

Figure 7.4 plots the distribution of the area-weighted and zonally-integrated potential temperature change $\triangle\theta_i$ as a function of neutral density, along the four zonal WOCE sections, to show the contribution of each layer to the overall change in temperature. Note that these are similar to the differences shown in Figure 7.3, which are the arithmetic means of potential temperature differences on isobars along the various sections.

Unlike changes in salinity, where the upper waters exhibit different changes to the intermdiate layers, the distribution of temperature change shows no such vertical features. In fact, the vertical distribution is almost monotonic with depth. In the subarctic Pacific, the entire water column experienced heat loss along 47°N, with the biggest loss being through the shallower layers, and lesser through the deeper levels (Figure 7.4 a). On the other hand, in the subtropical and tropical North Pacific, the water column down to 27.5 γ^n ($\approx$ 1000 dbar) has gained heat. Along 24°N, the largest amount of heat gain is at the 26.5 γ^n level, while along 10°N, the largest heat gain is at the 27.0 γ^n level (Figure 7.4 b,c). These are the upper density ranges of NPIW and

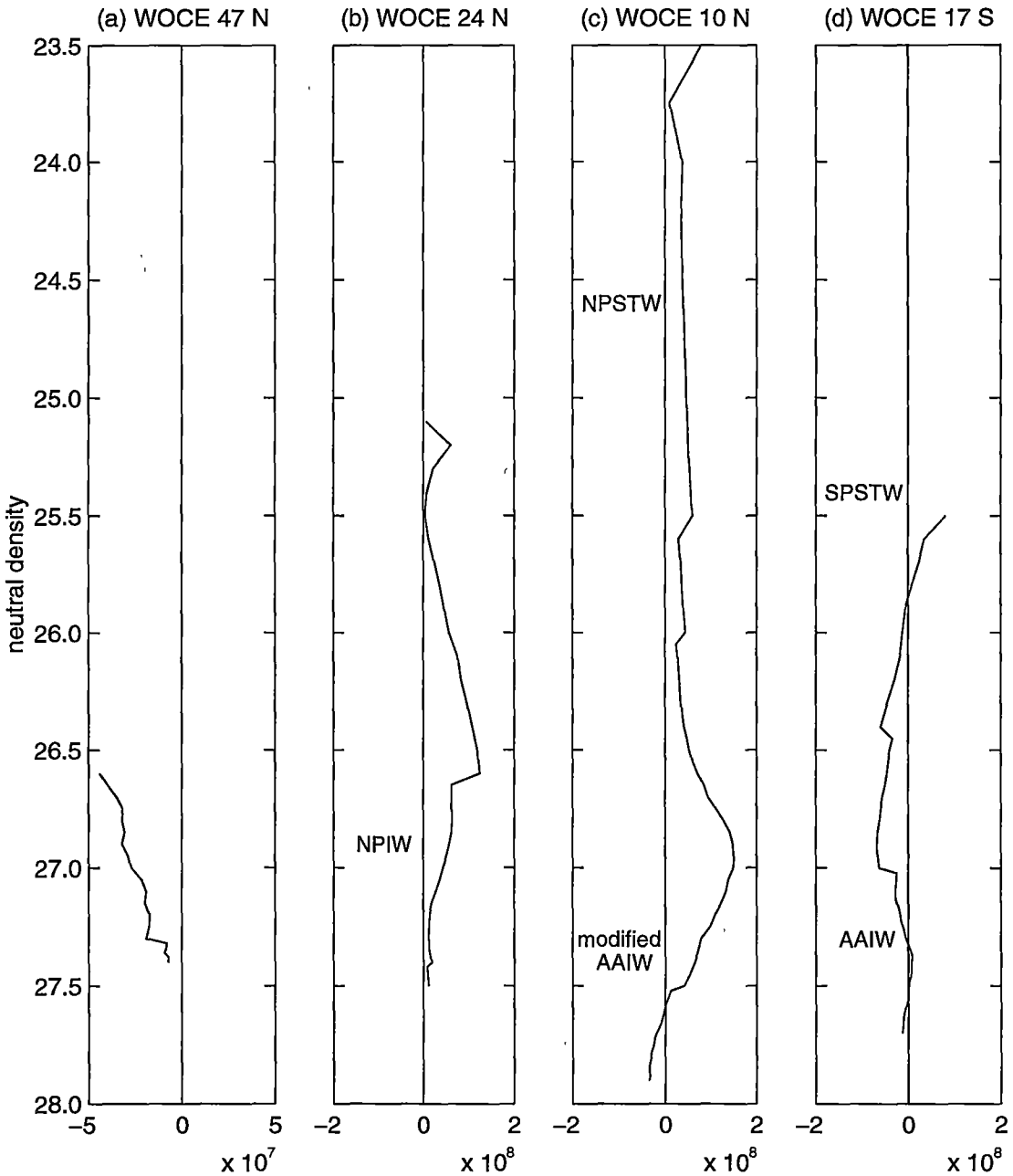

Figure 7.4: The distribution of the area weighted and zonally integrated potential temperature change $\triangle\theta_i$ (°C m^2) for each neutral surface layer, along the four zonal WOCE sections. Note that the scale for (a) is different from (b), (c) and (d).

modified AAIW respectively, and are both at about 500 dbar.

For comparison, in the North Atlantic along 24°N, the maximum warming has been observed at about 1100 dbar, and continues down to 2000 dbar (Bryden et al. 1996). Similarly, the time-series at Bermuda ($\approx$ 32°N) shows long-term warming in the deeper waters between 1500-2500 dbar (Joyce and Robbins 1996). Recent findings by Joyce et al. (1999) have shown that the western part of the North Atlantic subtropical gyre between 20°N and 35°N have experienced significant warming between 800 and 2500 m from 1954-58 to 1997. Thus, relative to the subtropical North Atlantic, the subtropical North Pacific has gained heat at shallower depths. The more active vertical convection in the North Atlantic might account for the difference in maximum change depths between these two oceans.

Within the North Pacific itself, the opposite trends in temperature change that have been observed between the subarctic (47°N) and the subtropical (24°N and 10°N) gyres are in agreement with other studies on decadal variability in the ocean interior. For example, Zhang and Levitus (1997) revealed a subsurface (250 m) thermal anomaly that circulates around the North Pacific in a clockwise manner, and could account for the observed opposite trends. Levitus et al. (1994) have also shown a quasidecadal oscillation in the temperature anomaly field at 125 m in the North Atlantic Ocean.

In the South Pacific, the P21 section at 17°S behaves differently from the other three zonal sections in the North Pacific, in that there is a change of sign in the vertical heat change profile. Above 26.0 γ^n, the water column has gained heat; below 26.0 γ^n, the water column has mostly lost heat (Figure 7.4 d). The biggest heat loss is near the 27.0 γ^n level, which is the upper density range of AAIW along 17°S.

The WOCE P16 section at 210°E shows meridional variation to this pattern. Around 17°S ($\pm$10° latitude), the water column below 300 dbar ($\approx 26.5\,\gamma^n$) shows mostly cooling, and so supports the observation along the WOCE P21 section at 17°S. However, south of about 25°S, where the main body of Subantarctic Mode Water (SAMW) and AAIW is found along 210°E, the water column shows warming to 1000 dbar ($\approx 27.4\,\gamma^n$). Similarly, Bindoff and Church (1992) have found that in the Tasman Sea along 43°S, the largest warming was found near 700 dbar. Hence the opposite temperature trends observed below 300 dbar along 17°S and south of 25°S along the 210°E meridian may be a decadal-scale variability pattern in the South Pacific, that is similar to that in the North Pacific as described by Zhang and Levitus (1997).

The average heat content change $\triangle Q$ along a section as a result of the temperature differences is then given by:

$$\triangle Q = \rho \cdot C_p \cdot \overline{\triangle \theta} \cdot H \tag{7.4}$$

and has unit in Jm^{-2}. H (m) is the average depth of the water column, as defined in Equation 7.1. Table 7.3 lists the overall observed potential temperature change and the resultant heat content change along the four zonal WOCE sections. The specific heat of a water parcel is a function of pressure, temperature and salinity (Gill 1982). Here, C_p is taken to be 3.99×10^3 J K^{-1} kg^{-1}, which is the specific heat of seawater with $S = 35$ at surface pressure. Other C_p values are within $\pm 0.2 \times 10^3$ of this value. ρ is taken to be 1028 kg m^{-3} as the average density of seawater. All limits in the vertical and zonal integrations are the same as in Table 7.1.

	P1 at 47°N	P3 at 24°N	P4 at 10°N	P21 at 17°S
$\overline{\triangle \theta}$ (K or °C)	−0.1475	0.1701	0.0930	−0.0558
$\triangle Q$ ($\times 10^8$ Jm^{-2})	−2.55	4.82	6.73	−2.23
average time between WOCE and historical data (yr)	19	15	20	27
$\triangle Q / \triangle t$ (Wm^{-2})	−0.4253	1.0182	1.0663	−0.2617

Table 7.3: Area-weighted averages of the observed temporal potential temperature change $\overline{\triangle \theta}$, and the resultant heat content change $\triangle Q$, along the four zonal WOCE sections. The depth ranges of integration are shown in Table 7.1. Positive $\overline{\triangle \theta}$ indicates an overall increase in potential temperature, and results in a positive $\triangle Q$, indicating a heat gain by the section.

Overall, along 47°N and 17°S, the ocean has lost heat that amounts to -0.4253 Wm^{-2} and -0.2617 Wm^{-2} respectively, while along 24°N and 10°N, the ocean has gained heat of the amounts 1.0182 Wm^{-2} and 1.0663 Wm^{-2} respectively. Comparatively, between 1500 and 2500 dbar at Bermuda, the rate of temperature rise amounts to 0.7 Wm^{-2} (Joyce and Robbins 1996). The resulting rate of heat content change of 1.1082 Wm^{-2} along 24°N is comparable to estimates from coupled climate models of oceanic heat flux for doubling of atmospheric CO_2 along similar latitudes averaged around the globe (about 1.33 Wm^{-2} from Manabe et al. (1990)).

The largest overall temperature change is 0.1701°C per 15 years

(0.007°C/yr) along 24°N ($\approx$ 1970 to 1985), between 160 and 990 dbar. This is larger than the deep observations in the North Atlantic of 0.1°C per 25 years (0.004°C/yr), between 800 and 2500 m (1957 to 1981) (Antonov 1993), and of 0.57°C per century (0.0057°C/yr) in the western North Atlantic between 800 and 2500 m (1954-58 to 1997) (Joyce et al. 1999).

Between P1, P3 and P4, the overall area-weighted (horizontal area) heat content change in the North Pacific is a net gain of 4.07×10^8 Jm^{-2}. In the South Pacific, because P21 is the only zonal section, its overall heat loss of 2.23×10^8 Jm^{-2} is taken to be the South Pacific net heat loss estimate.

7.3 Pacific steric height change

The halosteric and thermosteric changes discussed in the previous two sections combine to give a total steric height change estimate between the WOCE period and the historical data period. To calculate the steric height change, or sea level change, as a result of the observed temporal temperature and salinity differences ($\theta'|_z$ and $S'|_z$), the Equation of State for seawater in the form $\triangle\rho/\rho = \beta S'|_z - \alpha\theta'|_z$ is used. The depth-integrated steric height change $\triangle h$ (in metres) is calculated as:

$$\begin{aligned} \triangle h &= \int_{\gamma_x^n}^{\gamma_y^n} \triangle\rho/\rho \, dz_\gamma \\ &= \int_{\gamma_x^n}^{\gamma_y^n} \beta S'|_z - \alpha\theta'|_z \, dz_\gamma \\ &= \int_{\gamma_x^n}^{\gamma_y^n} \beta S'|_z \, dz_\gamma - \int_{\gamma_x^n}^{\gamma_y^n} \alpha\theta'|_z \, dz_\gamma \end{aligned} \tag{7.5}$$

Figure 7.5 shows the profile of sea level change $\triangle h$ along the four zonal WOCE sections. The limits of integration are the same as in Table 7.1. Positive $\triangle h$ means that sea level has risen. The vertical distributions of the halosteric and thermosteric contributions are similar to Figures 7.2 and 7.4, and so are not shown. Also similar to the freshwater content change and the heat content change, the steric height change is due to vertical isopycnal movements, that are the result of non density-compensating water mass property changes (see Chapter 2) and vertical heave (without water mass changes).

The largest amplitudes of sea level change occur along 10°N (−15 cm to 31 cm, relative to about 2000 dbar), and the smallest occur along 47°N (−5 cm to 4 cm, relative to about 650 dbar). In particular, along 47°N and east of 207°E, sea level has risen in the order of 1 mm/yr (relative to 650 dbar)

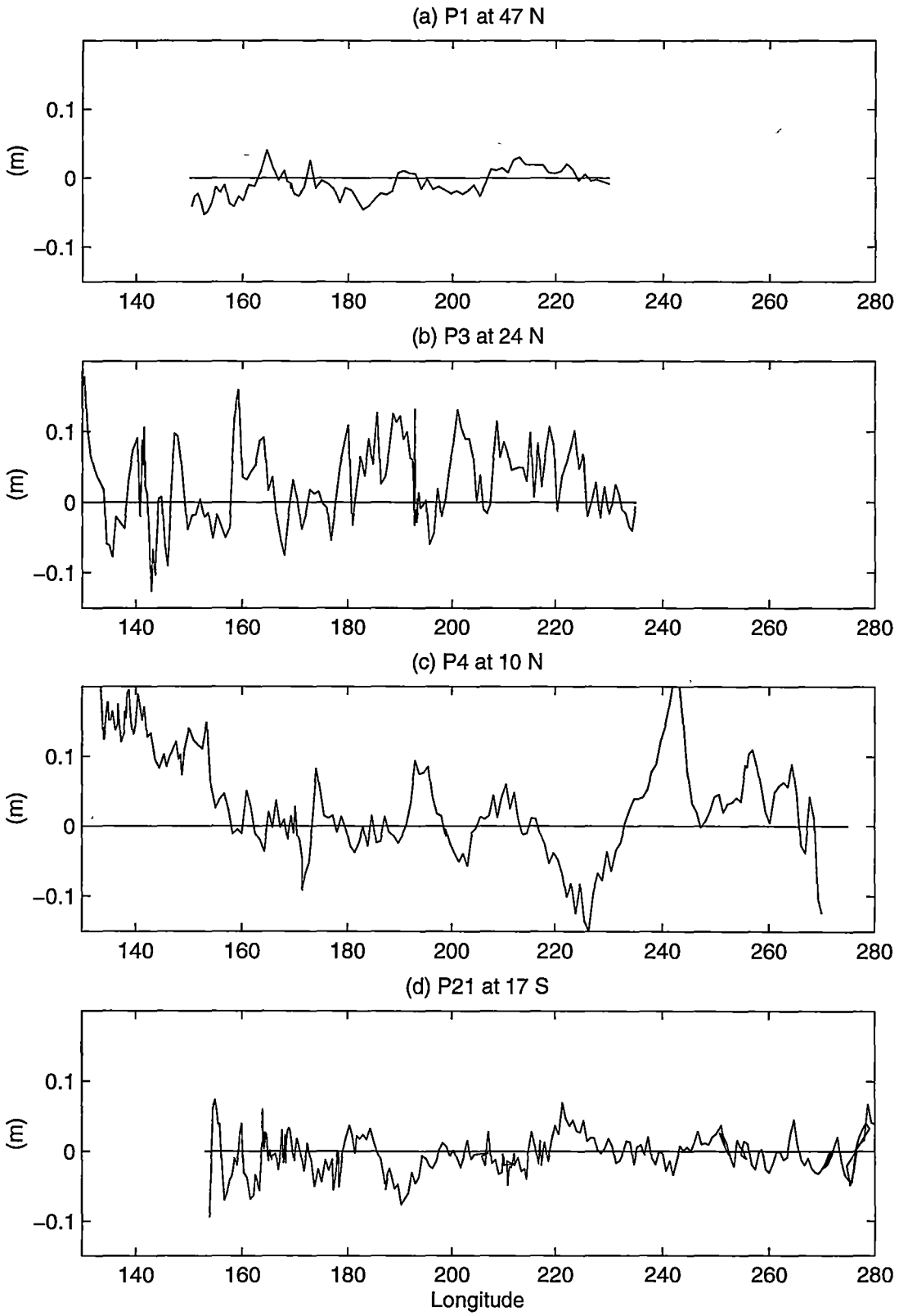

Figure 7.5: Depth-integrated steric height change $\triangle h$ (m) along the four zonal WOCE sections, between the WOCE data and the historical data. The depth ranges of integration are shown in Table 7.1. Positive $\triangle h$ means that sea level has risen. Note that all four profiles have been plotted on the same longitudinal and vertical axes to ease comparison.

between the WOCE period and the historical data period. This estimate is consistent with steric height trends relative to 1000 dbar in the northeast Pacific Ocean, measured at Ocean Station PAPA at 50°N, 145°W (Thomson and Tabata 1987). At about 230°E along 24°N, sea level has also risen in the order of 1 mm/yr (relative to 990 dbar), which is consistent with observations along the southwest U.S. coast by Roemmich (1992).

Table 7.4 lists the average steric height change along each of the four zonal WOCE sections, and the respective thermosteric and halosteric components. It is obvious that in the open ocean away from coastal processes, thermosteric effect dominates the total steric height change. In particular, the thermosteric component accounts for 85-94% of the sea level rise along 24°N and 10°N.

	P1 at 47°N	P3 at 24°N	P4 at 10°N	P21 at 17°S
average steric sea level change (mm)	−9.4	26.6	41.8	−4.2
thermosteric component (mm)	−7.7	22.5	39.4	−9.9
halosteric component (mm)	−1.7	4.1	2.4	5.7
% steric sea level change*				
due to $\alpha\theta'\|_z$	82%	85%	94%	63%
due to $\beta S'\|_z$	18%	15%	6%	37%
average steric sea level change per yr (mm/yr)	−0.49	1.77	2.09	−0.15

Table 7.4: Average steric height changes along the four zonal WOCE sections, and the respective thermosteric ($-\int \alpha\theta'|_z dz_\gamma$) and halosteric ($\int \beta S'|_z dz_\gamma$) components. * % steric sea level change due to $\alpha\theta'|_z$ is calculated as $|\alpha\theta'|_z|/(|\alpha\theta'|_z| + |\beta S'|_z|)$. Similarly for % steric sea level change due to $\beta S'|_z$.

The steric sea level rise along 24°N and 10°N far outweights the sea level drop along 47°N and 17°S. Overall, the area-weighted steric height change for the North Pacific from 60°N to 3.5°S, based on the three sections at 47°N, 24°N and 10°N, is estimated to be a rise of 1.4 mm/yr. If the South Pacific section at 17°S is included in the estimate, then the area-weighted steric height change from 60°N to 31.5°S is a rise of 0.85 mm/yr. Therefore, because of significant ocean warming from the subtropical North Pacific, the overall steric sea level in the Pacific has risen in the 20 years between the 1960s and 1985-94.

Studies from other regions have also quoted similar sea level rise estimates. For example, in the Tasman Sea, Bindoff and Church (1992) estimated a steric sea level increase of 2 to 3 mm/yr over 22 years. In the western subtropical

North Atlantic, Joyce et al. (1999) estimated a steric sea level rise of 1 mm/yr in the 40 years between 1954-58 and 1997. In the Indian Ocean along 32°S, Bindoff and McDougall (in press) estimated a rise of 1.6 mm/yr over 25 years. On a global-scale, Douglas (1991) has obtained a mean sea level rise value of 1.8 mm/yr $\pm$ 0.1 over 76 years, based on tide gauge records.

In the IPCC (Intergovernmental Panel on Climate Change) Second Assessment Report, contribution from thermal expansion to sea level rise over the the last 100 years based on model simulations is estimated to be in the range 0.2 to 0.7 mm/yr (p. 380, IPCC (1995)). Thus, these ocean observations are beginning to reveal increases in sea level due to thermal expansion that are larger than that estimated by present numerical models. There is a possibility that the lower rates of sea level rise estimated by the models are a result of the longer time span used in the averaging than most observational studies. In other words, these observational studies may be reflecting an increase in thermal expansion rate in recent decades. Results such as those presented in this thesis are therefore important in providing observational evidence to test the effectiveness of numerical models in simulating the climate system. Such rigor is essential for accurate projection of global climate conditions under an enhanced greenhouse effect.

Chapter 8

Conclusions and Scope for future work

The primary aim of this study is to provide a systematic large-scale analysis of changes in the interior of the North and South Pacific oceans over a roughly 20-year period, using historical data collected mainly from the late 1960s, and five modern trans-oceanic sections collected under the World Ocean Circulation Experiment. In summary, statistically significant changes have been detected in the water masses that occur in the top 2000 dbar of the water column, while properties of the deep waters remain essentially constant, or beyond instrumental detection. This is in accord with the long time-scales, relative to the observations, needed to ventilate the deep waters of the Pacific.

Of all the observed temporal differences between the two sets of observations, the large-scale reduction in salinity of water masses formed at the high-latitude regions of the Southern Ocean and the North Pacific Ocean, namely Antarctic Intermediate Water (AAIW) and North Pacific Intermediate Water (NPIW), is the most striking. This observed freshening in AAIW and NPIW can be due to natural interdecadal variability in the Pacific climate system. However, the implied increased freshwater input into the ocean at the polar regions is qualitatively consistent with results from coupled climate model experiments with increasing greenhouse gases. Similar freshening of AAIW has also been observed by Bindoff and Church (1992), Johnson and Orsi (1997), and Bindoff and McDougall (in press). It is therefore tantalizing to speculate that the freshening of AAIW is circumpolar in extent. The North Atlantic does not produce a significant intermediate salinity minimum, but decadal changes in Labrador Sea Water, which is a water mass that derives its characteristics from the high-latitude North Atlantic, are well documented.

Complementing the salinity reduction in AAIW and NPIW is a salinity increase in North Pacific Subtropical Water (NPSTW) and South Pacific Subtropical Water (SPSTW), both of which derive their properties from under the high evaporative cells of the two subtropical gyres. A possible cause of this increase in salinity is a decreased P-E rate over the mid-latitude regions. The combined implications of the observed changes, of freshening of NPIW and AAIW, and salinification of NPSTW and SPSTW, therefore suggest a strengthening of the hydrological cycle over the study period in the Pacific.

As for temperature changes, the subtropical North Pacific has shown warming of the water column down to 1000 dbar. On the other hand, the subarctic Pacific has experienced an overall heat loss. The observed opposite trend in temperature changes between the subarctic and the subtropical Pacific suggests an oscillatory pattern in the North Pacific climate system as described by Zhang and Levitus (1997). The subtropical South Pacific has warmed to a shallower depth of 300 dbar, but south of 25°S, warming has been detected down to 1000 dbar along the 210°E meridian. Overall, relative to the North Atlantic, the depths to which water mass changes have been detected in the Pacific are shallower, and reflect the deeper mixing mechanisms in the North Atlantic.

This large-scale warming pattern observed in the Pacific Ocean is consistent with the transient response, in the top 300 dbar, of the ocean component of a coupled climate model with increasing atmospheric CO_2. The freshening of NPIW and AAIW in the Pacific is also revealed in the model response, but the spatial distribution of their freshening is different from observations, because of poor water mass structures in the model.

The estimated steric sea level change for the area in the Pacific between 60°N and 31.5°S is a rise of 0.85 mm/yr over the study period of roughly 20 years. This rate is larger than the sea level rise due to thermal expansion estimated by models for the last 100 years, and may reflect an increase in thermal expansion rate in recent decades.

Observational studies such as this are invaluable for understanding large-scale variability of the ocean, and useful for testing the effectiveness of numerical models in simulating the natural variability of the climate system. Such improvements in numerical models are necessary if reliable projection of the climate conditions under the enhanced greenhouse effect is to be made. In order to provide more certainty in making global estimates, more observational studies on temporal changes around the global oceans should therefore be encouraged. Although trans-oceanic sectional comparisons provide information

on changes between time-snapshots and not as time-series, such as those from tide guages and oceanic weather stations, they are useful in providing large-scale estimates of steric sea level change, as well as large-scale information on the spatial nature of water masses changes. They therefore complement well the kind of oceanic variability studies that are based on time-series.

This study has also demonstrated the importance of top-to-bottom CTD data sets in areas with abundant historical data, and of repeat hydrographic sections in general, for climate change detection work. Deep ocean salinity observations are also useful in detecting changes to P-E rates over oceanic regions on a global scale. The South Pacific Ocean is especially sparse in historical hydrographic data. However, comparison work can be done in the mid to high latitudes of the South Pacific if the full Scorpio sections at 28°S and 43°S are repeated. These two sections will add to the reliability of the freshwater content change and steric sea level change estimates of the South Pacific. Repeating the 43°S section will also provide more information on recent changes to AAIW near its formation region. Outside the South Pacific, an exciting and natural extension to this study is to analyse hydrographic data from the South Atlantic Ocean and the South Indian Ocean, so that the circumpolar nature of changes that have occured to AAIW can be investigated.

Appendix A

Using the three "pure" processes to derive a linear system

By the Equation of State, the change in *in-situ* density at a constant pressure z can be expressed as: $\rho^{-1}\rho'|_z = \beta S'|_z - \alpha\theta'|_z$.

By Equations 2.2 and 2.3, changes on isobars and on isopycnals are related, to first order accuracy, by the Taylor's series expansion: $\alpha\theta'|_n - \alpha\theta'|_z = \alpha N'\theta_z$ and $\beta S'|_n - \beta S'|_z = \beta N' S_z$. Together with the definition of a neutral surface (Equation 2.1) and the definition of R_ρ (Equation 2.4), the two variables, $\alpha N'\theta_z$ and $\beta N' S_z$, can be expressed in terms of $\rho^{-1}\rho'|_z$ as:

$$\alpha N'\theta_z = \frac{\rho^{-1}\rho'|_z}{R_\rho - 1} \cdot R_\rho \tag{A.1}$$

$$\beta N' S_z = \frac{\rho^{-1}\rho'|_z}{R_\rho - 1} \tag{A.2}$$

Let A^w, A^f and A^h be the proportion of change that is the result of *pure warming/cooling*, *pure freshening/salinification* and *pure heaving* respectively, and that $A^w + A^f + A^h = 1$. Then the six "observable" variables can be expressed in terms of $\rho^{-1}\rho'|_z$ as follows:

$\alpha N'\theta_z$ and $\beta N' S_z$:

$$\begin{aligned} \alpha N'\theta_z &= \frac{\rho^{-1}\rho'|_z}{R_\rho - 1} R_\rho \cdot [A^w + A^f + A^h] \quad \text{by (A.1)} \\ \beta N' S_z &= \frac{\rho^{-1}\rho'|_z}{R_\rho - 1} \cdot [A^w + A^f + A^h] \quad \text{by (A.2).} \end{aligned}$$

$\underline{\alpha\theta'|_z}$:

$$\begin{aligned}
\alpha\theta'|_z &= -(R_\rho - 1)\,\beta N' S_z && \text{for } \textit{pure warming/cooling} \\
&= -\alpha N' \theta_z && \text{for } \textit{pure heaving} \\
\Longrightarrow \alpha\theta'|_z &= -(R_\rho - 1)\,\beta N' S_z \cdot A^w - \alpha N' \theta_z \cdot A^h \\
&= \frac{\rho^{-1}\rho'|_z}{R_\rho - 1}\left[-(R_\rho - 1)\cdot A^w - R_\rho \cdot A^h\right] && \text{by (A.1) and (A.2).}
\end{aligned}$$

$\underline{\alpha\theta'|_n}$:

$$\begin{aligned}
\alpha\theta'|_n &= \beta N' S_z && \text{for } \textit{pure warming/cooling} \\
&= \alpha N' \theta_z && \text{for } \textit{pure freshening/salinification} \\
\Longrightarrow \alpha\theta'|_n &= \beta N' S_z \cdot A^w + \alpha N' \theta_z \cdot A^f \\
&= \frac{\rho^{-1}\rho'|_z}{R_\rho - 1}\left[A^w + R_\rho \cdot A^f\right] && \text{by (A.1) and (A.2).}
\end{aligned}$$

$\underline{\beta S'|_z}$:

$$\begin{aligned}
\beta S'|_z &= \frac{R_\rho - 1}{R_\rho}\,\alpha N' \theta_z && \text{for } \textit{pure freshening/salinification} \\
&= -\beta N' S_z && \text{for } \textit{pure heaving} \\
\Longrightarrow \beta S'|_z &= \frac{R_\rho - 1}{R_\rho}\,\alpha N' \theta_z \cdot A^f - \beta N' S_z \cdot A^h \\
&= \frac{\rho^{-1}\rho'|_z}{R_\rho - 1}\left[(R_\rho - 1)\cdot A^f - A^h\right] && \text{by (A.1) and (A.2).}
\end{aligned}$$

$\underline{\beta S'|_n}$:

$$\begin{aligned}
\beta S'|_n &= \beta N' S_z && \text{for } \textit{pure warming/cooling} \\
&= \alpha N' \theta_z && \text{for } \textit{pure freshening/salinification} \\
\Longrightarrow \beta S'|_n &= \beta N' S_z \cdot A^w + \alpha N' \theta_z \cdot A^f \\
&= \frac{\rho^{-1}\rho'|_z}{R_\rho - 1}\left[A^w + R_\rho \cdot A^f\right] && \text{by (A.1) and (A.2).}
\end{aligned}$$

These relations are well-defined for all values of R_ρ except when $R_\rho = 1$.

A linear system of the form $\mathrm{G}\,\mathbf{m} = \mathbf{d}$ can now be written as:

$$\frac{\rho^{-1}\rho'|_z}{R_\rho - 1} \cdot \begin{bmatrix} -(R_\rho - 1) & 0 & -R_\rho \\ 1 & R_\rho & 0 \\ R_\rho & R_\rho & R_\rho \\ 0 & (R_\rho - 1) & -1 \\ 1 & R_\rho & 0 \\ 1 & 1 & 1 \end{bmatrix} \cdot \begin{bmatrix} A^w \\ A^f \\ A^h \end{bmatrix} = \begin{bmatrix} \alpha\theta'|_z \\ \alpha\theta'|_n \\ \alpha N'\theta_z \\ \beta S'|_z \\ \beta S'|_n \\ \beta N' S_z \end{bmatrix}$$

In the case where $R_\rho = \pm\infty$, $\alpha\theta'|_n = \beta S'|_n = 0$ in *pure warming/cooling.* This is exactly the criteria for *pure heaving.* Therefore when $R_\rho = \pm\infty$, these two processes collapse into one. $\alpha\theta'|_z = -\alpha N'\theta_z = -\rho^{-1}\rho'|_z$ and $\beta S'|_z = -N'\beta S_z = 0$ for *pure heaving.* $\alpha\theta'|_n = \beta S'|_n = \beta S'|_z = \alpha N'\theta_z = \rho^{-1}\rho'|_z$ for *pure freshening/salinification.* The linear system therefore becomes:

$$\rho^{-1}\rho'|_z \cdot \begin{bmatrix} -1 & 0 & -1 \\ 0 & 1 & 0 \\ 1 & 1 & 1 \\ 0 & 1 & 0 \\ 0 & 1 & 0 \\ 0 & 0 & 0 \end{bmatrix} \cdot \begin{bmatrix} A^w \\ A^f \\ A^h \end{bmatrix} = \begin{bmatrix} \alpha\theta'|_z \\ \alpha\theta'|_n \\ \alpha N'\theta_z \\ \beta S'|_z \\ \beta S'|_n \\ \beta N' S_z \end{bmatrix}$$

$$\Longrightarrow \rho^{-1}\rho'|_z \cdot \begin{bmatrix} -1 & 0 \\ 0 & 1 \\ 1 & 1 \\ 0 & 1 \\ 0 & 1 \\ 0 & 0 \end{bmatrix} \cdot \begin{bmatrix} A^w \parallel A^h \\ A^f \end{bmatrix} = \begin{bmatrix} \alpha\theta'|_z \\ \alpha\theta'|_n \\ \alpha N'\theta_z \\ \beta S'|_z \\ \beta S'|_n \\ \beta N' S_z \end{bmatrix}$$

In the case where $R_\rho = 0$, $\alpha\theta'|_n = \beta S'|_n = 0$ in *pure freshening/salinification.* So *pure freshening/salinification* and *pure heaving* collapse into one process, and the linear system becomes:

$$\rho^{-1}\rho'|_z \cdot \begin{bmatrix} 1 & 0 & 0 \\ 1 & 0 & 0 \\ 0 & 0 & 0 \\ 0 & -1 & -1 \\ 1 & 0 & 0 \\ 1 & 1 & 1 \end{bmatrix} \cdot \begin{bmatrix} A^w \\ A^f \\ A^h \end{bmatrix} = \begin{bmatrix} \alpha\theta'|_z \\ \alpha\theta'|_n \\ \alpha N'\theta_z \\ \beta S'|_z \\ \beta S'|_n \\ \beta N' S_z \end{bmatrix}$$

$$\Longrightarrow \rho^{-1}\rho'|_z \cdot \begin{bmatrix} 1 & 0 \\ 1 & 0 \\ 0 & 0 \\ 0 & -1 \\ 1 & 0 \\ 1 & 1 \end{bmatrix} \cdot \begin{bmatrix} A^w \\ A^f \parallel A^h \end{bmatrix} = \begin{bmatrix} \alpha\theta'|_z \\ \alpha\theta'|_n \\ \alpha N'\theta_z \\ \beta S'|_z \\ \beta S'|_n \\ \beta N' S_z \end{bmatrix}$$

Appendix B

Objective mapping procedure

A description of the method of objective mapping can be found in McIntosh (1990). On each neutral surface, three property fields: potential temperature θ, salinity S and pressure P, have been objectively mapped as follows:

1. For each WOCE transect, a group of nearby historical data, $\mathbf{d}$, is selected for objective mapping to the coordinates of that WOCE transect. The group usually consists of historical casts that are within $\pm 10°$of the WOCE casts. Gross outliers are removed. The distributions of the selected historical data for mapping to the respective WOCE transects can be found in Chapters 4 and 5.

2. The mean value, $\overline{\mathbf{d}}$, of each group of historical data is assumed to be the *a priori* value of the field to be estimated. As each data point d_i contains a true signal s_i and some random noise η_i (i.e. $d_i = s_i + \eta_i$), each group of historical data $\mathbf{d}$ will have associated with it, a signal variance $\mathrm{var}(s_\mathbf{d})$, and a noise variance $\mathrm{var}(\eta_\mathbf{d})$. The signal variance $\mathrm{var}(s_\mathbf{d})$ is estimated by

$$\mathrm{var}(s_\mathbf{d}) = \frac{1}{\mathbf{n}} \sum_{i=1}^{\mathbf{n}} (d_i - \overline{\mathbf{d}})^2$$

where $\mathbf{n}$ is the number of historical data points on the neutral surface. The noise variance $\mathrm{var}(\eta_\mathbf{d})$, also known as the *a priori* noise, is estimated by

$$\mathrm{var}(\eta_\mathbf{d}) = \frac{1}{2\mathbf{n}} \sum_{i=1}^{\mathbf{n}} (d_i - d_j)^2$$

where d_i and d_j are pairs of closest historical data points on the neutral surface. This estimate of the noise variance assumes that the noise has a

short length scale and uniform variance, and that it is uncorrelated over the distance. It also assumes that the signal has uniform variance and a longer correlation distance than the distance between historical points. The noise variance in a data set therefore represents the random processes in the ocean that cannot be measured, such as disturbances caused by mesoscale eddies and internal waves. Note that the noise variance of a data set, as defined above, is different from the instrumental noise.

3. A set of long length scales is used in the first mapping step, where the historical data, $\mathbf{d}$, are mapped to the WOCE coordinates. The long-scale objective estimates at the WOCE coordinates, which are denoted by $\mathbf{d}_{grid}$ here, are given by

$$\mathbf{d}_{grid} = \overline{\mathbf{d}} + C_{dg}C_{dd}^{-1} \cdot (\mathbf{d} - \overline{\mathbf{d}}) \tag{B.1}$$

where C_{dg} denotes the data-grid covariance matrix, multiplied by the signal variance $\mathrm{var}(s_{\mathbf{d}})$. C_{dd} denotes the data-data covariance matrix, multiplied by the signal variance $\mathrm{var}(s_{\mathbf{d}})$, and with the noise variance $\mathrm{var}(\eta_{\mathbf{d}})$ added to the diagonal elements. The covariance function is of the form

$$\mathrm{cov}_{ij} = \exp(-[(\frac{x_i - x_j}{long.scale})^2 + (\frac{y_i - y_j}{lat.scale})^2])$$

with a longitudinal (zonal) scale and a latitudinal (meridional) scale. The longitudinal scale is larger than the latitudinal scale for water masses in the Pacific.

4. Using the same long length scales, the historical data are mapped to itself. The result is subtracted from the original data, and the difference is called the long-scale residuals, $\mathbf{r}$. Associated with this set of residuals $\mathbf{r}$ is another signal variance, $\mathrm{var}(s_{\mathbf{r}})$. It is assumed that the noise variance remains constant, i.e. $\mathrm{var}(\eta_{\mathbf{r}}) = \mathrm{var}(\eta_{\mathbf{d}})$, because, as discussed previously, the noise variance represents the random oceanic processes which cannot be measured, and so does not alter with scales.

5. A set of short length scales is used in the second mapping step, where the long-scale residuals, $\mathbf{r}$, are mapped to the WOCE coordinates by

$$\mathbf{r}_{grid} = \overline{\mathbf{r}} + C_{dg}C_{dd}^{-1} \cdot (\mathbf{r} - \overline{\mathbf{r}}) \tag{B.2}$$

where C_{dg} and C_{dd} are as in Equation B.1, except that $\mathrm{var}(\eta_{\mathbf{r}}) = \mathrm{var}(\eta_{\mathbf{d}})$ and $\mathrm{var}(s_{\mathbf{r}})$ are used. Using the same short length scales, the long-scale

residuals are mapped to itself, and the difference is called the short-scale residuals, ε.

6. The final estimated field at the WOCE coordinates is therefore the sum of the long-scale estimates and the short-scale estimates, $\mathbf{d}_{grid} + \mathbf{r}_{grid}$ (Equations B.1 + B.2).

The different length scales used for mapping to the various WOCE transects are listed below:

WOCE transects	long scale		short scale	
	longitudinal	latitudinal	longitudinal	latitudinal
P1	20°	15°	7°	5°
P3	20°	15°	7°	5°
P4	20°	15°	7°	5°
P16	20°	15°	7°	5°
S4	25°	15°	8°	5°
P21	20°	15°	8°	7°
SR3	25°	15°	8°	5°

In objective mapping, the choice of length scales depends on the features that need to be resolved and the separation of the data points. Scales that are too long will give just the overall mean and not many features, while scales that are too short will produce "bull's eyes" in the map. A good way to judge whether the length scales are appropriate for mapping of a data set is to consider the residuals. Since the residuals are the difference between the original data and the result of the data being mapped to itself, they are a good indicator of how well the objective map fits the data. In a good-fit map, the statistical distribution of the residuals should resemble that of the *a priori* noise in the original data.

In our two-step mapping procedure, the residuals to be considered are the short-scale residuals, ε. The mean of ε should be close to zero. The ratio of the standard deviation of ε, to the standard deviation of the noise in the original data set, should be close to 1 if the map is a good fit, i.e.

$$\frac{\text{std. dev.}\,(\varepsilon)}{\sqrt{\text{var}(\eta_d)}} \approx 1 \tag{B.3}$$

If the ratio is smaller than 1, the length scales used are likely to be too short. If the ratio is greater than 1, the length scales used are likely to be too long.

The advantage of using a two-step mapping procedure is to resolve features on two different length scales, but not to reduce the mapping errors. In fact, the long-scale estimates alone will give smaller mapping errors because using long length scales means that more data are being averaged. Examination of the mapping errors confirmed that errors associated with the long-scale estimates $\mathbf{d}_{grid}$ are small, so it is justified to only consider the errors from the short-scale estimates $\mathbf{r}_{grid}$ as the overall mapping error associated with this two-step mapping. For each grid point i, the mapping error is thus given by the square root of the error variance from $\mathbf{r}_{grid}$:

$$\sqrt{\mathrm{var}(s_\mathrm{r}) - (\mathrm{i^{th}\ row\ of}\ C_{dg}) \cdot C_{dd}^{-1} \cdot (\mathrm{i^{th}\ row\ of}\ C_{dg})^\mathrm{T}} \qquad \text{(B.4)}$$

Appendix C

Confidence intervals

All confidence intervals used in this thesis have been calculated at the 90% level, based on the T-distribution. Formally, let $\mathbf{X} = \{X_1, X_2, \ldots, X_k\}$ be a random sample of a normal random variable with mean μ and variance σ^2. Then the 90% confidence interval for μ is $\overline{\mathbf{X}} \pm \frac{E \cdot T^k_{0.95}}{\sqrt{k}}$ (Larson (1982), p.385).

Strictly speaking, E is calculated from $E^2 = \frac{1}{k-1}\sum_{i=1}^{k}(X_i - \overline{\mathbf{X}})^2$. E^2 is called the sample variance and has expected value σ^2. $E = \sqrt{E^2}$ is called the sample standard deviation and gives a sense of how "spread out" the sample is. In other words, it is equivalent to the noise within a set of measurements. However, E^2 defined in this manner is the same as the signal variance $\mathrm{var}(s_{\mathbf{X}})$ discussed in Appendix B. To be consistent within the framework set down in Appendix B, we deviate from the formal definition and, instead, use the noise variance $\mathrm{var}(\eta_{\mathbf{X}})$ to calculate the confidence intervals. Hence, on every neutral surface, the 90% confidence interval for the mean value of any set of properties $\mathbf{X}$ is

$$\overline{\mathbf{X}} \pm \frac{\sqrt{\mathrm{var}(\eta_{\mathbf{X}})} \cdot T^k_{0.95}}{\sqrt{k}}$$

This defines the basic equation used in the calculations of confidence intervals in this thesis. However, the final method is different for every variable. The following details the methods of evaluation of confidence intervals for the various variables in this thesis. To avoid clumsy notations, we will hereafter denote $\mathrm{var}(\eta_{\mathbf{X}})$ by $E^2_{\mathbf{X}}$, and $\sqrt{\mathrm{var}(\eta_{\mathbf{X}})}$ by $E_{\mathbf{X}}$.

$\overline{\theta'|_n}$, $\overline{S'|_n}$, $\overline{P'|_n}$

When discussing $\overline{\theta'|_n}$, such as those in Figure 4.11 in Chapter 4, the random sample concerned is the set of $\{\theta_{woce} - \theta_{historical}\}$ on a neutral surface, and the 90% confidence interval for $\overline{\theta'|_n}$ is

$$\overline{\theta'|_n} \pm \frac{E_{\theta_{woce}-\theta_{historical}}|_n \cdot T^k_{0.95}}{\sqrt{k}}$$

where $E^2_{\theta_{woce}-\theta_{historical}}|_n = E^2_{\theta_{woce}}|_n + E^2_{\theta_{historical}}|_n$. However, on any neutral surface, the differences between closest station pairs in the WOCE data are smaller than those in the historical data, i.e. $E^2_{\theta_{woce}}|_n < E^2_{\theta_{historical}}|_n$, because the historical data are more widely spaced. Therefore, $E^2_{\theta_{woce}-\theta_{historical}}|_n < 2 \cdot E^2_{\theta_{historical}}|_n$. Consequently, a conservative approximation is made and all confidence intervals for $\overline{\theta'|_n}$ are calculated as

$$\overline{\theta'|_n} \pm \frac{\sqrt{2} \cdot E_{\theta_{historical}}|_n \cdot T^k_{0\,95}}{\sqrt{k}} \qquad \text{(C.1)}$$

where

$$E^2_{\theta_{historical}|_n} = \frac{1}{2\mathbf{n}} \sum_{i=1}^{\mathbf{n}} (\theta_i|_n - \theta_j|_n)^2$$

$\mathbf{n}$ is the total number of data points on the neutral surface (all data points on the neutral surface are used in the evaluation of E^2), and $(\theta_i|_n\,,\,\theta_j|_n)$ are the closest station pairs in the historical data on the neutral surface. Similarly, 90% confidence interval for $\overline{S'|_n}$ is

$$\overline{S'|_n} \pm \frac{\sqrt{2} \cdot E_{S_{historical}}|_n \cdot T^k_{0\,95}}{\sqrt{k}}$$

and for $\overline{P'|_n}$,

$$\overline{P'|_n} \pm \frac{\sqrt{2} \cdot E_{P_{historical}}|_n \cdot T^k_{0.95}}{\sqrt{k}}$$

Note that $\overline{P'|_n}$ is the same as $\overline{N'}$.

$\overline{\alpha\theta'|_n}$, $\overline{\beta S'|_n}$, $\overline{\alpha\theta'|_z}$, $\overline{\beta S'|_z}$, $\overline{\alpha N'\theta_z}$, $\overline{\beta N'S_z}$

The confidence intervals for these 6 variables, although not directly quoted in the text, have been used in the calculations for the confidence intervals for $\overline{\rho^{-1}\rho'|_z A^w}$, $\overline{\rho^{-1}\rho'|_z A^f}$, and $\overline{\rho^{-1}\rho'|_z A^h}$. Hence it is essential that they are defined explicitly here. The equations are essentially the same as Equation C.1; the only difference is with the calculations of the respective E^2.

Following the same deduction as for Equation C.1, the 90% confidence interval for $\overline{\alpha\theta'|_n}$ on a neutral surface is

$$\overline{\alpha\theta'|_n} \pm \frac{\sqrt{2} \cdot E_{\alpha\theta_{historical}}|_n \cdot T^k_{0.95}}{\sqrt{k}} \tag{C.2}$$

where

$$E^2_{\alpha\theta_{historical}}|_n = \frac{1}{2\mathbf{n}} \sum_{i=1}^{\mathbf{n}} [\alpha_{p_m} \cdot (\theta_i|_n - \theta_j|_n)]^2$$

Here, p_m is the average depth of the neutral surface between points i and j in the historical data set; $\mathbf{n}$ and $(\theta_i|_n\,,\,\theta_j|_n)$ are as defined before. Similarly, the 90% confidence interval for $\overline{\beta S'|_n}$ is

$$\overline{\beta S'|_n} \pm \frac{\sqrt{2} \cdot E_{\beta S_{historical}}|_n \cdot T^k_{0\,95}}{\sqrt{k}} \tag{C.3}$$

For $\overline{\alpha\theta'|_z}$ and $\overline{\beta S'|_z}$ associated with a neutral surface, the 90% confidence intervals are, respectively,

$$\overline{\alpha\theta'|_z} \pm \frac{\sqrt{2} \cdot E_{\alpha\theta_{historical}}|_z \cdot T^k_{0.95}}{\sqrt{k}} \tag{C.4}$$

and

$$\overline{\beta S'|_z} \pm \frac{\sqrt{2} \cdot E_{\beta S_{historical}}|_z \cdot T^k_{0.95}}{\sqrt{k}} \tag{C.5}$$

where

$$E^2_{\alpha\theta_{historical}}|_z = \frac{1}{2\mathbf{n}} \sum_{i=1}^{\mathbf{n}} [\alpha_{p_m} \cdot (\theta_i|_z - \theta_j|_z)]^2$$

Points i and j are still the closest station pairs on the neutral surface in the

historical data, while $\theta_i|_z$ and $\theta_j|_z$ have been linearly interpolated to p_m, defined above.

For $\overline{\alpha N'\theta_z}$ and $\overline{\beta N'S_z}$, the 90% confidence intervals are, respectively,

$$\overline{\alpha N'\theta_z} \pm \frac{\sqrt{2} \cdot E_{\alpha N'\theta_z|_{historical}} \cdot T^k_{0\,95}}{\sqrt{k}} \tag{C.6}$$

$$\overline{\beta N'S_z} \pm \frac{\sqrt{2} \cdot E_{\beta N'S_z|_{historical}} \cdot T^k_{0.95}}{\sqrt{k}} \tag{C.7}$$

We make use of the Taylor's series $\alpha N'\theta_z = \alpha\theta'|_n - \alpha\theta'|_z$ (see Appendix A), and evaluate $E_{\alpha N'\theta_z|_{historical}}$ from

$$E^2_{\alpha N'\theta_z|_{historical}} = \frac{1}{2\mathrm{n}} \sum_{i=1}^{\mathrm{n}} [\alpha_{p_m} \cdot (\theta_i|_n - \theta_j|_n) - \alpha_{p_m} \cdot (\theta_i|_z - \theta_j|_z)]^2$$

$\overline{\rho^{-1}\rho'|_z A^w}$, $\overline{\rho^{-1}\rho'|_z A^f}$, $\overline{\rho^{-1}\rho'|_z A^h}$

The confidence intervals for these 3 variables on a neutral surface are,

$$\overline{\rho^{-1}\rho'|_z A^w} \pm D_{\rho^{-1}\rho'|_z A^w}$$

$$\overline{\rho^{-1}\rho'|_z A^f} \pm D_{\rho^{-1}\rho'|_z A^f}$$

$$\overline{\rho^{-1}\rho'|_z A^h} \pm D_{\rho^{-1}\rho'|_z A^h}$$

The evaluation of $D_{\rho^{-1}\rho'|_z A^w}$, $D_{\rho^{-1}\rho'|_z A^f}$, and $D_{\rho^{-1}\rho'|_z A^h}$ leans on some basic inverse theory. In a linear system $\mathrm{G}\,\mathbf{m} = \mathbf{d}$, the covariance of the model parameters $\mathbf{m}$ depends on the covariance of the data $\mathbf{d}$, and is a function of G and the generalised inverse G^{-g}. If the data $\mathbf{d}$ are uncorrelated, and have uniform variance $\sigma^2_{\mathbf{d}}$, then a data covariance matrix [cov $\mathbf{d}$] can be written as

$$[\operatorname{cov} \mathbf{d}] = \begin{bmatrix} \sigma_{\mathbf{d}}^2 & \cdots & 0 \\ \vdots & \sigma_{\mathbf{d}}^2 & \\ 0 & & \ddots \end{bmatrix}$$

where the diagonal elements are $\sigma_{\mathbf{d}}^2$, and the off-diagonal elements are zeros. A model convariance matrix [cov **m**] can then be defined as

$$[\operatorname{cov} \mathbf{m}] = \mathrm{G}^{-g} [\operatorname{cov} \mathbf{d}] \mathrm{G}^{-g^{\mathrm{T}}}$$

(Menke (1984), p.27, 65). In anology to the covariance matrices, a matrix $[D_{\mathbf{m}}^2]$ can be defined as

$$[D_{\mathbf{m}}^2] = \mathrm{G}^{-g} [D_{\mathbf{d}}^2] \mathrm{G}^{-g^{\mathrm{T}}} \tag{C.8}$$

The model parameters that are of concern here, are $\mathbf{m} = \left[\overline{\rho^{-1}\rho'|_z A^w}, \overline{\rho^{-1}\rho'|_z A^f}, \overline{\rho^{-1}\rho'|_z A^h} \right]$. With G defined as in Appendix A, and $\mathrm{G}^{-g} = W V_k \Lambda_k^{-1} U_k^{\mathrm{T}}$ as defined in Chapter 2 (Section 2.4, Equation 2.10), the corresponding data are $\mathbf{d} = \left[\overline{\alpha\theta'|_z}, \overline{\alpha\theta'|_n}, \overline{\alpha N'\theta_z}, \overline{\beta S'|_z}, \overline{\beta S'|_n}, \overline{\beta N' S_z} \right]$. Equation C.8 can therefore be written as

$$\begin{bmatrix} D^2_{\overline{\rho^{-1}\rho'|_z A^w}} & \cdots & \\ & D^2_{\overline{\rho^{-1}\rho'|_z A^f}} & \\ \vdots & & D^2_{\overline{\rho^{-1}\rho'|_z A^h}} \end{bmatrix}$$

$$= \mathrm{G}^{-g} \begin{bmatrix} D^2_{\alpha\theta'|_z} & & \cdots & & & 0 \\ & D^2_{\alpha\theta'|_n} & & & & \\ \vdots & & D^2_{\alpha N'\theta_z} & & & \vdots \\ & & & D^2_{\beta S'|_z} & & \\ & & & & D^2_{\beta S'|_n} & \\ 0 & & \cdots & & & D^2_{\beta N' S_z} \end{bmatrix} \mathrm{G}^{-g^{\mathrm{T}}}$$

The 6 diagonal elements in the 6×6 matrix can be obtained from Equations C.2 to C.7. For example, $D_{\alpha\theta'|_z} = \dfrac{\sqrt{2} \cdot E_{\alpha\theta_{historical}|_z} \cdot T^k_{0\,95}}{\sqrt{k}}$. The square root of the 3 diagonal elements of the 3×3 matrix are then used in the calculations of confidence intervals for $\overline{\rho^{-1}\rho'|_z A^w}$, $\overline{\rho^{-1}\rho'|_z A^f}$ and $\overline{\rho^{-1}\rho'|_z A^h}$.

One last word concerning all confidence intervals ...

When the mean values are taken over different portions of a transect, the value of k changes (i.e. the number of data points in the portion). On every neutral surface, $\mathrm{var}(\eta_{\mathbf{X}})$ is calculated using all data points on the neutral surface, so $\mathrm{var}(\eta_{\mathbf{X}})$ is a constant. The value of $T^k_{0.95}$, will, of course, vary according to k, but for ease of computation, $T^k_{0\,95}$ has been fixed at 1.658, where $k = 120$. Therefore the only difference between averaging over different portions of a transect, is that the denominator $\sqrt{k}$ will vary. So when averaging over a shorter portion, the confidence intervals will be larger than when averaging over a wider portion on the same neutral surface. For $k > 120$, the value of $T^k_{0.95}$ differs from $T^{120}_{0\,95}$ by less than 0.013. Hence the error associated with fixing $T^k_{0\,95}$ at 1.658 is small (less than 1%).

References

Antonov, J., 1993: Linear trends of temperature at intermediate and deep layers of the North Atlantic and the North Pacific Oceans: 1957-1981, *Journal of Climate*, **6**, 1928–1942.

Barnett, T., and M. Schlesinger, 1987: Detecting changes in global climate induced by greenhouse gases, *Journal of Geophysical Research*, **92**(D12), 14772–14780.

Bindoff, N., and J. Church, 1992: Warming of the water column in the southwest Pacific Ocean, *Nature*, **357**, 59–62.

———, and T. McDougall, 1994: Diagnosing climate change and ocean ventilation using hydrographic data, *Journal of Physical Oceanography*, **24**(6), 1137–1152.

Bindoff, N., and ———, in press: Decadal changes along an Indian Ocean section at 32°S and their interpretation.

———, and C. Wunsch, 1992: Comparison of synoptic and climatologically mapped sections in the South Pacific Ocean, *Journal of Climate*, **5**(6), 631–645.

Bingham, F., T. Suga and K. Hanawa, 1992: Comparison of upper ocean thermal conditions in the western North Pacific between two pentads: 1938-42 and 1978-82, *Journal of Oceanography*, **48**, 405–425.

Bretherton, F., R. Davis and C. Fandry, 1976: A technique for objective analysis and design of oceanographic experiments applied to MODE-73, *Deep-Sea Research*, **23**, 559–582.

Brewer, P., W. Broecker, W. Jenkins, P. Rhines, C. Rooth, J. Swift, T. Takahashi and R. Williams, 1983: A climatic freshening of the deep Atlantic north of 50°N over the past 20 years, *Science*, **222**, 1237–1239.

Bryden, H., M. Griffiths, A. Lavin, R. Millard, G. Parrilla and W. Smethie, 1996: Decadal changes in water mass characteristics at 24°N in the subtropical North Atlantic Ocean, *Journal of Climate*, **9**(12 Part 1), 3162–3186.

Budd, W., P. Reid and L. Minty, 1995: Antartic moisture flux and net accumulation from global atmospheric analyses, *Annals of Glaciology*, **21**, 149–156.

Church, J., J. Godfrey, D. Jackett and T. McDougall, 1991: A model of sea level rise caused by ocean thermal expansion, *Journal of Climate*, **4**, 438–456.

Cochrane, J., 1958: The frequency distribution of water characteristics in the Pacific Ocean, *Deep-Sea Research*, **5**, 111–127.

Curry, R., M. McCartney and T. Joyce, 1998: Oceanic transport of subpolar climate signals to mid-depth subtropical waters, *Nature*, **391**, 575–577.

Dickson, R., J. Lazier, J. Meincke, P. Rhines and J. Swift, 1996: Long-term coordinated changes in the convective activity of the North Atlantic, *Progress in Oceanography*, **38**, 241–295.

Douglas, B., 1991: Global sea level rise, *Journal of Geophysical Research*, **96**(C4), 6981–6992.

Favorite, F., A. Dodimead and K. Nasu, 1976: Oceanography of the subarctic Pacific region, 1960-71, *International North Pacific Fisheries Commission Bulletin*, **33**, 1–187.

Freeland, H., and F. Whitney, 1997: Evidence of secular change in the northeast Pacific Ocean, *International WOCE Newsletter*, **26**, 34–36.

Garreaud, R., and D. Battisti, 1999: Interannual (ENSO) and interdecadal (ENSO-like) variability in the southern hemisphere tropospheric circulation, *Journal of Climate*, **12**(7), 2113–2123.

Gent, P., and J. McWilliams, 1990: Isopycnal mixing in ocean circulation models, *Journal of Physical Oceanography*, **20**, 150–155.

Gill, A., 1982: *Atmosphere-ocean dynamics*, Academic Press, New York.

Gordon, A., E. Molinelli and T. Baker, 1982: *Southern Ocean Atlas*, Columbia University Press, New York.

Gordon, H., and S. O'Farrell, 1997: Transient climate change in the CSIRO coupled model with dynamic sea ice, *Monthly Weather Review*, **125**(5), 875–907.

Graham, N., 1994: Decadal-scale climate variability in the tropical and North Pacific during the 1970s and 1980s: observations and model results, *Climate Dynamics*, **10**, 135–162.

Hanawa, K., and T. Suga, 1995: A review on the subtropical mode water of the North Pacific (NPSTMW), in *Biogeochemical Processes and Ocean Fluxes in the Western Pacific*, edited by H. Sakai, and Y. Nozaki, pp. 613–627, Terra Scientific Publishing Company, Tokyo.

Harris, J., 1996: Mean Southern Ocean Circulation from Raw Hydrographic Data, Ph.D. thesis, University of Tasmania.

Hirst, A., in press: The Southern Ocean response to global warming in the CSIRO

coupled ocean-atmosphere model, *Environmental Modeling and Software: Special issue on Global Change.*

———, and T. McDougall, 1996: Deep-water properties and surface buoyancy flux as simulated by a z-coordinate model including eddy-induced advection, *Journal of Physical Oceanography*, **26**(7), 1320–1343.

Holbrook, N., and N. Bindoff, 1997: Interannual and decadal temperature variability in the southwest Pacific Ocean between 1955 and 1988, *Journal of Climate*, **10**(5), 1035–1049.

Huang, R., and B. Qiu, 1994: Three-dimensional structure of the wind-driven circulation in the subtropical North Pacific, *Journal of Physical Oceanography*, **24**(7), 1608–1622.

IPCC, 1995: *Climate Change 1995: The Science of Climate Change*, Cambridge University Press, Cambridge.

Jackett, D., and T. McDougall, 1995: Neutral density, *International WOCE Newsletter*, **19**, 30–33.

———, and ———, 1997: A neutral density variable for the world's oceans, *Journal of Physical Oceanography*, **27**(2), 237–263.

Jacobs, G., H. Hurlburt, J. Kindle, E. Metzger, J. Mitchell, W. Teague and A. Wallcraft, 1994: Decade-scale trans-Pacific propagation and warming effects of an El Niño anomaly, *Nature*, **370**, 360–363.

Johnson, G., and D. Moore, 1997: The Pacific subsurface countercurrents and an inertial model, *Journal of Physical Oceanography*, **27**, 2448–2459.

———, and A. Orsi, 1997: Southwest Pacific Ocean water mass changes between 1968/9 and 1990/1, *Journal of Climate*, **10**(2), 306–316.

Johnson, G., D. Rudnick and B. Taft, 1994: Bottom water variability in the Samoa Passage, *Journal of Marine Research*, **52**, 177–196.

Jones, P., 1988: Hemispheric surface air temperature variations: recent trends and an update to 1987, *Journal of Climate*, **1**, 654–660.

Joyce, T., R. Pickart and R. Millard, 1999: Long-term hydrographic changes at 52 and 66°W in the North Atlantic subtropical gyre & Caribbean, *Deep-Sea Research*, **46**, 245–278.

———, and P. Robbins, 1996: The long-term hydrographic record at Bermuda,

Journal of Climate, **9**(12), 3121–3131.

Karoly, D., J. Cohen, G. Meehl, J. Mitchell, A. Oort, R. Stouffer and R. Wetherald, 1994: An example of fingerprint detection of greenhouse climate change, *Climate Dynamics*, **10**, 97–105.

Kessler, W., in press: Interannual variability of the subsurface high-salinity tongue south of the equator at 165°E, *Journal of Physical Oceanography.*

Larson, H., 1982: *Introduction to probability theory and statistical inference*, John Wiley & Sons, New York, 3rd edition.

Latif, M., and T. Barnett, 1994: Causes of decadal climate variability over the North Pacific and North America, *Science*, **266**, 634–637.

———, and ———, 1996: Decadal climate variability over the North Pacific and North America: dynamics and predictability, *Journal of Climate*, **9**(10), 2407–2423.

Levitus, S., 1982: *Climatological Atlas of the World Ocean*, NOAA Professional Paper 13, National Oceanic and Atmospheric Administration, U.S. Department of Commerce, Washington, D.C.

———, 1989: Interpentadal variability of temperature and salinity at intermediate depths of the North Atlantic Ocean, 1970-1974 versus 1955-1959, *Journal of Geophysical Research*, **94**(C5), 6091–6131.

Levitus, S., J. Antonov and T. Boyer, 1994: Interannual variability of temperature at a depth of 125 meters in the North Atlantic Ocean, *Science*, **266**, 96–99.

Lie, H., and M. Endoh, 1991: Seasonal and interannual variability in temperature of the upper layer of the northwest Pacific, 1964-1983, *Journal of Physical Oceanography*, **21**, 385–397.

Lozier, M., M. McCartney and W. Owens, 1994: Anomalous anomalies in averaged hydrographic data, *Journal of Physical Oceanography*, **24**(12), 2624–2638.

Luyten, J., J. Pedlosky and H. Stommel, 1983: The ventilated thermocline, *Journal of Physical Oceanography*, **13(2)**, 292–309.

Manabe, S., K. Bryan and M. Spelman, 1990: Transient response of a global ocean-atmosphere model to a doubling of atmospheric carbon dioxide, *Journal of Physical Oceanography*, **20**, 722–749.

Mantua, N., S. Hare, Y. Zhang, J. Wallace and R. Francis, 1997: A Pacific interdecadal climate oscillation with impacts on salmon production, *Bulletin of the*

American Meteorological Society, **78**(6), 1069–1079.

Mantyla, A., and J. Reid, 1983: Abyssal characteristics of the world ocean waters, *Deep-Sea Research*, **30**(8A), 805–833.

McCartney, M., 1977: Subantarctic Mode Water, *Deep-Sea Research*, **24**(Suppl.), 103–119.

McDougall, T., 1987: Neutral surfaces, *Journal of Physical Oceanography*, **17**, 1950–1964.

McIntosh, P., 1990: Oceanographic data interpolation: objective analysis and splines, *Journal of Geophysical Research*, **95**(C8), 13529–13541.

Menke, W., 1984: *Geophysical data analysis: discrete inverse theory*, Academic Press, Orlando, Florida, USA.

Mikolajewicz, U., B. Santer and E. Maier-Reimer, 1990: Ocean response to greenhouse warming, *Nature*, **345**, 589–593.

Olbers, D., V. Gouretski, G. Seib and J. Schröter, 1992: *Hydrographic Atlas of the Southern Ocean*, Alfred Wegener Institute, Bremerhaven.

Parker, D., P. Jones, C. Folland and A. Bevan, 1994: Interdecadal changes of surface temperature since the late nineteenth century, *Journal of Geophysical Research - Atmosphere*, **99**(D7), 14373–14399.

Parrilla, G., A. Lavin, H. Bryden, M. Garcia and R. Millard, 1994: Rising temperatures in the subtropical North Atlantic Ocean over the past 35 years, *Nature*, **369**, 48–51.

Piola, A., and D. Georgi, 1982: Circumpolar properties of Antarctic Intermediate Water and Subantarctic Mode Water, *Deep-Sea Research*, **29**(6A), 687–711.

Qiu, B., and T. Joyce, 1992: Interannual variability in the mid- and low-latitude western North Pacific, *Journal of Physical Oceanography*, **22**, 1062–1079.

Read, J., and W. Gould, 1992: Cooling and freshening of the subpolar North Atlantic Ocean since the 1960s, *Nature*, **360**, 55–57.

Reid, J., 1965: *Intermediate waters of the Pacific Ocean*, The Johns Hopkins Oceanographic Studies Number 2, The Johns Hopkins Press, Baltimore.

———, 1973: The shallow salinity minima of the Pacific Ocean, *Deep-Sea Research*, **20**, 51–68.

Ridgway, K., and J. Godfrey, 1996: Long-term temperature and circulation changes off eastern Australia, *Journal of Geophysical Research*, **101**(C2), 3615–3627.

Roemmich, D., 1983: Optimal estimation of hydrographic station data and derived fields, *Journal of Physical Oceanography*, **13**, 1544–1549.

———, 1992: Ocean warming and sea level rise along the southwest U.S. coast, *Science*, **257**, 373–375.

Roemmich, D., and T. McCallister, 1989: Large scale circulation of the North Pacific Ocean, *Progress in Oceanography*, **22**, 171–204.

———, ——— and J. Swift, 1991: A transpacific hydrographic section along latitude 24°N: the distribution of properties in the subtropical gyre, *Deep-Sea Research*, **38**(Suppl. 1), S1–S20.

Roemmich, D., and C. Wunsch, 1984: Apparent changes in the climatic state of the deep North Atlantic Ocean, *Nature*, **307**, 447–450.

Santer, B., U. Mikolajewicz, W. Brüggemann, U. Cubasch, K. Hasselmann, H. Höck, E. Maier-Reimer and T. Wigley, 1995: Ocean variability and its influence on the detectability of greenhouse warming signals, *Journal of Geophysical Research*, **100**(C6), 10693–10725.

Shuto, K., 1996: Interannual variations of water temperature and salinity along the 137°E meridian, *Journal of Oceanography*, **52**, 575–595.

Stouffer, R., S. Manabe and K. Bryan, 1989: Interhemispheric asymmetry in climate response to a gradual increase of atmospheric CO_2, *Nature*, **342**, 660–662.

Suga, T., and K. Hanawa, 1995: The Subtropical Mode Water circulation in the North Pacific, *Journal of Physical Oceanography*, **25**(5), 958–970.

———, and ———, 1995a: Interannual variations of North Pacific Subtropical Mode Water in the 137°E section, *Journal of Physical Oceanography*, **25**, 1012–1017.

Suga, T., K. Hanawa and Y. Toba, 1989: Subtropical Mode Water in the 137°E section, *Journal of Physical Oceanography*, **19**(10), 1605–1618.

Sverdrup, H., M. Johnson and R. Fleming, 1946: *The Oceans: their physics, chemistry, and general biology*, Prentice-Hall, New York.

Swift, J., 1995: Comparing WOCE and historical temperatures in the deep southeast Pacific, *International WOCE Newsletter*, **18**, 15–17.

Taft, B., 1995: Subarctic gyre of the western Pacific, *International WOCE Newsletter*, **19**, 6–8.

Talley, L., 1985: Ventilation of the subtropical North Pacific: the shallow salinity minimum, *Journal of Physical Oceanography*, **15**, 633–649.

———, 1991: An Okhotsk Sea water anomaly: implications for ventilation in the North Pacific, *Deep-Sea Research*, **38**(Suppl. 1), S171–S190.

Talley, L., 1993: Distribution and formation of North Pacific Intermediate Water, *Journal of Physical Oceanography*, **23**, 517–537.

———, T. Joyce and R. DeSzoeke, 1991: Transpacific sections at 47°N and 152°W: distribution of properties, *Deep-Sea Research*, **38**(Suppl. 1), S63–S82.

Tanimoto, Y., N. Iwasaka, K. Hanawa and Y. Toba, 1993: Characteristic variations of sea surface temperature with multiple time scales in the North Pacific, *Journal of Climate*, **6**, 1153–1160.

Tereschenkov, V., A. Sokov and S. Dobroliubov, 1995: WHP section A3 across 36°N aboard RV Professor Multanovskiy, *International WOCE Newsletter*, **19**, 25–27.

Thomson, R., and S. Tabata, 1987: Steric height trends at Ocean Station PAPA in the northeast Pacific Ocean, *Marine Geodesy*, **11**, 103–113.

Toggweiler, J., K. Dixon and W. Broecker, 1991: The Peru upwelling and the ventilation of the South Pacific thermocline, *Journal of Geophysical Research*, **96**(C11), 20467–20497.

Tomczak, M., and J. Godfrey, 1994: *Regional Oceanography: An Introduction*, Pergamon Press, Britain, 1st edition.

Trenberth, K., and J. Hurrell, 1994: Decadal atmosphere-ocean variations in the Pacific, *Climate Dynamics*, **9**, 303–319.

Tsuchiya, M., 1968: *Upper waters of the intertropical Pacific Ocean*, The Johns Hopkins Oceanographic Studies Number 4, The Johns Hopkins Press, Baltimore.

———, 1981: The origin of the Pacific Equatorial 13°C Water, *Journal of Physical Oceanography*, **11**, 794–812.

Tsuchiya, M., 1982: On the Pacific upper-water circulation, *Journal of Marine Research*, **40**(Suppl.), 777–799.

———, 1991: Flow path of the Antarctic Intermediate Water in the western

equatorial South Pacific Ocean, *Deep-Sea Research*, **38**(Suppl. 1), S273–S280.

Tsuchiya, M., and L. Talley, 1996: Water-property distributions along an eastern Pacific hydrographic section at 135W, *Journal of Marine Research*, **54**, 541–564.

———, and ———, 1998: A Pacific hydrographic section at 88°W: water-property distribution, *Journal of Geophysical Research*, **103**(C6), 12899–12918.

Turner, J., 1981: Small-scale mixing processes, in *Evolution of Physical Oceanography*, edited by B. Warren, and C. Wunsch, pp. 236–263, MIT Press, Cambridge, Massachusetts.

Van Scoy, K., R. Fine and H. Göte Östlund, 1991: Two decades of mixing tritium into the North Pacific Ocean, *Deep-Sea Research*, **38**(Suppl. 1), S191–S219.

Warner, M., J. Bullister, D. Wisegarver, R. Gammon and R. Weiss, 1996: Basin-wide distributions of chlorofluorocarbons CFC-11 and CFC-12 in the North Pacific: 1985-1989, *Journal of Geophysical Research*, **101**(C9), 20525–20542.

Watanabe, T., and K. Mizuno, 1994: Decadal changes of the thermal structure in the North Pacific, *International WOCE Newsletter*, **15**, 10–13.

White, W., and R. Peterson, 1996: An Antarctic circumpolar wave in surface pressure, wind, temperature and sea-ice extent, *Nature*, **380**, 699–702.

Wijffels, S., E. Firing and J. Toole, 1995: The mean structure and variability of the Mindanao Current at 8°N, *Journal of Geophysical Research*, **100**(C9), 18421–18435.

———, M. Hall, T. Joyce, D. Torres, P. Hacker and E. Firing, 1998: Multiple deep gyres of the western North Pacific - a WOCE section along 149°E, *Journal of Geophysical Research*, **103**(C6), 12985–13009.

Wijffels, S., J. Toole, H. Bryden, R. Fine, W. Jenkins and J. Bullister, 1996: The water masses and circulation at 10°N in the Pacific, *Deep-Sea Research*, **43**(4), 501–544.

Wong, A., N. Bindoff and J. Church, 1999: Large-scale freshening of intermediate waters in the Pacific and Indian oceans, *Nature*, **400**, 440–443.

Woods, J., 1985: The physics of thermocline ventilation, in *Coupled Ocean-Atmosphere Models*, edited by J. Nihoul, pp. 543–590, Elsevier Oceanography Series, Amsterdam.

Wyrtki, K., and B. Kilonsky, 1984: Mean water and current structure during the Hawaii-to-Tahiti Shuttle Experiment, *Journal of Physical Oceanography*, **14**,

242–254.

Yuan, X., and L. Talley, 1992: Shallow salinity minima in the North Pacific, *Journal of Physical Oceanography*, **22**, 1302–1316.

Zhang, R., and S. Levitus, 1997: Structure and cycle of decadal variability of upper-ocean temperature in the North Pacific, *Journal of Climate*, **10**(4), 710–727.